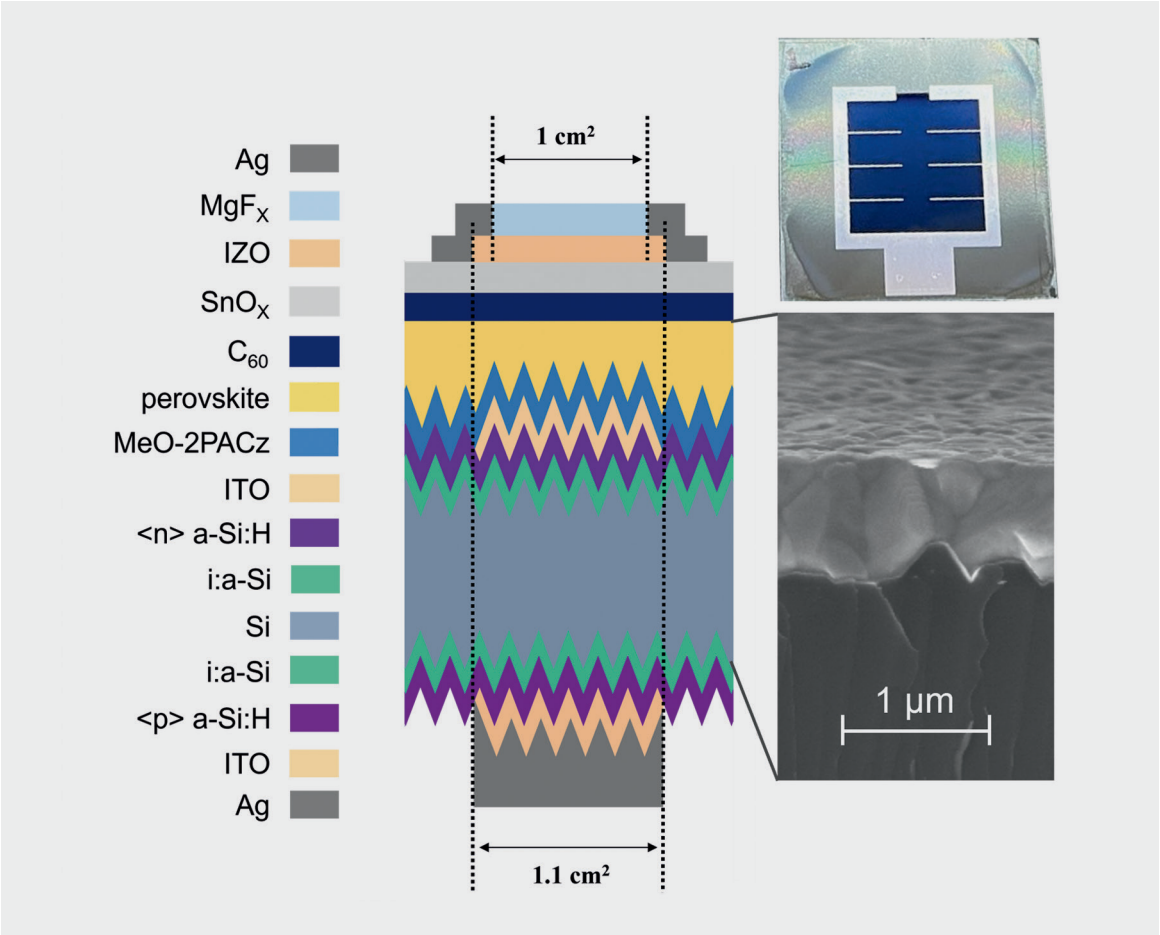

Development of High-Efficiency Perovskite / Silicon Tandem Solar Cells

Qing Yang

Energie & Umwelt / Energy & Environment
Band / Volume 710
ISBN 978-3-95806-921-3

Mitglied der Helmholtz-Gemeinschaft

JÜLICH
Forschungszentrum

Schriften des Forschungszentrums Jülich
Reihe Energie & Umwelt / Energy & Environment Band / Volume 710

Forschungszentrum Jülich GmbH
Institute of Energy Materials and Devices (IMD)
Photovoltaik (IMD-3)

Development of High-Efficiency Perovskite/Silicon Tandem Solar Cells

Qing Yang

Schriften des Forschungszentrums Jülich
Reihe Energie & Umwelt / Energy & Environment Band / Volume 710

ISSN 1866-1793 ISBN 978-3-95806-921-3

Bibliografische Information der Deutschen Nationalbibliothek.
Die Deutsche Nationalbibliothek verzeichnet diese Publikation in der
Deutschen Nationalbibliografie; detaillierte Bibliografische Daten
sind im Internet über http://dnb.d-nb.de abrufbar.

Herausgeber und Vertrieb:	Forschungszentrum Jülich GmbH Zentralbibliothek, Verlag 52425 Jülich Tel.: +49 2461 61-5368 Fax: +49 2461 61-6103 zb-publikation@fz-juelich.de www.fz-juelich.de/zb
Umschlaggestaltung:	Grafische Medien, Forschungszentrum Jülich GmbH
Druck:	Grafische Medien, Forschungszentrum Jülich GmbH
Copyright:	Forschungszentrum Jülich 2026

Schriften des Forschungszentrums Jülich
Reihe Energie & Umwelt / Energy & Environment, Band / Volume 710

D 82 (Diss. RWTH Aachen University, 2026)

ISSN 1866-1793
ISBN 978-3-95806-920-6 (Print)
ISBN 978-3-95806-921-3 (E-Book)

Vollständig frei verfügbar über das Publikationsportal des Forschungszentrums Jülich (JuSER)
unter www.fz-juelich.de/zb/openaccess.

This is an Open Access publication distributed under the terms of the Creative Commons Attribution License 4.0, which permits unrestricted use, distribution, and reproduction in any medium, provided the original work is properly cited.

Contents

Abstract 5

Zusammenfassung 9

1. Introduction 13

2. Fundamental 17

2.1. S-Q limit of single-junction solar cells ····· 18
2.2. Concept, architecture and operation principles of tandem solar cells ··· 22
2.3. Literature review ····· 27
2.3.1. Different two-terminal tandem solar cells ····· 27
2.3.2. Two-terminal perovskite/silicon tandem solar cells ····· 30

3. Characterization methods 37

3.1. Characterization of materials and semi-devices ····· 37
3.1.1. Optical properties ····· 37
3.1.2. Electrical properties ····· 40
3.1.3. Structural properties ····· 42
3.2. Characterization of solar cells ····· 46
3.3. Tools for numerical simulations ····· 47
3.4. Film deposition techniques ····· 49
3.4.1. Tin oxide by atomic layer deposition ····· 49
3.4.2. Transparent conductive oxide by magnetron sputtering ····· 50

4. Process development for perovskite/silicon tandem solar cells 53

4.1. Device configurations and fabrication process ····· 53
4.1.1. Silicon heterojunction bottom cell ····· 55
4.1.2. Perovskite top cell ····· 59

4.2. Mask design for sub-cells fabrication ····· 65
4.2.1. Silicon heterojunction bottom cell ····· 66
4.2.2. Perovskite top cell ····· 69

5. Tin Oxide Development, Application, and Working Mechanism 85

5.1. Homogeneity modulation and device optimization ····· 85
5.1.1. Reaction mechanism of ALD-SnO_X ····· 85
5.1.2. Possible reasons for film inhomogeneity ····· 87
5.1.3. Adjustments to the deposition parameters ····· 89
5.1.4. Optimization of SnO_X in perovskite solar cells ····· 96
5.2. Working mechanisms of SnO_X ····· 102
5.2.1. Dependence of V_{OC} and J_{SC} ····· 104
5.2.2. Dependence of *FF* ····· 113
5.2.3. Preliminary simulations and band diagram ····· 122
5.2.4. Corrected simulations ····· 130

6. Transparent Conductive Oxides Development and Setup Process for Semi-transparent Perovskite Solar Cells 139

6.1. Setup process ····· 139
6.1.1. Device configuration and mask design ····· 140
6.1.2. Device fabrication ····· 144
6.2. Development of transparent conductive oxides ····· 146
6.1.1. Tin-doped Indium Oxide (ITO) ····· 146
6.1.2. Zinc-doped Indium Oxide (IZO) ····· 152
6.3. Mitigation of sputter-induced damage ····· 154
6.4. Origin of sputtering damage during ITO deposition ····· 161
6.4.1. Decouple plasma radiation and ion bombardment ····· 162
6.4.2. Impact of plasma radiation ····· 167
6.4.3. Impact of ion bombardment ····· 171

7. Efficiency Improvement of Perovskite/Silicon Tandem Solar Cells 183

7.1. From 9% to 19%: Workflow and troubleshooting ····· 184
7.1.1. Workflow testing ····· 184
7.1.2. Troubleshooting ····· 186
7.2. From 19% to 31%: optoelectrical optimization ····· 194

7.2.1. From planar to nanotexture ····· 194
7.2.2. Utilization of antireflective coating ····· 198
7.2.3. Optimization of Ag electrode ····· 202
7.2.4. Some critical layers ····· 205
7.3. From 31% to 33%: surface treatment ····· 211
7.3.1. Impact of surface treatment on tandem solar cell ····· 211
7.3.2. Impact of surface treatment on silicon bottom cell ····· 215
7.3.3. Impact of surface treatment on perovskite top cell ····· 219

8. Summary and Outlook 227

8.1. Fabrication process of solar cells ····· 227
8.1.1. Summary ····· 227
8.1.2. Outlook ····· 228
8.2. Tin oxide buffer layer ····· 229
8.2.1. Summary ····· 229
8.2.2. Outlook ····· 230
8.3. Semi-transparent solar cells ····· 231
8.3.1. Summary ····· 231
8.3.2. Outlook ····· 233
8.4. Perovskite/silicon tandem soalr cells ····· 234
8.4.1. Summary ····· 234
8.4.2. Outlook ····· 236

A. Abbreviations and symbols 239

B. List of Publications 249

C. Curriculum Vitae 251

References 253

Acknowledgements 263

Abstract

Due to the rapid depletion of finite conventional fossil fuels and the resultant greenhouse effect, high-efficiency solar cells that convert renewable and clean solar energy into electricity have rapidly gained prominence in the energy market and become a dominant force in the field of renewable energy. The objective of this thesis is to develop high-efficiency perovskite/silicon tandem solar cells, as the tandem configuration surpasses the theoretical efficiency limit of single-junction solar cells and demonstrates significant potential for generating increased electricity at comparable costs. In particular, entire fabrication chain of tandem solar cells, tin oxide (SnO_X) as the buffer layer and transparent conductive oxides (TCOs) as transparent electrode in the perovskite top cells, and various techniques for the efficiency improvement from 9% to 33% have been investigated. The main focus of the SnO_X and TCOs lies on the fundamental understanding of the material properties, whereas for the perovskite/silicon tandem solar cell topic, developments on device level and investigation of working mechanism are the key aspects.

The configuration of perovskite/silicon tandem solar cells differs from that of both single-junction perovskite and silicon solar cells. Consequently, the entire fabrication process for tandem devices is not a simple combination of the fabrication processes of two single-junction devices. Rather, it requires the targeted design and adjustment of deposition masks for different substrates and for each film, taking into account the substrate thickness, film area, and the characteristics of the various deposition techniques employed for film preparation. Following the successful establishment of the complete fabrication process, the initial batch of perovskite/silicon tandem solar cells was produced for workflow testing, yielding a maximum initial efficiency of 9%.

The implementation of TCOs in perovskite top cells as transparent electrodes, typically prepared by magnetron sputtering, necessitates a robust buffer layer to mitigate the inevitable sputter-induced damage to the underlying organic films, in order to achieve

high efficiency. Following the successful development of atomic layer depositions of homogeneous SnO_X single layer, the transitional structure (single-junction) was fabricated with high efficiency exceeding 20% through a systematic optimization of the deposition parameters. Although SnO_X has been widely utilized as a sputter buffer layer in perovskite/silicon tandem solar cells, independent research on its working mechanisms has rarely been conducted. Consequently, the working mechanism of SnO_X at the C_{60}/Ag interface was investigated as an ideal reference for understanding the working mechanism of SnO_X in perovskite top cells. This study examines the correlation between the SnO_X process and the photovoltaic parameters using a series of experiments, characterizations, and simulations. It is observed that the efficiency increased with thicker SnO_X, and the results suggest that thicker SnO_X has the potential to suppress non-radiative recombination, decrease the series resistance of perovskite solar cells, and ensure an overall improved selectivity of the contact for charge carrier collection.

Owing to the complex configuration of tandem solar cells, semi-transparent perovskite solar cells are typically fabricated and investigated as a reference to address the corresponding issues associated with the insertion of window stack, comprising a buffer layer and a transparent electrode, in perovskite top cells. After the successful establishment of the fabrication chain of semi-transparent devices, TCOs as the transparent electrode were developed using magnetron sputtering and the optoelectrical properties were tuned to minimize parasitic absorption and electrical losses. The origin of S-shape in the current density-voltage (*JV*) characteristics was revealed to be the presence of an extraction barrier at the SnO_X/TCO interface and was completely eliminated by increasing the thickness of SnO_X buffer layer in the semi-transparent devices, which is generally known as the mitigation of sputter damage. The conventional understanding of the origin of sputtering damage is attributed to high-kinetic-energy ion bombardment and/or plasma radiation generated during sputtering. In fact, through decoupling these two factors, our investigation of their individual effects on bare films, layer stacks, and complete devices revealed that the sputtering damage of ITO to perovskite/C_{60} stacks primarily originates from ion bombardment rather than plasma radiation due to the generation of vacancy defects within the C_{60} and the dissociation of C=N bonds at the perovskite surface. In contrast, plasma radiation exhibits great potential for suppressing nonradiative recombination within perovskite films.

After the optimization of the fabrication chain, perovskite-related layer stack, and window stack, the maximum efficiency of perovskite/silicon tandem solar cells increased

to 19%. Subsequently, a series of methodologies, primarily focused on optical and electrical aspects, were implemented to further enhance the efficiency to 31%. Ultimately, surface treatment on the silicon bottom cells was found to exert a significant influence on surface morphology, potential distribution, energy levels, coverage, wettability, crystallization, and optical response of certain critical films in subcells, consequently affecting device performance. After the optimization of the O_2 plasma treatment and wet-chemical cleaning, a peak efficiency of 33% was achieved for perovskite/silicon tandem solar cells.

Zusammenfassung

Aufgrund der raschen Erschöpfung der endlichen konventionellen fossilen Brennstoffe und des daraus resultierenden Treibhauseffekts haben hocheffiziente Solarzellen, die erneuerbare und saubere Sonnenenergie in Strom umwandeln, auf dem Energiemarkt rasch an Bedeutung gewonnen und sind zu einer dominierenden Kraft im Bereich der erneuerbaren Energien geworden. Ziel dieser Arbeit ist es, hocheffiziente Perowskit-/Silizium-Tandemsolarzellen zu entwickeln, da die Tandemkonfiguration die theoretische Wirkungsgradgrenze von Einfachsolarzellen übertrifft und ein erhebliches Potenzial für die Erzeugung von mehr Strom bei vergleichbaren Kosten aufweist. Insbesondere wurden die gesamte Herstellungskette von Tandemsolarzellen, Zinnoxid (SnO_X) als Pufferschicht und transparente leitfähige Oxide (TCOs) als transparente Elektroden in den Perowskit-Topzellen sowie verschiedene Techniken zur Verbesserung des Wirkungsgrads von 9 % auf 33 % untersucht. Bei den SnO_X und TCOs liegt der Schwerpunkt auf dem grundlegenden Verständnis der Materialeigenschaften, während bei den Perowskit/Silizium-Tandemsolarzellen die Entwicklungen auf Bauelementebene und die Untersuchung des Funktionsmechanismus im Vordergrund stehen.

Die Konfiguration von Perowskit-/Silizium-Tandemsolarzellen unterscheidet sich von der Konfiguration von Perowskit- und Silizium-Solarzellen mit einem Übergang. Folglich ist der gesamte Herstellungsprozess für Tandem-Bauelemente nicht eine einfache Kombination der Herstellungsprozesse von zwei Bauelementen mit Einzelübergang. Vielmehr müssen die Abscheidungsmasken für verschiedene Substrate und für jede Schicht gezielt entworfen und angepasst werden, wobei die Substratdicke, die Schichtfläche und die Eigenschaften der verschiedenen für die Schichtpräparation verwendeten Abscheidungsverfahren zu berücksichtigen sind. Nach der erfolgreichen Etablierung des gesamten Herstellungsprozesses wurde die erste Charge von Perowskit/Silizium-Tandemsolarzellen für die Prüfung des Arbeitsablaufs hergestellt, wobei ein maximaler Anfangswirkungsgrad von 9 % erreicht wurde.

Der Einsatz von TCOs in Perowskit-Topzellen als transparente Elektroden, die in der Regel durch Magnetronsputtern hergestellt werden, erfordert eine robuste Pufferschicht, um die unvermeidliche, durch das Sputtern verursachte Beschädigung der darunter liegenden organischen Schichten abzumildern und einen hohen Wirkungsgrad zu erzielen. Nach der erfolgreichen Entwicklung von Atomlagenabscheidungen von homogenen SnO_X-Einzelschichten wurde die Übergangsstruktur (Einzelübergang) mit einem hohen Wirkungsgrad von über 20 % durch eine systematische Optimierung der Abscheidungsparameter hergestellt. Obwohl SnO_X als Sputter-Pufferschicht in Tandem-Solarzellen aus Perowskit und Silizium weit verbreitet ist, wurden Forschungen zu seinen Funktionsmechanismen bisher kaum durchgeführt. Daher wurde der Funktionsmechanismus von SnO_X an der C_{60}/Ag-Grenzfläche als ideale Referenz für das Verständnis des Funktionsmechanismus von SnO_X in Perowskit-Topzellen untersucht. In dieser Studie wird die Korrelation zwischen dem SnO_X-Prozess und den photovoltaischen Parametern anhand einer Reihe von Experimenten, Charakterisierungen und Simulationen untersucht. Die Ergebnisse deuten darauf hin, dass dickeres SnO_X das Potenzial hat, die nicht-radiative Rekombination zu unterdrücken, den Serienwiderstand von Perowskit-Solarzellen zu verringern und eine insgesamt verbesserte Selektivität des Kontakts für die Ladungsträgersammlung zu gewährleisten.

Aufgrund der komplexen Konfiguration von Tandem-Solarzellen werden in der Regel halbtransparente Perowskit-Solarzellen hergestellt und als Referenz untersucht, um die entsprechenden Probleme im Zusammenhang mit der Einfügung eines Fensterstapels, bestehend aus einer Pufferschicht und einer transparenten Elektrode, in Perowskit-Topzellen zu lösen. Nach der erfolgreichen Etablierung der Herstellungskette von halbtransparenten Bauelementen wurden TCOs als transparente Elektrode mittels Magnetronsputtern entwickelt und die optoelektrischen Eigenschaften so abgestimmt, dass parasitäre Absorption und elektrische Verluste minimiert werden. Der Ursprung der S-Form in den Stromdichte-Spannungs-Charakteristiken (*JV*) wurde durch das Vorhandensein einer Extraktionsbarriere an der SnO_X/TCO-Grenzfläche aufgedeckt und konnte durch Erhöhung der Dicke der SnO_X-Pufferschicht in den halbtransparenten Bauelementen vollständig beseitigt werden, was allgemein als Abschwächung von Sputterschäden bekannt ist. Das herkömmliche Verständnis des Ursprungs von Sputterschäden wird dem Ionenbeschuss mit hoher kinetischer Energie und/oder der während des Sputterns erzeugten Plasmastrahlung zugeschrieben. Durch die Entkopplung dieser beiden Faktoren ergab unsere Untersuchung ihrer individuellen Auswirkungen auf nackte Schichten, Schichtstapel und komplette Bauelemente, dass die Beschädigung von ITO auf Perowskit/C_{60}-Stapeln durch Sputtern in

erster Linie durch Ionenbeschuss und nicht durch Plasmastrahlung verursacht wird, und zwar durch die Erzeugung von Leerstellen im C_{60} und die Dissoziation von C=N-Bindungen an der Perowskit-Oberfläche. Im Gegensatz dazu hat Plasmastrahlung ein großes Potenzial zur Unterdrückung der nichtradiativen Rekombination in Perowskitfilmen.

Nach der Optimierung der Herstellungskette, des Perowskit-Schichtstapels und des Fensterstapels stieg der maximale Wirkungsgrad von Perowskit-Silizium-Tandemsolarzellen auf 19 %. Anschließend wurde eine Reihe von Methoden, die sich in erster Linie auf optische und elektrische Aspekte konzentrierten, eingesetzt, um den Wirkungsgrad weiter auf 31 % zu steigern. Schließlich wurde festgestellt, dass die Oberflächenbehandlung der Silizium-Bodenzellen einen erheblichen Einfluss auf die Oberflächenmorphologie, die Potenzialverteilung, die Energieniveaus, die Bedeckung, die Benetzbarkeit, die Kristallisation und die optische Reaktion bestimmter kritischer Schichten in den Unterzellen hat, was sich folglich auf die Leistung der Vorrichtung auswirkt. Nach der Optimierung der O_2-Plasmabehandlung und der nasschemischen Reinigung wurde ein Spitzenwirkungsgrad von 33 % für Perowskit/Silizium-Tandemsolarzellen erreicht.

1. Introduction

The global increase in energy demand necessitates the development and adoption of alternative energy sources, as conventional sources such as fossil fuels are projected to be depleted within the next century. Solar energy, a long-term natural energy source, presents a viable solution and can be utilized for both photothermal power generation, harnessing the thermal effect of sunlight, and photovoltaic power generation, leveraging the photovoltaic effect. In recent years, photovoltaic power generation has emerged as one of the most cost-effective and environmentally sustainable renewable energy sources. Researchers and professionals in the field of photovoltaic power generation have long pursued the dual objectives of enhancing the photovoltaic conversion efficiency of solar cells and achieving industrial-scale production at minimal cost. Crystalline silicon solar cells have dominated over 90% of the photovoltaic (PV) market with the highest efficiency of 26.8% [1]. However, they suffer from significant spectral mismatch losses, and their efficiency is approaching the Shockley-Queisser (S-Q) theoretical limit [2], including the non-absorbed photons, extraction and thermalization losses, resulting in a total of 67% [3] of solar energy not being available for electricity conversion . The current challenge is minimizing thermal losses due to their larger proportion compared to the other two factors. Tandem solar cells demonstrate considerable potential to reduce the total losses from 67% to 55% [3] by incorporating an absorber on top of the silicon solar cell with an optimal bandgap of 1.67-1.75 eV, increasing the theoretical efficiency limit from 29.8% to 42% [4]. From a practical standpoint, monolithic perovskite/silicon tandem solar cells have been demonstrated to be the most promising candidate among the existing combinations of top and bottom cells.

In recent years, perovskite [5] materials have garnered considerable attention due to their advantageous properties, including tunable bandgap, high absorption coefficient and carrier mobility, long diffusion length, and straightforward fabrication methods. Within a decade, the efficiency of single-junction perovskite solar cells (PSCs) has exhibited remarkable improvement, attaining 26.7% [6], which is comparable to the highest efficiency

of crystalline silicon solar cells. Consequently, an increasing allocation of research resources has been directed toward the development of monolithic perovskite/silicon tandem solar cells, resulting in a substantial increase in the record efficiency from 13.7% [7] to 34.6% [6] over the past few years.

In contrast to the fabrication of silicon solar cells, where films are symmetrically prepared on both sides of the silicon wafer, the layers in PSCs are fabricated sequentially from the bottom to the top on corning glass, typically coated with a tin-doped indium oxide (ITO) film and completed with an opaque metal electrode. Consequently, the output characteristics of opaque PSCs can only be measured from the glass side, also referred to as the rear side. When PSCs are prepared atop the silicon bottom cell, the opaque electrode must be replaced with TCOs to allow light to enter the cells from the opposite side, also termed the front surface. Generally, TCOs are predominantly prepared by radio frequency (RF) magnetron sputtering. Although TCOs offer several notable advantages such as high deposition rate, excellent adhesion, coverage, and uniformity [8], an inevitable issue is that the sputtering process of TCOs is susceptible to damaging the underlying organic layers, particularly the perovskite light-absorbing layer. This damage is attributed to the high kinetic energy ion bombardment rather than plasma radiation generated during the sputtering process [9], resulting in performance degradation of devices. The most effective method of mitigating sputtering damage is utilizing a buffer layer on top of the organic layers prior to the fabrication of transparent electrodes. In monolithic perovskite/silicon tandem solar cells, the layer stack consisting of a buffer layer and a TCO layer is generally known as the window stack.

This research addresses the development and optimization of high-efficiency monolithic perovskite/silicon heterojunction (SHJ) tandem solar cells, and the window stack with high transparency and excellent conductivity, encompassing four primary areas of investigation. The initial focus pertains to the development of monolithic perovskite/silicon tandem solar cells, with the objective of fabricating a functional device exhibiting efficiency exceeding 0% for subsequent research. The second area of inquiry centers on the development of a homogeneous tin oxide buffer layer utilizing atomic layer deposition (ALD), optimization of device performance, and examination of its working mechanism in the perovskite top cell. The third investigation concentrates on the optoelectrical optimization of TCOs, mitigation of sputter-induced damage at the device level, and exploration of the origins of such damage. The fourth area of research involves the investigation of factors contributing to suboptimal efficiency in tandem devices and the

enhancement of performance primarily through optimization of workflow, reduction of non-radiative recombination, refinement of substrate morphology, improvement of optical response, enhancement of carrier collection, and alignment of energy bands, and surface treatment.

Chapter 2, comprising two sections, provides a concise introduction to fundamental principles and a review of literature pertaining to monolithic perovskite/silicon tandem solar cells. Section 2.1 commences with an examination of the theoretical efficiency limit of single-junction solar cells, followed by an elucidation of the general principles underlying the tandem solar cell concept. Section 2.2 presents various two-terminal tandem solar cells, primarily focusing on the efficiency enhancements achieved in two-terminal perovskite/silicon tandem solar cells utilizing an inverted (p-i-n) structure perovskite top cell over the past decade, concluding with a brief introduction to the research topic at hand. Chapter 3 delineates the characterization methods, simulation tools, and deposition techniques employed in this study. Given the diverse analytical techniques utilized for characterizing a wide array of films, semi-devices, and complete solar cells, each method is introduced succinctly without specifying the measured materials and structures. Section 3.1 offers an overview of the characterization methods for materials and semi-devices employed to analyze optoelectrical and structural properties. Section 3.2 encompasses the characterization methods for complete solar cells. Section 3.3 introduces the tools for numerical simulations used to investigate the penetration depth profile of ions and the band diagram of solar cells. Section 3.4 elucidates the working principles of the deposition techniques utilized for key films.

Chapter 4 constitutes the most fundamental component of this research, examining the development process of monolithic perovskite/silicon tandem solar cells to establish a baseline of tandem fabrication for subsequent investigations. Section 4.1 analyzes the configuration of tandem devices and the requirements for each step in the fabrication process of SHJ bottom cells and perovskite top cells. Section 4.2 elucidates the design, inherent challenges, and refinement of the masks employed to fabricate top and bottom cells utilizing a diverse array of deposition techniques.

Chapters 5, 6, and 7 constitute the principal components of this research. Chapter 5 examines the synthesis of SnO_X utilizing ALD and its application as a buffer layer in PSCs. Section 5.1 elucidates the reaction mechanism of SnO_X, the comprehensive material development process for achieving a homogeneous film with saturated growth, and the optimization of SnO_X to ensure robust film properties and ohmic electrical contact for the

fabrication of high-efficiency tandem solar cells. Section 5.2 investigates the working mechanism of the SnO_X buffer layer in PSCs through a systematic combination of experimental and numerical simulations, serving as a framework to elucidate its functional mechanism in the perovskite top cell. Chapter 6 addresses the development of transparent and conductive TCOs utilizing RF magnetron sputtering, the design and fabrication process of high-efficiency semi-transparent perovskite solar cells, and an investigation into the origin of sputter damage. Section 6.1 examines the configuration of semi-transparent devices and introduces the design and refinement of masks employed in device fabrication. Section 6.2 delineates the optoelectrical optimization of two TCO materials. In Section 6.3, the causes of sputter-induced S-shaped *JV* curves are analyzed, and the sputter damage is effectively mitigated through the insertion of a robust SnO_X buffer layer, thereby facilitating the development of high-efficiency tandem devices. Section 6.4 investigates the origin of sputter damage to the underlying organic perovskite/C_{60} layer stacks by decoupling the plasma radiation and ion bombardment that occur simultaneously during the sputtering process. Chapter 7 investigates the pathway of improving the efficiency of tandem solar cells from 9% to 33% through a series of optimizations. Section 7.1 focuses on the workflow testing for tandem solar cells to reach the most basic requirements of high efficiency that is fabricating a tandem device with efficiency exceeding 0, and on the troubleshooting tasks to ensure that most of the layers, especially the organic and inorganic layers in the perovskite top cell, works at their perfect status that allows for a stable baseline with moderate-level efficiency. Section 7.2 shows a series of methods to optimize the optoelectrical performance primarily through the introduction of new materials and structure and the adjustment on film thickness. Section 7.3 analyzes the impact of surface treatment on the performance of tandem solar cells, which is conducted on the bottom cell while having a significant effect on the surface morphology and potential of the interconnection layer, the optical response of the silicon bottom cell, and the subsequent coverage and growth of the organic films in the perovskite top cell. However, the importance of surface treatment in enhancing efficiency and in elucidating the working mechanism of the interconnection layer in monolithic tandem solar cells has been underappreciated by the scientific community for an extended period. Chapter 8 provides a summary and outlook.

2. Fundamental

The development of renewable, environmentally friendly energy sources, such as solar, wind, geothermal, and hydro energy, is primarily driven by two factors: the severe greenhouse effect resulting from the uncontrolled use of fossil fuels and the scarcity of non-renewable energy sources. The greenhouse effect describes an increase in the Earth's surface temperature due to the absorption and reradiation of thermal radiation emitted from the Earth's surface by certain gases in the atmosphere, such as carbon dioxide (CO_2) and methane (CH_4), which are also known as greenhouse gases. Without the greenhouse effect, the Earth's average temperature would be significantly lower and unable to sustain existing ecosystems. With a moderate greenhouse effect, the Earth's surface maintains a temperature conducive to the survival of living organisms. However, due to the increasing demands of industrial development and rising living standards on fossil fuel consumption, human activities have led to a rapid increase in the concentration of greenhouse gases, exacerbating the greenhouse effect and resulting in global warming and climate change. Solar cells are capable of converting solar energy into electricity without generating greenhouse gases, and solar energy originates from the hydrogen-helium fusion of hydrogen atoms within the sun, which releases substantial amounts of nuclear energy. Therefore, the development of efficient and cost-effective solar cells presents a promising approach to address both the scarcity of energy sources and the intensification of the greenhouse effect.

In this chapter, we first discuss the theoretical limit of single-junction solar cells and introduce the concept of multi-junction solar cells. Second, we examine the classification of tandem solar cells according to different electrical connections, the working principles of tandem solar cells, and various options for two-terminal tandem solar cells. Finally, we present a trouble-shooting-oriented literature review on the most efficient two-terminal perovskite/silicon heterojunction tandem solar cells and introduce the research topic.

2.1. S-Q limit of single-junction solar cells

During the conversion process of solar radiation into electricity for solar cells, light absorbing material is required to absorb the incident photons and create electron-hole pairs. With the assistance of built-in electric fields, such as p-n junction, these electron-hole pairs are separated and subsequently collected by the electrodes at two terminals of solar cell. Crystalline silicon solar cells currently dominate over 90% of the PV market, suggesting that more than 90% of light absorbers are crystalline silicon, which is a semiconductor with a bandgap (E_g) of 1.12 eV. The generation of electron-hole pairs within silicon require a photon energy (E) equals to or exceeding 1.21 eV ($E \geq E_{g,Si}$), while the portion of the initial E above the $E_{g,Si}$ is released as thermal losses. If the E_g of absorber approaches 0, available energy is maximized but at the expense of significant thermal losses; if the E_g of absorber approaches ∞, thermal losses minimized but little available energy remains. Therefore, an optimal E_g of single-junction solar cells exists.

The S-Q limit delineates the maximum conversion efficiency, also referred to as the theoretical limit, of a single-junction solar cell, wherein the light absorber is a semiconductor with E_g and only one absorber is present. The simplest form of the S-Q limit encompasses four fundamental assumptions: (1) All photons with $E \geq E_g$ are absorbed through the generation of an electron-hole pair, while the absorption probability is 0 if $E < E_g$. (2) All photogenerated electrons and holes thermalize to the edge of the conduction band and valence band, respectively, with the excess portion of the photon energy dissipated as heat. (3) All electron-hole pairs are collected at short-circuit. (4) Apart from the non-absorbed photons with $E < E_g$ and thermal loss due to $E \geq E_g$, radiative recombination of electron-hole pairs constitutes the sole mechanism for energy losses. The maximum short-circuit current density ($J_{SC,SQ}$) defined by these assumptions is given by Eq. 2.1 as

$$J_{SC,SQ} = q \int_0^\infty a(E)\Phi_{inc}(E)\mathrm{d}E = q \int_{E_g}^\infty \Phi_{inc}(E)\mathrm{d}E \tag{2.1}$$

where q represents the elementary charge. The absorptance $a(E)$ denotes the percentage of the absorbed photons at a specific E, and $\Phi_{inc}(E)$ represents the photon flux of incident light. Given that the absorption probability follows a step function under assumption (1), the

equation 2.1 can be simplified to the product of q and the $\Phi_{inc}(E)$ integral, which is solely influenced by the E_g of the absorber. With a stable light source, $\Phi_{inc}(E)$ remains constant at a given E, consequently, a higher E_g results in a lower $J_{SC,SQ}$.

To express the following equations, it is necessary to introduce an idealized concept known as a black body. A black body absorbs all incoming radiation from the environment without transmission or reflection. Subsequently, as the body temperature increases, it emits radiation to the environment, a phenomenon referred to as black-body radiation, which adheres to Kirchhoff's law [10] as expressed in Eq. 2.2

$$a(E) = e(E) \tag{2.2}$$

where $e(E)$ denotes the emission of black body at a specific temperature. The sun is treated as black body. Under thermal equilibrium conditions, the product of the concentration of electrons (n) and holes (p), and the emitted photon flux $\phi(E)$ in an ideal solar cell can be expressed by Eq. 2.3 and 2.4 as

$$np = n_i^2 \tag{2.3}$$

$$\phi(E) = a(E)\phi_{bb}(E) \tag{2.4}$$

while under thermal non-equilibrium conditions, such as when subjected to bias voltage V, it follows the Eq. 2.5 and 2.6 as

$$np = n_i^2 \exp\left(\frac{qV}{k_B T}\right) \tag{2.5}$$

$$\phi(E) = a(E)\phi_{bb}(E) \exp\left(\frac{qV}{k_B T}\right) \tag{2.6}$$

where n_i is the intrinsic carrier concentration, k_B is Boltzmann constant, T is temperature and $\phi_{bb}(E)$ is the photons flux of the black body from environment. In the dark, an idea solar

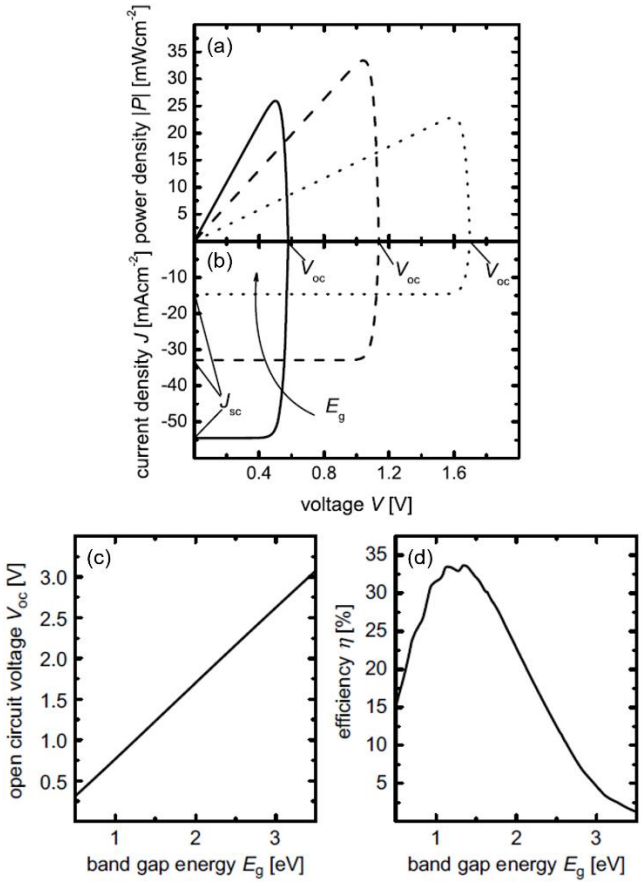

Figure 2.1.: *(a) Power-voltage and (b) current-voltage curves of ideal solar cells with different bandgaps of* 0.8, 1.4, *and* 2.0 eV. *(c) Open-circuit voltage and efficiency of ideal solar cell as a function of bandgap energy calculated using Shockley-Queisser limit under AM* 1.5 *Global spectrum (*1000 W/m^2*) [11].*

cell undergoes the absorption of the photons emitted by the black body from the environment and the emission of radiation due to radiative recombination of electron-hole pairs. Therefore, the corresponding recombination current density $J_{rec,SQ}$ can be expressed by the Eq. 2.7 as

$$J_{\mathrm{rec,SQ}} = q\int_0^{\infty} a(E)\phi_{\mathrm{bb}}(E)\exp\left(\frac{qV}{k_{\mathrm{B}}T}\right)\mathrm{d}E = q\int_{E_{\mathrm{g}}}^{\infty} \Phi_{\mathrm{bb}}(E)\exp\left(\frac{qV}{k_{\mathrm{B}}T}\right)\mathrm{d}E \tag{2.7}$$

The total current density $J(V)$ of the ideal solar cell under a specific bias voltage and illumination is defined by Eq. 2.8 as

$$J(V) = J_{\mathrm{rec,SQ}} - J_{\mathrm{SC,SQ}} = q\int_{E_{\mathrm{g}}}^{\infty} \Phi_{\mathrm{bb}}(E)\exp\left(\frac{qV}{k_{\mathrm{B}}T}\right)\mathrm{d}E - q\int_{E_{\mathrm{g}}}^{\infty} \Phi_{\mathrm{inc}}(E)\mathrm{d}E \tag{2.8}$$

Given that $\Phi_{\mathrm{inc}}(E)$ comprises the photons flux of the sun spectrum Φ_{sun} and the black body spectrum from the environment, it can be substituted with $\Phi_{\mathrm{sun}} + \Phi_{\mathrm{bb}}$; consequently, Eq. 2.8 can be simplified to Eq. 2.9 as

$$J(V) = q\int_{E_{\mathrm{g}}}^{\infty} \Phi_{\mathrm{bb}}(E)\mathrm{d}E\left[\exp\left(\frac{qV}{k_{\mathrm{B}}T}\right) - 1\right] - q\int_{E_{\mathrm{g}}}^{\infty} \Phi_{\mathrm{sun}}(E)\mathrm{d}E \tag{2.9}$$

The $J(V)$ is zero without bias voltage and solar illumination. The power-voltage and current-voltage curves of ideal solar cells are plotted with different E_{g} of 0.8, 1.4, and 2.0 eV, as illustrated in Fig. 2.1, where the power density (P) is the product of $J(V)$ and V. A larger E_{g} of the absorber corresponds to a larger open-circuit condition (V_{OC}) of ideal solar cell. However, the maximum power density (P_{max}) does not exhibit a similar trend, as the P_{max} for the 1.4 eV scenario exceeds that of the other two scenarios.

The voltage at open-circuit condition can be evaluated from Eq. 2.9 and follows from Eq. 2.10 as

$$V_{\mathrm{OC}} = \frac{k_{\mathrm{B}}T}{q}\ln\left(\frac{\int_{E_{\mathrm{g}}}^{\infty} \Phi_{\mathrm{sun}}(E)\mathrm{d}E}{\int_{E_{\mathrm{g}}}^{\infty} \Phi_{\mathrm{bb}}(E)\mathrm{d}E} + 1\right) = \frac{k_{\mathrm{B}}T}{q}\ln\left(\frac{J_{\mathrm{SC,SQ}}}{J_{0,\mathrm{SQ}}} + 1\right) \tag{2.10}$$

where the saturated current density $J_{0,SQ}$ follows Eq. 2.11 as

$$J_{0,SQ} = q\int_0^{\infty} a(E)\Phi_{bb}(E)\mathrm{d}E = q\int_{E_g}^{\infty} \Phi_{bb}(E)\mathrm{d}E \tag{2.11}$$

$J_{0,SQ}$ denotes the minimum saturated current density for the ideal solar cell without bias voltage, generated from the absorption of black body radiation from the environment. The V_{OC} as a function of E_g is plotted in Fig. 2.1(c), wherein V_{OC} increases approximately linearly as E_g increases. The efficiency (η) of is defined as the ratio of the maximum output power density ($P_{max,out}$) to the maximum input power density ($P_{max,in}$), as expressed in Eq. 2.12:

$$\eta = \frac{P_{max,out}}{P_{max,in}} = \frac{-\max(J(V)\times V)}{\int_{E_g}^{\infty} E\Phi_{sun}(E)\mathrm{d}E} \tag{2.12}$$

where $-\max(J(V)\times V)$ denotes the maximum of the negative power density of the solar cell. According to the S-Q theory, the η of an ideal single-junction solar cell under the illumination of AM 1.5 Global spectrum (1000 W/m^2) is depicted in Fig. 2.1(b) as a function of E_g, wherein the theoretical limit is 33.7% and is achieved with an E_g of 1.34 eV.

2.2. Concept, architecture and operation principles of tandem solar cells

For single-junction silicon solar cells with a less favorable E_g of 1.12 eV, the S-Q limit is calculated to be 32.9%. From a practical perspective, the theoretical limit is determined to be 29.8% [12] due to the utilization of measured optical absorption instead of a step function, and the consideration of additional loss mechanisms: Auger recombination and free carrier recombination, rather than solely radiative recombination. In the past decade, the focus of the photovoltaic community has shifted from single-junction silicon solar cells to tandem

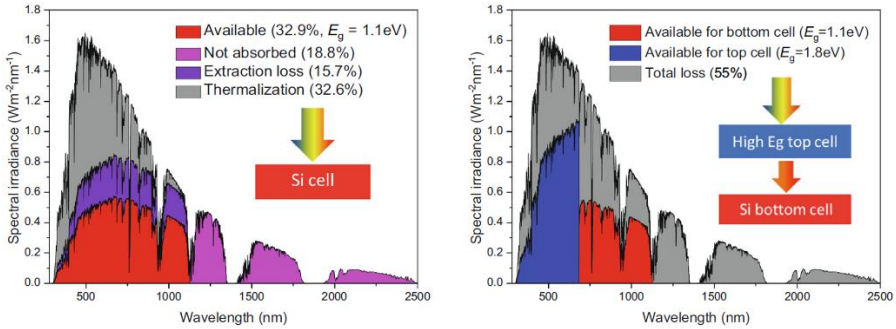

Figure 2.2.: *Energy losses analysis of (a) single-junction silicon solar cell and (b) a tandem solar cell with silicon bottom cell under AM* 1.5 *Global spectrum (*1000 W/m^2*) [3].*

solar cells, primarily due to two factors: (1) single-junction solar cells continue to suffer from significant spectral mismatch, accounting for 67% of the total solar energy, including unabsorbed photons, extraction and thermalization losses, as illustrated in the energy losses analysis in Fig. 2.2(a); (2) the record efficiency of 27.3% (234.1 cm^2) for single-junction silicon solar cells [6] is approaching the theoretical limit.

To minimize spectral mismatch losses, the solar spectrum is divided into several regions, and two light absorbers with different E_g are simultaneously employed in solar cells to maximize the utilization of photon energy in each region. This concept of tandem solar cells was first proposed by E. D. Jackson in 1955 [13]. Generally, the absorber with larger E_g is positioned on top, designated as the top cell, while the absorber with smaller E_g is positioned at the bottom, designated as the bottom cell. Considering the substantial spectral mismatch losses in the short wavelength region, silicon solar cells typically function as the bottom cell in tandem configurations. By incorporating a wide-bandgap (1.8 eV) absorber above the silicon bottom cell, the spectral utilization in the short wavelength region significantly increases, as illustrated in Fig 2.2(b). Consequently, the total losses due to spectral mismatch across the entire wavelength range decrease from 67% to 55%, indicating higher conversion efficiency of tandem solar cells compared to that of single-junction silicon solar cells.

The theoretical limit of efficiency for tandem solar cells is defined as a sum of the maximum power densities of top and bottom cells. The optimum efficiency of 42% is calculated using the detailed balance principle, and the corresponding E_g of top and bottom

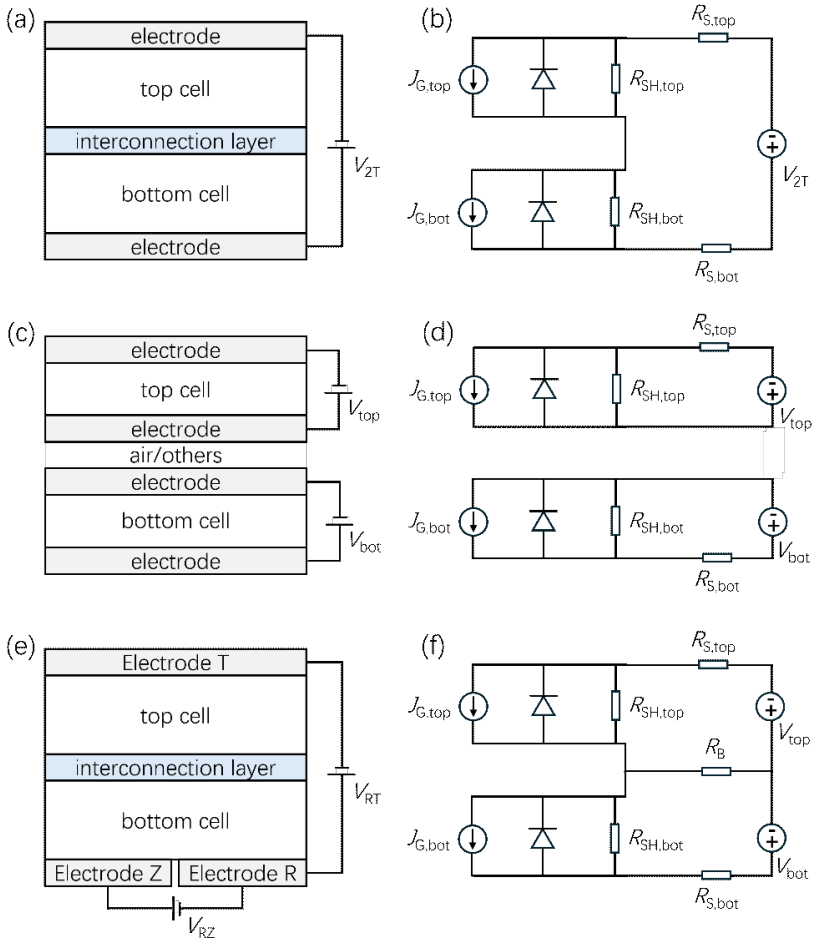

Figure 2.3.: *Schematic of (a) two-terminal, (c) four-terminal, and (e) three-terminal tandem solar cells. Equivalent electrical circuit for (b) two-terminal, (d) four-terminal, and (f) three-terminal tandem solar cells.*

cells are 1.9 eV and 1.0 eV, respectively [4]. The calculation process for tandem solar cells is analogous to that of the S-Q limit, however, the $\Phi_{inc}(E)$ of each subcell comprises three components: (i) the photons flux of solar spectrum Φ_{sun}, the black body spectrum from (ii) the environment Φ_{bb}, and (iii) another subcell. Different to the Φ_{sun} and Φ_{bb}, the black body

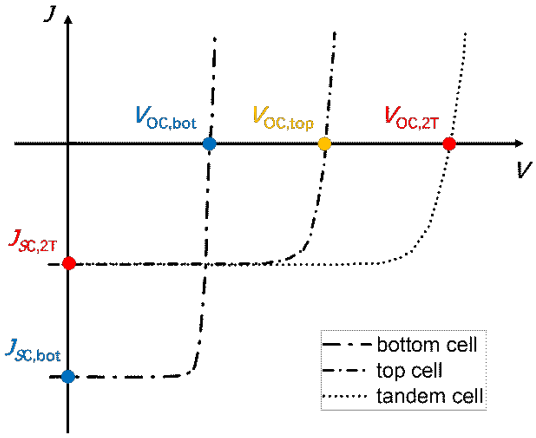

Figure 2.4.: *Current density-voltage curve of a tandem solar cell, top cell and bottom cell.*

spectrum from bottom (top) cell is affected by the partial bias voltage of bottom (top) cell $V_{\mathrm{bot(top)}}$, which is proportional to $\exp(qV_{\mathrm{bot(top)}}/kT)$.

According to different types of electrical connection, the architecture of tandem solar cells is typically categorized into two-terminal (2T), three-terminal (3T) and four-terminal (4T) configurations. In the 2T architecture, the top and bottom cells are monolithically integrated and electrically connected in series, as illustrated in Fig. 2.3(a). The equivalent electrical circuit of the 2T architecture is depicted in Fig. 2.3(b), wherein the total current density at short circuit ($J_{\mathrm{SC,2T}}$) is determined by the minimum value that adheres to $J_{\mathrm{SC,2T}} = \min[J_{\mathrm{SC,top}}, J_{\mathrm{SC,bot}}]$. Concurrently, the total $V_{\mathrm{OC,2T}}$ is equivalent to the sum of the voltages of the two subcells, following $V_{\mathrm{OC,2T}} = V_{\mathrm{OC,top}} + V_{\mathrm{OC,bot}}$, and the total power of the 2T architecture is calculated as the product of the minimum sub-current density and the sum of voltages, as depicted in Fig. 2.4. In the 4T architecture, two subcells are mechanically stacked and operate independently. The schematic and equivalent circuit are presented in Fig. 2.3(c, d). The top and bottom cells in the 4T architecture function at their individual maximum power points independently, and the total power is derived from the sum of the power outputs of the two subcells.

Compared to 2T and 4T, the electrical connection of 3T architecture is significantly more complex, comprising two independent electrical circuits, as shown in Fig. 2.3(e, f).

In the current match scenario ($J_{SC,top} = J_{SC,bot}$ and $J_{RZ} = 0$), no excessive electrons can be extracted from the Z contact. Consequently, no current flows through the RZ circuit, and the 3T architecture functions similarly to its 2T counterpart. In the current mismatch scenario, two possibilities exist: (1) When the cell is top-limited ($J_{SC,top} < J_{SC,bot}$), the excessive electrons generated in the bottom cell are collected by the electrode Z after the holes and electrons from the top and bottom cells recombine with each other within the interconnection layer. Both electrical circuits operate simultaneously, and the total power of the top-limited 3T architecture is the sum of two circuits of $P_{top} + P_{bot}$. (2) When the cell is bottom-limited ($J_{SC,top} > J_{SC,bot}$), the Z contact injects electrons into the bottom cell, which recombine with the holes from the top cell within the interconnection layer, generating a current J_{RZ} equal to $J_{SC,bot} - J_{SC,top}$ and a negative power of $P_{RZ} < 0$ in the RZ circuit. The excessive electrons within the top cell flow through the RT circuit and recombine at the R contact, generating an excessive power ΔP_{RT}. Therefore, the total power of a bottom-limited 3T architecture is the sum of three components of $P_{RT} + \Delta P_{RT} - |P_{RZ}|$, where ΔP_{RT} and P_{RZ} share the same current J_{RZ} that equals to the current mismatch of $J_{SC,bot} - J_{SC,top}$ but with different voltages. Since the voltage for the RT circuit is larger than that for the RZ circuit, $\Delta P_{RT} - |P_{RZ}| > 0$, indicating that the 3T architecture generates higher power than that of the 2T architecture under current mismatch conditions due to the presence of the third electrode on the bottom cell.

Over the past decade, 2T tandem solar cells have been the most extensively studied among the three architectures in the photovoltaic community, primarily due to their simpler fabrication process and reduced parasitic absorption and reflection losses compared to their two counterparts.

To evaluate the performance of solar cells, whether single-junction or tandem, there are three critical photovoltaic parameters in addition to η: short-circuit current density (J_{SC}), V_{OC}, and fill factor (FF). The first two parameters are extracted at short circuit and open circuit, respectively, which have been discussed in the previous section. FF is defined by Eq. 2.13 as

$$FF = \frac{J_{SC} \times V_{OC}}{P_{mpp}} = \frac{J_{SC} \times V_{OC}}{J_{mpp} \times V_{mpp}} \tag{2.13}$$

where P_{mpp}, J_{mpp}, and V_{mpp} denote the power, current density and voltage extracted at the maximum power point (MPP), as shown in Fig. 2.5. The FF is affected by the series

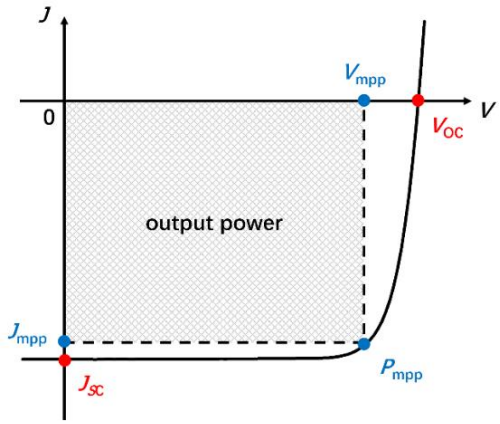

Figure 2.5.: *Current density-voltage curve of a solar cell.*

resistance (R_S) and sheet resistance (R_{SH}) of solar cells. A smaller R_S or larger R_{SH} results in a higher *FF*.

2.3. Literature review

2.3.1. Different two-terminal tandem solar cells

The theoretical efficiency limit of 2T tandem solar cells determined the optimal E_g ranges for top and bottom cells. Based on these ranges, various types of solar cells are suitable for functioning as subcells, including silicon (1.12 eV) solar cells, perovskite (1.17-3.1 eV) solar cells, III-V (1.42-3.4 eV) solar cells, organic solar cells, and Cu(In,Ga)Se_2 (1.04-1.68 eV) solar cells. Silicon solar cells can only be utilized as bottom cells due to their lower E_g values, while other solar cells with adjustable E_g can be employed for either top or bottom cells. According to the latest version of the best research-cell efficiency chart maintained by the National Renewable Energy Laboratory (NREL), the three 2T tandem solar cells that have consistently ranked in the top three positions in terms of efficiency over the past decade—with the highest efficiencies being continuously updated—are

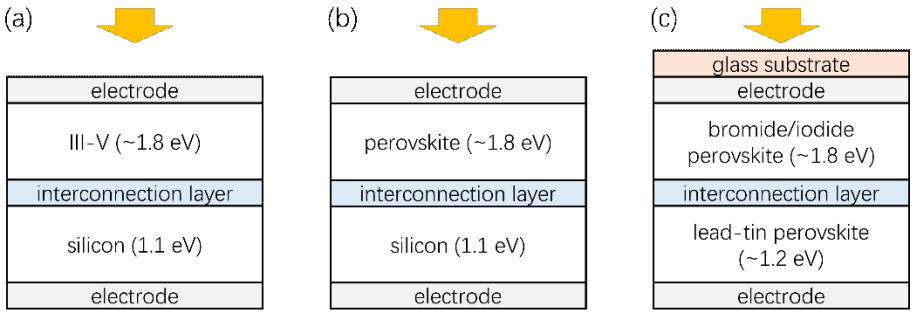

Figure 2.6.: *Schematics of two-terminal a) III-V/silicon, b) perovskite/silicon, and c) all-perovskite tandem solar cells, wherein the optimal E_g of silicon, lead-tin perovskite, (bromide/iodide) perovskite and III-V materials are approximately 1.1, 1.2, 1.8 and 1.8 eV. The yellow arrow indicates the illumination direction.*

III-V/silicon, perovskite/silicon, and all-perovskite tandem solar cells, with recorded champion efficiencies of 36.1% (area: 3.987 cm^2), 34.6% (area: 1.004 cm^2), and 30.1% (area: 0.04934 cm^2), respectively. The configurations are illustrated in Fig. 2.6.

Single-junction III-V solar cells exhibit higher conversion efficiency than that of silicon solar cells because the III-V materials are generally direct bandgap semiconductors, such as Ga and As, while Si is an indirect bandgap semiconductor. The primary distinction between direct and indirect bandgap semiconductors is that the latter materials necessitate the absorption of phonons during the electron excitation process, indicating a lower absorption coefficient, a less distinct absorption edge, and a requirement for thicker material to achieve complete light absorption. Furthermore, III-V materials demonstrate higher thermal resistance compared to their Si counterparts, rendering them suitable for concentrator photovoltaic systems. However, due to high manufacturing costs, primarily attributed to the substrates (InP or GaAs), the market share of III-V solar cells remains limited and struggles to compete with that of silicon solar cells (90%). The development of III-V/silicon tandem solar cells enables the replacement of expensive substrates with Si, significantly reducing manufacturing costs while simultaneously improving efficiency. The principal challenges associated with Si substrates are the mismatches in both thermal expansion coefficients and lattice constants between the Si substrate and epitaxial III-V layers [14], which adversely affect crystallization quality and result in a high density of dislocations, consequently diminishing efficiency. The highest reported efficiency for dual-junction III-V/silicon

tandem solar cells is 32.8% [15], achieved using a mechanically stacked 4T configuration rather than a series-connected 2T configuration due to superior performance. Indeed, the world record efficiency of 36.1% for III-V/silicon tandem solar cells has been attained with a GaInP/GsInAsP/Si device featuring triple junctions. Therefore, in comparison to the performance of perovskite/silicon and all-perovskite tandem solar cells, III-V/silicon tandem solar cells do not demonstrate advantages in efficiency with respect to dual-junction devices.

Perovskite solar cells are a promising candidate for the top cell of 2T tandem solar cells due to several factors: (1) the E_g of perovskite absorber is tunable between 1.17 and 3.1 eV through compositional engineering; (2) the high absorption coefficient of perovskite enables complete light absorption with approximately 500 nm absorbing layer, whereas more than 100 μm-thick silicon wafer is required for silicon solar cells; (3) they are fabricated through simple methods, such as spin-coating and thermal evaporation; (4) they have relatively low manufacturing costs and high conversion efficiency of 26.7%. The key challenges associated with perovskite solar cells and perovskite-related tandem solar cells are poor device stability due to internal issues and environmental influences [16]. Single-junction silicon solar cells are the optimal candidate for the bottom cell due to numerous advantages: (1) the E_g value of silicon (1.12 eV) is extremely close to the optimum values of bottom cell (~1.1 eV) for achieving theoretical limit; (2) they have the largest photovoltaic market share of 90%; (3) their excellent stability allows for a 25-year operational lifetime; (4) they have relatively low manufacturing costs and high conversion efficiency of 27.3% compared to other single-junction counterparts. Among all types of silicon solar cells, SHJ and those with tunnel oxide passivating contacts (TOPCon) are the two types that have been used most frequently for 2T perovskite/silicon tandem solar cells. Tandem devices with SHJ as the bottom cell typically exhibit higher conversion efficiency, which also holds the world record efficiency of 34.6% [6] for the broad category of dual-junction 2T tandem devices.

The tunable E_g of perovskite from 1.17 to 3.1 eV through compositional engineering facilitates the fabrication of all-perovskite tandem solar cells. In these devices, a mixed bromide/iodide wide-bandgap perovskite layer with an E_g of approximately 1.8 eV is initially prepared on the conductive glass substrate as the front cell, followed by the preparation of a lead-tin narrow-bandgap perovskite layer with an E_g of approximately 1.2 eV atop the wide-bandgap layer as the bottom cell. The stacking arrangement of wide-bandgap and narrow-bandgap absorbers for all-perovskite tandem solar cells is inverse to

that of perovskite/silicon tandem devices due to differences in substrates and illumination direction. When measuring the *JV* characteristics of tandem devices, incident light should first traverse the wide-bandgap absorber and subsequently the narrow-bandgap absorber. In the all-perovskite configuration, the glass substrate coated with TCO is analogous to that of single-junction perovskite solar cells, wherein the preparation of the wide-bandgap absorber precedes that of the narrow-bandgap absorber on the substrate, and the *JV* measurement is conducted from the side of the glass not covered by films. Conversely, in the silicon-based configuration, the substrate is a silicon wafer that also serves as the narrow-bandgap absorber in the bottom cell, and the *JV* measurement is performed from the front side of the top cell with a wide-bandgap absorber. In comparison to perovskite/silicon tandem solar cells, the fabrication procedure of all-perovskite solar cells is considerably simpler, and the manufacturing cost is substantially lower. However, the relatively inferior conversion efficiency and poor operational stability under moisture and heat render it less favorable. Consequently, in the subsequent subsection, we exclusively address the key challenges and review literature pertaining to 2T perovskite/silicon tandem solar cells.

2.3.2. Two-terminal perovskite/silicon tandem solar cells

The conversion efficiency, which characterizes the capacity to transform solar radiation into electrical energy, necessitates a focus on the optical and electrical performance of solar cells as the two primary properties of interest. Consequently, this subsection's literature review on 2T perovskite/silicon tandem solar cells is bifurcated into two segments: optical and electrical optimizations. These segments chronologically summarize a series of efficacious methodologies employed to enhance device efficiency.

Optical optimization

In 2015, Stanford University reported the first 2T perovskite/silicon tandem solar cell [7] with η of 13.7% (1 cm^2) and J_{SC} of 11.5 mA/cm^2, which demonstrated that the hole transporting layer (HTL), 2,2',7,7'-Tetrakis[N,N-di(4-methoxyphenyl)amino]-9,9'-spirobifluorene (spiro-OMeTAD), in the perovskite top cell with a conventional structure (n-i-p) resulted in current losses of 5.9 and 2.0 mA/cm^2 for top and bottom cells, respectively, due to its parasitic absorption in visible and infrared wavelengths. By reducing the layer thickness of spiro-OMeTAD, the absorption losses can be effectively mitigated, and furthermore, they can be completely eliminated by replacing spiro-OMeTAD with a p-

type heterojunction contact exhibiting good conductivity and low parasitic absorption. In 2016, researchers from the Swiss Federal Technology Institute of Lausanne (EPFL) discovered that the recombination layer, zinc tin oxide (ZTO), significantly influences the optical interference pattern in the silicon bottom cells [17]. This effect is evidenced by changes in the external quantum efficiency of tandem devices as a function of ZTO layer thickness and is hypothesized to be strongly correlated with the refractive index (n_{ref}) mismatch at the interface of ZTO (n_{ref}~2.5) and TiO2 (n_{ref}~2), which serves as the electron transporting layer (ETL) in the perovskite top cell, resulting in substantial internal reflection losses at the interface. To address this optical issue, an alternative ETL with a similar n should be utilized, such as fullerene-based ETL (n_{ref}~1.9). Additionally, the current losses in the silicon bottom cell due to the parasitic absorption of spiro-OMeTAD can be optically improved by substituting the dual-sided planar silicon substrate with a rear-sided textured substrate featuring a planar front surface. The reported efficiency and corresponding J_{SC} were 16.3% (1.43 cm^2) and 15.3 mA/cm^2, respectively. In the same year, this research group also investigated the effect of interconnecting layer thickness [18] on the optical response of subcells. With the thickness varied from 25 to 70 nm, the integrated current of the silicon bottom cell decreases due to parasitic absorption, and the thickness increment shifts the situation from top-cell-limited to bottom-cell-limited, demonstrating an optimal thickness of 40 to 50 nm for matching currents and an improved J_{SC} of 15.8 mA/cm^2.

For perovskite-related tandem solar cells, the ultraviolet (UV) induced degradation and parasitic UV absorption due to the perovskite layer and the transporting layer at the illumination side in the perovskite top cell, respectively, affect the device performance and stability. The research group from the University of New South Wales (UNSW) addressed this issue by converting the near UV light into visible light using a down-shifting layer incorporated into the textured anti-reflection (AR) foil [19]. Consequently, a 2T perovskite/silicon tandem solar cell was achieved with η of 23.1% (4 cm^2) and J_{SC} of 16.5 mA/cm^2. Due to enhanced light-trapping effects and re-emission of green light, an improvement in the optical response was observed across the entire wavelength region for the perovskite top cell and near the infrared wavelength region for silicon bottom cells, contributing to a current gain of approximately 2 mA/cm^2. To mitigate optical losses resulting from reflection between air and the top surface of tandem solar cells, AR coatings, typically deposited using thermal evaporation or E-beam, such as magnesium fluoride (MgF_2) and lithium fluoride (LiF), are also viable alternatives to AR foil.

Prior to 2017, the research on 2T perovskite/silicon tandem solar cells focused on the standard configuration (n-i-p) due to its outperforming efficiency compared to the inverted counterpart. As the performance of the perovskite solar cells with an inverted structure (p-i-n) is getting close to the standard one, more attentions haven been attracted to this configuration. In 2017, the first 2T perovskite/silicon tandem solar cell using an inverted perovskite top cell was reported with an impressive efficiency of 23.6% (1 cm^2) [20], in which a silicon nanoparticle (SiNP)/silver stack with a low n_{ref} of 1.4 and high transmittance at long wavelengths of above 100 nm was implemented to enhance the response of silicon bottom cell to the infrared spectrum. This method effectively increased the internal reflection between silicon substrate and back metal reflector that is attributed to the reduction in the fraction of light that reaches the lossy metal electrode. In addition, the thickness of top ITO layer was reduced to decrease the optical parasitic absorption losses, thus, the J_{SC} was efficiently improved to 18.1 mA/cm^2. To reduce the reflection losses progressively, the n_{ref} of the functional layers along the direction of incident light should increases. Based on this concept, the n-type doped amorphous silicon layer in the SHJ solar cell that is close to the illuminated side was replaced by the nanocrystalline silicon oxide (nc-SiO_X) [21] layer to meet the requirement of increasing refractive index, which was conducted by the research group from Helmholtz-Zentrum Berlin (HZB). Simulation results demonstrate that the increasing refractive index primarily affects the optical response of bottom cell while not affecting top cell, and suggests an optimal n_{ref} of approximately of 3, which were proved by the corresponding experimental results. By increasing the n_{ref} from 2.2 to 3, the optical response enhancement was observed almost cross the entire wavelength of silicon bottom cell, leading to a current gain of 1.3 mA/cm^2. Another critical parameter involved here is the layer thickness, as the minimum reflection is achieved when the optical thickness, defined as the product of n_{ref} and layer thickness, approximates a quarter of the incident wavelength. Therefore, after the thickness optimization of the nc-SiO_X layer with a high n_{ref} and a more dedicated optical thickness optimization, the J_{SC} was ultimately increased to 19.02 mA/cm^2. The research group from EPFL also adjusted their device configuration to this more efficient one and obtained a champion η of 25.2% (1.42 cm^2) [22] though optimizing the E_g and thickness of perovskite layer to maximize the integrated current of subcells to 19.5 mA/cm^2 and achieve the current matching conditions as well.

The world record J_{SC} of 21 mA/cm^2 [23] is achieved by the research group from King Abdullah University of Science and Technology (KAUST). A series of methods was adapted to enhance current effectively, including (1) replacing the interconnection ITO

layer with more transparent indium zinc oxide (IZO) layer, (2) reducing the interconnection IZO layer thickness from 20 to 5 nm to reduce the parasitic absorption losses, (3) reducing the thickness of the front-sided IZO electrode to 40 nm and narrow the finger width of the front-sided electrode from 100 μm to approximately 40 μm to minimize the current loss due to shading effect, (4) reducing the thickness of the rear-sided IZO electrode from 120 to 5 nm, and (5) implementing an advanced electrode structure at rear side that consists of silver grids, a 200 nm thermally evaporated MgF_2 film, a sputtered Ag film and the Ag busbars at the edge, which maximize the internal reflection.

Electrical optimization

Optical optimization enhances current, while electrical optimization not only improves *FF* but also increases voltage to a certain degree. However, unlike the gradual increase in J_{SC}, the *FF* does not exhibit a clear trend of growth, and it is difficult to summarize a pathway how tandem researchers improve the *FF* through a series of electrical optimizations. I therefore selected some typical cases to give you a broad concept what researchers have done to optimize electrical performance and how these methods affect *FF* and V_{OC}. Since 2017, the primarily investigated tandem configuration is integrated with perovskite top cell with inverted structure, we therefore discuss the electrical optimizations related to this configuration after 2017. Regarding *FF*, there is another critical time point that the reported *FF* were all below 80% before 2022. Until the end of that year, the research group from HZB broke the bottleneck and boosted the *FF* to 80.2% [24].

Indeed, the first 2T perovskite/silicon tandem solar cell with an inverted top structure developed by the research group from Stanford University in 2017 has already improved the *FF* to an excellent level of 79% [20], which, although not comparable to the optimal *FF* value of 83.6% [6] achieved by the research group from Longi in 2024, was ranked among the top three between 2017 and 2021. The methods of electrical enhancements utilized to attain this exceptional *FF* by Stanford University, published in Nature Energy in 2017, are summarized as follows: (1) An ultra-thin LiF film with a thickness of 1 nm was inserted between the perovskite layer and ETL to impede shunt pathways resulting from the high surface roughness of perovskite, with working principles analogous to the implementation of an insulating silicon oxide (SiO_2) interlayer in thin-film silicon solar cells. (2) An ultra-thin ZTO film was inserted between the sputtered top ITO and SnO_X buffer layer to reduce

the contact resistivity at this interface, and the thickness of the ZTO interlayer was optimized to lower the total R_S of the complete device, ultimately achieving the optimal *FF*. (3) A thick top ITO transparent electrode with a thickness of 150 nm and R_{SH} of 30 Ω/sq was applied to reduce the R_S originating from the lateral transport of electrons within ITO, but introduced current loss due to parasitic absorption of thick ITO. Currently, the balance between the absorption-induced current loss and series-resistance-induced electrical loss has been effectively adjusted by integrating several ultra-narrow metal fingers to the electrode frame to reduce the lateral transport pathway of electrons, thereby allowing the ITO thickness to be reduced to a minimum of 40 nm [23] to minimize optical absorption loss.

Subsequent to 2022, three research groups reported certified tandem efficiencies exceeding 32% [25-27] with *FF* enhancement from approximately 80% to above 81%, reaching a maximum of 83%. Consequently, this study traces their progress and summarizes the key modifications from an electrical perspective. In the research conducted by HZB, the *FF* bottleneck of 80% was surpassed, increasing from 79.4% to 81.2% through the application of an organic passivation layer, piperazinium iodide (PI) [25], on the top surface of the perovskite. This modification improves the band alignment and enhances charge extraction at the electron-selective contact. Similarly, the *FF* reported in KAUST's publications between 2022 and 2024 was enhanced from 80% [23] to more than 81.3% [26] due to improved perovskite film crystallization achieved by incorporating an additive, methylenediammonium dichloride ($MDACl_2$), into the perovskite precursor. The world record *FF* of 83% [27] was achieved by Longi, and the pathways of corresponding electrical optimization are related to the interface passivation as well. In contrast to single-layer passivation, the champion tandem solar cell utilized a double passivation layer, comprising LiF and ethylenediammonium diiodide (EDAI) [27], to mitigate interfacial recombination and reduce contact resistivity at the interface between the perovskite and fullerene (C_{60}). LiF, which typically induces field passivation, is deposited using thermal evaporation with a film thickness of 1 nm. Transmission electron microscopy (TEM) imaging revealed that this ultra-thin film is discontinuous, thus providing insufficient passivation efficacy. The EDAI layer is deposited via spin-coating atop LiF and can chemically passivate the remaining uncovered areas after 1 nm LiF deposition, effectively preventing direct contact between the perovskite and C_{60}, thereby suppressing interfacial recombination. LiF facilitates electron tunneling at the expense of high contact resistivity; however, this limitation can be effectively addressed by the subsequent deposition of the EDAI layer, which provides additional pathways for electron transport. In summary, these methods

applied to passivate the perovskite bulk or adjacent interfaces not only enhance *FF* due to improved carrier extraction but also increase V_{OC} as a result of recombination suppression.

Our institute has a stable baseline to fabricate high-efficiency silicon heterojunction solar cells and silicon bottom cells, as well as the capability to fabricate perovskite solar cells with good efficiency. From theoretical and practical perspectives, the development of perovskite/silicon tandem solar cells is feasible. This research focuses on developing window stacks, fabricating 2T perovskite/silicon heterojunction tandem solar cells to establish a stable fabrication chain, and maximizing efficiency. Consequently, the research commenced with the development of the fabrication process, necessitating a comprehensive understanding of the tandem configuration, the characteristics of each layer, and the requisite equipment and deposition masks for preparing these functional films. Upon establishing a stable baseline for tandem device fabrication, targeted optimization of either films or interfaces needs to be systematically conducted from both optical and electrical perspectives, particularly for novel components, such as Ag top electrode with a U-shaped pattern, transparent oxide electrode, and corresponding buffer layer.

3. Characterization methods

This chapter explores the characterization methods employed to evaluate the diverse properties and performance of the different types of samples in this thesis. The first section provides an overview of the techniques used to investigate the optical, electrical, and structural properties of materials and semi-devices, including bare films and layer stacks. The second section describes the characterization of the complete solar cells, and the final section details the simulation tools utilized in the analysis.

3.1. Characterization of materials and semi-devices

Compared with the characterization of complete devices that primarily focus on the output efficiency and long-term stability, the evaluation of materials and semi-devices involves a multidimensional approach for the quantitative and qualitative evaluation of materials and semi-devices are numerous and significantly more complex.

3.1.1. Optical properties

Spectrophotometry Calibrated Ultraviolet-Visible-Near Infrared Spectroscopy (UV-Vis-NIR), Perkin Elmer LAMBDA 950, was used to measure the spectral transmittance ($T(\lambda)$) and reflectance (R) of the bare film deposited on the Corning glass substrate. The system was equipped with a deuterium/halogen dual light source. The wide wavelength range of 250–1500 nm can be measured with the assistance of a photomultiplier tube and an InGaAs detector. A 150 mm diameter integrating sphere with a highly refractive, diffuse internal coating and a port configuration of 0°/8° was installed to gather and guide the scattered light

into the detector. In general, we measured $T(\lambda)$ and R within the range of 300 – 1200 nm, with a step of 5 nm. The sample was positioned in front of the optical entrance of the sphere, with the films facing the incident light, for transmittance measurement. For the reflectance measurement, the sample was positioned behind the optical exit located at the opposite side of the sphere without changing the sample orientation. We often measure more than one sample each time, and it is recommended to first perform the transmittance measurement for all samples and subsequently shift to the reflectance measurement to save time and simplify the operation. Note that the film thickness for bare films is required to be kept constant for a quantitative comparison of the optical properties when it is not the variation. For instance, comparing the transmittance of a 110 nm ITO film to that of a 50 nm IZO film makes no sense. Regarding semi-devices, the sample structure is also required to be the same if the variation is characteristic of a specific film instead of the structure itself. In the course of processing data, the spectral absorptance (A) can be calculated by the equation of A=1-$T(\lambda)$-R, and the comparison should be based on the premise of either same thickness for bare films or same structure for semi-devices. To exclude the influence of film thickness, the absorption coefficient (α), which describes the intensity attenuation of light passing through a material, is well established for a qualitative comparison of the light absorption capability, even if the film thickness is varied. For instance, the 50 nm and 100 nm homogeneous IZO films have the same α, whereas the values are different for the ITO and IZO films. Two methods are generally used to obtain α: (i) computing using $T(\lambda)$, R and thickness, known as the Hishikawa method [28], and (ii) computing using the extinction coefficient (κ) and wavelength (λ). Both methods were used in Chapter 5 to calculate the α and E_g of the SnO_X.

Ellipsometry As a nonconductive optical measurement method, ellipsometry is commonly used to study the dielectric properties of thin films, providing various types of information. The instrument used was a J.A. Woollam Co. M2000® UV ellipsometer, and the retrieved data is analyzed with the COMPLETEEASE® software. An important function of an ellipsometer is to measure the thickness of either a bare film or the films in a layer stack. Two modes can be used for thickness measurement: i) measuring a specific spot; you will obtain the film thickness of that spot, and ii) measuring lot of spots one by one with their positions determined in advance. The second mode, called thickness mapping, is generally used to monitor the homogeneity of thickness distribution in a selected area. Moreover, the

κ and n_{ref}, known as the optical constant, can be directly extracted from the properly fitted model of the target layer.

Steady-State Photoluminescence (ssPL) This method was carried out to investigate non-radiative recombination by evaluating the absolute photoluminescence (PL) spectra and quantum yields of the devices. The main components of the PL setup are the excitation laser and the monochromator. The excitation laser must have photon energy greater than the bandgap of the material being measured and sufficient power to generate an adequate PL signal. Typically, continuous laser powers in the range of watts can be used, but tens of milliwatts are often sufficient to produce a strong signal for indirect bandgap semiconductors such as perovskites. However, the required power depends on the material properties, optical throughput of the system, and sensitivity of the detector. After generation, the PL signal passes through a single-grating monochromator, which selects the desired wavelength for transmission to the detector. The system's ability to accurately measure photon energy—its resolution—is determined by the focal length of the monochromator, while the grating spacing dictates the wavelength range. For instance, a 0.22 m monochromator with a 1200 grooves/mm grating can cover the visible to near-infrared spectrum with an energy resolution of approximately 1 meV in the mid-range. For indirect bandgap semiconductors with low PL efficiencies, such as silicon, increasing the laser power indefinitely is not an option. High laser intensities at the focal point, in the order of watts per square centimeter, can damage the sample, necessitating careful control of the laser power to avoid degradation. We used the PL setup from QY.Berlin. This was accomplished using a laser with a wavelength of 532 nm and spot size of 0.10 cm^2. The laser intensity was set to replicate the solar intensity equivalent to 1 sun. The temperature is another important factor to consider. The most precise PL spectra were obtained from the samples kept below room temperature, as this reduced the thermal broadening of the excited carrier energies. The extent of thermal broadening at T is approximately equal to $k_B T$. At room temperature (300 K), this results in a broadening of approximately 25 meV, which can be reduced to approximately 7 meV at 77 K. Thus, cooling the sample results in sharper and more distinguishable PL peaks. In addition to improving the spectral resolution, cooling also minimizes the impact of competing non-radiative recombination pathways and inhibits impurity centers caused by thermal ionization, further enhancing the quality of the PL signal.

3.1.2. Electrical properties

Four-point probe The four-point probe is a portable, convenient, nondestructive, and quick measurement technique for R_{SH}. In this thesis, it was frequently used to determine the R_{SH} of ITO and IZO films during the TCOs development stage. The measurement setup consisted of four contact needles arranged in a line, and a sensing unit in 4-wires configuration. Every time the four needles were pressed onto the film surface, a current (I) was passed through the two outer needles, also known as probes, and a V was induced in the inner needles. Based on reading I and V, the R_{SH} of the small contacting area can be determined via Eq. 3.1:

$$R_{SH} = \frac{V}{I}\frac{\pi d}{\ln 2} \tag{3.1}$$

where d is the thickness of the film. This process can be repeated unlimited times with four needles in contact with either the same or different positions. For different position measurements, a summary of the results can provide information about the distribution of the R_{SH}, similar to R_{SH} mapping.

Hall effect measurement Hall effect measurement is a powerful technique for characterizing the basic electrical properties of semiconductor materials, including the doping/conductivity type, charge carrier mobility (μ), carrier concentration, resistivity (ρ), and Hall voltage. The physical mechanism of the Hall effect is the Lorentz force, which consists of both electric and magnetic forces. In a magnetic field, when an electric current flows through a thin flat conductor or semiconductor in a direction perpendicular to the magnetic field, the electrons and holes within the material are subjected to the Lorentz force in the magnetic field to move in the opposite direction. This results in the accumulation of charges with different polarities on both sides of the material, creating an electric field across the width of the sample, which is also known as the Hall voltage. The Hall voltage is perpendicular to both the electric and magnetic fields.

To measure the electrical characteristics of a semiconductor film in our lab, the thin film should be deposited on a Corning glass substrate in the step of sample preparation and

should be cut into a small square with a size of 1.2 × 1.2 cm^2. Subsequently, the sample was loaded into a homemade chuck with four corners of the target film in contact with four metal pins integrated into the chunk. If the conductive sample is properly loaded, the contact resistivity between the pins and films should not exceed the measurement range and allow current to pass through, which is the premise of a successful measurement.

Coplanar conductivity In this thesis, the electrical conductivity (σ) of the charge carrier within the ultrathin SnO_X films failed to be obtained from either four-point probe or Hall effect measurements due to an extremely large R_{SH} and poor electrical contact between the pins and film, respectively. Conductivity measurements enabled the characterization of the lateral conductivity of SnO_X in the dark through two rectangular coplanar silver contacts with a size of 3.5 × 5 cm^2 deposited using a thermal evaporator, and the vertical distance between the silver contacts was 0.5 mm. The measurement was conducted at room temperature in dark ambient air, and the scanning voltage range was generally set to -100 V and +100 V in steps of 10 V. When the resulting current exceeds the upper limit of 1 mA, the probe voltage should be adjusted accordingly. The lateral dark conductivity of the semiconductor film was determined using Eq. 3.2:

$$\sigma = \frac{I}{V}\frac{w}{\mathrm{d}l} \tag{3.2}$$

where w is the vertical distance between the Ag contacts, d is the film thickness of the target semiconductor, and l is the contact length.

Transfer Length Method (TLM) The transfer length method was used to determine the sum of the contact resistivity (ρ_c) at the SnO_X/ITO interface and intrinsic resistivity of the SnO_X film within the window stack. The sample structure for the TLM measurements was glass/full ITO/full SnO_X/patterned ITO/patterned Ag. Eight patterned ITO and Ag pads were deposited on top of the layer stack with increasing spacing between each pad and the same thickness as that used in semi-transparent perovskite solar cells, and the Ag pads were in contact during the TLM measurement. According to the pathway of current flow, the total R_S consists of four times the contact resistance at the SnO_X/ITO interface ($R_{S,SnOx/ITO}$),

two times the intrinsic resistance of SnO_X layer ($R_{S,SnOx}$), and the resistance ($R_{S,ITO}$) generated within the full ITO layer owing to the lateral flow of current from one pad to its adjacent one, whereas the extremely low contact resistances related to the ITO/Ag interface, Ag, and ITO pad can be neglected. The resistances between each adjacent pad extracted from the JV curves were plotted as a function of the distance between two adjacent pads, from which a linear curve was fitted with an equation. The general description of the equation for our scenario is written as

$$R_S = R_{S,\,ITO} + 4R_{S,SnOx/ITO} + 2R_{S,\,SnOx} = \frac{R_{SH,ITO}}{W} \times L + \left(4\rho_{c,SnOx/ITO} + 2\rho_{SnOx}\right) \times \frac{d_{SnOx}}{A} \quad (3.3)$$

where $R_{SH,ITO}$ is the sheet resistance of the full ITO film, W is the width of the Ag pad, L is the distance between two adjacent pads, $\rho_{c,SnOx/ITO}$ is the contact resistivity at the SnO_X/ITO interface, ρ_{SnOx} and d_{SnOx} are the resistivity and film thickness of SnO_X, and A is the area of the Ag pad. Therefore, the sum value of $\rho_{c,SnOx/ITO}$ and ρ_{SnOx} can be calculated using the intercept. Further details can be found in Chapter 8.

Space-Charge-Limited Current (SCLC) transport measurements SCLC transport measurement is well known and is mostly used to determine the charge-carrier mobilities of intrinsic and lightly doped semiconductors. This measurement relies on the interpretation of the dark *JV* curves of single-carrier devices, electron-only or hole-only devices, under forward and reverse bias voltages. In a single-junction device, if the contact work functions are asymmetric at both ends, a built-in voltage (V_{BI}) is present. A simple method has been developed to extract the V_{BI} from SCLC *JV* data based on the Mott-Gurney (MG) law [29,30].

3.1.3. Structural properties

Thickness As previously mentioned, ellipsometry can accurately measure the film thickness and thickness distribution in selected areas without damaging the samples. In addition to ellipsometry, thickness measurements were performed using a profilometer

(Veeco Dektak 6M Stylus Profiler). This method involves the use of a probe tip that directly contacts the sample and scans across a sharp step between the substrate and the film. The thickness of the film or layer stack was determined to be equal to the thickness difference between the substrate and film. However, this sharp step often requires a destructive preparation process, which varies depending on the material.

Mechanically soft perovskite films that are hundreds of nanometers thick can be easily scratched away from a glass substrate using the sharp tip of tweezers. Different approaches have been employed to measure the thickness of the films in SHJ solar cells. One technique involves placing dots on a bare substrate with a permanent marker prior to film deposition. After deposition, the dots were carefully scratched away using a scalpel and then cleaned with isopropanol to reveal the step. Another method involves placing small wafer pieces on the substrate as masks before deposition, which are then removed to create a sharp step.

X-ray photoelectron spectroscopy (XPS) / Ultraviolet photoelectron spectroscopy (UPS) measurements The XPS/UPS system is a MULTIPROBE MXPS system from Scienta Omicron with an ARGUS hemispherical electron spectrometer, which is part of the Jülich Online Semiconductor Growth Experiment for Photovoltaics (JOSEPH) cluster system at the research center Jülich. The base pressure in the XPS/UPS system is $3 \cdot 10^{-11}$ mbar. XPS measurements are generally performed after UPS measurements. because of the longer irradiation time required. The samples were transferred from the glovebox to the ultra-high vacuum (UHV) cluster using a sealed nitrogen-filled container.

XPS measurements The X-ray excitation source is a XM 1000 AlKα X-ray excitation source operated at 300 W. The resulting spectra were collected in constant Analyzer-Energy (CAE) mode with a path energy of 100 eV for the survey spectrum and 20 eV for the high-resolution spectra. In the setup, the source analyzer angle is 90° and the takeoff angle of the electrons with respect to the surface normal is 21°.The energy resolution as estimated by the full-width at half-maximum (FWHM) of the Au 4f peak was ca. 0.6 eV. The intensities were determined by measuring the area of each peak after subtracting a Shirley-type background and fitting the experimental curve to a combination of Lorentzian and Gaussian lines with a fixed proportion of 30:70. Fitting was done with the help of the XPST Plugin (M. Schmid, Philipps University Marburg) in Igor Pro (Wavemetrics).

XPS was performed to investigate the local chemical bonding on surface using a MULTIPROBE MXPS system from Scienta Omicron with an ARGUS hemispherical electron spectrometer, which is part of the JOSEPH cluster system in the research center Jülich. The samples were transferred from the glovebox to the UHV cluster under an inert gas. The base pressure in the XPS system was $1 \cdot 10^{-10}$ mbar.

The uncertainty of the results for a quantitative analysis of XPS spectra depend on multiple factors: for example, giving only the standard deviation of the least-squares fit as an error for the final result of the atomic composition would be misleading, as the fit is heavily influenced by the initial assumptions, which include the utilized fit function, the number of components and the starting value of each parameter (position, width and area of the peaks). The biggest contribution to the uncertainty of the final results has the background function, which must usually be manually defined in the standard XPS analysis software. (This involves selecting start- and end energy for the background function.) In this work, we employed the commonly utilized Shirley function, which is a simple assumption of the background shape caused by inelastic scattering [31]. Changing the background consecutively also changes the results of the least-squares fit procedure. Finally, to determine the atomic compositions the integrated areas of the fits must be corrected by the analysis depth, which is the inelastic-mean-free-path and typically an unknown function of the photoelectron energy. In this study, we had to rely on the usually used "universal" function developed by Powell [32].

The only thing that principally could have been done to obtain statistical data for the final results would have been to repeat the measurement and analysis multiple times. However, this approach would introduce a new complication, as the extended exposure to the x-ray beam (approximately 30 minutes per measurement) would likely result in radiation damage to the perovskite material, thereby potentially influencing the outcome. To provide an estimate of the uncertainty for the determined atomic compositions, we can refer to values cited in surface analysis textbooks such as [33]. These sources suggest an error margin of $< \pm 10\%$ for the results of the quantitative analysis.

UPS measurements The light source for the UPS measurement was a HIS13 HeI gas discharge vacuum ultraviolet (VUV) source from FOCUS GmbH (main line HeI_{α} 21.218 eV). To mitigate radiation damage, the light intensity was attenuated by a factor of 100 by using a filter (Luxel Corporation). Spectra are collected with a path energy (PE) of

2 eV, a digital resolution of 0.01 eV and a sample bias of 6 V at a takeoff angle of 0°. For all the samples, the measurements were repeated at six positions on the sample.

The binding energy scale was referenced to the Fermi edge measured on a freshly evaporated gold sample under identical conditions. Spectra are corrected for the satellite emissions of HeI at 23.09 (HeI_{β}) and 23.74 (HeI_{γ}).
The work functions were determined from the spectra by measuring the position of the cutoff at high binding energies using linear fits at the background and steep edge. The same linear fit method was applied to the leading edge of the UPS spectra to determine the valence band positions of all materials. For perovskite with a low density of states at the band edge, it is recommended that the valence band maximum be determined on a semilogarithmic scale. Because this method is highly susceptible to the background level, dark measurements were performed to determine the noise level and subtract it from the spectra. Subsequently, the band edge was determined by exponential fitting to the leading edge and the background.

X-ray diffraction (XRD) measurements XRD was performed to investigate the crystal structural changes using a RIGAKU SmartLab with a Cu Kα radiation source. The X-ray generator was set to 40 kV and 40 mA, and 2θ scans between 5° and 60° were collected with a step size of 0.02°.

Scanning electron microscopy (SEM) Surface and cross-sectional SEM images of the samples were investigated with Carl Zeiss AURIGA® CrossBeam® Workstation using in-lens detector with the electron acceleration voltage of 5 kV.

Kelvin probe force microscope (KPFM) KPFM measurements were conducted within an argon-filled glove box (O_2 < 0.1 ppm, H_2O < 0.1 ppm, MBraun). All images were acquired using PeakForce KPFM mode. A cantilever equipped with a boron-doped diamond tip (ADAMA, AD-2.8-AS) was employed in tapping mode to perform measurements of the plane-view of selected samples. To ensure accuracy and reliability, a minimum of two random locations were examined.

3.2. Characterization of solar cells

JV characteristics For single-junction perovskite solar cells and perovskite/silicon tandem solar cells, the *JV* characteristics were measured using a calibrated AM1.5 spectrum of a class ABB solar simulator (Lot Oriel LCS-100) directly integrated into the glovebox, which was also used for MPP tracking. A monocrystalline silicon reference cell (Oriel 91150V) provides a power density of 100 mW/cm^2, which has been certified by the Newport Corporation's PV Lab (North Logan, UT), an ISO/IEC 17025 accredited photovoltaic calibration and test laboratory. The measurements were performed in accordance with the ASTM E948 and E1021 standard methods developed and used by the NREL. An illumination mask with an aperture area of 1.21 cm^2 was used for *JV* measurements of the tandem solar cells. Ref. [34] is recommended for further reading.

LED-solar simulator measurements In addition to the current-voltage characterization on the calibrated class AAA solar simulator, another setup directly integrated into the glove box was used for (*JV*-curves), MPP and $J_{sc}V_{oc}$ measurements at different light intensities.

This solar simulator is equipped with a white light LED (Cree XLamp CXA3050), whose illuminance has been adjusted to one sun conditions using the short-circuit current resulting from the quantum efficiency measurement of a perovskite cell. A 2450 Keithley is used as a source measure unit.

Suns-V_{oc} and dark JV measurements To get insides of the behavior at different illumination intensities we measured J_{SC} and V_{OC} of the solar cells at different illumination intensities at the LED. The illumination intensity varied from 0.005 suns to 1.5 sun and back to 0.005 suns in logarithmic-spaced steps. We measured dark *JV* from −0.1 V to 1.25 V in steps of 0.01 V with a scan speed of 20 mV/s in forward and reverse voltage scan.

External quantum efficiency ($Q_{e,PV}$) $Q_{e,PV}$ is defined as the fraction of charge carriers collected by the solar cells per incident phonon as a function of the wavelength. The J_{SC} that is integrated using the $Q_{e,PV}$ spectrum is calculated by the following equation

$$J_{\mathrm{SC,Q_{e,PV}}} = q \int Q_{\mathrm{e,PV}}(\lambda)\phi_{\mathrm{AM1.5}}(\lambda)\mathrm{d}\lambda \tag{3.4}$$

where $\phi_{\mathrm{AM1.5}}(\lambda)$ is the photo flux of the standard AM1.5 spectrum and q is the elementary charge. The $Q_{\mathrm{e,PV}}$ setup consisted of a xenon light source (Osram XPO150W) and Bentham monochromator (TMC300) with a spectral range of 300-1150 nm in steps of 10 nm. A calibrated silicon photodiode (Gigahertz-Optik SSO-PD100-04) was used as a reference for simulated light calibration. The device was placed behind a quartz glass window in a sealed nitrogen-filled measurement box during the measurement to prevent performance degradation. Thus, a lower integrated current density was obtained compared with the short-circuit current density extracted from the *JV* curve. A detailed description of the $Q_{\mathrm{e,PV}}$ setup is given in Ref. [35].

Regarding single-junction devices, such as perovskite solar cells or SHJ solar cells, no bias light or bias voltage are required during measurement. However, both components are required for perovskite/silicon solar cells. When measuring the perovskite top cell, a high-intensity infrared bias light is required to dramatically increase the J_{SC} of the bottom cell. Consequently, the J_{SC} of the tandem device was limited by the top cell, and its value was recorded by the setup as the J_{SC} of the perovskite top cell. In addition, a positive bias voltage of about 0.7 V is needed to put the bottom cell at short-circuit. When measuring the silicon bottom cell, blue bias light of high intensity and a positive bias voltage of approximately 1.2 V are required for the same reasons.

3.3. Tools for numerical simulations

Stopping and Range of Ions in the Matter (SRIM) SRIM software [36] is generally used to simulate the penetration depth profile of incident ions. This program can analyze how the incident ions penetrate the target matter and lose energy by inputting the type and initial energy of the incident ions, film thickness, density of the target matter, compositional atoms of the target material, and corresponding atomic stoichiometry. The penetration profile of the ions in the matter provides abundant information, such as the penetration depth and a comprehensive analysis of the energy losses that are used for ionization, creating vacancies,

and being released as phonons. In this thesis, the SRIM program was used to investigate ion-bombardment-related sputter damage by simulating the penetration depth of the highly energetic negative ions that are present in the plasma during the ITO sputtering process in different types of layers and layer stacks.

One-dimensional Drift-Diffusion simulation One-dimensional drift-diffusion simulations were performed using Solar Cell Capacitance Simulator (SCPAS) software [37] developed at the University of Gent. Originally developed to simulate thin-film solar cells, such as $Cu(In,Ga)S_2$ and CdTe, SCAPS software has recently been applied to simulate the behavior of amorphous silicon and organic solar cells by solving the Poisson and continuity equations for electrons and holes. In addition to steady-state simulations, it also performs frequency-domain simulations, allowing modeling of the capacitance of a complete device as a function of frequency, voltage, or temperature. The Solar Cell Definition panel allows users to set all parameters to define the properties of the contacts and active layers of the target device, including the selection of the bulk recombination mechanism and surface recombination at the contacts. SCAPS simulations can be conducted either in the dark or under illumination; however, an additional optical simulator is required if users wish to apply sophisticated optical models. In this thesis, SCAPS simulations were often conducted with the energy levels extracted from the UPS measurements to obtain a deeper insight into band alignments, which have a significant impact on the charge extraction and recombination in solar cells.

Quokka3 Quokka3 is a commercial solar cell simulator [38-40] which can numerically solve the 3D charge carrier transport in silicon devices in a quasi-neutral state with satisfactory precision [41-43]. In this thesis, Quokka3 was used to analyze the interplay between three factors using two silicon solar cells with a p-n junction on the front and rear surfaces as a function of the surface recombination velocity at both interfaces. The three factors are: (i) the wavelength region of EQE response enhancement (long wavelength or entire range), (ii) the location of the passivated interface (front-sided or rear-sided), and (iii) the illumination direction during EQE measurements (top or bottom).

3.4. Film deposition techniques

3.4.1. Tin oxide by atomic layer deposition

In the top cell of perovskite-related tandem solar cells, SnO_X is a buffer layer typically used to protect the underlying electron transport layer and the perovskite layer from sputter damage during the deposition of TCOs that is extremely essential for obtaining a working device, and naturally for achieving high efficiencies. In perovskite/silicon tandem solar cells with an inverted structure (p-i-n), instead of continuing to use BCP as the buffer layer between the ETL and electrode, most researchers opted for SnO_X, which is often deposited by ALD onto the ETL, C_{60}. The reason could be multiple, and the primary reason is that thermally evaporated C_{60} is not as dense as ALD-SnO_X. Thus, a thicker Bathocuproine (BCP) is required to mitigate sputtering-induced damage, which inevitably increases parasitic absorption losses. Owing to the non-conductive nature of BCP, thicker films exhibit more pronounced electrical losses.

ALD enables precise atomic-level control and conformal deposition via sequential self-limiting surface reactions. Most ALD processes rely on binary reaction sequences, in which the sample surface is exposed to the two precursors gases separated by N_2 purging of the chamber to prevent reactions in the gas phase. In Fig. 3.1, after precursor A pulse and N_2 purge, a monolayer of the first precursor was formed due to a saturated absorption of molecules onto the sample surface. Subsequently, precursor B was introduced into the chamber by pulsing as well, which reacted with precursor A within the as-deposited monolayer, and the following N_2 purge carried the excessive, unreacted precursors to leave of the chamber. Consequently, two surface reactions occur to form a binary compound film. The deposition process is limited to a controlled number of surface species, because the number of reactive sites on the surface is not infinite. When both reactions are self-limiting, they can proceed sequentially, allowing the deposition of thin films with atomic precision [44]. One of the key advantages of ALD is its ability to achieve precise thickness control on the Ångstrom (Å) or monolayer scale. The self-limiting nature of ALD ensures excellent step coverage and uniform deposition even on high-aspect-ratio structures. Note that the chemical vapor deposition (CVD) of two precursors must be prevented in the ALD system, which means all the precursors present at the same time and react in the gas phase, resulting

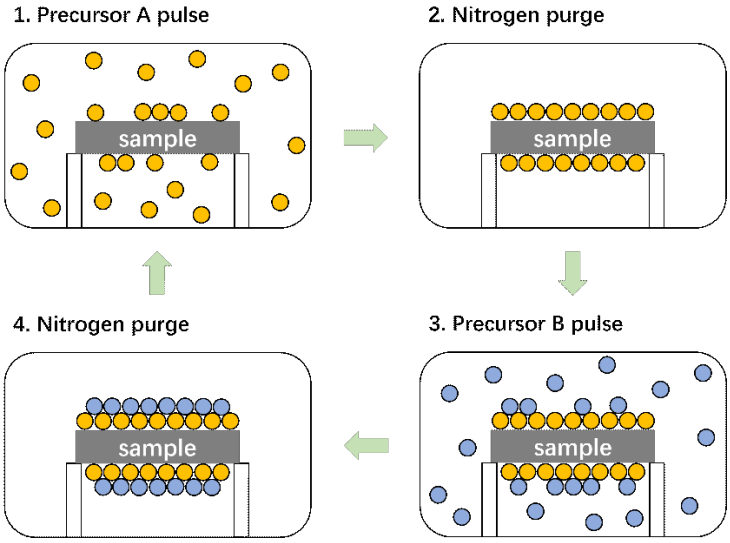

Figure 3.1.: *The binary reaction process in atomic layer deposition system for a hypothetic system of components A and B.*

in reduced reactivity and undesirable film properties. Increasing purge time is an effective way to prevent the occurrence of CVD.

3.4.2. Transparent conductive oxide by magnetron sputtering

The deposition techniques of TCOs include physical vapor deposition (PVD) and CVD, such as vacuum evaporation, electron beam evaporation, magnetron sputtering, pulsed laser deposition etc. under the category of PVD, and molecular beam epitaxy, atomic layer epitaxy, ion implantation, sol-gel method under the category of CVD. Among all the deposition methods, the primary ones currently suitable for mass production are magnetron sputtering and the sol-gel process, which have formed an industry. Among these, magnetron sputtering is particularly advantageous because of its excellent controllability, making it easier to produce large-area, uniform films.

Sputtering is a physical process in which atoms from a solid target are ejected into

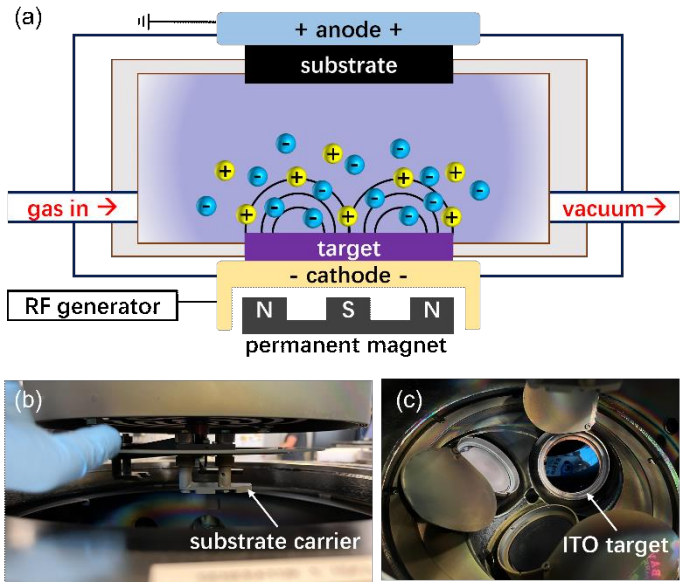

Figure 3.2.: *(a) Schematic of a RF magnetron sputtering system. Images of (b) the substrate carrier and ITO target inside the JOSEPH sputtering system in our lab.*

the gas phase after being struck with high-energy ions. The process can be divided into several steps. 1) Sputtering usually occurs in a vacuum chamber filled with an inert gas, argon (Ar), which is ionized under a high-voltage electric field applied across the chamber, forming a plasma consisting of positively charged Ar ions (Ar^+) and free electrons. 2) Ar^+ from the plasma is accelerated towards the target by the electrical field because the target is connected to the cathode. 3) The energetic Ar^+ bombarded the surface of the solid target and transferred the energy to the targeted atoms, causing some of the atoms to be ejected into the gas phase. 4) The ejected atoms travel through the vacuum and deposit onto the substrate, forming a thin film. One of the key advantages of sputtering is its ability to deposit thin films of high-melting-point materials at relatively low temperatures. The deposited thin film also maintained the original composition of the target, making it widely used in semiconductor devices and integrated circuit manufacturing.

The sputtering systems that are typically used in practice include direct current (DC), RF and magnetron sputtering [45]. The difference is that the target is composed of metal in the DC sputter system, while the target is insulator in RF sputtering system. Since the

deposition rates of sputtering system are lower than other vacuum deposition techniques due to higher pressure (1~5 Pa), magnetic field is introduced to improve the deposition rate and film uniformity. Owing to the magnetic field created by a circular or rectangular magnet placed behind the target, electrons are confined near the target surface due to this trapping effect and move in a helical path, as shown in Fig. 3.2. The accumulated electrons due to the formation of a drift loop close to the target surface increase the collision rates with Ar atoms, implying a higher ionization of the inert gas and denser plasma near the target surface. Consequently, the deposition rate increased as a result of the higher density of Ar^+ bombarding the target; thus, more targeted atoms were ejected into the gas phase and the sputtering rate increased effectively.

4. Process development for perovskite/silicon tandem solar cells

This chapter focuses on the development and optimization of the fabrication process for monolithic perovskite/silicon tandem solar cells, from the design of the device configuration to the design of the masks used for each layer, to the iterative adjustments and modifications necessitated by practical challenges. The design of masks was a collaborative effort; I proposed the idea and provided a preliminary draft, which our technicians then refined into professional drafts using their expertise.

4.1. Device configurations and fabrication process

2T perovskite/silicon tandem solar cells consist of a perovskite top cell and silicon bottom cell, which are fabricated from bottom to top layer by layer. According to the tandem configurations mentioned in recent publications, most research groups are working on the perovskite/silicon tandem solar cells (2 cm × 2 cm) with an aperture area of approximately 1 cm^2 in the center [23,25,46]. We also used 1 cm^2 as the aperture area for tandem device development.

The device architecture of perovskite/silicon tandem solar cells is determined by the configurations of two sub-cells: SHJ and perovskite solar cells (PSCs). However, this is slightly different from the simple combination. In SHJ solar cells, all layers are deposited on both sides of the silicon substrate, starting with intrinsic hydrogenated amorphous silicon (a-Si:H (i)) and finishing with screen-printed Ag electrodes, and the *JV* characteristics are allowed to be measured from both sides. The SHJ solar cell structure followed the sequence Ag/ITO/a-Si:H (p)/a-Si:H (i)/c-Si (n)/a-Si:H (i)/a-Si:H (n)/ITO/Ag from bottom to top, as shown in Fig. 4.1 (a). In single-junction PSCs, all layers are fabricated sequentially from

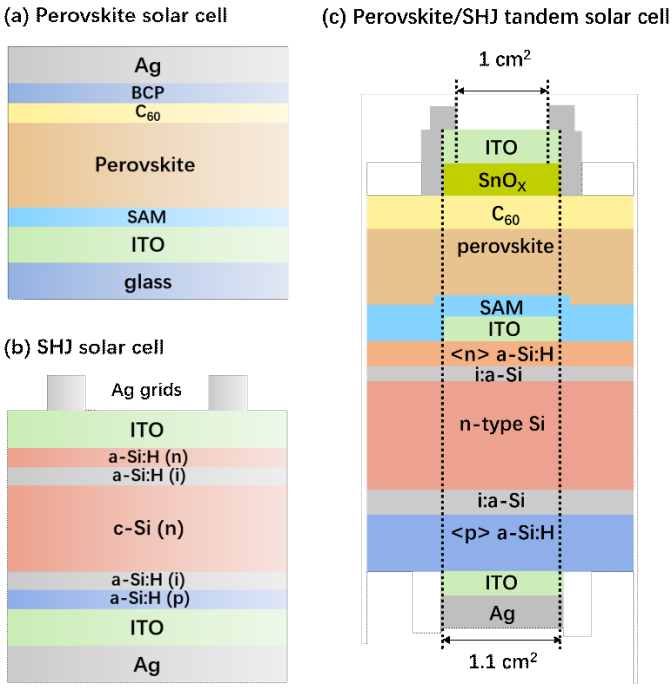

Figure 4.1.: *Schematic illustrations of (a) silicon heterojunction solar cell, (b) perovskite solar cell with inverted structure (p-i-n), and (c) perovskite/silicon heterojunction tandem solar cells.*

bottom to top on a glass substrate with a TCO coating, and finished with an opaque metal electrode. As a result, cell performance can only be measured from the glass side. A typical schematic of a PSC with an inverted structure (p-i-n), from bottom to top, is glass/ITO/SAM/perovskite/C_{60}/BCP/Ag, as depicted in Fig. 4.1 (b), in which a SAM is the HTL, C_{60} is the ETL, and BCP is the buffer layer.

In the 2T tandem structure, an interconnection layer (ICL) is necessary to facilitate the recombination of oppositely charged carriers from the subcells. TCOs are ideal candidates for ICL, eliminating the need to screen print the top silver grid when the SHJ solar cell serves as the bottom cell. The front-side ITO of the SHJ bottom cell naturally functions as the ICL in the 2T tandem device, with PSCs deposited directly on it, as shown in Fig. 4.1 (c). When inverted PSCs (p-i-n) are used as the top cells in 2T perovskite/silicon tandem

solar cells, the HTL, perovskite layer, and ETL are sequentially fabricated on the silicon bottom cell following the same procedure as for single-junction PSCs. However, the opaque silver electrode was replaced by a conductive window stack consisting of a TCO and a buffer layer to allow light to enter the cell from the ETL side. TCOs are mostly prepared by sputtering, which offers advantages such as high deposition rates, excellent adhesion, and uniformity [47-50]. However, the sputtering process of TCOs tends to damage the underlying organic layers, particularly the perovskite layer [51,52]. The most common method for mitigating sputter-induced damage is covering the ETL with a buffer layer before TCOs sputtering. In addition, the Ag frame was thermally evaporated onto the edge of the TCOs layer for carrier collection, and the uniformly distributed, ultrathin Ag grids were also evaporated on the surface of the TCOs to minimize the R_S caused by the lateral transport of electrons within the TCOs layer before they were collected by the Ag frame. Therefore, the active area of the 2T perovskite/silicon tandem solar cell is defined by the area of the TCO region, which is surrounded by a silver frame on the top surface.

Following the determination of the structure for the 2T perovskite/silicon tandem solar cells and the expected configuration of each layer, we proceeded to visualize the entire fabrication process. In this study, rear-emitter SHJ solar cells were used as the bottom cells, whereas the top cells comprised PSCs with an inverted structure.

4.1.1. Silicon heterojunction bottom cell

For the fabrication of the SHJ bottom cells, the process was divided into five steps, and each step will be discussed individually. The first step is the selection of the silicon wafers. For the most basic components in the manufacturing process, there are two options: Czochralski (CZ) and float-zone (FZ) wafers. The latter generally have better quality and naturally higher prices. In addition, various wet-chemical treatments on silicon wafers further broaden our choices, including the planar surface formed by chemical polishing and textured surface formed by chemical texturing. Planar wafers contained mirror-polished FZ wafers and alkaline/acid-polished CZ wafers. However, the surfaces of the latter were not as smooth as those of the former. With respect to the number of polished surfaces, planar wafers can be classified into double-sided polished (DSP), single-sided polished (SSP), and double-sided textured (DST) wafers, as shown in Fig. 4.2 (a-c). Textured wafers contain nanotextured wafers with pyramid sizes varying from several hundred nanometers to 1 μm

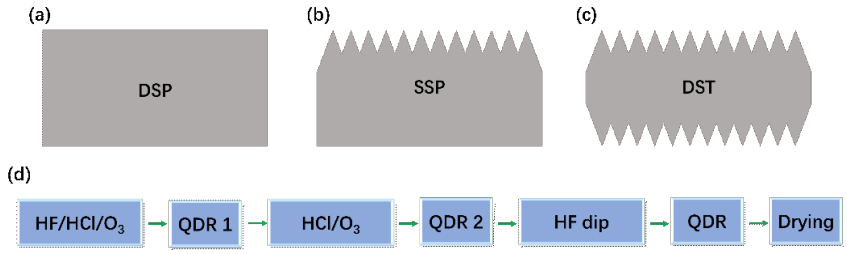

Figure 4.2.: *All types of silicon wafers: (a) double-sided polished (DSP), (b) single-sided polished (SSP), and (c) double-sided textured (DST) wafers. (d) Process flow chart for wet chemical cleaning of silicon wafers with ozone.*

and industrial-scale textured wafers with pyramid sizes of 3–5 µm. Moreover, the intrinsic properties of silicon wafers, such as the carrier lifetime, wafer thickness, resistivity, crystallographic orientation of the wafer surface, doping type, and concentration, are essential for achieving high-quality products. Because an excellent baseline for SHJ solar cell manufacturing had been established in our institute [53], we were able to quickly move into the fabrication of SHJ bottom cells after all the deposition masks specially designed for tandem devices were completed. During the first few years of the experiments DSP n-type FZ wafers were used as substrates.

Second, the silicon wafers were treated by ozone (O_3) cleaning in a wet bench, which was cleaned three times in different solution mixtures and each cleaning step was followed by a quick dump rinse (QDR) in deionized (DI) water. From the detailed process flow of O_3 cleaning shown in Fig 4.2 (d), O_3 was used in both the first and third steps for disinfection, reduction of the organic carbon in rinsing water, and SiO_2 formation. Metallic impurities and organic residues were removed using hydrochloric acid (HCl), and native oxide was removed using diluted hydrofluoric acid (HF). The main advantages compared to the traditional Radio Corporation of America (RCA) clean are the reduction of the consumption of hazardous chemicals and saving of DI water due to much shorter rinsing time.

Third, after wet-chemical cleaning, the wafers were immediately transferred into a plasma-enhanced chemical vapor deposition (PECVD) system called AK 1000 In-line from Meyer Burger Technology AG for both intrinsic and doped hydrogenated amorphous silicon film deposition. The deposition system consists of three process modules (PM1,

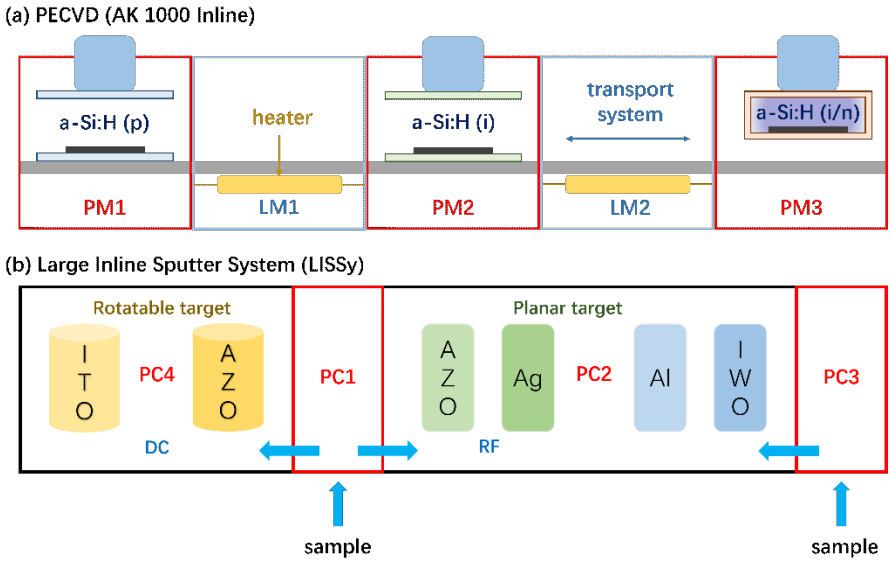

Figure 4.3.: Side *view of (a) the PECVD deposition system (AK 1000 Inline) and (b) Large Inline Sputter System (LISSy).*

PM2, and PM3) and two loading modules (LM1 and LM2). The wafers were loaded into the system through the chamber of the LM and automatically transported to the chamber of the PM. In real cases, various types of silicon wafers were used for fabricating the bottom cells; here, we used a DSP wafer as an example. A sketch of the AK 1000 In-line is shown in Fig. 4.3(a). The standard deposition sequence was as follows: 1) loaded wafers on LM2 and transport in PM3; 2) deposited 4 nm a-Si:H (i) layer on the front surface in PM3; 3) deposited 4 nm phosphorus-doped hydrogenated amorphous silicon (a-Si:H (n)) layer on the front surface in PM3; 4) unloaded samples from LM2, flipped to the other side and reloaded into LM1; 5) transported samples to PM2 and deposit a 6 nm a-Si:H (i) layer on the rear surface; 6) transported samples PM1 and deposit a 13 nm boron-doped hydrogenated amorphous silicon (a-Si:H (p)) layer on the rear surface; and 7) unloaded samples from LM1. Briefly, the a-Si:H (i)/a-Si:H (n) stack was deposited on the front side in the same chamber with a thickness of 4 nm/4 nm, followed by the deposition of the a-Si:H (i)/a-Si:H (p) stack on the rear side with a thickness of 6 nm/13 nm in separate chambers to minimize boron contamination of the rear intrinsic layer. In addition, the

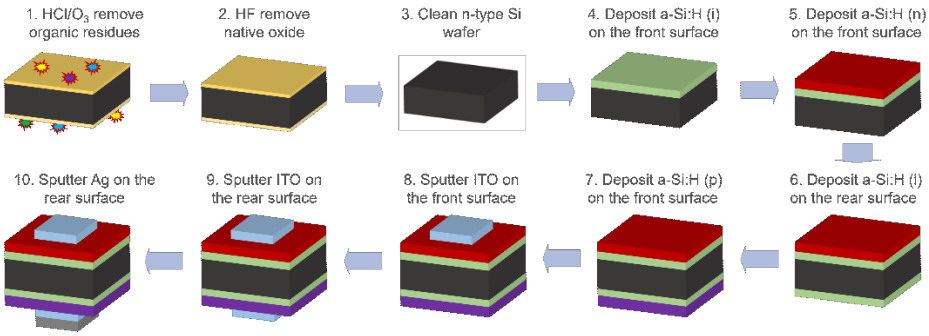

Figure 4.4.: *Process flow chart for the fabrication of SHJ bottom cells with rear p-n junctions.*

intrinsic layer was deposited at 50 W with an H_2 flow of 650 sccm and a SiH_4 flow of 145 sccm. The n-type layer was prepared in a PECVD system with a plasma excitation frequency of 13.56 MHz, a power density of 80 mW/cm^2, a deposition pressure of 2.5 mbar, and a heater temperature of 200°C. The precursor gases used were SiH_4, H_2, PH_3 (1% diluted in H_2), and CO_2. The p-type layer was deposited at 90 W with a H_2 flow of 500 sccm, a SiH_4 flow of 50 sccm, and 1% trimethylboron in a H_2 flow of 100 sccm.

After the deposition of the PECVD stacks, the wafers were transferred to a sputtering system called a Large Inline Sputter System (LISSy) for TCOs and pure metal deposition. The deposition system consists of two process modules (PC4 and PC2) and two loading modules (PC1 and PC3). Rotatable ITO and Al-doped zinc oxide (AZO) targets were installed in PC4. Planar targets including AZO, Ag, Al, and tungsten-doped indium oxide (IWO) were installed in PC2. The wafers were loaded into the system through chambers PC1 or PC3 and were automatically transported to the sputtering chamber. A schematic of the magnetron sputtering system is shown in Fig. 4.3(b). The standard sputtering sequence was as follows: 1) loaded samples on PC1 and transport in PC4; 2) deposited a 20 nm ITO layer on top of the a-Si:H (n) layer in PC4; 3) unloaded samples from PC1, flipped to the other side and reloaded into PC1; 4) transported samples to PC4 and deposited a 70 nm ITO layer on top of the a-Si:H (p) layer; 5) transported samples to PC2 and deposited a 1 μm Ag layer on top of the ITO layer on the p side; and 6) unloaded samples from PC1. In brief, the ITO layer was deposited on the front side in the PC4 with a thickness of 20 nm as the ICL, followed by the deposition of the ITO/Ag stack on the rear side with a thickness of

70 nm/1μm in PC4 and PC2, respectively. The ITO layers were DC-sputtered from a 3% Sn-doped In_2O_3 cylindrical target at 200 °C using a high-purity Ar/O_2 gas mixture under a given pressure. Both-sided ITO and rear-sided Ag were deposited in the center of the sample surface using deposition masks customized for the bottom cells. The process flow chart for the fabrication of an SHJ bottom cell with rear p-n junctions is shown in Fig. 4.4.

Finally, large 4-inch or M2+ (157 mm × 157 mm) wafers were cut into small cells (2 cm × 2 cm) using a picosecond laser from the front side, which effectively protected the p-n junction at the rear side from being damaged by the laser. Generally, the wafers are not cut through by laser; thus, each small bottom cell remains connected to the four surrounding cells, and the disconnection can be quickly and easily done by hand. Freshly prepared SHJ bottom cells were kept in an N_2-filled box to prevent oxidation and contamination.

4.1.2. Perovskite top cell

The process can be divided into eight steps for the fabrication of the perovskite top cells. Figure 4.5 presents the process flow chart of the first three steps, from the surface cleaning of silicon bottom cells using O_2 plasma treatment to the spin-coating of HTL, followed by the perovskite/passivation layer stack. Each step is individually introduced in detail in the following.

Surface treatment of the substrate plays a crucial role in the subsequent preparation of high-quality functional layers. O_2 plasma treatment and ultraviolet/ozone (UV(O)) treatment are well-known methods for cleaning and modifying the surface properties of TCO coated on glass substrates for PSCs fabrication. When PSCs were utilized as the top cells in 2T tandem devices, surface treatment was directly applied to the silicon bottom cell. Therefore, this is the first step in the fabrication of the perovskite top cells. In this study, we used O_2 plasma treatment, which is a technique that exposes the substrate to a low-pressure plasma in an O_2 atmosphere. Plasma was generated by ionizing the O_2 in a vacuum chamber by applying an electrical field to the inner gas. It is a highly energetic state that consists of charged particles (ions and electrons) and radicals. Subsequently, the energetic ions accelerated towards the substrate surface owing to the presence of an electric field. Ions bombard the surface with an initial kinetic energy imparting to the atoms or molecules on the surface, which can lead to physical processes, such as sputtering (ejection of surface atoms) and surface roughening. In addition, the removal of dirt particles is accomplished by

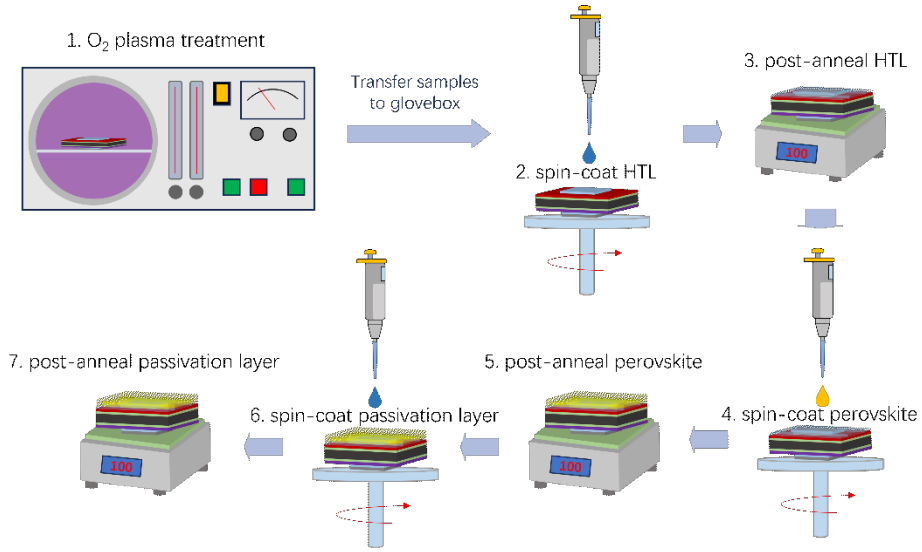

Figure 4.5.: *Process flow chart for oxygen (O_2) plasma treatment and spin-coating of hole transporting layer (HTL)/perovskite/passivation layer stack on a silicon bottom cell.*

chemical reactions that occur on the substrate surface with reactive species, such as oxygen radicals generated in the plasma due to the dissociation and ionization of oxygen molecules. These radicals can react with the top surface of the substrate (generally with the ITO layer on the silicon bottom cells), forming new chemical bonds or altering existing ones, finally leaving the surface. For instance, oxygen radicals can introduce oxygen-containing functional groups (e.g., hydroxyl and carbonyl groups) onto a surface, thereby improving the wettability and adhesion of the substrate surface.

After treatment with oxygen plasma (Diener Zepto, 50 W) for 12 min, SHJ bottom cells were immediately transferred to an N_2-filled glovebox. The recipes for the HTL/perovskite/ETL layer stack were optimized throughout the entire development process, and four typical recipes that were used in different stages are listed here. The first recipe comprised of 2PACz/$Cs_{0.05}(FA_{0.87}MA_{0.13})_{0.95}Pb(I_{0.87}Br_{0.13})_3/C_{60}$. 80 µL of 2PACz (0.3 mg/mL in dry ethanol) solution was spin-coated onto the ITO substrates at 3000 rpm for 30 s with a ramping rate of 1000 rpm, followed by thermally annealing at 100 °C for 10 min and afterwards cooled down to room temperature. Perovskite precursors were

prepared following the typical triple-cation process. PbI_2 and $PbBr_2$ were dissolved in a solution of DMF: DMSO = 4:1 in volume and stirred at 60 °C overnight, then the 1.5M nominal stock solutions were added to FAI and MABr with 9% PbX_2 excess, respectively (X= I or Br), and stirred for 10 min at 60 °C. $FAPbI_3$ and $MAPbBr_3$ were mixed in a volume ratio of 5:1 to obtain $FA_XMA_{1-X}Pb(I_XBr_{1-X})_3$ and stirred for 10 min at 60 °C. Finally, 5 vol% of 1.5M nominal CsI in DMSO was added to the obtained "triple cation" perovskite and stirred at 60 °C for 10 min. 100-110 µL of perovskite (1.63 eV) was spread on the glass/ITO/2PACz layer stacks and spin-coated at 5500 rpm for 35 s at a ramping rate of 800 rpm using a one-step spin-coating method. Ten seconds before the end of the program, 300 µL of anisole, as an anti-solvent, was drop-casted onto the spinning substrates, and the films were immediately annealed on a hot plate at 100 °C for 30 min. 25 nm C_{60} was thermally evaporated in a separate vacuum chamber (< 5×10^{-6} Pa) as the ETL.

The second recipe is Me-4PACz/$Cs_{0.05}(FA_{0.73}MA_{0.22})_{0.95}Pb(I_{0.78}Br_{0.22})_3$/PEAI/$C_{60}$ stack. 80 µl of Me-4PACz (0.3 mg/ml in dry ethanol) solution was spin-coated onto the substrates at 3000 rpm for 30 s with a ramping rate of 1000 rpm, followed by thermally annealing at 100 °C for 10 min and afterwards cooled down to room temperature. The perovskite precursors were prepared with a higher band gap of 1.68 eV for better performance by mixing PbI_2 (0.67 M), FAI (0.73 M), $PbBr_2$ (0.33 M), MAI (0.22 M), and CsI (0.05 M) in a solution of DMF: DMSO = 4:1 in volume, and 0.2 mg/ml poly(methylmethacrylate) (PMMA) was added, stirred at 60 °C for 1 h, and filtered through a 0.45 µm polytetrafluoroethylene (PTFE) filter. 100-110 ul of perovskite was spread on the top of the Me-4PACz layer by a two-consecutive step spinning program at 2000 rpm for 15 s (4s acceleration) and 6000 rpm for 60 s (5s acceleration). Thirty seconds before the end of the program, 300 µL of anisole as an anti-solvent was dropped onto the spinning substrates, and the films were immediately annealed on a hot plate at 100 °C for 20 min. 20 nm C_{60} was thermally evaporated in a vacuum chamber (< 5×10^{-6} Pa).

The third recipe is a mixed SAM/PTAA/$Cs_{0.05}(FA_{0.8}MA_{0.15})_{0.95}Pb(I_{0.75}Br_{0.25})_3$/$C_{60}$ stack. 80 µl of Me-4PACz: MeO-2PACz=1:1 (v:v) (0.3 mg/ml in dry ethanol) mixture solution was spin-coated onto the substrates at 3000 rpm for 15 s with a ramping rate of 600 rpm, followed by thermally annealing at 100 °C for 10 min and afterwards cooled down to room temperature. Subsequently, 90 µl of PTAA (0.5 mg/ml in toluene) solution was spin-coated onto the substrates at 4000 rpm for 25 s at a ramping rate of 800 rpm, followed by thermal annealing at 100 °C for 10 min and cooling to room temperature. The perovskite precursors were prepared with a band gap of 1.68 eV by mixing PbI_2 (0.7 M), FAI (0.8 M),

$PbBr_2$ (0.3 M), MABr (0.15 M), and CsI (0.05 M) in a solution of DMF: DMSO = 4:1 in volume, and 0.8 mg/ml 4F-PEAI was added, stirred at room temperature overnight, and filtered with a 0.45 μm PTFE filter. Perovskite (100–110 μL) was spread on top of the PTAA layer using a three-consecutive step spinning program at 200 rpm for 2 s (1s acceleration), 2000 rpm for 40 s (3s acceleration), and 5000 rpm for 10 s (4s acceleration). About 6-10 s before the end of the program, 250 μL of ethyl acetate as an anti-solvent was drop-casted onto the spinning substrates, and the films were immediately annealed on a hot plate at 100 °C for 20 min. 20 nm C_{60} was thermally evaporated in a vacuum chamber (< 5×10^{-6} Pa).

The fourth recipe was a MeO-2PACz/$Cs_{0.05}(FA_{0.77}MA_{0.23})_{0.95}Pb(I_{0.77}Br_{0.23})_3$/PI/$C_{60}$ stack. 80 μl of MeO-2PACz (1 mg/ml in dry ethanol) solution was spin-coated onto the substrates at 3000 rpm for 30 s with a ramping rate of 3000 rpm, followed by thermal annealing at 100 °C for 10 min and cooling to room temperature. Subsequently, perovskite precursors (1.68 eV) were prepared for better performance by mixing PbI_2 (0.77 M), FAI (0.77 M), $PbBr_2$ (0.23 M), MABr (0.23 M), and CsI (0.05 M) in a solution of DMF: DMSO = 4:1 volume ratio with 3% $MAPbCl_3$ additive, stirred at 50 °C for 2 h, and filtered through a 0.45 μm PTFE filter. Perovskite (100–110 μL) was spread on top of the MeO-2PACz layer by a two-consecutive step spinning program at 1000 rpm for 7 s with a ramping rate of 1000 rpm and 3000 rpm for 25 s with a ramping rate of 1000 rpm/s. Ten seconds before the end of the program, 300 μL of ethyl acetate (EA), an anti-solvent, was dropped onto the spinning substrates and the films were immediately annealed on a hot plate at 100 °C for 15 min. 15 nm C_{60} was thermally evaporated in a vacuum chamber (< 5×10^{-6} Pa).

The remaining process flow chart for the fabrication of the C_{60}/SnO_X/IZO/Ag/antireflective coating (ARC) stack is depicted in Fig. 4.6. After C_{60} evaporation, the samples were placed in a sealed, N_2-filled plastic bag and transferred from the glovebox to ALD (TFS200, Beneq) for 15 nm SnO_X buffer layer deposition. Tetrakis (dimethylamino)tin(IV) (TDMASn) and deionized water were sequentially pulsed into the reaction chamber as tin and oxygen precursors, respectively. Deionized water was maintained at room temperature, while liquid TDMASn was maintained at 55 °C during the ALD process. Highly pure N_2 gas with a flow rate of 500 sccm was used as the carrier gas and continuously purged the inner reaction chamber. Additionally, N_2 at a flow rate of 100 sccm from the same gas source was continuously purged into the outer chamber to create a stable pressure difference between the inner and outer chambers to compress the precursors. Each ALD cycle consisted of the following sequence: TDMASn pulse (1 s)/ N_2

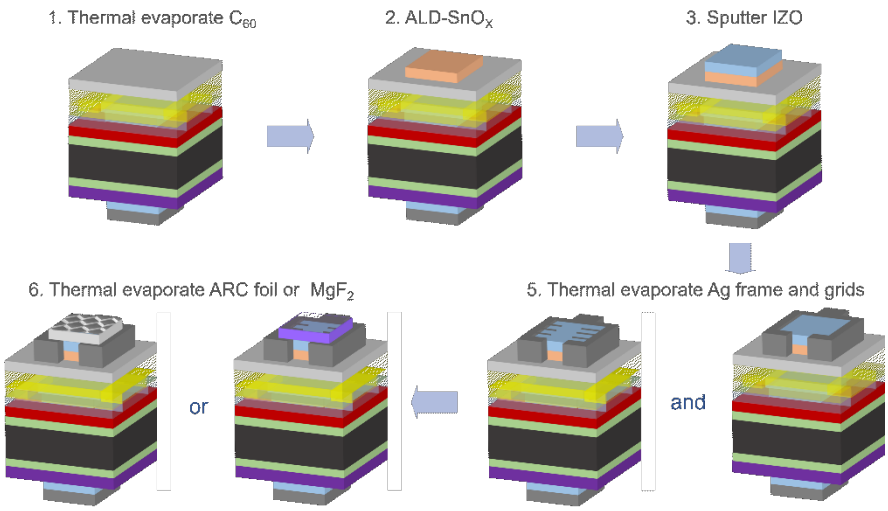

Figure 4.6.: *Process flow chart for fabrication of C_{60}/SnO_X/IZO/Ag/anti-reflection coating stack on semi-devices*

purge (30 s)/ deionized water (1 s)/ N_2 purge (30 s), with a saturated growth rate of 1.5 Å per cycle.

Subsequently, owing to the integration of various deposition and characterization systems named JOSEPH (more information about the JOSEPH system can be found in Chapter 6), the semi-devices were transferred from the ALD system to the sputtering system using a homemade robot under UHV conditions. Typically, a 40 nm IZO film was sputtered on top of the SnO_X via RF magnetron sputtering at a background pressure of less than 2×10^{-5} Pa and room temperature. The entire sputtering process took approximately 20 min at a deposition rate of 2.19 nm/min. The ceramic IZO target consisted of 90 wt. % In_2O_3 and 10 wt. % ZnO. The sputtering power used in this work was 50 W with a power density of 0.69 W/cm^2. The flow rate ratio of Ar/O_2 and working pressure were set to 14 sccm: 1 sccm and 0.5 Pa, respectively. In the initial stage, before the installation of the IZO target and the application of Ag grids, a thick ITO film (110 nm) was sputtered on top of the SnO_X using the same sputtering parameters as that of IZO to reduce the electrical losses caused by the lateral transport of electrons within the window stack, but at the cost of transparency

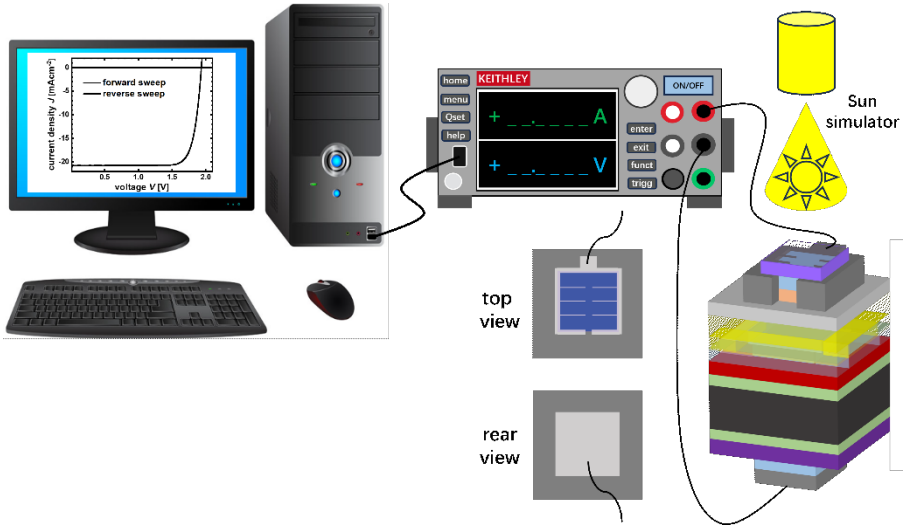

Figure 4.7.: *Schematic illustration of the current-voltage measurement of the tandem device.*

losses. Both SnO_X and IZO were deposited using the same deposition mask at the center of the device to align the patterned ITO and Ag in the silicon bottom cell.

The last two steps, the Ag electrode and ARC, were completed in a glovebox using thermal evaporation. The Ag electrode with a thickness of 500 nm consists of a U-shaped frame and several ultra-thin grids, aimed at collecting electrons within the IZO layer and reducing resistance losses, respectively. A commercial foil or a 100 nm MgF_2 film was used as the ARC, both of which improved the J_{SC} of the tandem devices by approximately 1 mA/cm^2. In summary, the entire fabrication process of a monolithic perovskite/silicon heterojunction tandem solar cell involves 15 layers and five deposition techniques, with devices transferred between gloveboxes and various deposition chambers.

Last but not least, the *JV* characteristics of tandem devices need to be obtained by current-voltage measurement, which is the most important, fundamental, and effective method to evaluate the performance of tandem solar cells. The essential components for this measurement include a working cell, a calibrated light source with an intensity equivalent to one sun named sun simulator, a Keithley electrometer, a computer to display *JV* curves, and many cables for connection, as shown in Fig. 4.7. In addition, the issue of obtaining

reliable results from *JV* measurements must be seriously addressed. Basically, six requirements must be met: (1) good electrical contact with both the anode and cathode, (2) precisely defined illuminated area, (3) a spectrum that matches the target spectrum of AM1.5G, (4) homogeneous light distribution, (5) temperature control to ensure that the device under test is at 25°C, and (6) the device under test has to be at steady state for every measurement point. To meet the first requirement, the tandem device must be tightly sandwiched between the highly conductive metallic plate and the contact pin. To meet the second requirement, a well-defined black illumination mask must be placed on the tandem device and perfectly aligned with the active area in the center. The opening area (1.21 cm^2) was designed to be a little bit larger than the active area (1 cm^2) of tandem solar cell confined by the inner edges of U-shape Ag frame because the length tolerance of 0.1 cm could effectively avoid a potential underestimation of the active area during *JV* measurement owing to the misalignment between mask and device. However, when the active area ≥ mask area, the reflection losses are easily ignored [54]. This issue can be properly solved by carefully modulating the mask area to be larger than the active area and smaller than the area confined by the outer edges of the U-shaped Ag frame. To meet the fourth requirement, first, the light source must be calibrated to ensure that the distribution of light intensity is homogeneous in a limited illumination zone; second, the position of the tandem solar cell must be fixed in the center of the illumination zone during *JV* measurement to prevent variations in illumination due to movements from sample to sample, introducing uncontrollable variables. If the active area is not determined properly during the *JV* measurement, not only the J_{SC} value is wrong, but also the *FF* and V_{OC} are affected to some extent. The reliability of the J_{SC} value extracted from the *JV* measurement can be verified by the integrated J_{SC} value obtained from the $Q_{e,PV}$ measurement.

4.2. Mask design for sub-cells fabrication

Following extensive experimentation resulting in numerous unsuccessful outcomes, it became evident that the deposition masks played a critical role in determining the functionality and efficiency of the tandem solar cell. Images of the tandem devices prepared using substandard deposition masks are shown in Fig. 4.8 (a). In this section, the design of all deposition masks used in the entire fabrication procedure for tandem devices is discussed in detail. Considering that the preparation processes of the subcells are relatively

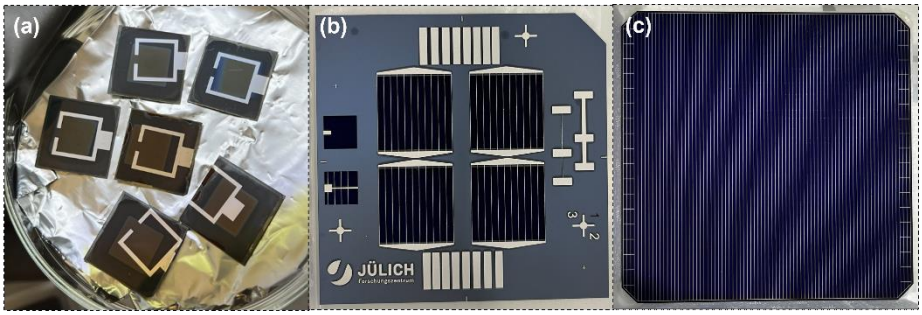

Figure 4.8.: *(a) Various types of mismatches occur during the tandem solar cell fabrication process owing to the substandard mask design. Images of silicon heterojunction solar cells (b) with a small size of* 78 × 78 *cm*^{2} *for a lab-scale performance optimization, and (c) with a large size of* 156.8 × 156.8 *cm*^{2} *for an industrial-scale solar cell module.*

independent and using different film deposition techniques, the mask design section was divided into two subsections: a silicon bottom cell and a perovskite top cell. With a clear concept of the composition of a 2T perovskite/silicon heterojunction tandem solar cell, including the materials, thickness, area, location, and preparation methods, we discuss the design of the masks used for each layer, the specific problems encountered in the process of using it, and the corresponding solutions.

4.2.1. Silicon heterojunction bottom cell

The silicon wafers used for fabricating bottom cells have three types of size: (1) 156.75 × 156.75 cm^2 wafer named as M2+, (2) 78 × 78 cm^2 wafer, and (3) 4-inch circular wafer with a diameter of 100 mm, all of which are much larger than the silicon bottom cells with a size of 2 cm × 2 cm. These silicon wafers are typically used as substrates for single-junction SHJ solar cells, which are either fabricated into small cells for lab-scale performance optimization or into the basic component of industrial-scale SHJ modules, as depicted in Fig. 4.8 (b, c). The bottom cell consists of seven layers, in which the a-Si:H (i), a-Si:H (n), and a-Si:H (p) layers were deposited via PECVD, fully covering the silicon wafers; thus, the corresponding deposition masks used in PECVD are not required to confine the active

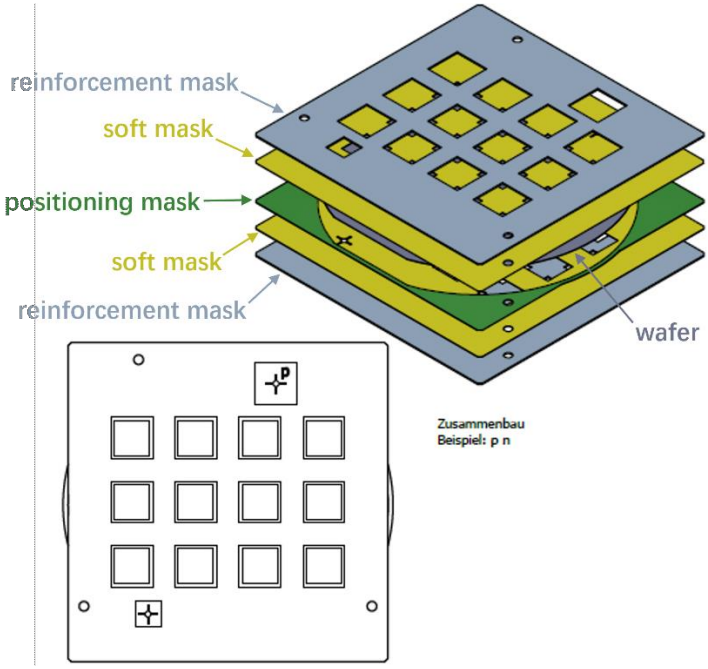

Figure 4.9. *Drafts of the cross-section and top view of the "sandwich" masks designed for 4-inch wafers.*

area. However, regarding the patterned ITO and Ag layers prepared by sputtering, four requirements are necessary: 1) a film area of 1.1 cm × 1.1 cm must be precisely defined by mask; 2) the film must be deposited exactly in the center; 3) the silicon wafers must not move around in the holder during the long process of loading, sputtering and unloading; and 4) a good alignment of all patterned films must be ensured. It seems that the first and second requirements could be easily accomplished by setting the opening area to 1.1 cm × 1.1 cm and to the center of the region corresponding to each individual tandem solar cell, respectively. However, the unexpected movement of silicon wafers in the deposition masks also has a significant impact. Since we have gained a lot of experience on how to prepare films for high-efficiency SHJ solar cells, a "sandwich" design, consisting of a soft mask, reinforcement mask, and positioning mask, was developed to perfectly address these four requirements. The areas of the ITO and Ag layers were precisely defined using a soft mask, with the assistance of a reinforcement mask. The cross section and top view of the

"sandwich" design are shown in Fig. 4.9, and a 4-inch silicon wafer was used as an example to explain the function of each component. During the sputtering process, the ultra-thin soft mask with a thickness of 0.1 mm effectively mitigated the shadow effect induced by thick mask, which resulted in an underestimated area. Considering the flexible and bendable nature of ultrathin metals, a hard reinforcement mask with a thickness of 0.5 mm was used to tightly press the soft mask onto the wafer. This design not only diminished the gap between the soft mask and the surface of the wafer, preventing underestimation or overestimation of the film area, but also made it impossible for the wafer to move around after mounting into the holder.

Because it is impossible to completely diminish the film misalignment, the tolerance of the side length was set to 0.1 cm to maintain the misalignment within tolerable limits, which is one-tenth of the side length of the aperture area of the tandem solar cell. Therefore, the opening area of the soft mask was accordingly set to 1.1 cm × 1.1 cm with its position located at the center, implying that the patterned ITO and Ag films were slightly larger than the aperture area of tandem device (1 cm^2). The drafts of the three soft masks used for depositing the ITO layers onto the a-Si:H (p) and a-Si:H (n) layers and depositing the Ag layer at the rear side are shown in Fig. 4.10(a-c), respectively. In the "sandwich" design, the soft mask must be used in conjunction with a reinforcement mask, thus the opening area of reinforcement mask was tailored to be slightly larger than that of soft one, with a side length of 1.3 cm, as shown in Fig. 4.10(d). Moreover, two markings were added in the top-right corner and bottom-left corner of each ultrathin mask to monitor the misalignment of the patterned layers, which consisted of a plus sign and a short name of the targeted film. Accordingly, two square openings are added to the reinforcement mask at the same positions as the markings. After depositing the ITO film on top of the a-Si:H (n) layer, the wafers were manually removed from the holder, flipped, re-mounted onto the holder, and aligned to the mask designed for the a-Si:H (p) layer. In the last step of bottom cell fabrication, a patterned Ag layer was deposited onto the a-Si:H (p) layer using a soft mask marked with "Ag" at the top-right corner for distinction. Note that, compared to the square silicon wafer, the 4-inch circular wafer was extremely difficult to align precisely to multi-layer square masks. Therefore, a customized positioning mask was created specifically to assist with the proper mounting of the 4-inch circular wafer, and the draft is shown in Fig. 4.10(e).

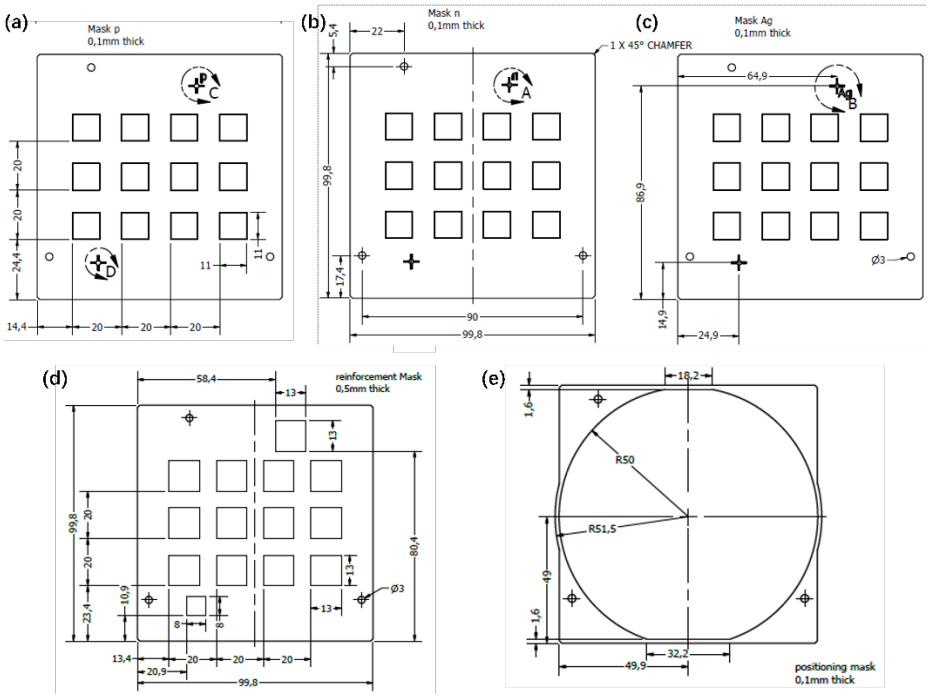

Figure 4.10.: *Drafts of soft masks used to deposit the ITO layer on top of a) p-type and b) n-type a-Si:H layers and to deposit c) the Ag layer on top of the ITO layer on the rear side. The active area defined by soft masks are the same of* 1.1 *cm* × 1.1 *cm. d) Reinforcement mask with an opening area of* 1.3 *cm* × 1.3 *cm. e) Positioning mask for a* 4*-inch circular silicon wafer. All these masks were specially designed for a* 4*-inch silicon wafer.*

4.2.2. Perovskite top cell

All films (amorphous silicon, ITO, and Ag) of the silicon bottom cells were deposited onto a large silicon wafer; for instance, in our lab, an M2+ wafer accommodates 36 bottom cells, whereas a 4-inch wafer only accommodates 12 bottom cells. In contrast, the preparation of the perovskite top cell was accomplished on a small, single bottom cell after the large wafer with deposited films was separated into individual bottom cells of size 2 cm × 2 cm by laser cutting for the subsequent procedure. The top cell consists of eight layers, half of which were prepared to fully cover the front surface of the bottom cells, including the spin-coated

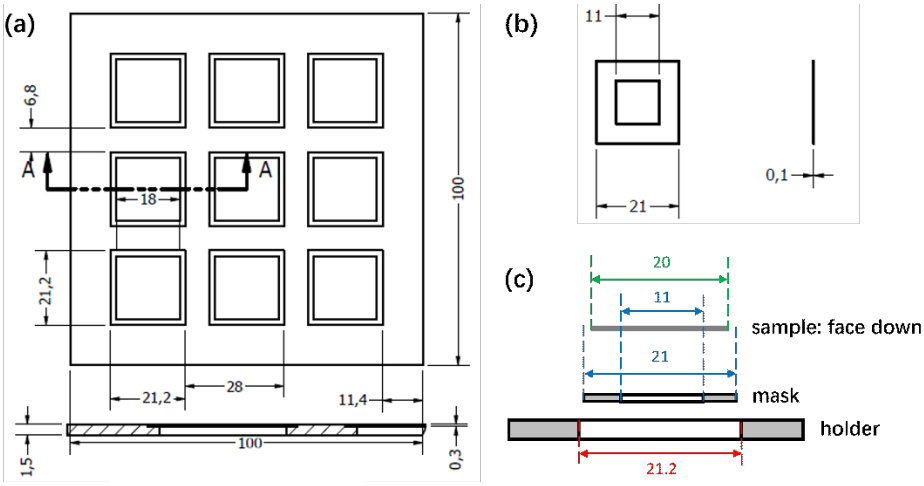

Figure 4.11.: *Drafts of a) holder and b) mask for the SnO_X/IZO stack deposit with an active area of* 1.21 cm^2. *c) Cross-section of sample loading.*

layer stack SAM/perovskite/passivation layer and evaporated C_{60}. Thus, no deposition masks were required before ALD-SnO_X.

For the remaining half of the layers, none of them were prepared in the full area, either presenting in a small square or in a specific shape. To obtain high-efficiency tandem solar cells, the following requirements must be satisfied: 1) the patterned films must be deposited in the center; 2) the film area must be precisely defined by the deposition masks; 3) the small wafers must not move around in the holder during every deposition process; and 4) all patterned films must align perfectly. Considering that three deposition techniques–ALD, sputtering, and thermal evaporation – were used to prepare the patterned layer stack SnO_X/IZO/Ag/ARC, the mask design must be individually customized to fit the different features of each technique.

4.2.2.1. Window stack

Initial version

The ALD and sputtering systems were integrated into a part of the JOSEPH system under conditions, in which samples were transferred with the assistance of a robot without venting. Therefore, the same mask was used for the SnO_X/IZO window stack, indicating that the features of both ALD and sputtering must be taken into consideration in this regard. Note that there should be no gap between the mask and the front surface of the silicon bottom cell, and the backside should be fully protected by the holder, because the gas precursor mixture fills the entire ALD chamber. Thus, the SnO_X film grew on all surfaces that were not properly protected.

The maximum size of the sample holder that is allowed to be placed in the JOSEPH deposition system is 10 cm × 10 cm; thus, the size of the deposition mask is 10 cm × 10 cm as well, which accommodated nine tandem solar cells arranged in a 3 × 3 array. The initial version consists of two parts: a holder and nine independent but identical patterns, as shown in Fig. 4.11(a, b). Nine masks were first placed into the holder, and then the samples were loaded face down, as shown in Fig. 4.11(c). The mask thickness was set to 0.1 mm due to the shadow effect induced by a thick mask during film deposition, while the holder was 0.3 mm thick to prevent bending. However, the initial version always had all sorts of unexpected problems and proved to be a failure in practice. First, the tandem device (20 mm × 20 mm) moved around in the holder because the slot (21.2 mm × 21.2 mm) was too large, resulting in severe misalignment of the patterned films. Second, either the random movement or the difficulty in unloading the sample led to scratches on the surface of the tandem solar cells by the unsmooth stainless-steel mask, ultimately resulting in shunting. Third, because the rear side of the device was not protected, the insulated SnO_X film also grew on the surface of the Ag electrode unintentionally, resulting in poor electrical contact for *JV* measurements. Fourth, the actual area of the SnO_X film was larger than the desired area of 1.12 cm^2 because the deposition mask had not been tightly pressed to the semi-device; thus, there was still room between the mask and the device surface, which allowed the penetration of gas precursors and reaction to the surface. Ultimately, the film area was larger than that defined by the mask. Fifth, because the loaded tandem solar cells were not fixed by the holder or mask, some cells jumped outside the slot owing to unintentional up and down movement during transportation, loading, and unloading. Finally, the

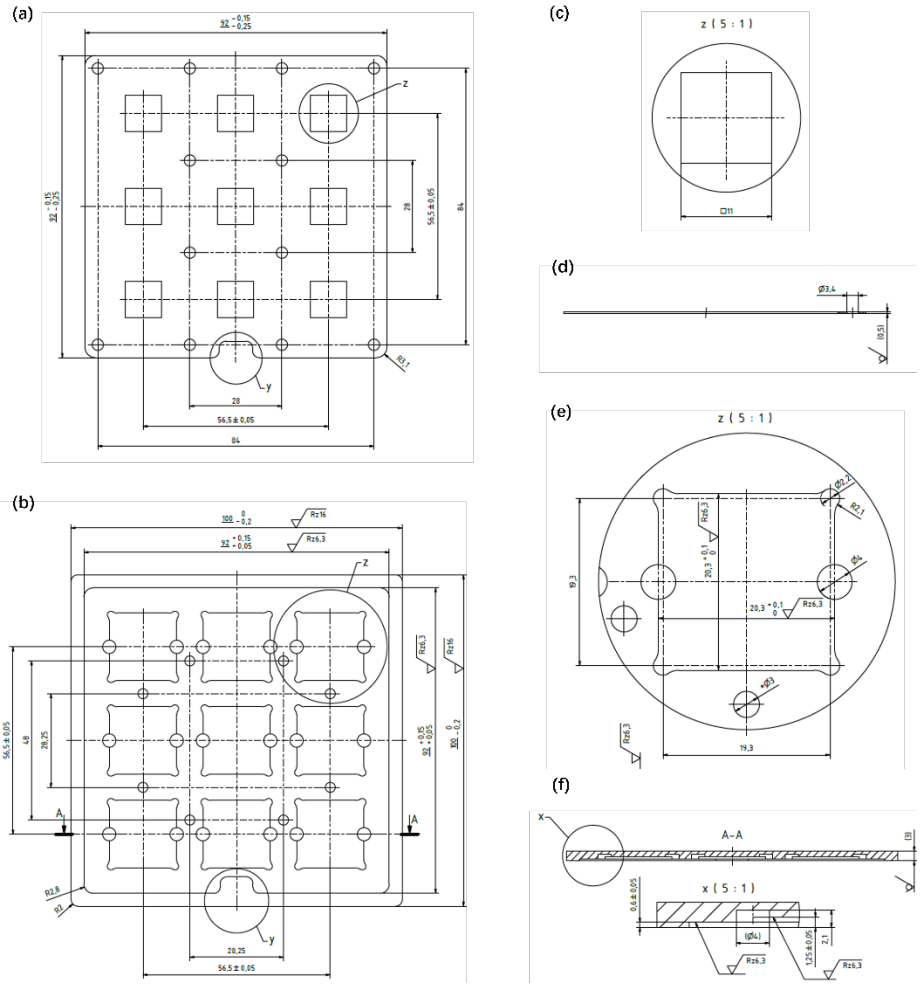

Figure 4.12.: *Drafts of a) the deposition masks used to deposit the SnOx/ITO window and of b) corresponding holder. Magnified drafts of the c) pattern and d) cross section of the deposition mask. Magnified drafts of the e) slot and f) cross section of the holder.*

independent ultrathin deposition masks are prone to bending owing to frequent grabbing with tweezers.

Mid-term version

With support from experienced designers and technicians, multiple modifications were adopted for the second version design and managed to address more than half of issues brought by the first version, which was also the mid-term version. First, the method of loading the sample was modified. Using the mid-term version, the samples were placed facing upwards in the holder. Second, the side length of the slot in the holder decreased from 21.2 mm to 20.3 ± 0.10 mm, ensuring that there was not much space left for the samples to move when they were transported from ALD to sputter. Third, the slot for the first version was 1.2 mm that was deep enough to better trap silicon wafers, but the vertical movement of the wafers in the slot was inevitable owing to unintended perturbations and the absence of means to immobilize the samples. Thus, the slot depth decreased to 0.65 ± 0.05 mm to reduce the vertical vibration of silicon wafers. Fourth, nine pieces of small independent masks with a size of 21 mm × 21 mm were merged into a big mask with a size of 92 mm × 92 mm, while the opening area corresponding to each pattern remained the same as the first version. Fifth, the mask thickness was increased from 0.1 mm to 0.5 mm to prevent bending owing to repeated use, with a negligible shadow effect. In addition, two circular spaces on both sides of the slot were left for tweezers to easily load/unload the samples. The drafts for both the top view and cross section of the deposition mask and holder, the pattern for window stack, and the top view of the single slot were shown in Fig. 4.12(a-f). Before the deposition of window stack, nine semi-devices were loaded in the holder with facing upwards, then the deposition mask was placed on the holder with four edges being fixed using high-temperature tapes, as depicted in Fig. 4.13(a). After the deposition of window stack, the surface color of the patterned layer changed to yellow, and then the tapes and mask were removed carefully. The images before and after removing mask were given in Fig. 4.13(b-d), in which the image of nine complete tandem solar cells loaded in the holder was given as well and discussed in the following section. These improvements in mask design not only enabled the operators to load/unload samples in an easier and quicker manner, but also enabled the sample surface to no longer suffer from scratching during the process of loading/unloading.

Theoretically speaking, a schematic of the film misalignment is shown in Fig. 4.13(e), wherein the first patterned blue film does not grow in the center because the sample moves to the lower left corner of the large slot (21.2 mm × 21.2 mm) during transfer, while the second yellow film with the same pattern grows in the center of the sample. Consequently,

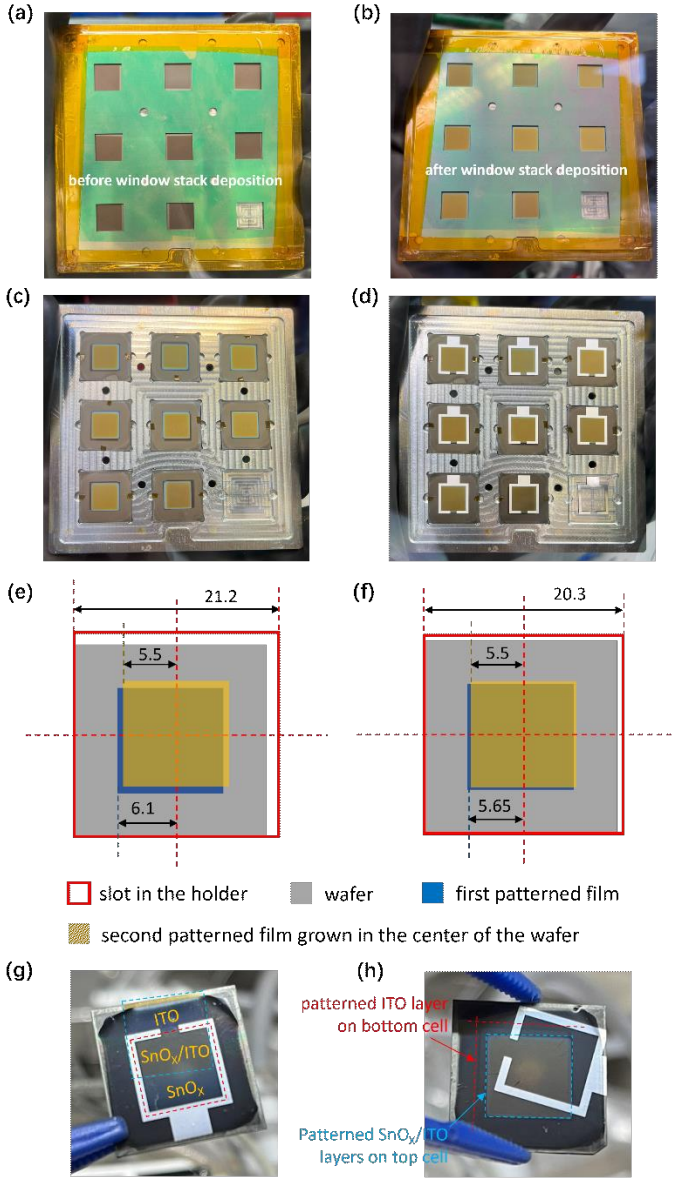

Figure 4.13.: *Schematics of the deposition mask with eight tandem devices loaded a) before and after the deposition of the window stack. Images of the semi-device after the deposition of c) the window stack and d) Ag frame. Top views of a wafer moved to the corner of e) the*

*large slot (*21.2 *mm* × 21.2 *mm) in the first-version masks and f) of the small slot (*20.3 *mm* × 20.3 *mm) in the second-version mask. Film mismatch of the g) SnO_X/ITO and h) SnO_X/ITO/Ag layer stacks occurred in practice using first-version masks during the deposition process in the JOSEPH and thermal evaporation systems.*

a mismatch of 0.6 mm may occur between the left edges of the two patterned films, which exceeds the half-tolerance of the 0.5 mm of the active area of the tandem device, implying that the overlapped area of all patterned films was less than 1 cm^2. In the worst-case scenario, if the second patterned yellow film were to grow at the upper right corner, the mismatch would reach the maximum value of 1.2 mm. In practice, it was found that the film misalignment due to arbitrary movement of the sample was more severe than predicted owing to a combined effect, where only half of the ITO film overlapped the SnOx film, and the active area was obscured by the U-shaped Ag frame, as shown in Fig. 4.12(g) and Fig. 4.12(h), respectively. This combined effect was primarily caused by the gap between the ultrathin devices and the mask, because tapes only fixed the mask but did not press the devices tightly to the holder. Therefore, several wafers moved out of the slot occasionally, making trouble to the determination of the actual active area of the tandem device for *JV* measurements. In Fig. 4.12(b), when the slot was slightly larger than the wafer, even if the wafer moved to any corner of the slot (20.3 mm × 20.3 mm), the theoretical mismatch between the patterned films was limited to 0.15 mm and 0.3 mm in the most extreme scenario, which is substantially smaller than the half tolerance of the active area. Therefore, the overlapped area of all the patterned layers must be larger than 1 cm^2, and the active area of the tandem device can be defined as 1 cm^2 using an illumination mask during the *JV* measurement.

Advanced version

The last advanced version, called cassette, was developed still with great support from experienced designers and technicians, which consisted of three parts–holder, mask, and lid–managed to solve the remaining issues, as shown in Fig. 4.14(a). Similar to the second version, the samples were still placed facing upwards in the holder, while the first difference was that a lid integrated with a deposition mask was placed on top of the holder with four

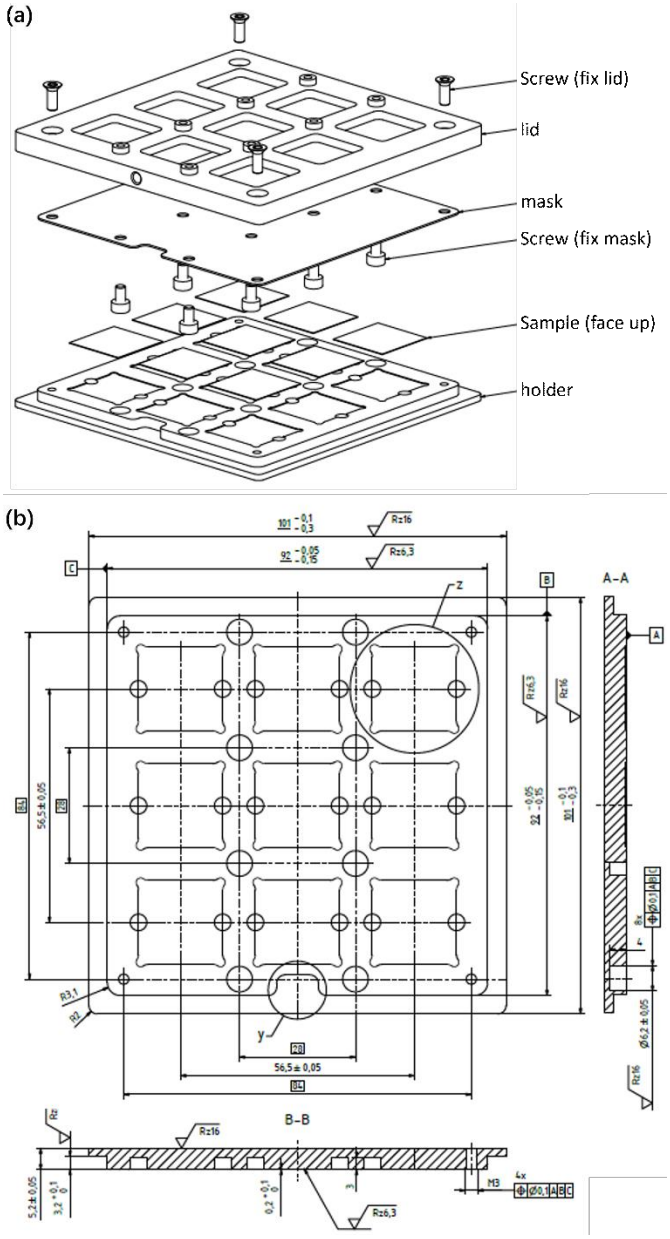

Figure 4.14.: *a) Schematic of the advanced cassette. b) Draft of the holder with two cross-section views inserted at bottom and right.*

corners fastened using screws to press the samples in place to ensure that they did not move out of the slot when the cassette was flipped over, because the deposition of the SnO_X/ITO/Ag layer stack requires the sample to face down. Another critical difference was a further reduction in the slot depth to extremely close to the wafer thickness, including both CZ and FZ wafers, and the aim was to mitigate the gap between sample and mask and holder as much as possible. For the mid-term version, the slot was still too deep for the silicon wafers because the semi-devices must be pressed firmly into the holder by a mask to prevent a series of undesirable outcomes. When the sample faced down, the gap between the mask and sample front surface and between the holder and sample back surface allowed the penetration of the gas mixture and the reaction of the precursors to the sample surface during the deposition process of ALD-SnO_X, owing to the combined effect that the weight of a small piece of wafer cannot make itself attached to the mask tightly; thus, the insulated SnO_X film was grown on the backside of the wafer, and the area of SnO_X on top of C_{60} was larger than 1.21 cm^2. Therefore, the slot depth was reduced from 0.65 ± 0.05 mm to 0.2 ± 0.10 mm to fit wafer thickness, and the draft of the cross section of the slot and holder was depicted in Fig. 4.14(b). By doing so, the semi-device was tightly sandwiched between the holder and mask. The advantages of this tight "sandwich" design was multiple: 1) the wafers could only slightly move in the slot but never move out; 2) the Ag electrode on the backside was protected against unintentional SnO_X growth; 3) the actual area of SnO_X film was the same as the area of the pattern on the deposition mask. In our case, the results revealed that the slot depth of 0.2 ± 0.10 mm was perfectly compatible with both CZ (0.1~0.2 mm) and FZ (0.2~0.3 mm) wafers with the patterned SnO_X area of 1.21 cm^2 and the absence of SnO_X on the backside. The design of two circular spaces on both sides of the slot were kept for easy sample loading/unloading. In addition, the mid-term version of deposition masks was perfectly compatible with the advanced cassette that could be directly used. These changes perfectly addressed the remaining problems in practice and simultaneously brought about multiple advantages. The lid enabled the operators to load/unload samples in a much easier and quicker manner compared to using tapes, and the immobilization of the devices enabled the sample surface to no longer suffer from scratching during the entire transportation process because the cassette must be placed face down only when entering either the JOSEPH system or the thermal evaporator. It is worth mentioning that there was no shunting any longer due to scratches on the active area of the tandem solar cell since we used the advanced cassette.

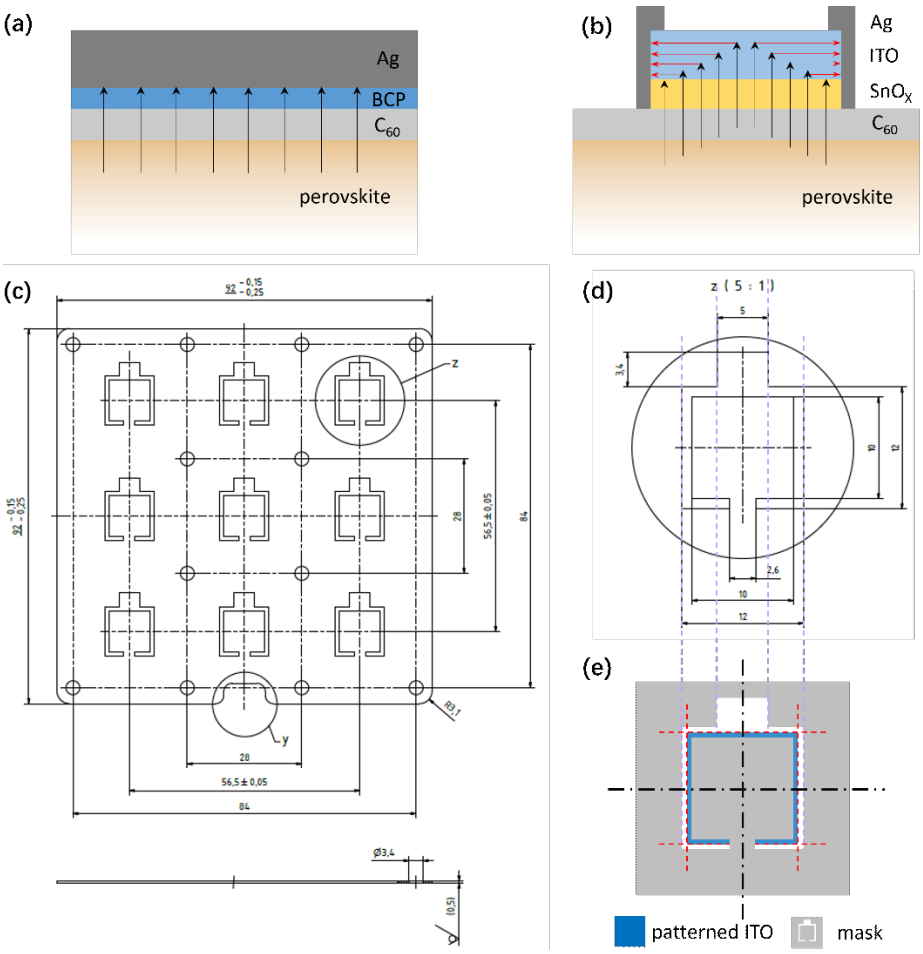

Figure 4.15.: *Movement of electrons within the relevant layers in (a) single-junction PSC and (b) perovskite top cell. (c) Draft of deposition mask designed for U-shaped Ag frame. Magnified view of (d) U-shaped pattern and (e) overlap of patterned ITO and U-shaped mask.*

In summary, owing to the successful design, small ultrathin tandem solar cells were easily, safely, and tightly loaded/unloaded in this sandwich-like cassette with the SnO_X/ITO

layer stack precisely deposited in the center not only with a well-defined film area but also with good alignment to other patterned films.

4.2.2.2. Metallization

Initial version

For the metallization of single-junction PSCs (p-i-n), owing to the extremely poor horizontal conductivity of the BCP layer deposited prior to the Ag, the opaque film electrode must fully cover the surface to allow the vertical transport of the electrons within the BCP before being collected, as shown in Fig. 4.15(a). However, for the tandem device scenario, a transparent electrode consisting of Ag and ITO was used because of the change in illumination direction. The movement of the electrons within the transparent film electrode of the perovskite top cell is shown in Fig. 4.15(b), where the electrons move vertically to the ITO layer, and subsequently, they move horizontally within the highly transparent and conductive ITO layer towards the surrounding Ag; finally, the electrons are collected by the U-shaped Ag frame standing on the four edges of the patterned ITO layer.

In Fig. 4.15(c) the deposition mask designed for the Ag electrode consists of nine identical U-shaped patterns with a mask thickness of 0.5 mm, which was produced together with the deposition mask for the window stack in Fig. 4.12(a) and to be used with the holder in the mid-term, as shown in Fig. 4.12(b), and it was also perfectly compatible with the advanced cassette in Fig.4.15. The width of the frame surrounding the patterned ITO layer was 1 mm, with half of the width in contact with the ITO surface and the other half in contact with the C_{60} surface, as shown in Fig. 4.15(d, e). Therefore, the active area of the tandem solar cell (1 cm^2) was confined by the inner edge of the “bold” U-shaped Ag frame. Note that the disruption of the bottom edge of this U-shape was necessary, which is essential for fixing the small piece of stainless steel in the center of the entire mask; otherwise, this small piece would fall off without any immobilization, and Ag would grow on the IZO layer with a full area instead of a well-defined U-shape frame. A top view of the Ag frame deposited on the tandem solar cell was previously shown in Fig. 4.13(d).

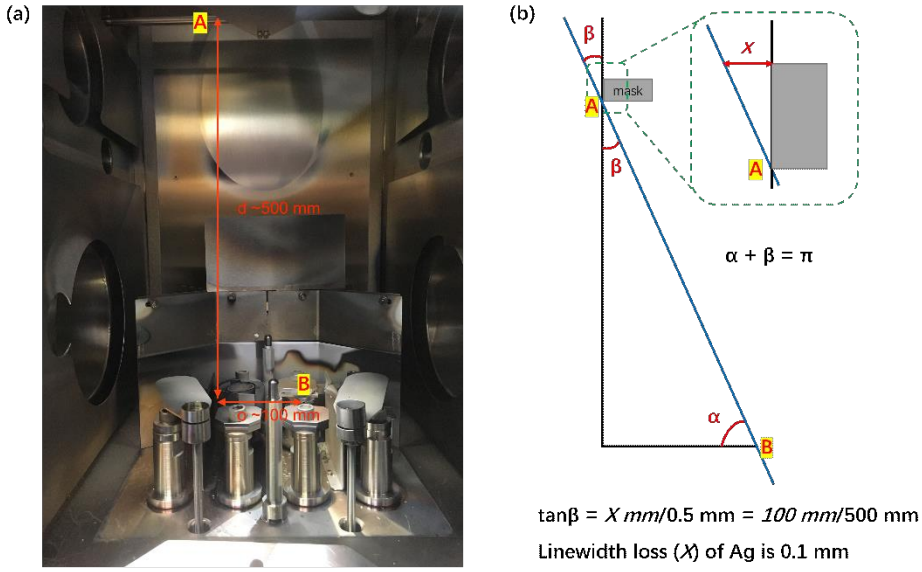

Figure 4.16.: *(a) Inner view of the thermal evaporation chamber. (b) Schematic for calculating the linewidth loss of Ag due to shading effect.*

Mid-term version

To reduce the parasitic absorption losses, the film thickness of the TCOs needs to be reduced to allow more incident light into the subcells, but the inevitable problem is the increase in R_{SH}, resulting in unwanted electrical losses. Therefore, ultrathin Ag fingers were added to the U-shaped Ag frame to improve the lateral collection of electrons in the TCOs. Referring to the patterns of the Ag electrode in previous publications, the design for fingers with a similar width of 100 µm was added to the previous version of the deposition mask. Unlike the screen-printed Ag fingers on SHJ solar cells, the perovskite top cell cannot withstand the high post-annealing temperature of 200 °C for liquid Ag paste, suggesting that the thermal evaporation was required to deposit Ag fingers as well.

For such a narrow pattern with a width down to 100 µm, the shadow effect originating from the thick mask becomes fatal during thermal evaporation. An example of the shadow effect is presented below: Fig. 4.16(a) shows the inner view of the chamber of the thermal

evaporator that we used, where A marks the edge of the cassette and B marks the location of the Ag source. Apparently, the Ag source was far from the cassette and was offset to the edge of the cassette. After simple calculations, we found that a linewidth loss of Ag is up to 0.1 mm that is equal to the width of Ag fingers when the deposition mask is as thick as 0.5 mm, as depicted in Fig. 4.16(b). The results of the calculations demonstrate that nearly 100% of the total width of the Ag fingers was not evaporated on samples at all.

Considering the issues induced by the shadow effect, the 0.5 mm-thick deposition mask was split into two masks: a 0.1 mm-thick, soft mask with only finger patterns and a 0.4 mm-thick reinforcement mask, as shown in Fig. 4.17(a, c). The number of fingers for each cell was set to six, and the vertical distance between the left and right fingers was the same as the disruption gap at the bottom edge of the frame. The horizontal distance between the three fingers was the same on both the left and right sides, as shown in Fig. 4.17(b). The benefits of this new design are threefold: (1) Ag fingers are deposited through the thin mask without worrying about the reduction in finger width owing to the shadow effect; (2) the total thickness of these two masks is still 0.5 mm, which is still compatible with the lid without making any modifications to the cassette; (3) the number and position of Ag fingers that were deposited on the tandem solar cell are allowed for arbitrary combinations by means of blocking the undesirable finger pattern with tape or other proper methods if you are not sure whether six fingers are the best scenario. The details of the experiments and the corresponding results are discussed in Chapter 7.

Advanced version

During *JV* measurements, the portion of the tandem solar cells that were obscured by the Ag fingers was still counted as the active area and played a crucial role in the determination of J_{SC}, although no current was generated in this area because of the obscuring of the incident light. Generally, the illumination area is larger than the area confined by the inner edges of the U-shaped frame and smaller than the area confined by its outer edges, as shown previously in Fig. 4.15(e). Therefore, the influence of light obscuring by Ag frame on the current density was excluded by calculating J_{SC} using an active area that was exactly the same as the area confined by the inner edges of the frame. However, for light obscuring owing to Ag grids, an effective method is to reduce the total area of the fingers, among which narrowing down the finger width from 100 to 30 μm is commonly used [23], as

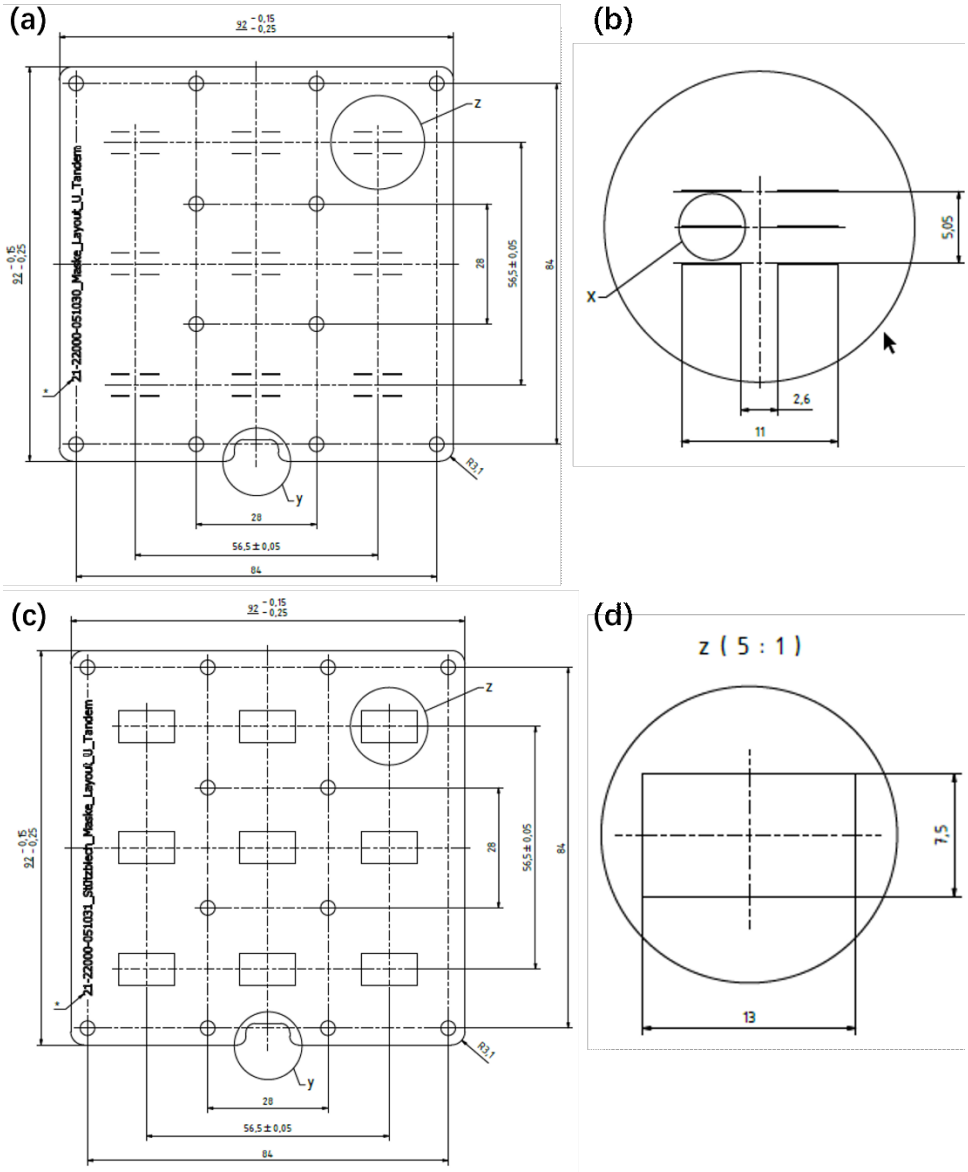

Figure 4.17.: *Draft of the mask designed for Ag fingers. (a) Soft mask with a thickness of 0.1 mm and (b) magnified view of the pattern. (c) Reinforcement mask with the thickness of 0.4 mm and (d) magnified view of the pattern.*

shown in Fig. 4.18(c). In the previous version, the Ag frame and fingers were evaporated separately due to the shadow effect. To further reduce the consumption of the Ag source, the thick frame mask and thin finger mask were integrated into a single mask, suggesting that both the frame and fingers could be deposited in just one evaporation. The thickness of the single mask was 0.1 mm to prevent the shadow effect and a relatively thick reinforcement mask with thickness of 0.4 mm is required to press the soft mask, keeping it flat and tightly attached to the sample surface during thermal evaporation. We have also considered replacing the reinforcement mask with magnets, but two practical uncertainties made us give up this idea: (i) the magnetic properties of the magnet are susceptible to being affected by high temperatures in the thermal evaporator and ALD system; (ii) the magnets are susceptible to collision with the robot in the JOSEPH system owing to a narrow operating space for the cassette. Figure 4.18(a-d) displays the drafts of the soft and reinforcement masks and the corresponding drafts of the magnified patterns. The drafts of the overlapped soft and reinforcement masks are shown in Fig. 4.18(e) to provide a clear concept of how advanced masks work.

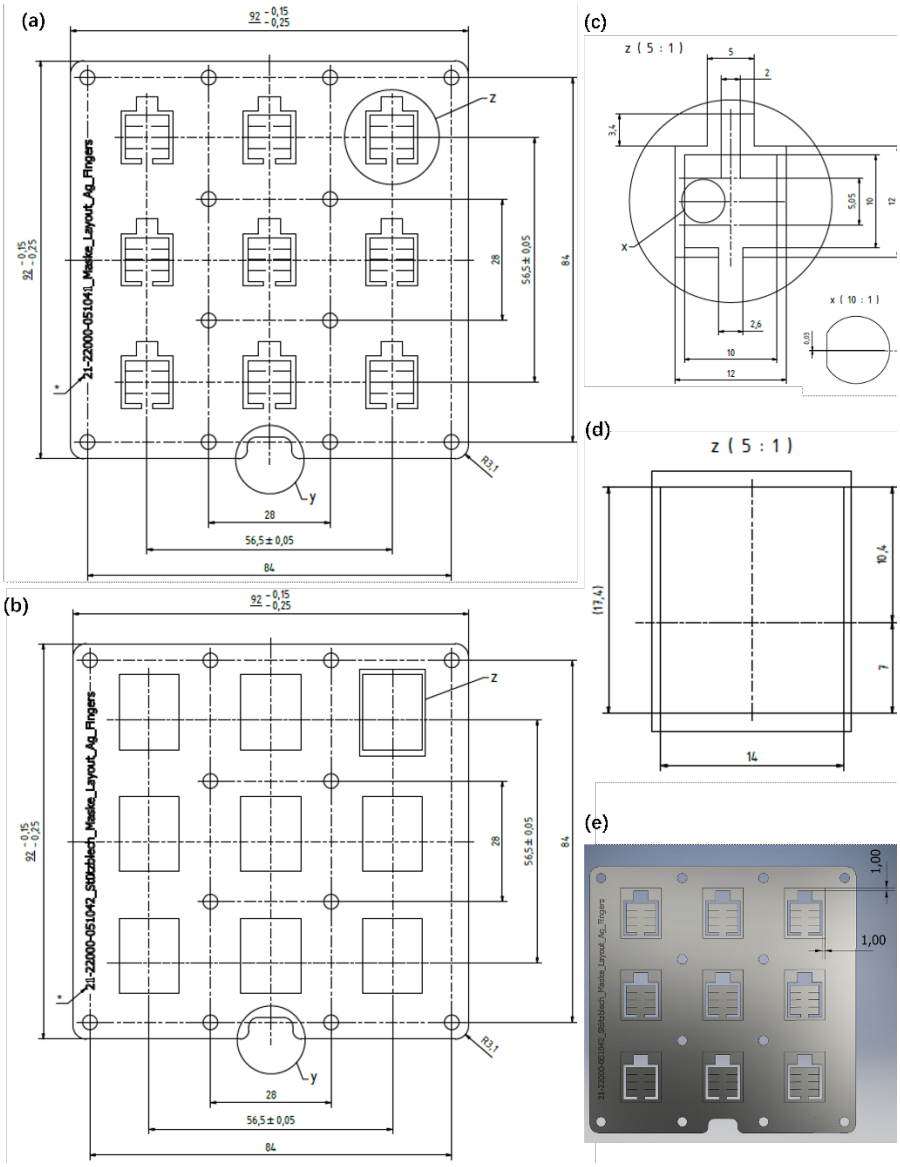

Figure 4.18.: *Draft of (a) the soft mask with a thickness of 0.1 mm and (b) the reinforcement mask with the thickness of* 0.4 *mm for the Ag electrode. Magnified view of the patterns for (c)soft and (d) reinforcement masks. Draft of overlapped soft and reinforcement masks for advanced Ag electrode design.*

5. Tin Oxide Development, Application, and Working Mechanism

In this chapter, we first introduce the ALD system and the reaction mechanism of SnO_X using TDMASn and deionized water. We then discuss the possible reasons for the formation of an inhomogeneous SnO_X film during the ALD procedure (Sec. 3.4.1) and the process for solving this issue by systematically adjusting the deposition parameters. Since SnO_X is prepared following the C_{60} as a buffer layer in perovskite/silicon tandem solar cells to mitigate the sputter damage induced by the top TCO electrode, we therefore replaced the C_{60}/BCP stack with a C_{60}/SnO_X stack in opaque single-junction PSCs and optimized the reaction temperature of ALD- SnO_X, precursor pulse length, and SnOx film thickness to achieve good electrical contact between C_{60} and SnO_X. Optimization of SnO_X into a robust buffer layer and investigation of its working mechanisms are essential for achieving high efficiencies in perovskite/silicon tandem solar cells. In the last subsection, specific characterization methods and numerical simulations were performed to understand the working mechanism of SnO_X in perovskite top cells.

5.1. Homogeneity modulation and device optimization

5.1.1. Reaction mechanism of ALD-SnO_X

The ALD system in our institute was produced by a Finland manufacturer called Beneq with a 40-year history of development, which established the world's first industrial production using ALD. The model of the ALD equipment used in this work is the TFS 200,

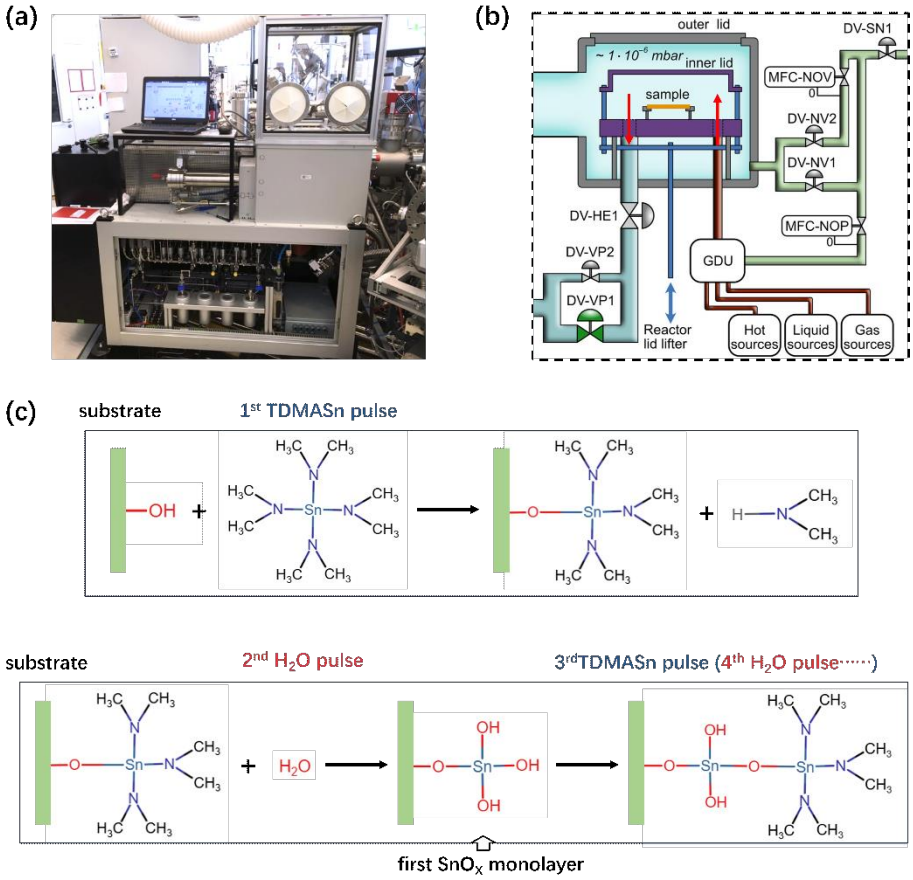

Figure 5.1.: *(a) Photograph and (b) side view of atomic layer deposition system (TFS*200*, Beneq). (c) Reaction mechanism of TDMASn and H_2O to form an SnO_X film in the ALD sequence.*

designed for academic and corporate Research & Development (R&D), as shown in Fig. 5.1(a). A side view of the ALD system (TFS 200, Beneq) is depicted in Fig. 5.1(b), in which the carrier gas (pure N_2) flows into the chambers through the green pipes at the top right and is controlled by the main valve of the DV-SN1. The carrier gas is separated into two streams: one stream continues purging the outer chamber with the flow rate controlled by the MFC-NOV valve. Another stream has two functions: purging the inner chamber or

acting as a carrier gas, which brings gaseous precursors into the inner chamber. The flow rate is controlled using an MFC-NOP valve. The inner chamber is the reaction chamber. The purpose of setting up two N_2 streams with diverse flow rates is to form pressure differentials between the outer and inner chambers, thus confining the reactive precursors within the inner chamber. The reactive precursors (hot sources, liquid, and gas sources) flow into the inner chamber through the thin brown pipes at the bottom right, and the exhaust flows out of the inner chamber through the thick blue pipe at the bottom left. An extremely thick blue pipe at the top left is used to transfer the sample under high-vacuum conditions.

Preheated TDMASn and room-temperature deionized water were used as counter-reactants, with TDMASn providing the tin source and water supplying oxygen, and the reaction occurred at an elevated temperature, as shown in Fig. 5.1(c). The corresponding reaction mechanism is

$$(OH)_x^* + Sn(DMA)_4 \rightarrow (O)_xSn(DMA)_{4-x}^* + xHDMA \quad (5.1)$$

$$(O)_xSn(DMA)_{4-x}^* + 2H_2O \rightarrow (OH)_x^* + SnO_2 + (4-x)HDMA \quad (5.2)$$

In these chemical equations, DMA represents the dimethylamino ligand and HDMA refers to the dimethylamine released into the gas phase. The * symbol denotes surface-bound species and *x* represents the number of DMA ligands released during the TDMASn pulse. Equation 5.1 highlights the critical role of the surface hydroxylation state in facilitating the initial adsorption of the precursor [55].

5.1.2. Possible reasons for film inhomogeneity

At the initial stage of film optimization, an extremely inhomogeneous SnO_X film was obtained on the rear surface of a 4-inch silicon wafer with a diameter of 10 cm^2, as shown in Fig. 5.2, where the circle (solid black) represents the circular wafer, and the black dots represent the points measured by an ellipsometer. Since the preparation of top TCO electrode requires sample facing down in JOSEPH system and the deposition of SnO_X needs to be compatible with the subsequent sputtering process during the entire fabrication flow

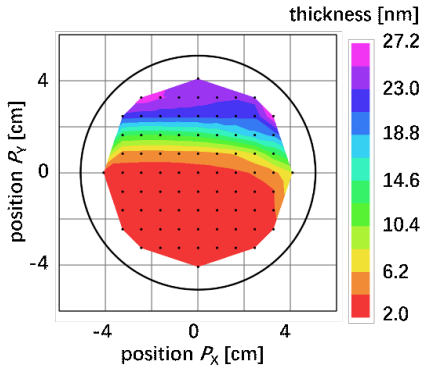

Figure 5.2.: *Thickness mapping of the SnO_X film deposited on the rear surface of a* 4*-inch polished Si wafer at the initial stage of optimization. The reaction temperature of* 80 ℃ *was applied as reported in most publications.*

of perovskite/silicon tandem solar cells (Sec. 4.2.2), the thickness mapping of SnO_X film was therefore carried out on the rear surface of the Si wafer. To solve this problem, we need to distinguish the factors that may lead to the formation of an inhomogeneous film from the large number of parameters involved in the ALD deposition process, understand their working mechanism, and troubleshoot these factors. Three factors are summarized here based on my investigations. First, the uneven temperature field inside the reaction chamber leads to film inhomogeneity because the preheating temperature of the reaction chamber, known as the reaction temperature, affects hydroxylation of the sample surface. Higher temperature, lower surface hydroxylation, fewer -OH groups, and therefore, a lower growth rate.

Second, an inadequate tin source can lead to an inadequate reaction progression, ultimately forming a uniform SnO_X film. The amount of gaseous tin precursor that enters the inner reaction chamber is co-determined by the vapor pressure in the source container and the duration of opening the valve of the container. The vapor pressure can be adjusted by the preheating temperature of the source container, and the duration of the valve opening is typically known as the pulse length of the precursors. Thus, the amount of tin source involved in the reaction can be effectively increased by either increasing the preheating temperature of the TDMASn container or prolonging the pulse length of TDMASn. In

addition, increasing the flow rate of carrier gas, N_2, could be helpful because it enables the delivery of more precursors into the reaction chamber at the same pulse length.

Third, an inadequate oxygen source leads to the formation of a uniform SnO_X film. The gaseous oxygen precursor is provided by deionized water, which is highly reactive with many metal sources, and the water container is generally maintained at room temperature (~ 22 °C) owing to a low vapor pressure, in which the water already exists in a gaseous state at the operational pressure typically used in ALD (~ 10^{-1} mbar). A sufficient pulse length of water is necessary for an adequate amount of gaseous source to enter the reaction chamber and subsequently ensure full coverage of the -OH group bonded to the surface of the substrate.

Note that if there are too many reactive precursors inside the reaction chamber that exceed the upper limit of the reaction requirements at the sample surface, the excess precursors floating in the reaction chamber are susceptible to reaction via PVD featuring line-of-sight deposition instead of the atomic-scale sequential self-limiting chemical reactions of ALD. Perhaps the issue of inhomogeneity can be addressed by adjusting only one to few parameters, but the process of "trouble shooting" requires considerable time for trial and error.

5.1.3. Adjustments to the deposition parameters

In our ALD system (TFS200, Beneq), a deposit recipe of SnO_X consists of more than 100 lines of code that are executed automatically after the start of the process. Among all of the adjustable parameters, I found that there are no more than ten parameters that are critical to film coverage uniformity, including the reaction temperature, pre-heating temperature of the Sn precursor, flow rates of the two carrier gas streams, purge and pulse lengths for each precursor in each ALD cycle, dwell time of the Sn precursor in the source container before pulsing, and orientation of the target sample surface. The inhomogeneity issue is not a hard-to-treat case but one that could be solved with a limited number of attempts.

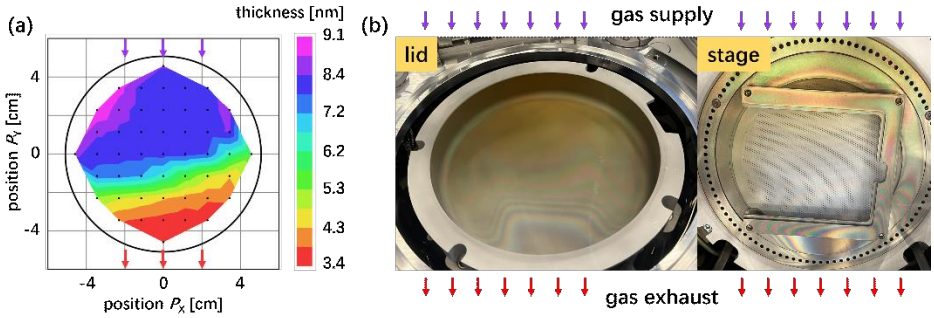

Figure 5.3.: *(a) Thickness mapping of the SnO_X film deposited on the rear surface of a* 4*-inch Si wafer at an elevated reaction temperature of* 100 *℃. Photographs of (b) inner surface of the lid and (c) stage of the reaction chamber in the ALD system (TFS* 200*, Beneq).*

Reaction temperature

First, the possibility of an uneven temperature field in the ALD reaction chamber can be quickly excluded because homogeneous ZnO films can be deposited using well tunned recipes. Considering the thermal instability of the perovskite films, the upper limit of the reaction temperature must be strictly controlled within 100 °C. However, when the reaction temperature increased from 80 °C that was used at the initial stage to 100 °C, the film remained inhomogeneous, as shown in Fig. 5.3(a). Therefore, a slight increment in the reaction temperature is incapable of improving film homogeneity.

Amount of reactive sources

To check whether there are contaminants in the reaction chamber hindering the formation of homogeneous SnO_X film, we stopped the vacuum and removed the inner lid of the reaction chamber. In Fig. 5.3 (b-c), close to the side of the gas exhaust, we observed a similar inhomogeneous pattern on both the inner surface of the inner lid and on the sample stage in the reaction chamber (see the positions of the inner lid and stage in Fig. 5.1(b), whereas no pattern was observed close to the side of the gas supply. This phenomenon demonstrates that the inhomogeneity of the SnO_X film is directly related to the direction of

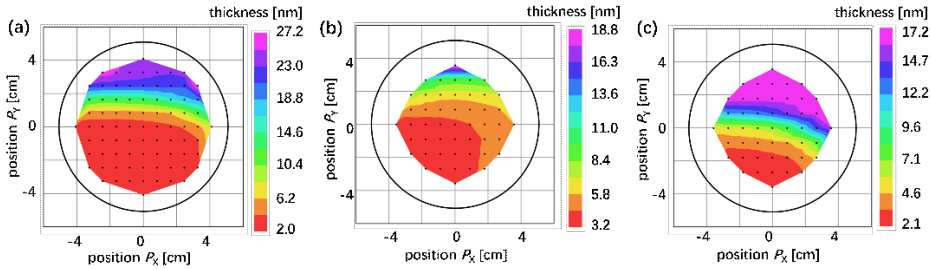

Figure 5.4.: *Thickness mapping of SnO_X films deposited on the rear surface* of *a* 4*-inch Si wafers with (a)* 90*, (b)* 200*, and (c)* 500 *sccm N_2 carrier gas during the ALD process.*

gas flow, and the reasons could be the present of inadequate reactive sources close to the side of the gas exhaust, leading to inadequate reaction progression, as discussed in subsection 5.1.2. The total amount of gaseous precursors that enter the reaction chamber is not only determined by the transportation capacity of the carrier gas but also determined by the absolute amount of the precursors leaving the source containers in a finite period of time. Therefore, a series of attempts were made to increase both the flow rate of the N_2 carrier gas and the absolute amount of tin and oxygen precursors leaving the source containers.

Flow rate of carrier gas

The impact of the flow rate of N_2 carrier gas that is controlled by the MFC-NOP valve on the thickness distribution of the SnO_X film was investigated. The thickness mapping results of the SnO_X films that were deposited using an increasing N_2 flow rate of 90, 200, and 500 sccm are shown in Fig. 5.4(a-c), and the other deposition parameters were kept constant. We observed that the thinnest part that is close to the side of the gas exhaust was only covered by 2~3 nm SnO_X film, whereas the film thickness of the thickest part that is close to the side of the gas supply decreased from approximately 27 to 17 nm. It is worth noting that the area of the red region (the thinnest part) decreases with the increasing N_2 flow rate, because the more the carrier gas, the more precursors travel from the gas-supply side to the gas-exhaust side, and the more homogeneous the film will be. These results illustrate that the inhomogeneity of the SnO_X film thickness in the 4-inch scale was partly improved by increasing the flow rate of N_2 carrier gas.

Absolute amount of precursors

As the N_2 flow rate increased from 90 to 500 sccm, a larger amount of gaseous precursors entered the reaction chamber; therefore, more precursors were carried to the exhaust side, which was furthest from the gas supply. This is the reason for the pronounced reduction in the area of the red part in Fig. 5.4(a-c); consequently, the film homogeneity was improved. However, the inhomogeneity issue was not completely solved by purely increasing the flow rate of N_2 carrier gas, suggesting the present of inadequate reactant precursors at the exhaust side during the ALD process. Therefore, the attempts of prolonging the pulse lengths and pre-heating temperature of precursors were made to boost the absolute amount of the Sn and oxygen precursors that leave the source containers.

Pulse length of water and TDMASn

First, the amount of oxygen precursor was increased by prolonging the pulse length of the water from 250 ms to 1 s. The thickness mapping results of the pristine and optimized SnO_X layers are shown in Fig. 5.5(a) and Fig. 5.5(b), respectively. For the pristine sample (250 ms H_2O), the SnO_X thickness varied from 2 to 20 nm on a 4-inch wafer and the thickest part was close to the side of the gas supply. In the optimized case (1 s H_2O), the upper limit of the thickness was reduced from approximately 20 nm to below 17 nm, but the SnO_X film remained inhomogeneous, suggesting that the thickness distribution was slightly improved by increasing the pulse length of water. Subsequently, the amount of Sn precursor was increased by extending the pulse length of TDMASn from 650 ms to 1 s. In Fig. 5.5(c), the area of the red region (the thinnest part) decreased, and the area of the purple region (the thickest part) increased compared to the thickness distribution in Fig. 5.5(b), indicating that we were heading in the right direction, and the upper limit of the thickness was further reduced to below 12 nm. Interestingly, the SnO_X film that was unintentionally deposited on the nontarget front surface (facing upwards in the reaction chamber) of the Si wafer was much more homogeneous than that deposited on the target rear surface (facing down in the reaction chamber), as shown in Fig. 5.5(d). The discrepancy between the homogeneity of SnO_X films on the front and rear surfaces could be attributed to a combination of inadequate source supply and boundary effects owing to the raised edges of the sample holder (Fig. 5.3(b)). Although increasing the pulse length of oxygen and Sn precursors improved non-uniform film thickness distribution to a certain level, more precursors were still required for

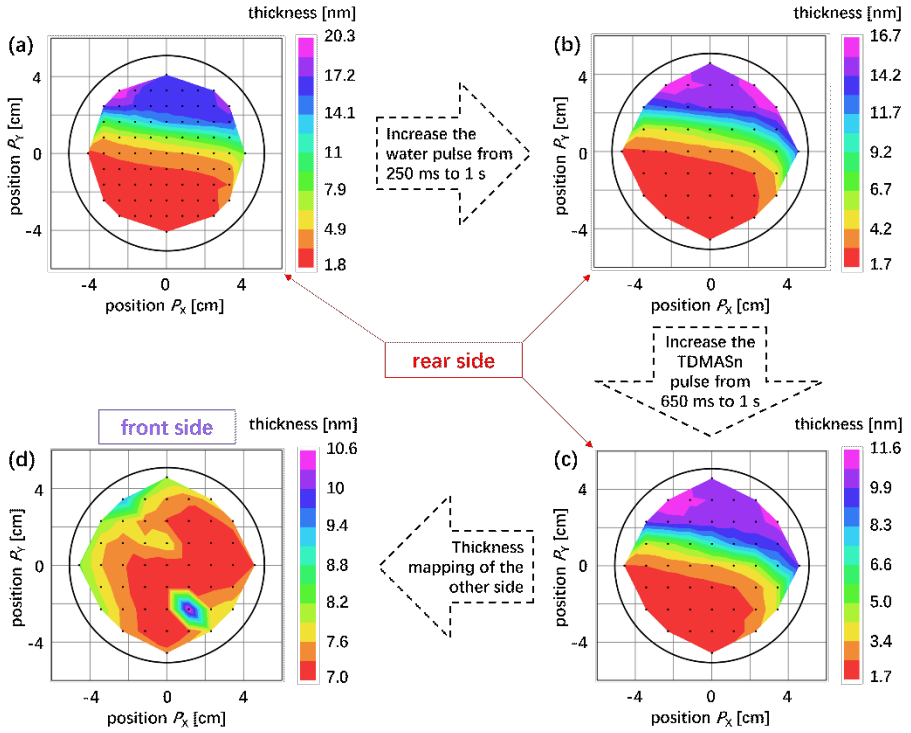

Figure 5.5.: *Thickness mapping of the SnO_X films deposited on (a-c) the rear and (d) front surface of a 4-inch Si wafer with increasing precursor pulse length.*

depositing an absolutely homogeneous SnO_X film, which should not be realized through a pure extension of pulse length.

Pre-heating temperature of TDMASn

When the flow rate of the carrier gas is constant, two methods are generally applied to flexibly tune the absolute amount of the precursors that leaves source container: the pulse length of the precursor and the pre-heating temperature of the source container. For the ALD system (TFS200, Beneq) that we used, two pipes are connected to the container for the TDMASn hot source, and the flow in and flow out of gas is controlled by the DV-BH1

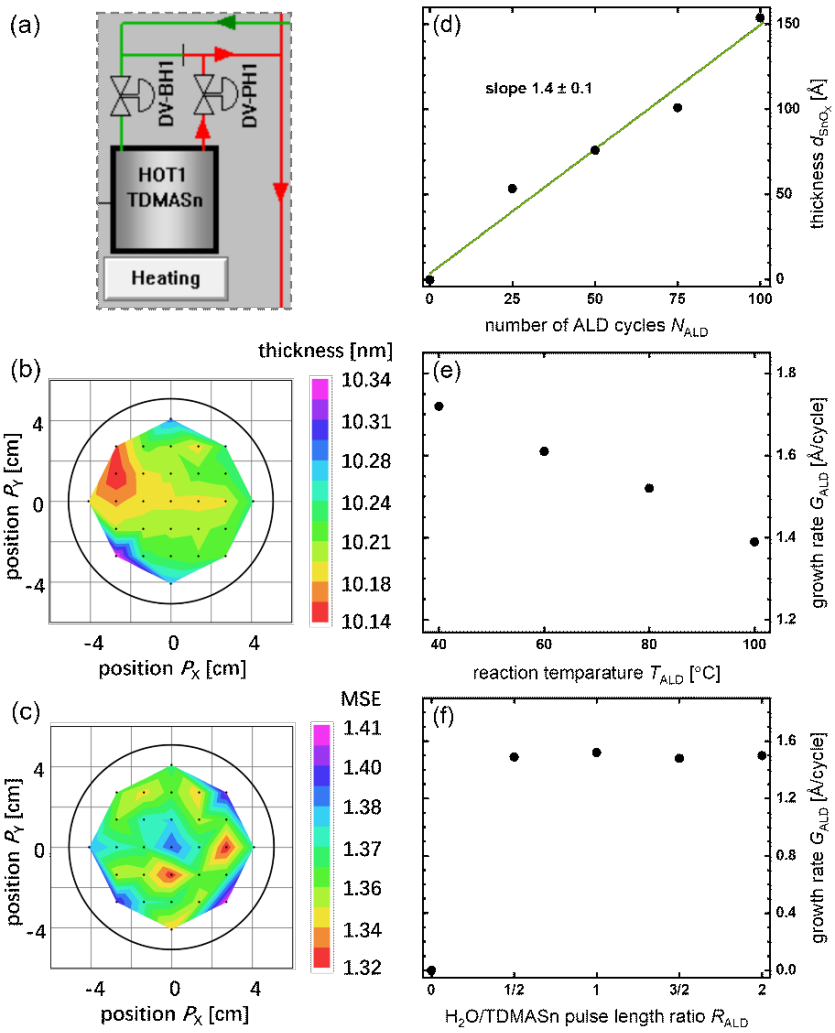

Figure 5.6.: *(a) Sketch of the container for hot source TDMASn from the Beneq software process screen. (b) Thickness mapping of SnO_X films on 4-inch Si wafers with elevated preheating temperature for the Sn precursor and (c) corresponding mean square error (MSE) values. Deposition rate as a function of (d) number of ALD cycles, (e) reaction temperature, and (f) precursor pulse length ratio.*

inlet and DV-PH1 outlet valve, respectively, as depicted in Fig. 5.6(a), where the inlet valve controls the entry of N_2 carrier gas and the outlet valve controls the leaving of the TDMASn and N_2 carrier gas mixture. Through controlling the opening and closing of two valves, three factors are tunable during the pulsing of Sn precursor: (1) the DV-BH1 inlet valve is opened first and closed after a short wait, and the time interval determines the amount of N_2 carrier gas entering the source container; (2) subsequently, two valves are closed and before the opening of DV-PH1 outlet valve, the carrier gas is trapped in the container and mixes with the gaseous Sn precursor, thus, the time interval between the closing of inlet valve and opening of outlet valve determines the duration of carrier gas in source container; (3) finally, the DV-PH1 outlet valve is opened first and closed after a short wait, and this time interval is so-called pulse length that determines the absolute amount of Sn precursor leaving the source container. Apart from the extension of the pulse length of Sn precursor, I also tried to extend the time interval between the opening and closing of the DV-BH1 inlet valve in order to allow a larger amount of N_2 enter the source container and hopefully carry out more Sn precursor, but the corresponding results showed that this did not work. Based on the principle of phase equilibrium, the transition between the liquid and gaseous TDMASn in the source container achieves dynamic equilibrium at a given temperature, suggesting that the vapor pressure has attained saturation. The saturated vapor pressure of TDMASn increases as the pre-heating temperature increases, implying that a larger volume of liquid-phase source evaporates into gas-phase source, and thus leave the container when the outlet valve is opened. Therefore, the preheating temperature of TDMASn was elevated from 45 to 55 °C to evaluate its effectiveness in improving film homogeneity. The mapping results of the SnO_X film that was deposited using a hotter TDMASn source and the corresponding mean square error (MSE) are shown in Fig. 5.6(a) and Fig. 5.6(b), respectively. The thickness variation in a 4-inch scale is well controlled within 0.5 nm with low MSE of below 10, suggesting that an extremely homogeneous SnO_X is finally obtained. The results demonstrate that the pre-heating temperature of TDMASn is the most critical deposition parameter to deal with the inhomogeneity issue of SnO_X film in our case.

Now, we can optimize the SnO_X in single-junction perovskite solar cells to realize a good contact to the C_{60} layer and obtain optimum device efficiency. The reasons why we decided to first perform the SnO_X optimization in the single-junction PSCs instead of the tandem devices are illustrated in Section 6.2. Note that the SnO_X film thickness must be kept constant when it is not a variable during the fabrication of solar cells. Figure 5.6(d-f) shows the deposition rate (G_{ALD}) of SnO_X as a function of the number of ALD cycles,

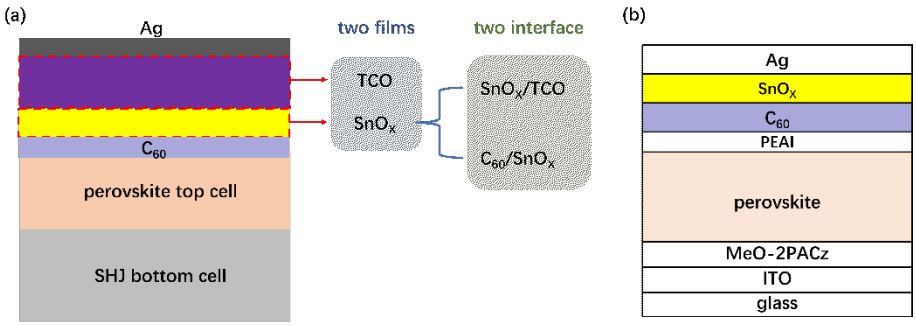

Figure 5.7.: *(a) Simplified configuration of the perovskite/silicon tandem solar cells. (b) Configuration of "structure B".*

reaction temperature, and precursor pulse length ratio. Since the film thickness was determined by the deposition rate and the number of ALD cycles, the G_{ALD} is therefore required to know before systematic optimization begins.

5.1.4. Optimization of SnO_X in perovskite solar cells

Comparing the commonly used configuration of a single-junction PSC (p-i-n) (Fig. 4.1(a)) with that of a perovskite top cell in a perovskite/silicon tandem solar cell (Fig. 4.1(b)), the primary differences can be concluded as two films (SnO_X and ITO) and two interfaces (C_{60}/SnO_X and SnO_X/ITO) that are formed subsequently. In Fig. 5.7(a), those films and interfaces that do not exist in the single-junction PSC were highlighted in the simplified configuration of tandem device, in which a robust SnO_X buffer layer is required to mitigate sputtering damage due to the application of sputtered ITO electrode. In the fabrication of single-junction PSC, a BCP layer is deposited after C_{60} deposition that effectively lowers the work function of the metal electrode to achieve good electrical contact at the C_{60}/Ag interface. However, because of the poor electrical conductivity of thick BCP film, the researchers primarily use SnO_X instead of BCP after C_{60} deposition when fabricating the perovskite/silicon tandem solar cell.

With the insertion of SnO_X, the C_{60}/SnO_X and SnO_X/ITO interfaces were successively formed in the top cell. To obtain high-efficiency perovskite/silicon tandem solar cell, we

need to solve the potential issues related to these emerging films and interfaces. The approach I used was to decouple the two interfaces through separating the SnO_X film from the ITO films so that the SnO_X film and the adjacent C_{60}/SnO_X interface could be optimized independently first. Once we were sure that the newly inserted SnO_X film and adjacent interface are unlikely to be the bottleneck in the preparation of high-efficiency tandem devices, we were able to focus on the optimization of the ITO film and adjacent SnO_X/ITO interface. Therefore, the entire optimization process for perovskite top cells was divided into several steps, each employing a specific device configuration to target a set of problems arising from the insertion of a specific film (Sec. 7.2.1). This approach is not only simpler and more intuitive than a direct investigation in tandem devices because of its complicated configuration but also guides us in optimizing the performance of tandem solar cells. From the perspective of the device configuration, SnO_X takes the place of BCP, thus, the optimization of the SnO_X film and adjacent C_{60}/SnO_X interface could be carried out in single-junction PSCs with a specific configuration of glass/ITO/MeO-2PACz/perovskite/PEAI/C_{60}/SnO_X/Ag, which is named as "structure B" (Sec. 7.2.1), as shown in Fig. 5.7(b).

Effect of reaction temperature

First, I investigated the impact of increasing reaction temperature from 60 ℃ to 100 ℃ in steps of 20 ℃, while the SnO_X layer thickness and pulse length of the tin and oxygen precursors were kept constant. The upper limit was set to 100 ℃ because it is the annealing temperature for the perovskite film. If the reaction temperature is elevated to be higher than the annealing temperature, the perovskite film is susceptible to thermal degradation owing to the long-term dwell in the reaction chamber. Figure 5.8 shows the solar cell parameters, that is, η, J_{SC}, *FF*, and V_{OC}, as a function of the ALD reaction temperature (T_{ALD}), from which 80 ℃ outperforms 60 ℃ and 100 ℃ due to higher V_{OC} and *FF*. Since the concentration of the impurities (e.g., carbon and nitrogen) within the SnO_X film decreases as the reaction temperature increases [56,57], V_{OC} gradually increases from 1.14 V to nearly 1.17 V at elevated temperature due to the reduction of defects. The solar cells prepared at 80 ℃ show highest *FF*, which is perhaps determined by the detailed balance between two factors [57]: (1) the resistivity of SnO_X film decreases due to the increases in oxygen vacancy density at elevated reaction temperature; (2) the impurities within the SnO_X film affect the bandgap because of the dehydroxylation at higher temperatures, which

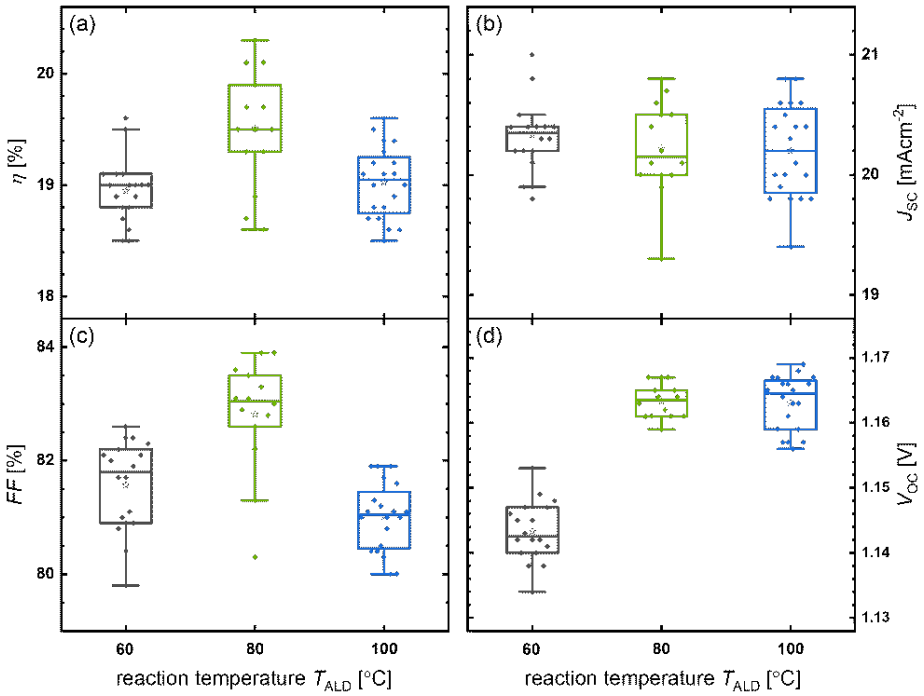

Figure 5.8.: *Solar cell parameters* η, J_{SC}, *FF*, and V_{OC} *of opaque perovskite solar cells ("structure B") as a function of deposition temperature* T_{ALD} *during the ALD process.*

indicate a decrease in the density of -OH groups located on the substrate surface. In Fig. 5.8(b), the J_{SC} remained almost constant when the reaction temperature is varied between 60-100 °C, which is in good agreement with the results published by the research group form HZB in 2019 regarding the almost constant integrated current density of the perovskite top cell as a function of reaction temperature [58]. Although the extinction coefficient in the UV spectrum and the refractive index across the entire spectrum of bare SnO_X film increase as temperature increases, the overall integrated current density of the perovskite top cell remains almost constant due to an increased absorption loss at wavelengths below 370 nm and an enhanced optical response at wavelengths above 370 nm.

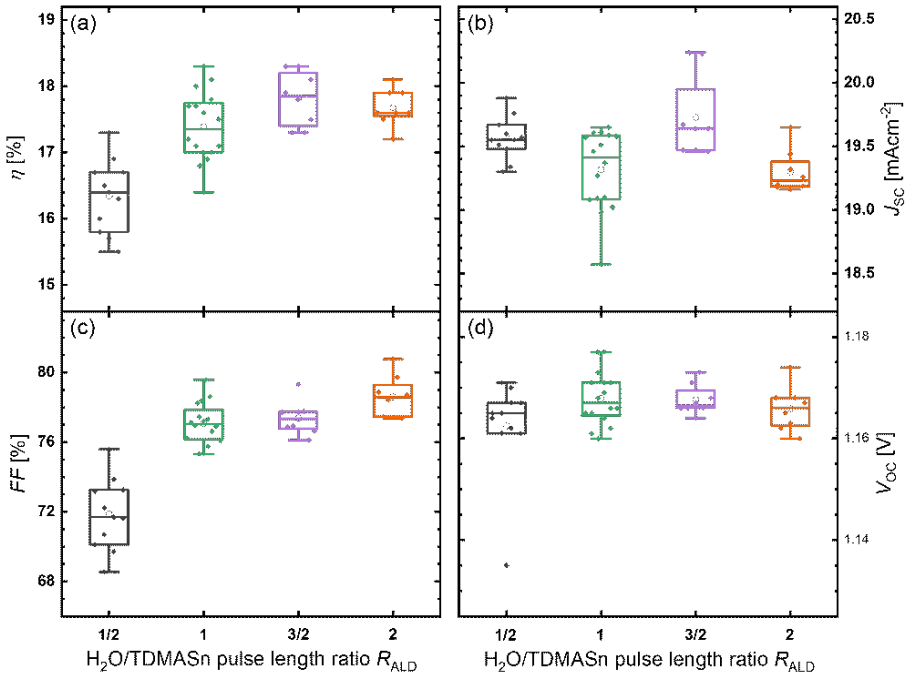

Figure 5.9.: *Solar cell parameters* η, J_{SC}, *FF*, and V_{OC} *of opaque perovskite solar cells ("structure B") as a function of the pulse length ratio of* H_2O*/TDMASn* R_{ALD} *during ALD process.*

Effect of the pulse length ratio of precursors

Second, the pulse length ratio of H_2O/TDMASn (R_{ALD}) varies from 1/2 to 2 by prolonging the water pulse length from 0.5 to 2 s with a step size of 0.5 s while keeping the TDMASn pulse length constant. The ALD sequence was 1 s TDMASn/30 s purge/0.5~2 s H_2O/30 s purge. In order to ensure the complete removal of the remaining gaseous precursors from the reaction chamber after each pulse, I set a relatively long purge time of 30 s. Otherwise, the remaining reactive sources that are not absorbed to the active sites on the sample surface will float in the reaction chamber, and these floating gaseous mixtures will be reacted in "air" via PVD rather than via ALD on the sample surface. In Fig. 5.9(a), with the R_{ALD} increases from 1/2 to 2, the average value of device efficiency increases and reaches a

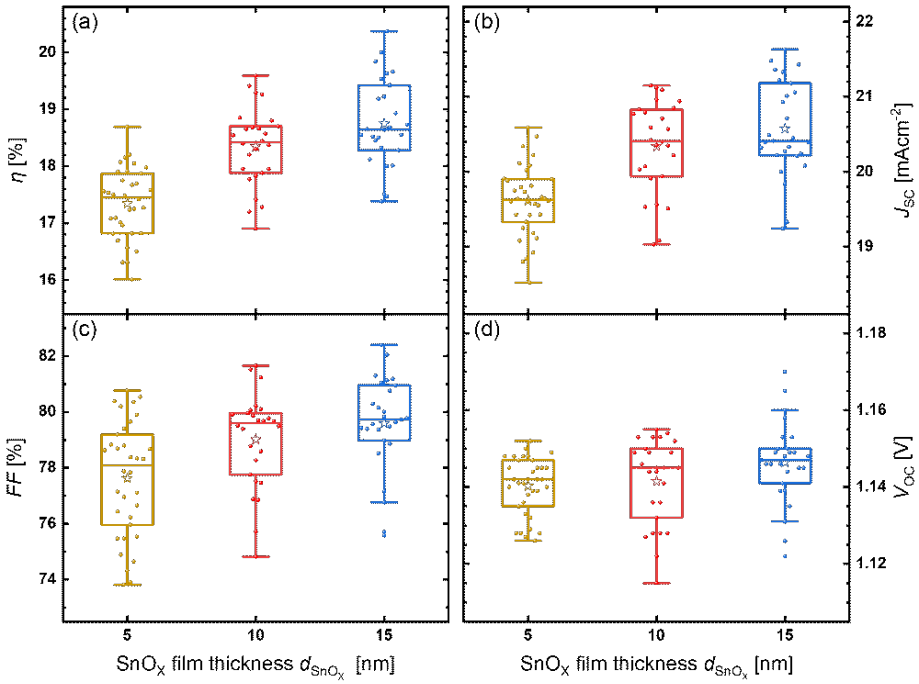

Figure 5.10.: *Solar cell parameters* η, J_{SC}, *FF*, and V_{OC} *of opaque perovskite solar cells as a function of* SnO_X *film thickness* d_{SnOx}.

maximum at R_{ALD} = 3/2, and then decreases with further increase in R_{ALD}. The sustained increases in *FF* of about 7% as the increase of R_{ALD} from 1/2 to 2 is probably attributed to the improved electrical performance due to the higher mobility [59], because the carrier concentration in the SnO_X film decreases as more oxygen participating in film growth, which suppresses the impurity scattering and facilitates the carrier transport, leading to a higher mobility [60,61]. The reasons for the maintenance of V_{OC} while the irregular fluctuation in J_{SC} are not fully understood, but it perhaps related to the degradation of perovskite layer due to a long-term exposure to the water pulse [59].

Effect of layer thickness

In contrast to the thermally evaporated BCP layer, the SnO_X buffer layer was deposited using ALD with a stable G_{ALD} of 1.5 Å /cycle on a silicon wafer at 80 °C and with a sequence of 1 s TDMASn/30 s purge/1 s H_2O/30 s purge. d_{SnOx}, precisely controlled by the number of ALD cycles, was increased from 5 to 15 nm in steps of 5 nm in the PSCs and the statistics of the solar cell parameters as a function of d_{SnOx} were shown in Fig. 5.10 (a-d). We observed that the average η increased from 17.4% at 5 nm to a maximum value of 18.8% at 15 nm, which was almost linearly proportional to d_{SnOx}. Compared to the performance of the PSCs with BCP film thickness increasing [62], the SnO_X scenario showed a reversed trend when the film thickness increased. To understand this "abnormal" behavior of SnO_X, we systematically studied the reasons for the variation of solar cells parameters with d_{SnOx} and the working mechanisms of SnO_X buffer layer in perovskite/silicon tandem solar cells in the next section.

In conclusion, the SnO_X optimization process comprised three distinct phases (initial, intermediate, and final), and the device performance of "Structure B" at each phase was summarized in Fig. 5.11(a-d) to evaluate the impact of various optimization strategies. In the initial stage, the statistics exhibit considerable dispersion, with efficiencies ranging from 10% to 17% due to the extremely poor homogeneity of the SnO_X film (Fig. 5.2). Following systematic adjustments to the deposition parameters in the ALD system, the variation in thickness distribution was effectively controlled within 1 nm, which had previously exceeded 20 nm, and the growth of SnO_X reached saturation with a constant deposition rate. Consequently, the statistical data exhibited significantly less dispersion at the intermediate stage, and the improvement in *FF* and V_{OC} was partially attributed to the concurrent optimization of the HTL/perovskite/passivation layer stack (Sec. 7.2.1). In the final stage, the average efficiency was enhanced from approximately 18% to 20% through the optimization of T_{ALD}, R_{ALD}, and d_{SnOx}. A champion efficiency of 20.3% was achieved in "Structure B," which was comparable to that of "Structure A" (PSC with BCP). The device configurations and *JV* curves are presented in Fig. 5.11(e) and Fig. 5.11(f), respectively. This result demonstrates that the optimized SnO_X film and corresponding C_{60}/ SnO_X interface were qualified for fabricating a high-efficiency tandem device.

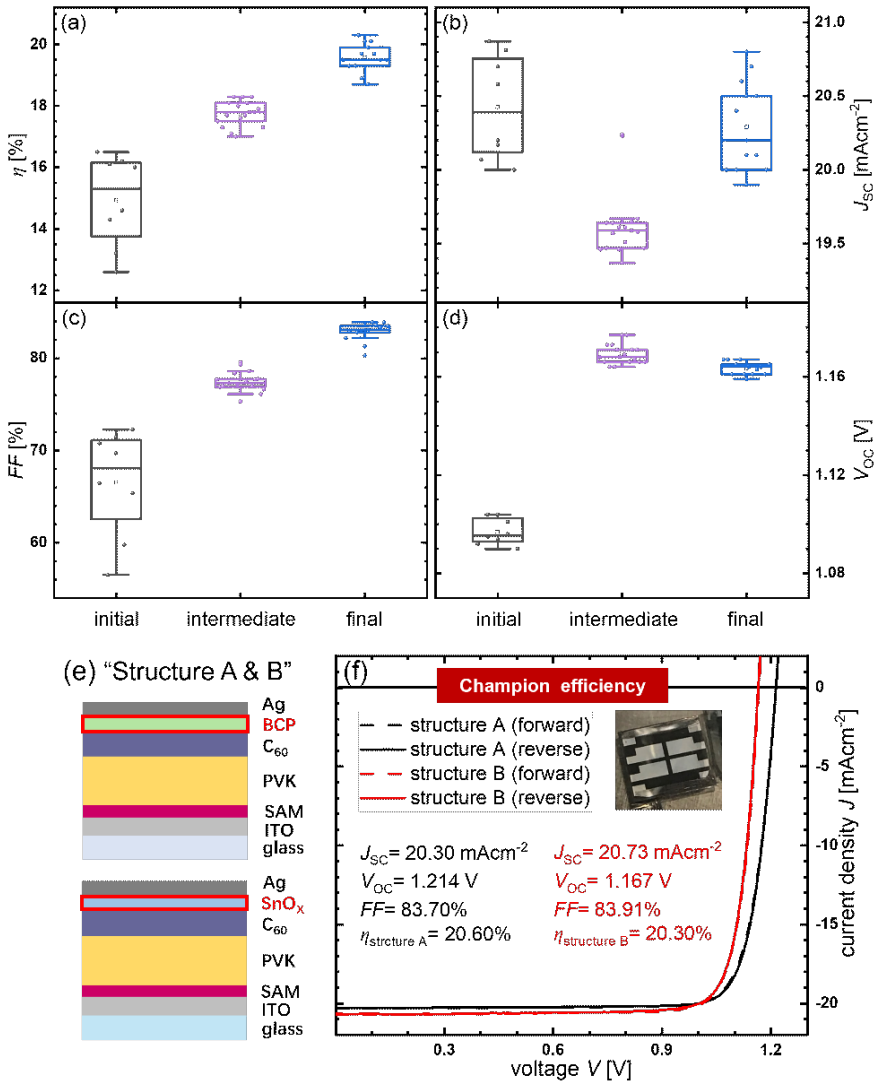

Figure 5.11.: *(a) η, (b) J_{SC}, (c) FF, and (d) V_{OC} statistics of the perovskite solar cells with "structure B" at the initial, intermediate and final phases of optimization. (e) Schematic of the cross section of "structure A" and "structure B". (f) Comparison of the JV curves of champion efficiencies with "structure A" and with "structure B". A realistic top view of the perovskite solar cells was inserted.*

5.2. Working mechanisms of tin oxide

While SnO_X has been extensively utilized as a sputter buffer layer in perovskite/silicon tandem solar cells, there has been a paucity of independent research investigating its working mechanisms. Does this provide purely physical protection to the underlying stacks against sputtering damage? Furthermore, it is unclear whether the C_{60}/SnO_X interface affects carrier extraction or whether the insertion of SnO_X alters the electrical properties or the passivation quality of the tandem device. Since SnO_X and BCP are in the same place, between the ETL and electrode, in the perovskite-related solar cells, we will first discuss the working mechanism of BCP.

The primary function of the BCP interlayer in the single-junction PSCs as reported is to lower the work function of adjacent metal electrode [63], improve the metal-semiconductor (MS) contact at the C_{60}/Ag interface, and consequently achieve energy band alignment and a high *FF*. In addition to the work function, the BCP film thickness also plays a key role in the performance of the PSCs. Most studies demonstrate that the optimal thickness of the BCP layer was 5–8 nm because the *FF* began to decrease as the thickness increased above 10 nm, however, only a few studies have interpreted this result [64-66]. The E_g of BCP (~ 2.5 eV) is larger than that of C_{60}, the highest occupied molecular orbital (HOMO) of BCP is around 1 eV deeper than that of C_{60}, and its lowest unoccupied molecular orbital (LUMO) is around 1 eV shallower. The work function of Ag is approximately 4.5 eV. From the perspective of the band diagram, these values indicate that the simultaneous presence of potential barriers in HOMO and LUMO at the C_{60}/BCP interface blocks the transport of holes and electrons, resulting in carrier accumulation at the interface. From the experimental results as reported [65], Ag atoms can diffuse into the BCP layer owing to their high mobility, which reacts with the phosphorus atom in the BCP molecule and generates the BCP:Ag complex, resulting in the presence of gap states. Electrons can hop through with the assistance of these favorable gap states within the BCP layer and only holes are blocked at the ETL/BCP interface. However, as the BCP thickness increased, the Ag atoms could hardly hop through the entire BCP layer, and the gap states were present only in the region near the BCP/Ag interface, therefore the electrons were simultaneously hindered at the interface.

The R_{SH} of BCP and SnO_X thin films exceeded the measurement range (10 mΩ/sq-10^4 Ω/sq) of the four-probe method [67] (Schuetz Messtechnik GMBH, MR-1), making

both films poor conductors with poor conductivity. Theoretically, the thicker the insulating film, the higher the risk of a low *FF,* but it seems that SnO_X is not controlled by this rule. From my experimental results (Fig. 5.10), the utilization of a 15 nm-thick SnO_X film remained favorable for cell performance and outperformed than that of 10 nm counterpart, which is different from the observations in BCP. Therefore, we conducted a series of experiments, characterizations, and simulations to understand the working mechanism of SnO_X at the C_{60}/Ag interface in inverted PSCs, which can serve as an ideal reference for understanding the working mechanism of SnO_X in perovskite top cells. Changes in the photovoltaic parameters were analyzed individually and the discussion proceeds in the order of V_{OC}, $J_{SC,}$ and *FF*.

5.2.1. Dependence of V_{OC} and J_{SC}

V_{OC} and ssPL

In Fig. 5.10(d), the values of V_{OC} slightly increased when the 5 nm SnO_X film became thicker. We studied the absolute PL spectra and quantum yields of the opaque PSCs as a function of d_{SnOx} because PL spectroscopy is a suitable tool for quantitatively evaluating changes in radiative and unwanted nonradiative recombination by comparing absolute or relative PL intensities as a function of sample geometry or processing without requiring electrical contacts. The average quasi-Fermi level splitting [68-70] ΔE_F can be determined from the absolute PL intensities by using

$$\Delta E_F = \Delta E_{F,rad} + k_B T \ln\left\{Q_{e,lum}\right\} \tag{5.3}$$

assuming a flat quasi-Fermi level where the radiatively limited $\Delta E_{F,rad}$ refers to the maximum achievable Fermi level splitting in the absence of nonradiative (defect) recombination, which can be determined using detailed balance arguments akin to those used for the Shockley-Queisser model [71]. The external quantum efficiency of the PL emission $Q_{e,lum} = \frac{Y_{em}}{Y_{rec}}$, defined as the ratio of the emitted photon flux (Y_{em}) to the

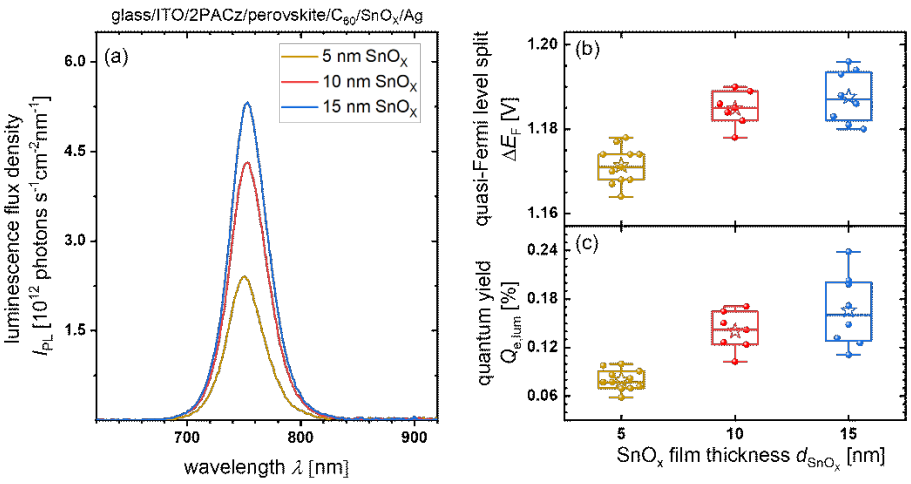

Figure 5.12.: *a) PL spectra of representative devices. Statistics of b) ΔE_F, and c) $Q_{e,lum}$ for opaque perovskite solar cells as a function of the SnO_X film thickness d_{SnOx}.*

recombination flux (Y_{rec}), can be directly obtained through experiments. k_B and T are the Boltzmann constant and the temperature, respectively. Figure 5.12(a-c) shows the PL spectra of the representative devices at open-circuit, the ΔE_F and the corresponding $Q_{e,lum}$ values of the PSCs as functions of d_{SnOx}. As the SnO_X thickness increases from 5 to 15 nm, the PL intensity, ΔE_F, and $Q_{e,lum}$ increase, suggesting a higher fraction of radiative recombination and a lower fraction of nonradiative recombination. The results demonstrate that thick SnO_X films reduce nonradiative recombination in PSCs, which explains the trend of slightly higher V_{OC} for thicker SnO_X films, as shown in Fig. 5.10(d).

According to our previous work [9], SnO_X is likely to exhibit a significantly lower work function than bare C_{60}, which will result in an upward shift of the Fermi level at the perovskite/C_{60} interface towards the conduction band of C_{60}. In the present study, the increase in SnO_X film thickness is likely to reduce the work function of bare SnO_X, suggesting that the Fermi level at the perovskite/C_{60} interface will be closer to the conduction band of C_{60} in the perovskite solar cells employing a thicker SnO_X buffer layer compared to the 5 nm counterpart, ultimately enabling the presence of a larger quasi-Fermi level splitting, as shown in Fig. 5.12(b). As the SnO_X film thickness increases, the upward

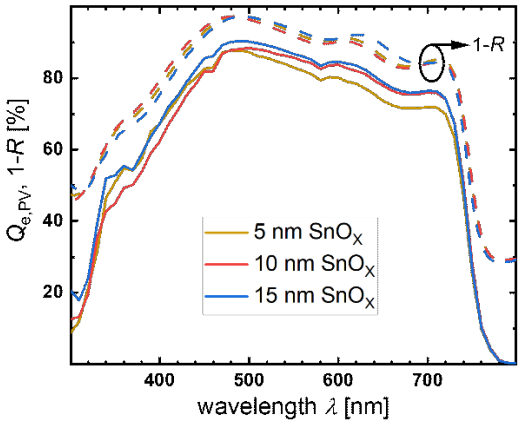

Figure 5.13.: *$Q_{e,PV}$, and 1-R of opaque perovskite solar cells as functions of the SnO_X film thickness d_{SnOx}.*

shift of the Fermi level at the perovskite/C_{60} interface reduced the hole concentration in the perovskite at the interface, thereby reducing the nonradiative recombination rate at the perovskite/C_{60} interface. Consequently, the PL intensity was enhanced as the SnO_X film thickness increased. The characterization of energy levels and the device simulations presented in following sections will substantiate this speculation.

J_{SC} and external quantum efficiency

Compared to V_{OC}, the increase in J_{SC} is much more pronounced, exceeding 1 mA/cm^2, as shown in Fig. 5.10(b). To gain deeper insight into the optical enhancement due to thicker SnO_X, $Q_{e,PV}$ measurements were performed on representative devices with increasing d_{SnOx}. Representative $Q_{e,PV}$, and the corresponding 1-reflectance (1-*R*) are shown in Fig. 5.13. We observed that thicker SnO_X showed an enhanced optical response at wavelengths between 490 and 730 nm; however, the corresponding reflectance of the finished devices did not show a significant difference over the wavelength range as d_{SnOx} increased. This result suggests that reflectance was not the dominant reason for the $Q_{e,PV}$ enhancement with thicker SnO_X. What factors are responsible for this result? In fact, the $Q_{e,PV}$ enhancement

within a specific wavelength range observed in PSCs unexpectedly overlaps with the simulation results of SHJ solar cells that we previously conducted [72], which aimed to explore the impact of the surface recombination velocity at both the front and rear interfaces on the external quantum efficiency of silicon solar cells under top and bottom illumination.

Simulations with Quokka 3, recombination velocity and $Q_{e,PV}$

In the simulations conducted with Quokka 3, we used two silicon solar cells: (1) a device with a p-n junction on the rear surface consisting of an n-type crystalline silicon (c-Si) substrate, a p-type layer on the rear side to form a p-n junction, and a heavily doped n-type (n^+) layer on the front side to form a high-low junction; (2) a device with a p-n junction on the front surface, a p-type c-Si wafer was utilized as the substrate, covered by an n-type layer on the front side and a heavily doped p-type (p^+) layer on the rear side. The $Q_{e,PV}$ values for various surface recombination velocities at the dual-side interfaces upon top and bottom illumination were calculated to demonstrate the significant impact of interface recombination on the optical response. Here, we primarily discuss the first solar cell in detail, because both solar cells yield similar results.

In Fig. 5.14(a), the $Q_{e,PV}$ response across the entire wavelength range of 300 nm – 1200 nm were enhanced by decreasing the surface recombination velocity at front interface (S_{front}) of n^+/n junction from 200 cm/s to 0.7 cm/s in the rear-sided p-n junction silicon solar cell upon top illumination (n-side), resulting in an increase of J_{SC} from 31.8 mA/cm^2 to 39.5 mA/cm^2, as shown in Fig. 5.14(c). When S_{front} was set to 0.7 cm/s and the surface recombination velocity at the rear interface (S_{rear}) of the p-n junction decreased from 200 cm/s to 0.7 cm/s, the $Q_{e,PV}$ response and J_{SC} did not exhibit any differences, as shown in Fig. 5.14(b, d). These simulated results are highly consistent with the experimental findings outlined in the aforementioned studies [73-76], which are not difficult to explain. For any wavelength, there is stronger absorption on the incident side than on the opposite side, which follows the Beer- Lambert law [77]. However, for long wavelengths, there was a much higher fraction of generation at the rear side than that at short wavelengths.

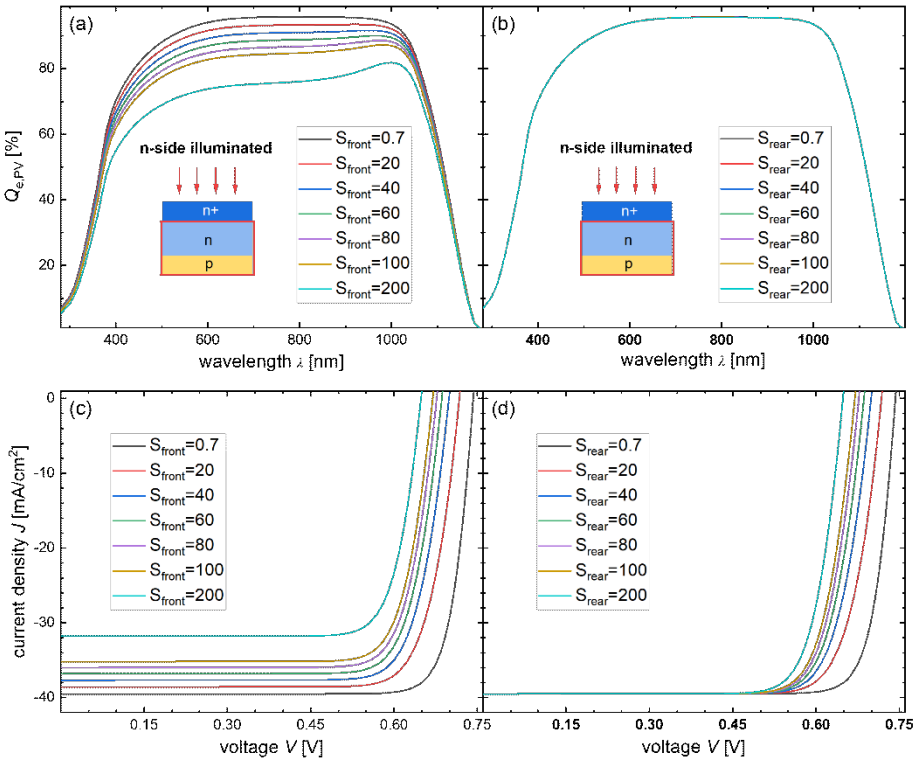

Figure 5.14.: *Simulated $Q_{e,PV}$ spectra of the rear-sided p-n junction silicon solar cell upon top illumination (n-side) as a function of surface recombination velocity at a) the front and b) the rear interfaces. Simulated JV curves of the rear-sided p-n junction silicon solar cell upon top illumination (n-side) as a function of surface recombination velocity at c) the front interface and d) the rear interface.*

Let us look deep inside the generation and separation of photogenerated electron-hole pairs upon dual illumination. Upon top illumination (n-side), the incident light over the entire wavelength spectrum generates a large number of electron-hole pairs near the front interface, where the n^+/n junction is located. However, only a small number of electron-hole pairs were generated near the rear interface, where the p-n junction was located, as shown in Fig. 5.15(a). Owing to a weaker electric field at the high-low junction, a decrease in S_{front} enables more electron-hole pairs to be efficiently collected, ultimately contributing to the

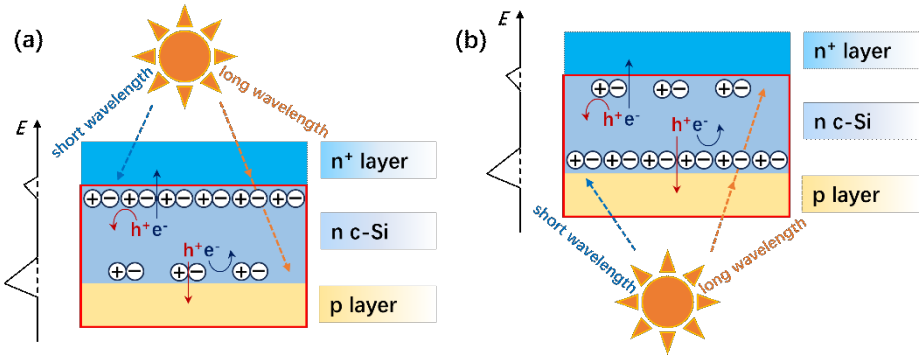

Figure 5.15.: *Electron-hole pairs were generated in the rear-sided p-n junction silicon solar cell under a) top illumination (n-side) and b) bottom illumination (p-side). Notably, the electric field of the p-n junction is stronger than that of the high-low junction, implying a more efficient separation of electron-hole pairs at the p-n junction.*

short-circuit current instead of recombination. Consequently, the $Q_{e,PV}$ response over the entire wavelength range was enhanced as S_{front} decreased in the rear-sided p-n junction silicon solar cell upon top illumination. In contrast, because of the stronger electrical field at the p-n junction compared to the high-low junction, the electron-hole pairs were more effectively separated. Therefore, the change in S_{rear} had an insignificant influence on the optical response.

For the same solar cell, merely altering the illumination direction from top to bottom yielded significantly divergent results. When S_{front} was decreased from 200 cm/s to 0.7 cm/s, an enhancement of the $Q_{e,PV}$ response was observed solely in the long-wavelength range between 700 nm and 1200 nm with a slight increase in J_{SC} from 34.6 mA/cm^2 to 35.6 mA/cm^2, as depicted in Fig. 5.16(a, c). This enhancement can be attributed to two facts: (i) long-wavelength light has a much higher fraction of generation at the rear side compared to short wavelengths, and (ii) a high-low junction does not separate electron-hole pairs as efficiently as a p-n junction, as illustrated in Fig. 5.15(b). Therefore, the surface recombination velocity in the vicinity of the high-low junction primarily affects the optical response in the long-wavelength range. These findings are in close agreement with the published experimental results [76]. Notably, the optical response and photo-generated current remained unaffected by S_{rear} for the same reason as discussed previously, as

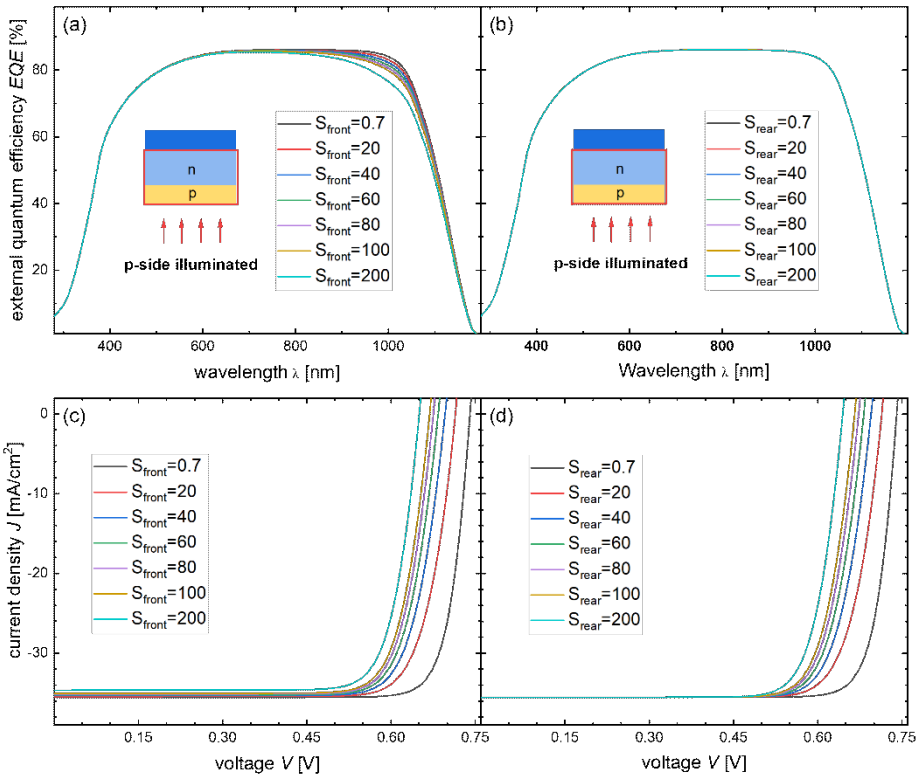

Figure 5.16.: *Simulated $Q_{e,PV}$ spectra of the rear-sided p-n junction silicon solar cell upon bottom illumination (p-side) as a function of surface recombination velocity at a) the front and b) the rear interfaces. Simulated JV curves of the rear-sided p-n junction silicon solar cell upon bottom illumination (p-side) as a surface function of recombination velocity at c) the front interface and d) the rear interface.*

depicted in Fig. 5.16(b, d). The validity of the simulations was further proved by the $Q_{e,PV}$ measurements on both transparent passivating contact (TPC) solar cells and SHJ solar cells [72]. For SHJ cells with a front-sided p-n junction, an optical response enhancement was observed in the long-wavelength range with increasing thickness of the rear a-SiO_X:H (i) buffer layer because of the improvement in the passivation quality of the c-Si/a-SiOx:H rear interface. The results obtained from the numerical simulations are highly consistent with

our experimental data for both SHJ and TPC solar cells, as well as the published experimental findings for various organic/inorganic solar cells [73-76]. From a practical perspective, the spectra of external quantum efficiency under dual-side illumination conditions provide guidelines for the quick diagnosis of "imperfect" passivation quality at the top and bottom interfaces of any type of solar cell.

The $Q_{e,PV}$ enhancement of PSCs with thicker SnO_X films (Fig. 5.13) is similar to that of rear-sided p-n junction silicon solar cell with suppressed surface recombination (Fig. 5.16(a)), mainly in the long-wavelength range. Based on the conclusions drawn from the simulations using Quokka 3, if the wavelength region of optical response enhancement undergoes any changes when the direction of illumination is altered, the $Q_{e,PV}$ enhancement of PSCs in the long-wavelength range is supposed to be related to the improvement of the passivation quality at the interface. Therefore, we fabricated semi-transparent PSCs with d_{SnOx} increasing from 5 to 15 nm, which allow for *JV* measurements upon double-sided illumination.

Semi-transparent solar cells

To identify whether the enhanced optical response at long wavelengths is directly related to imperfect interfacial passivation, the $Q_{e,PV}$ measurements for representative semi-transparent perovskite solar cells were performed from both the ETL and HTL (glass) sides. The results of $Q_{e,PV}$ are depicted with the corresponding 1-*R* in Fig. 5.17. Regardless of the illumination direction, the $Q_{e,PV}$ response of the representative semi-transparent devices increases by increasing d_{SnOx}. When the $Q_{e,PV}$ measurement was conducted from the HTL (glass) side, an enhanced optical response was observed between 490 nm and 720 nm (Fig. 5.17(a)), and this long wavelength region nearly overlaps with that of where optical enhancement is observed in opaque devices (Fig. 5.13). While no notable difference is observed at wavelengths below 490 nm in both opaque and semi-transparent devices. When $Q_{e,PV}$ measurement was performed from the opposite ETL (SnO_X) side, the optical response was enhanced across the entire wavelength range of 300-800 nm, as shown in Fig. 5.17(b). The results illustrate that the wavelength range of the optical response enhancement changes with illumination direction. Reflectance measurements of representative semi-transparent devices were conducted to exclude the impact of variations in the intrinsic optical properties

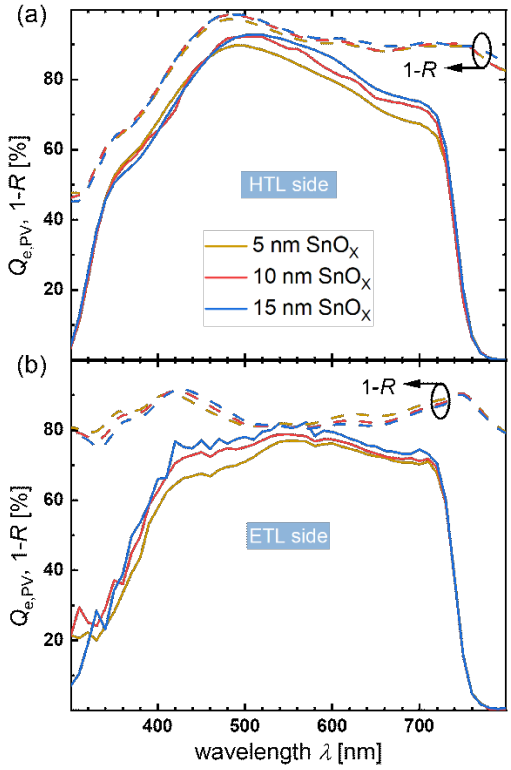

Figure 5.17.: *$Q_{e,PV}$ and 1-R of the semi-transparent perovskite solar cells as a function of the SnO_X film thickness d_{SnOx} measured from the a) HTL and b) ETL sides.*

on this change. The reflectance of the finished devices at short wavelengths upon HTL-side measurement did not show a significant difference over the wavelength range as d_{SnOx} increased. When reflectance was measured from the ETL side, the curve of 1-*R* was slightly red-shifted with increasing d_{SnOx}, but no significant difference was observed over the wavelength range of 300-800 nm. Therefore, reflectance is not the primary reason for the changes in the wavelength range of enhanced optical response. According to our previous analysis of the nonradiative recombination (Fig. 5.12), the reason is most likely to be the improvements in the "imperfect" interfacial passivation near the ETL side by employing a thicker SnO_X film. Upon HTL-sided illumination, the infrared spectra generate electron-hole pairs close to the ETL/perovskite interfaces, so that when the nonradiative

recombination at the ETL side was suppressed by a thicker SnO_X film, the $Q_{e,PV}$ enhancement primarily occurred at long wavelengths, corresponding to the infrared spectrum. Upon ETL-sided illumination, light over the entire wavelength range could generate carriers near the SnO_X layer, and thus the optical response across the wavelength range of 300-800 nm was improved owing to the inhibitory effect of the thicker SnO_X film on nonradiative recombination at the ETL side.

In summary, the analysis regarding V_{OC} and J_{SC} indicates that a thick SnO_X film has the potential of improving the passivation quality at "imperfect" interface at ETL side by suppressing nonradiative recombination. Future studies on thickness-dependent *FF* in the following section might help to determine the location of recombination.

5.2.2. Dependence of *FF*

Ideality Factor and photoshunt

In PSCs with an inverted structure (p-i-n) of glass/ITO/HTL/perovskite/C_{60}/BCP/Ag, the *FF* often decreases with increasing BCP film thickness, which is generally attributed to charge accumulation [65] and poor electrical contact [78]. Theoretically, the risk of obtaining a low *FF* increases with a thicker insulating film employed in a solar cell; however, the *FF* increases as d_{SnOx} increases from 5 to 15 nm (Fig. 5.10(c)). The possible reasons for this unusual trend in *FF* with buffer layer thickness are discussed as follows, which will assist in understanding the possible sources of *FF* losses in PSCs. In the absence of resistive losses, the upper limit on the *FF* is approximately given [79]

$$FF = \frac{v_{OC} - \ln(v_{OC} + 0.72)}{v_{OC} + 1} \tag{5.4}$$

and the normalized open-circuit voltage (v_{OC}) is given by

$$v_{OC} = (qV_{OC})/(n_{id}k_BT) \tag{5.5}$$

where q represents the elementary charge and n_{id} refers to the diode ideality factor. From Eq. 5.4 and 5.5, the value of FF depends only on n_{id}, V_{OC} and T, whereas the R_S and R_{SH} were not been taken into account. The FF equals to the ideal fill factor (FF_{id}) when n_{id} equals 1, which is limited only by radiative recombination without considering resistive losses.

The n_{id} is given by

$$n_{id} = \frac{q}{k_B T} \frac{dV_{OC}}{d\ln(J_{SC})} \tag{5.6}$$

The value of n_{id} can be determined by the measurement of the V_{OC} at different light intensity [80,81]. In PSCs, n_{id} ranges between 1 and 2, [82,83] providing insight into the recombination mechanism. n_{id} of one or close to one may indicate radiative band-to-band recombination of free charges, recombination via sufficiently shallow traps and any recombination mechanism within a sufficiently doped semiconductor.[84] However, most lead-based perovskites exhibit low doping densities [85] and luminescence quantum efficiencies well below unity, making n_{id} between 1 and 1.5 most consistent with Shockley-Read-Hall (SRH) recombination via states that are more or less shallow. In contrast, n_{id} approaching 2 suggest trap-assisted recombination through mid-gap impurities in an intrinsic semiconductor [84]. These states are not confined to be in the perovskite bulk but can also exist at the interfaces to electron and hole transport layers. Nonradiative recombination losses with $n_{id} > 1$ not only limit the V_{OC} but also reduce the FF of devices.

Recombination velocity

Parallel resistance can also be attributed to FF losses, as solar cells often exhibit shunt-like behavior under illumination, known as photoshunt [86]. This phenomenon is attributed to recombination currents that appear ohmic, showing an approximately linear J-V relationship

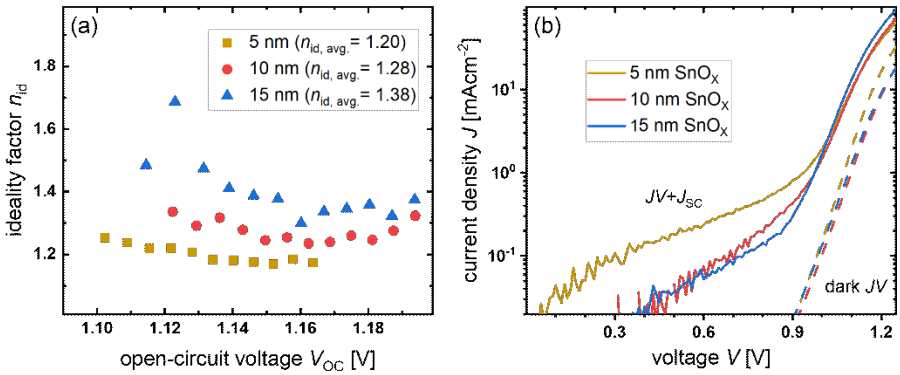

Figure 5.18: *(a) Ideality factor n_{id} derived from the Suns-V_{OC} measurement, along with the average value of n_{id} calculated from 1.1 V to the end of the measurement. (b) JV curves for representative devices under illuminated (solid lines) and dark (dashed lines) with varying SnO_X film thickness d_{SnOx}, plotted in the first quadrant.*

over a range of voltages. To quantify the *FF* losses due to a photoshunt, the *JV* curves of representative devices with varying d_{SnOx} were shifted to the first quadrant by adding the respective J_{SC}. These curves, along with the dark *JV* (JV_{dark}) curves, are plotted using a logarithmic current axis, as shown in Fig. 5.18(b). The illuminated *JV* curves display characteristics similar to those of a low shunt resistance, though this feature is absent in the JV_{dark} curves. The moderate slope in the lower voltage region, referred to as the photoshunt, results from slow carrier extraction at short circuits and low forward voltages results from slow carrier extraction at short circuits and low forward voltages [86]. This leads to a recombination current behaving as a shunt. The results revealed a significant reduction in the photoshunt as the SnO_X thickness increased from 5 nm to 10 nm. A slight further reduction was observed when the thickness increased to 15 nm, indicating that PSCs with 15 nm SnO_X may experience the lowest recombination current. In addition, I performed some simulations using SCAPS to quickly prove that the presence of photoshunt has a close relationship with the carrier recombination at the interfaces adjacent to the perovskite layer. Here, the recombination velocities at the MeO-2PACz/perovskite and perovskite/C_{60} interfaces varied from 10^0 cm/s to 10^6 cm/s. The predicted *JV* curves and corresponding ($JV + J_{SC}$) curves that were plotted in the first quadrant using a logarithmic

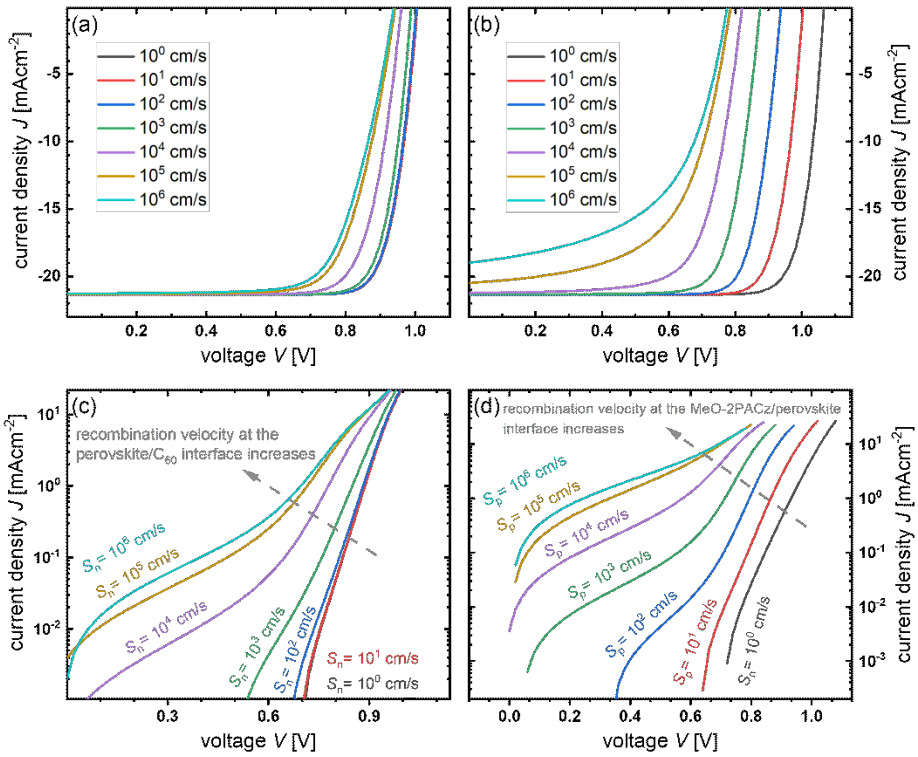

Figure 5.19: *Simulated JV curves of perovskite solar cells as a function of recombination velocity increasing from* 10^0 *to* 10^6 *cm/s at the a) perovskite/*C_{60} *and b) MeO-2PACz/perovskite interfaces. c) Corresponding* ($JV + J_{SC}$) *curves plotted in the first quadrant using a logarithmic current axis with increasing recombination velocity at the c) perovskite/*C_{60} *and d) MeO-2PACz/perovskite interfaces.*

current axis are depicted in Fig. 5.19(a, b) and Fig. 5.19(c, d), respectively, where either the recombination velocity of the electrons (S_n) at the perovskite/C_{60} interface or the recombination velocity of the holes (S_p) at the MeO-2PACz/perovskite interface were variables. From the changes in the JV and ($JV + J_{SC}$) curves as a function of S_n and S_p, we notice that the photoshunt is highly dependent on the recombination velocity at the perovskite/transporting layer interface in PSCs.

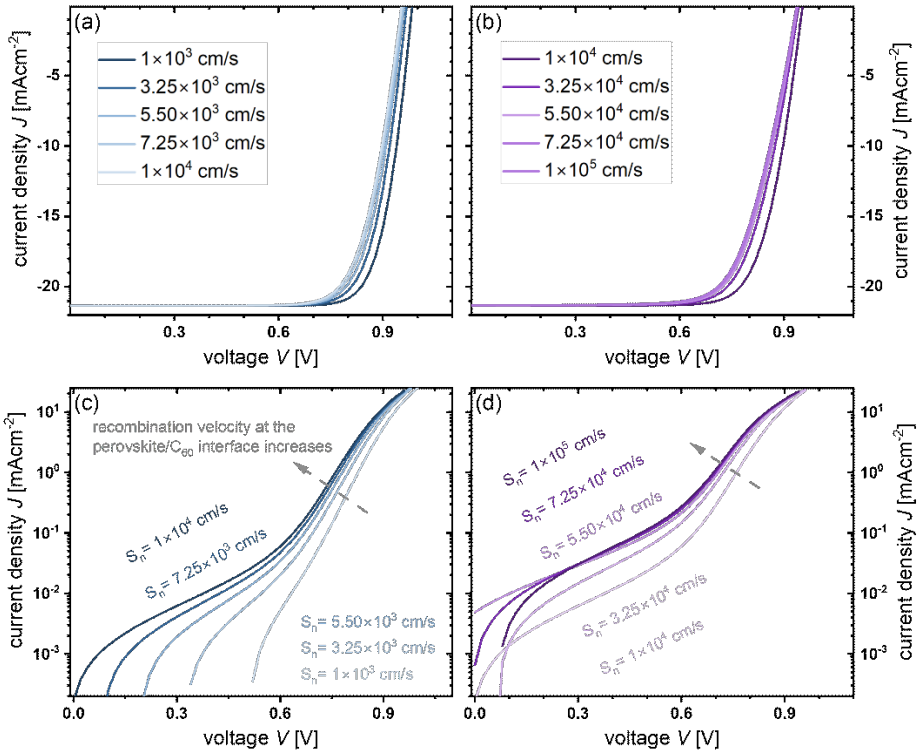

Figure 5.20: *Simulated JV curves of perovskite solar cells as a function of recombination velocity at the perovskite/C_{60} interface increased from a) 10^3 to 10^4 cm/s and b) 10^4 to 10^5 cm/s. c) Corresponding ($JV + J_{SC}$) curves plotted in the first quadrant using a logarithmic current axis with the recombination velocity at the perovskite/C_{60} increasing from c) 10^3 to 10^4 cm/s and d) from 10^4 to 10^5 cm/s.*

When d_{SnOx} increased from 5 to 15 nm in the PSCs, the representative ($JV + J_{SC}$) curves changed (Fig. 5.18(b)), which is similar to what was observed in the SCAPS simulations (Fig. 5.19(c, d)), suggesting that the recombination velocity at some interfaces decreased. After careful comparison of experimental and simulation results, the practical amplitude of the change in the shape of the ($JV + J_{SC}$) curves is more likely to be controlled by S_n at the perovskite/C_{60} interface with a rough range of 10^3 - 10^5 cm/s, because the MeO-2PACz/perovskite interface is less susceptible to the influence of SnO_X. Therefore, an

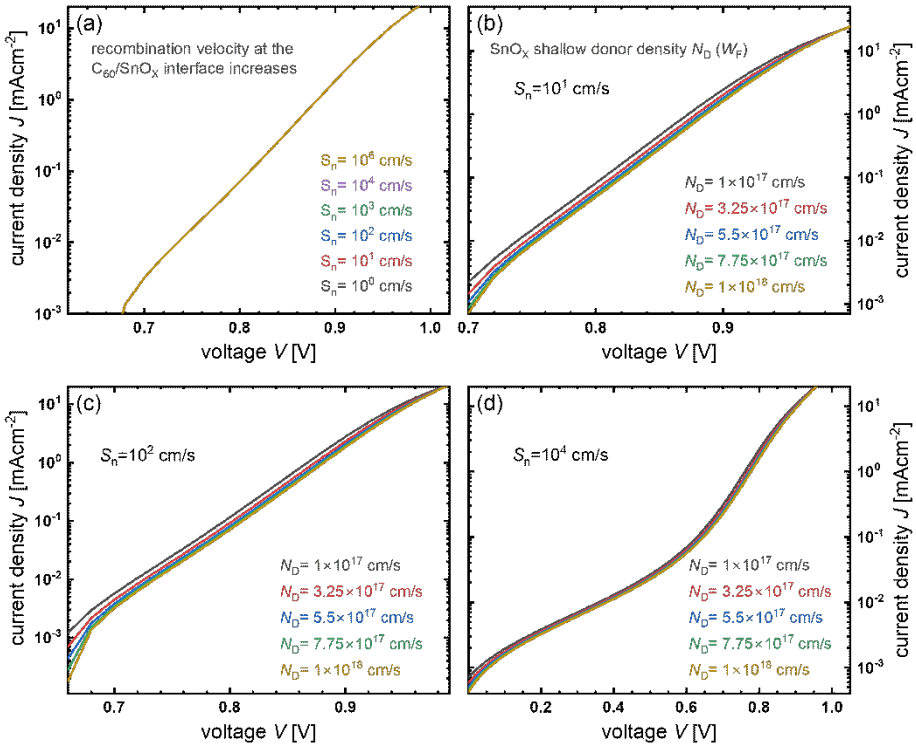

Figure 5.21: *Simulated JV curves of perovskite solar cells as a function of recombination velocity at a) C_{60}/SnO_X interface using a logarithmic current axis. Simulated JV curves of perovskite solar cells as a function of SnO_X shallow donor density (N_D, represents different Φ values) while maintaining the recombination velocity at the C_{60}/SnO_X interface constant at b)* 10^1 *cm/s, c)* 10^2 *cm/s, and d)* 10^4 *cm/s.*

independent simulation was carried out by varying the S_n value in smaller scales from 10^3 to 10^4 cm/s and from 10^4 to 10^5 cm/s to examine the impact of subtle changes in the recombination at the perovskite/C_{60} interfaces on the photoshunt, and the corresponding results are plotted in Fig. 5.20. By comparing the experimental results (Fig. 5.18(b)) with the simulated results (Fig. 5.20(c, d)), it can be inferred that the S_n value at the perovskite/C_{60} interfaces reduces by approximately one order of magnitude when d_{SnOx} increased from 5 nm to more than 10 nm, which indicates that a thicker SnO_X film can

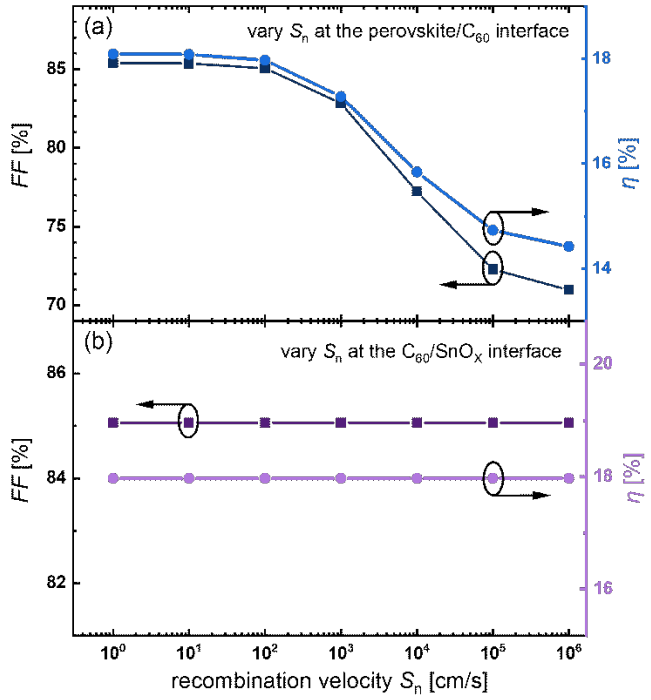

Figure 5.22: *Simulated FF and efficiency values of perovskite solar cells as a function of recombination velocity at a) perovskite/C_{60} interface and b) C_{60}/SnO_X interface.*

effectively suppress carrier recombination on the ETL side provided that the recombination at the HTL side was not affected, which also aligns well with the previous PL and $Q_{e,PV}$ results (Sec. 5.2.1).

Theoretically speaking, the thickness variation of the SnO_X should have a more direct effect on the carrier recombination at the C_{60}/SnO_X interface than at the perovskite/ C_{60} interface, which is around 15 nm away from the SnO_X layer. Therefore, we checked the impact of S_n at the C_{60}/SnO_X interface, which should be the first factor to be suspected of photoshunt behavior. However, the simulation results in Fig. 5.21(a) revealed that the photoshunt is hardly affected by S_n at the C_{60}/SnO_X interface. In addition, we found that the work function of SnO_X that was interpreted as the shallow donor density, also called the doping concentration (N_D), in the SCAPS software also has an insignificant impact on the

photoshunt when the S_n at the C_{60}/SnO_X interface was kept constant at 10^1 cm/s, 10^2 cm/s and 10^4 cm/s, as depicted in Fig. 5.21(b-d).

In Fig. 5.22, the *FF* and efficiency that were extracted from the SCAPS simulations are plotted as a function of either the S_n at the perovskite/C_{60} interface or the S_n at the C_{60}/SnO_X interface. The simulation results indicate that the *FF* is primarily affected by the carrier recombination at the perovskite/C_{60} interface with the S_n exceeding a critical value of 10^1 cm/s, but the conclusions are not always valid for all cases because the simulation results are strongly dependent on the combinations of all input parameters, which are generally obtained from experiments, literatures, or even experience. Only the closest simulation results to the experimental results obtained by constant correction of the simulations can tell us the exact reasons behind the thickness-dependent *FF*.

Fill factor

Transport losses of charge carriers lead to series resistance losses, which arise from the bulk, contact, and lateral resistance components. To quantify this loss, pseudo-*JV* (p*JV*) curve is necessarily to be mentioned here, which is the same as the illuminated *JV* curves but without the influence of the R_S. p*JV* curves are generally determined by the V_{OC} of the device at different illumination intensity and J_{SC}, which only reflects generation and recombination processes without the effect of the R_S, as the net current is zero at open circuit. Therefore, the effect of overall R_S on *FF* losses can be accurately evaluated by calculating the p*FF* from intensity-dependent J_{SC}/V_{OC} measurements. The difference between p*FF* and *FF* represents the *FF* loss caused by R_S, denoted as ΔFF_{R_s}. Additionally, *FF* losses due to $n_{id} > 1$ can be identified by ΔFF_{nid}, which is the difference between the p*FF* and FF_{id} extracted from the ideal *JV* curve (JV_{id}), where $n_{id} = 1$ and $R_S = 0$. ΔFF_{R_s} and ΔFF_{nid} can be expressed by the following equations

$$\Delta FF_{R_s} = pFF - FF \tag{5.7}$$

$$\Delta FF_{nid} = FF_{id} - pFF \tag{5.8}$$

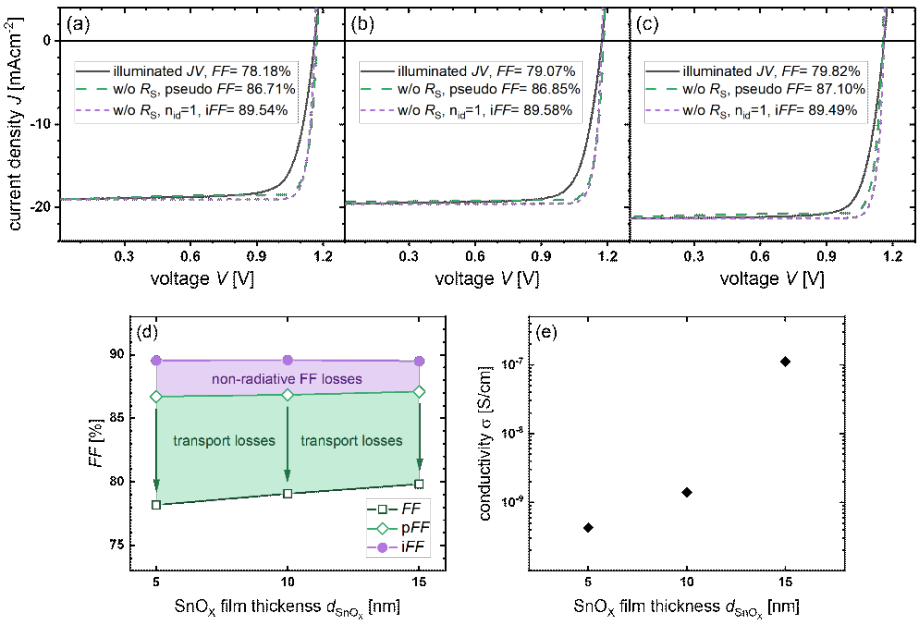

Figure 5.23: *Illuminated JV curves, pseudo-JV curves, and ideal JV curves of the studied cells with SnO_X film thicknesses d_{SnOx} of a) 5, b) 10, and c) 15 nm, respectively. c) Comparison of the FF from the JV curves, the pFF from the pseudo-JV curves (measured on the same cells), and the FF_{id} from the ideal JV curves in the radiative limit considering the increasing SnO_X film thickness of the devices. d) Lateral conductivity of the bare SnO_X films with various thickness.*

To intuitively compare the *FF* losses due to the nonideal n_{id} and R_S, the *FF*, p*FF*, and FF_{id} were calculated from the *JV*, p*JV*, and JV_{id} curves of representative devices, as shown in Fig. 5.23(a-c), and were plotted together as a function of d_{SnOx} in Fig. 5.23(d) with a dotted line. The detailed information is listed in Table 1. We observed that the ΔFF_{nid} increased from 2.6% for 5 nm to 2.9% for 10 nm, and further to 3.9% for 15 nm. By comparing the trends of the two contributions to *FF* losses, nonideal n_{id} and R_S with increasing d_{SnOx}, we found that ΔFF_{nid} increases with thicker SnO_X films due to a rise in n_{id}. In contrast, ΔFF_{R_s} decreased as d_{SnOx} increases. The reduction in R_S was identified as the primary factor behind the overall *FF* improvement with thicker SnO_X films. Lateral

conductivity measurements performed on bare SnO_X films in the dark showed a two-fold increase in conductivity (σ) as the film thickness increased from 5 to 15 nm, as shown in Fig. 5.23(e). The enhanced conductivity reduces the bulk resistance loss, contributing significantly to the improved *FF* in devices with thicker SnO_X.

Table 1. *The FFs from the JV, pJV, and iJV curves of representative devices with increasing SnO_X thickness d_{SnOx}, and the relative ΔFF_{R_s} and ΔFF_{nid}, reveal the losses caused by the overall series resistance and non-radiative recombination, respectively.*

SnO_X thickness	*FF* [%]	p*FF* [%]	i*FF* [%]	ΔFF_{R_s} [%]	ΔFF_{nid} [%]
5 nm	78.2	86.7	89.5	8.5	2.8
10 nm	79.1	86.9	89.6	7.8	2.7
15 nm	79.8	87.1	89.5	7.3	2.4

5.2.3. Preliminary simulations and band diagram

UPS and band diagram

To investigate the mechanism behind the improved conductivity of the thicker SnO_X layer in the complete device, we visualized the band diagram of a complete cell with the structure ITO/MeO-2PACz/perovskite/PEAI/C_{60}/SnO_X/Ag and examined how it varied as the d_{SnOx} increased from 5 to 15 nm. UPS measurements (Sec. 3.1.3) and numerical simulations using the drift-diffusion software SCAPS (Sec. 3.3) were performed to gain a deeper insight into the band alignments, which play a crucial role in charge extraction and recombination. For the UPS measurements, semi-devices with an ITO/MeO-2PACz/perovskite/C_{60}/SnO_X structure were prepared with 5, 10, and 15 nm SnO_X. The work function (Φ) was determined relative to the vacuum energy (E_{VAC}) from the UPS spectra by measuring the position of the cutoff at a high binding energy (E_B) using a linear fit at the background and steep edge, as shown in Fig. 5.24. The valence band (E_V) was similarly determined by applying the same linear fit to the leading edge of the UPS spectrum. These measurements, along with SCAPS simulations, provided valuable insight into how band alignment changes with SnO_X thickness, influencing the charge dynamics within the device. The electron affinity (χ),

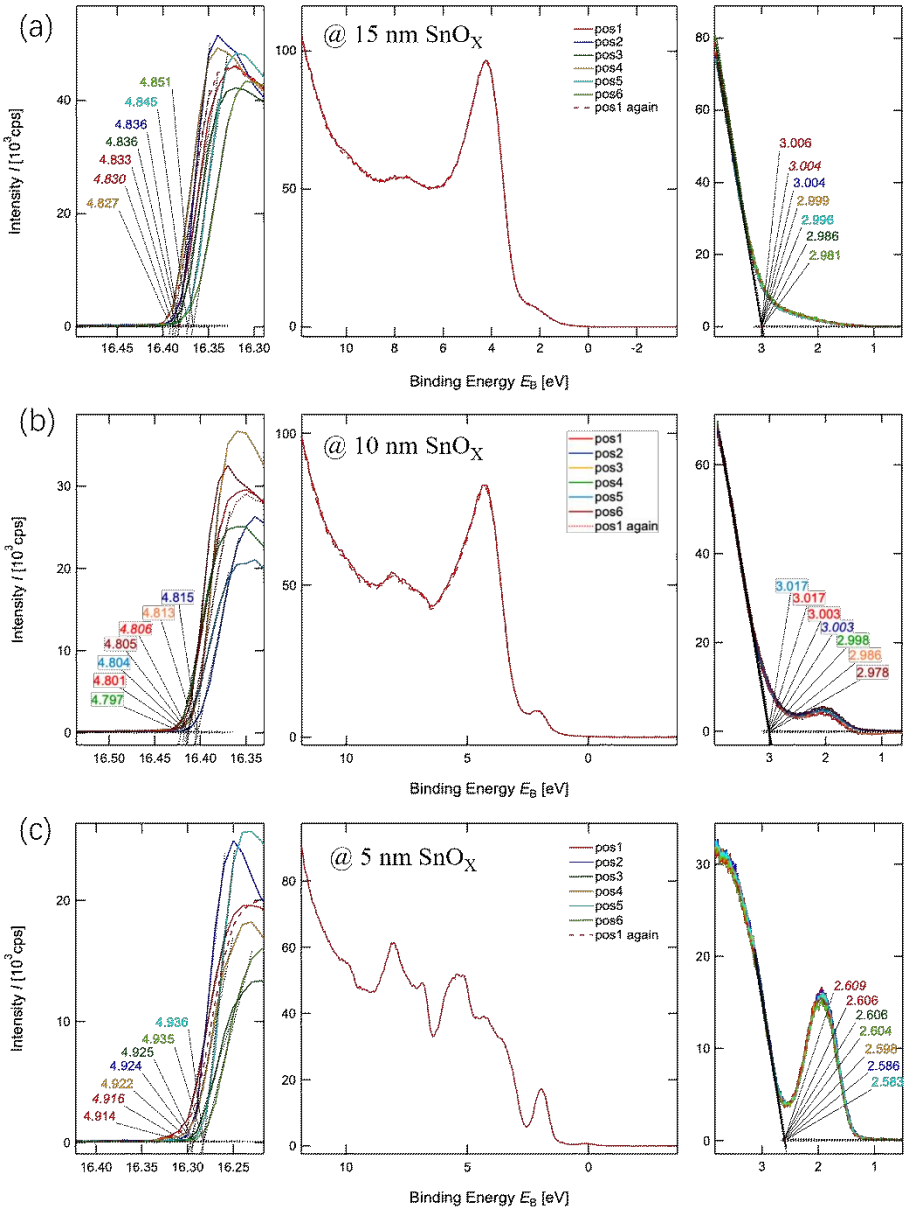

Figure 5.24: *UPS for ITO/MeO-2PACz/perovskite/C_{60}/SnO_X with SnO_X thicknesses d_{SnOx} of a)* 15*, b)* 10*, and c)* 5 *nm.*

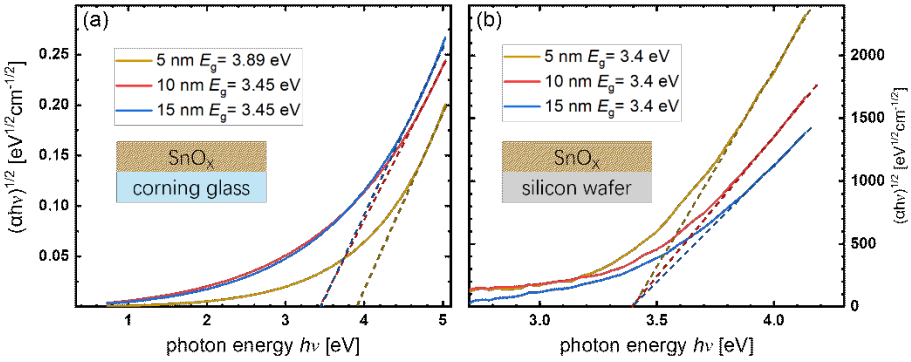

Figure 5.25: *Plots of* $(\alpha h\nu)^{1/2}$ *with linear fits (dashed lines) to the approximately linear portion of the curve, where α was determined either using a) Eq.* 5.9 *or b) Eq.* 5.10*. The band gaps of* SnO_X *with different film thicknesses* d_{SnOx} *were estimated from the intersection of the linear fit with* $(\alpha h\nu)^{1/2} = 0$.

which represents the energy difference between the conduction band (E_C) and E_{VAC}, was calculated using the measured E_V and E_g.

The E_g of the SnO_X films at different thicknesses was calculated using Tauc plots, based on the function $(\alpha h\nu)^{1/2}$ versus photon energy ($h\nu$). This method is appropriate for amorphous and indirect band gap semiconductors, revealing a linear segment near the absorption onset. The α [87] was determined using the equation

$$\alpha = 4\pi k_B / \lambda \tag{5.9}$$

where k_B and λ are the extinction coefficient measured using ellipsometry and wavelength, respectively. In addition, α also can be determined using the equation

$$\alpha = \frac{1}{d} \ln\left(\frac{1 - R}{T}\right) \tag{5.10}$$

where d represents the film thickness, R and T represent the reflection and transmission, respectively. The E_g values that were calculated using Eq. 5.9 and 5.10 are almost the same, as depicted in Fig. 5.25. In the following simulations, we used 3.45 eV as the E_g value for the SnO_X layer regardless of film thickness.

Preliminary simulations using SCAPS software

To visualize the band diagram of the PSCs, we conducted a preliminary simulation using the drift-diffusion simulation software SCAPS, inputting the experimentally measured energy levels of all layers. The thickness of perovskite and SnO_X were determined using ellipsometry, the order of magnitude of the effective density of states (DOS) and radiative-recombination coefficient k_{rad} were taken from literature.[5] If indicated the values are taken from literature else, they were determined by measurements or estimation. Detailed parameters of the SCAPS simulations are listed in Table 2 and 3.

The successful convergence in solving Poisson's equations and boundary conditions enabled the acquisition of both the band diagrams and *JV* curves. It is important to note that the conduction band minimum (CBM) of C_{60} has a significant impact on band alignment, influencing the simulation outcomes, including the *FF*. As previously discussed, χ was determined using the valence band maximum (VBM) (6.44 eV) obtained from UPS measurements, as shown in Fig. 5.26(a), and the E_g values from the literature, which range from 1.9 to 2.5 eV [88-91]. This range causes the CBM to shift between 4.54 to 3.94 eV, resulting in, for instance, substantial changes in the potential gap of E_C at the C_{60}/SnO_X (5 nm) interface from a maximum of 470 meV to a minimum of 30 meV. To ensure reliable simulation outcomes, we performed systematic simulations to evaluate the reported E_g values of C_{60}. We compared the *FF* values obtained from simulations using different E_g and χ values with the average *FF* values extracted from the experimental data, as shown in Fig. 5.26(b). The results indicate that an E_g of 2.0 eV for C_{60} is the most reasonable, as it closely aligns with both the absolute value and the trend of *FF* changes as a function of SnO_X thickness, matching real-world observations most accurately. Figure 5.26(c) displays the energy levels of the VBM, CBM, and Fermi energy with the E_{VAC} set to 0 eV for all layers in the PSCs studied in this work. The E_g of 5 nm SnO_X was set to 3.45 eV, matching that of 10 and 15 nm SnO_X to keep E_g constant. It was observed that CBM and Φ remained nearly

Table 2. *Detailed parameters used for the SCPAS simulations.*

parameter	value					
	MeO-2PACz	perovskite	C_{60}	SnO_X		
bandgap E_g (eV)	3.20	1.68	2.00 [92]	3.45		
electron affinity χ (eV)	2.09	4.22	4.44	4.38	4.36	4.07
thickness d (nm)	2	600	15	15	10	5
electron mobility μ_n (cm^2/Vs)	1×10^{-4}	20 [93]	6×10^{-4} [94]	1[95]		
hole mobility μ_p (cm^2/Vs)	1×10^{-1}	20 [93]	1×10^{-4}	1×10^{-4}		
relative dielectric permittivity ε_r	3	30 [96]	3.9	10		
Eff. DOS CB N_C (cm^{-3})	2×10^{18}	2×10^{18} [93]	1×10^{18}	3.51×10^{18} [97]		
Eff. DOS VB N_V (cm^{-3})	2×10^{18}	2×10^{18} [93]	1×10^{18}	1.13×10^{19} [97]		
thermal velocity $v_{th,e} = v_{th,h}$ (cm/s)	1×10^{7}	1×10^{7}	1×10^{7}	1×10^{7}		
radiative recombination coefficient k_{rad} (cm^3/s)	8×10^{-10}	8×10^{-11}	8×10^{-11}	6×10^{-10}		
trap1 energy over VB E_{t1} (eV)		1.52				
trap2 energy over VB E_{t2} (eV)		0.1				
single acceptor/donor defect density (cm^{-3})		1×10^{18}				
Carrier lifetime $\tau_n = \tau_p$ (ns)		1×10^{3}				
doping concentration N_D (cm^{-3})	0	0	0	7.5×10^{10}	7.5×10^{10}	1.6×10^{4}
work function Φ_{ITO} (eV)	5.4					
work function Φ_{Ag} (eV)	4.58					

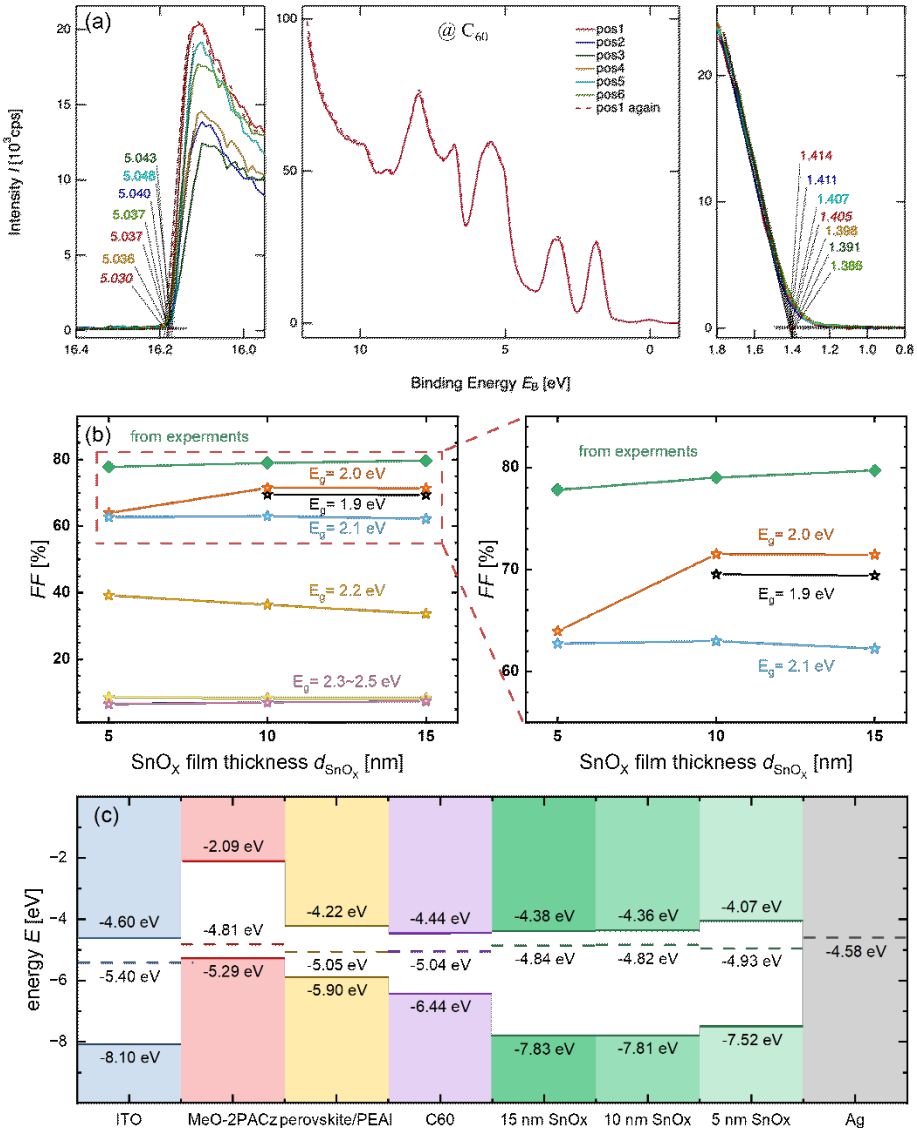

Figure 5.26: *a) UPS for ITO/MeO-2PACz/perovskite/C_{60}. b) Comparison of simulated FF using different bandgaps of C_{60} as a function of the SnO_X film thickness d_{SnOx}. Partial magnified view is inserted. (c) Schematic of energy levels for all layers measured using the UPS.*

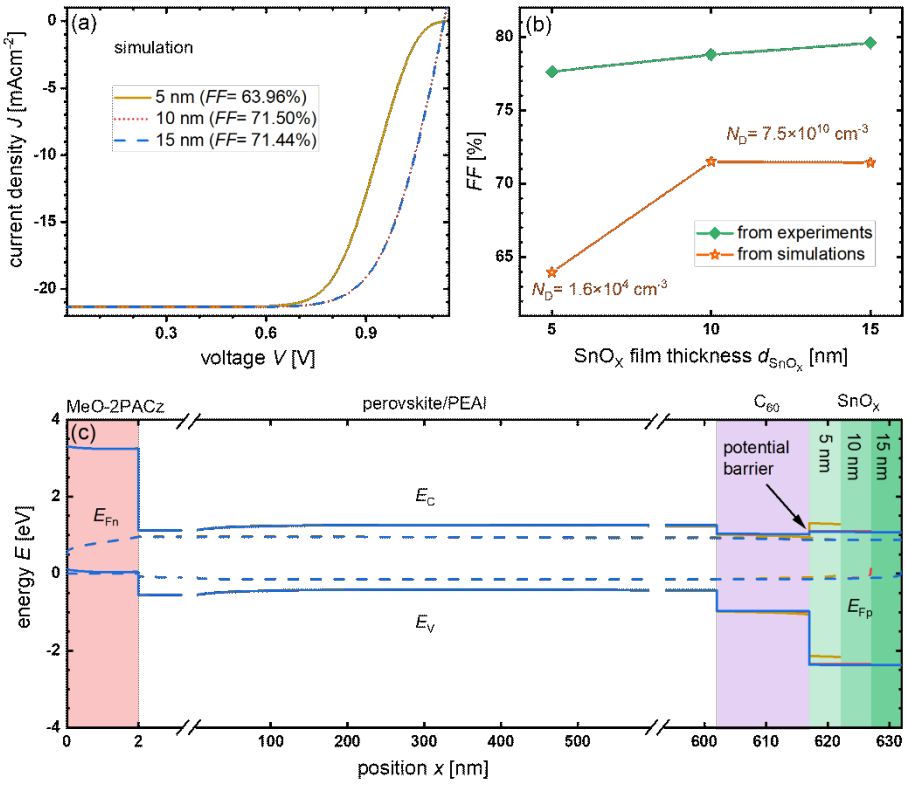

Figure 5.27: a) *Comparison of simulated JV curves with increasing SnO_X film thickness d_{SnOx}. b) Experimentally measured and numerically simulated FF as a function of SnO_X film thickness d_{SnOx}; the doping concentration of SnO_X used in the simulations is indicated for each scenario. c) Comparison of the simulated band diagram of a cell with MeO-2PACz/perovskite/PEAI/C_{60}/SnO_X with increasing SnO_X film thickness d_{SnOx} extracted at the maximum power point.*

unchanged as the SnO_X thickness decreased from 15 to 10 nm. However, when the layer thickness was further reduced to 5 nm, the CBM shifted upwards by 0.29 eV, and the Φ shifted downwards by ~0.11 eV.

In the simulations, Φ was interpreted as the N_D, and the predicted *JV* curves for the three scenarios using the experimentally measured energy levels are shown in Fig. 5.27(a).

For the 10 and 15 nm scenarios, the diode *JV* curves closely matched the experimental results. However, the non-diode *JV* curve observed for the 5 nm scenario suggests band misalignment in the simulation definition, primarily owing to the extremely shallow CBM of the 5 nm SnO_X compared to that of C_{60}. Figure 5.27(c) presents the simulated band diagrams, where we observed a pronounced potential barrier of 370 meV at the C_{60}/SnO_X (5 nm) interface, which hindered the extraction of charge carriers. As a result, the predicted *FF* value was below 70%.

Table 3. *Parameters of various interfaces for drift-diffusion simulations using the software SCAPS.*

parameter	value	
	MeO-2PACz/ perovskite	perovskite/C_{60}
intraband tunneling effective mass of electrons and holes $m_e = m_h$	1	
interface trap energy over VB E_{t1} (eV)	0.6	0.6
defect capture cross section electrons and holes $\sigma_e = \sigma_h$ (cm^2)	1×10^{-21}	5×10^{-20}
interface trap density N (cm^{-2})	1×10^{13}	1×10^{14}
interface recombination velocity S (cm/s)	1×10^{-1}	50

We compared the average *FF* values extracted from both the experiments and simulations as a function of SnO_X film thickness, as shown in Fig. 5.27(b). In the experiments, the average *FF* value increased gradually by approximately 1% with each thickness increment, whereas in the simulations the first 5 nm increment resulted in an 8% improvement in *FF*, attributed to the transition from band misalignment to band alignment. The N_D of SnO_X layer used for the simulations were indicated additionally, which was calculated based on the energy gap between the Φ and χ measured by UPS using following equation

$$\phi = \chi + k_B T \ln\left(\frac{N_C}{N_D}\right) \tag{5.11}$$

where N_C is the effective density of states of the conduction band. When the d_{SnOx} increased from 5 to 10 nm, N_D increased by six orders of magnitude but remained constant with

further increments in thickness, which appears to be contradicting to expectations. Therefore, we employed another method to evaluate the change in Φ with increasing d_{SnOx}.

5.2.4. Corrected simulations

SCLC measurements

SCLC measurements are widely recognized and are mostly used to determine the charge-carrier mobilities of intrinsic and lightly doped semiconductors [98,99]. This measurement relies on the interpretation of the dark *JV* curves of single-carrier devices and electron- or hole-only devices under forward and reverse bias voltages. In a single-junction device, if the contact work functions are asymmetric at both ends, a built-in voltage (V_{BI}) is generated. A simple method has been developed to extract the V_{BI} from SCLC *JV* data based on the Mott-Gurney (MG) law [30,100]. Using the high-voltage assumption of $|V| \gg V_{BI}$, the V_{BI} in an single-carrier device with one semiconductor layer sandwiched between two asymmetric ohmic contacts is given as [98]

$$V_{BI} = \frac{k_B T}{q} \ln\left(\frac{8}{9}\frac{qN_C L^2}{\varepsilon_r \varepsilon_0}\frac{J_f}{J_r}V^{-1}\right) \tag{5.12}$$

where $k_B T$ represents the thermal energy. L is the thickness of the semiconductor layer being probed, in this case, C_{60}. $\varepsilon_r \varepsilon_0$ denotes the permittivity. V is the applied voltage across the devices during the dark *JV* measurement. J_f/J_r is the ratio between the forward and reverse bias currents at the bias voltage.

We fabricated electron-only devices with a simple structure of glass/ITO/ZnO nanoparticles/C_{60}/SnO_X/Ag, in which only electrons dominate transport. Relative SCLC *JV* data were collected for this device, with the d_{SnOx} as the variable while other parameters remained constant. A decisive advantage of SCLC relative to UPS is that SCLC provides an observable current ratio (J_f/J_r) that depends exponentially on the changes in V_{BI}, that is, the changes in Φ. In contrast, the UPS signals exhibit larger error bars that depend linearly on the energy level. The errors in the energy level remain errors in the UPS and mess up the

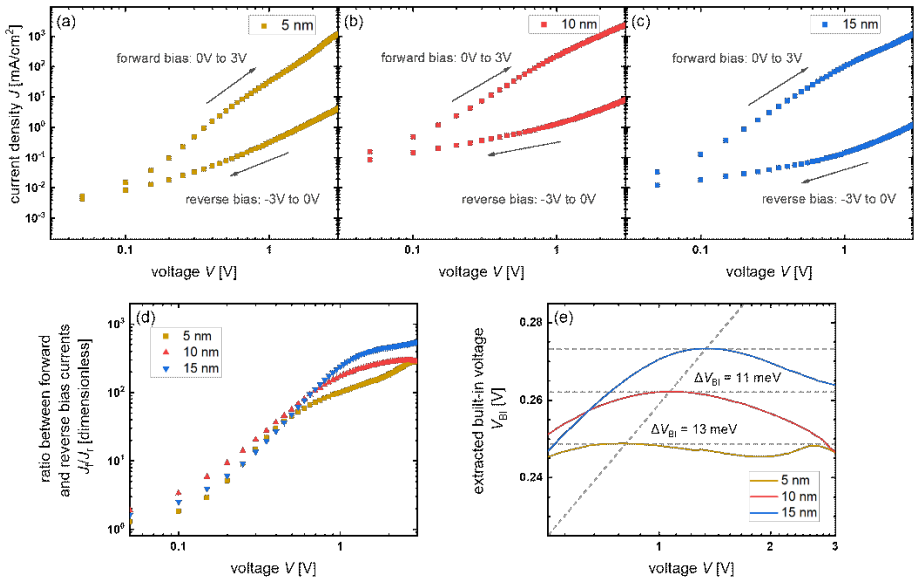

Figure 5.28: *SCLC JV curves of electron-only devices with a)* 5 *nm, b)* 10 *nm, and c)* 15 *nm* SnO_X*. The lower branch is the measurement from* -3 *V to* 0 *V (reverse current) and the upper branch is the measurement from* 0 *V to* 3 *V (forward current) with the same step size of* 0.05 *V. d) Comparison of the ratio between the current densities at forward and reverse bias with increasing* SnO_X *film thickness* d_{SnOx}*. e) Extracted* V_{BI} *values obtained by fitting Eq.* 6.12 *to the ratio of experimentally measured SCLC JV curves.*

result, while in the SCLC, they end up in the $\ln(J_F/J_r)$ and are therefore much less dramatic. Furthermore, SCLC is a measurement inside a device that measures the difference in Φ in a situation where it is relevant, whereas UPS measures the surfaces of layers in vacuum. These surfaces, when part of a complete device, interface with other layers. The layers on top of the targeted surface alter the properties of the surface and corresponding interface to some extent. The only downside of SCLC is that it can only measure relative, not absolute, values of the work function.

The SCLC *JV* curves of the electron-only devices with increasing d_{SnOx} are shown in Fig. 5.28(a-c), which were measured from -3 to 3 V and plotted on double logarithmic axes. The upper branch is the current for positive bias voltages from 0 to 3 V (forward bias), and

the lower branch corresponds to negative bias voltages from -3 to 0 V (reverse bias). We observed that the vertical distance between the two branches increased for thicker SnO_X at a certain applied voltage, suggesting an increase in V_{BI}. Figure 5.28(d) shows a comparison of the ratio between the current densities at forward and reverse bias, where thicker SnO_X brought an increase in J_f/J_r at high voltages of above 1 V. By solving the Eq. 5.12, V_{BI} can be extracted from Fig. 5.28(d), and the results are shown in Fig. 5.28(e). V_{BI} values were determined at a plateau for each curve. When the d_{SnOx} was increased from 5 to 10 nm and from 10 to 15 nm, V_{BI} increased, and the relative shifts (ΔV_{BI}) were 13 and 11 meV, respectively. Because ZnO nanoparticles have a higher Φ than SnO_X, this result demonstrates that the thicker the SnO_X, the closer it is to vacuum (lower Φ). Studies and experimental observations often show the thickness dependence of the work function in oxide semiconductor thin films and metallic films [101,102], which can be attributed to several factors: 1) The morphology and crystallinity of the film can change with thickness. Thicker films tend to have more bulk-like properties, while thinner films might be more amorphous, more susceptible to the properties of underlying films, or have different crystalline orientations, affecting the work function.[103] 2) The crystalline structure and defect density may also vary with film thickness, impacting the work function.[104] 3) In very thin films, Quantum Size Effects (QSE) can alter the electronic band structure when the film thickness approaches the electron's de Broglie wavelength, affecting the work function.[105]

Comparison to corrected simulations

We performed simulations based on the relative shift of Φ, which is equivalent to the ΔV_{BI} extracted from the SCLC *JV* curves, instead of Φ measured by UPS, to re-evaluate the impact of the changes in Φ on *FF* due to thickness variations of SnO_X. First, we treated the *FF* of the device employing 15 nm SnO_X as the starting point and adjusted the N_D in the simulations to ensure that the *FF* reached the same level as the experimental one. With this well-assumed N_D, Φ was calculated by solving Eq. 5.12. Subsequently, Φ for both 5 and 10 nm SnO_X can be determined using the ΔV_{BI} values extracted from the SCLC measurements. Finally, the corresponding N_D values for all scenarios were calculated and used to reperform the simulations. However, when we attempted to overlap the starting points of 15 nm, the predicted *FF* value could not reach the experimental level even if the

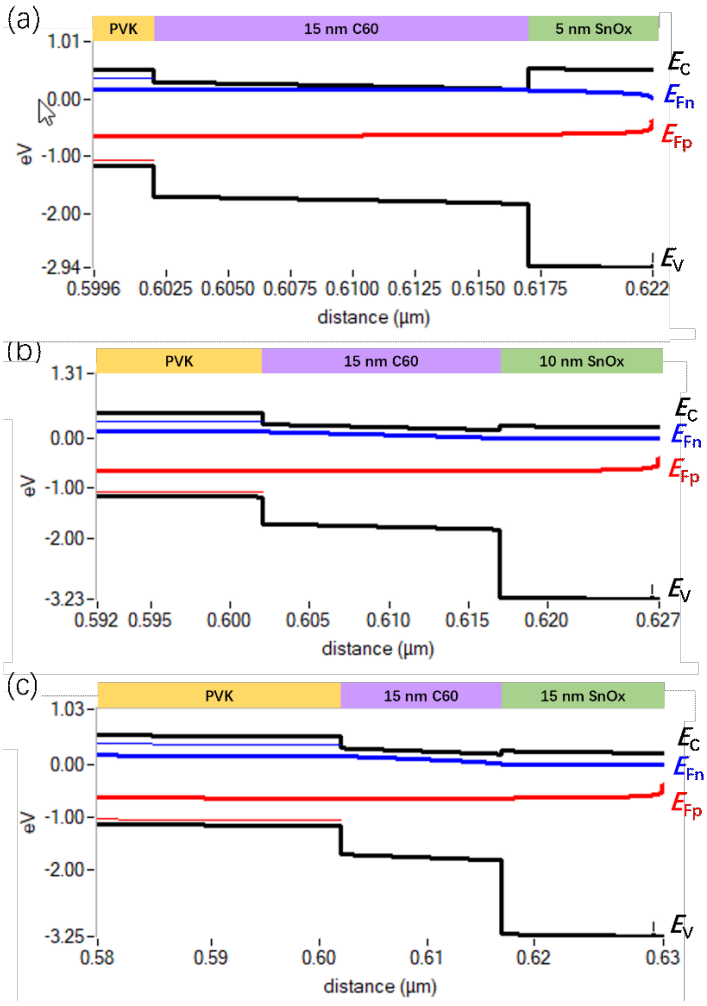

Figure 5.29: *Partial view of the simulated band diagram of a cell with MeO-2PACz/perovskite/PEAI/C_{60}/SnO_X extracted at the maximum power point with SnO_X thicknesses d_{SnOx} of a)* 5 *nm, b)* 10 *nm, and c)* 15 *nm.*

N_D was set as the maximum value of above 2×10^{18} cm^{-3}.For the device using 5 nm SnO_X, the electron Fermi energy (E_{F_n}) (blue line) in the C_{60} layer remained almost the same while

it decreased in the SnO_X layer, as shown in Fig. 5.29(a), suggesting that SnO_X was the main limiting factor for electron transport, and thus the simulation yielded an extremely low *FF* value in preliminary simulations (Sec. 5.2.3). For the devices using 10 and 15 nm SnO_X, the E_{F_n} decreased in the C_{60} layer while remaining constant in the SnO_X layer, as shown in Fig. 5.29(b, c), suggesting that C_{60} turned to be the primary limiting factor for electron transport when thicker SnO_X film was employed.

Carrier transport is essential for the electrical conductivity of a material, and the μ is used to describe how quickly carriers can move through a material in response to an electrical field. Materials with higher μ allow for more efficient carrier transport, leading to higher σ and higher *FF* in solar cells. The relationship between σ and μ is given by the following equation

$$\sigma = n \cdot q \cdot \mu \tag{5.12}$$

where n is the carrier concentration and q is the elementary charge. In preliminary simulations (Sec. 5.2.3), the μ of C_{60} and SnO_X were set to 6×10^{-4} cm^2/Vs and 1 cm^2/Vs, respectively, both of which were the minimum values obtained from literature [106,107]. For the scenarios of 10 and 15 nm, the electron transport is primarily limited by the C_{60} layer because the μ of C_{60} is far smaller than that of SnO_X.

In the corrected simulations, the μ of C_{60} and SnO_X were both set to 2×10^{-3} cm^2/Vs, only d_{SnOx} and N_D were changed for each scenario, and all the other parameters remained constant. In addition, the total R_S of a complete solar cell in the SCAPS software consists of external and internal components, where the external R_S can be set by users on the main panel, however, the internal R_S is embedded within the band diagram, which is affected by a combination of the parameters of all layers, and thus could not be set manually. In the preliminary simulations, the total R_S of 4.5 $\Omega \cdot cm^2$ was experimentally obtained by measuring the J_{SC} and V_{OC} of the perovskite solar cells at different illumination intensities and was input as the external R_S on the main panel of the software. In the corrected simulations, the external R_S was adjusted to a well-assumed value of 1 $\Omega \cdot cm^2$. With all parameters ready, first, we still treated the *FF* of the device employing 15 nm SnO_X as the starting point and adjusted the N_D in the simulations to ensure that the *FF* reached the same

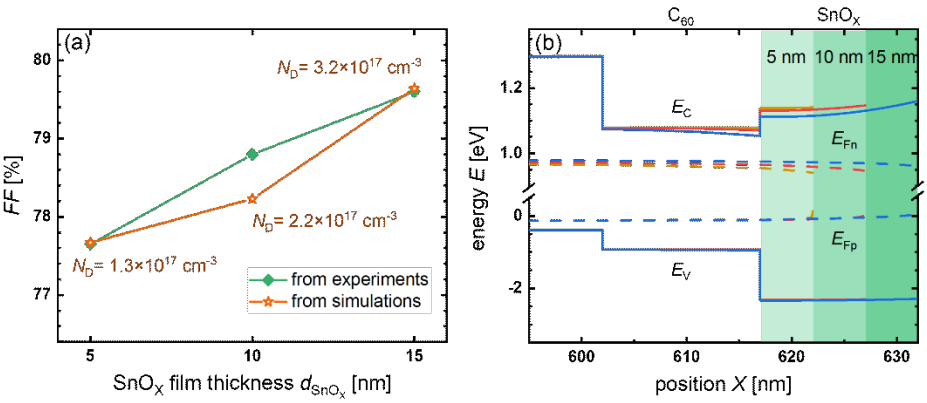

Figure 5.30: *a) Experimentally measured and numerically simulated FF as a function of SnO_X film thickness d_{SnOx}. The doping concentration of SnO_X used in the simulations was calculated using the built-in voltage extracted from the SCLC JV curves, and is indicated for each scenario. b) Partial view of the simulated band diagram of a cell with ITO/MeO-2PACz/perovskite/PEAI/C_{60}/SnO_X/Ag with increasing SnO_X film thickness d_{SnOx} extracted at the maximum power point.*

level as the experimental one. With this well-assumed N_D, Φ was calculated by solving Eq. 5.12. Here, the well-assumed value of N_D for 15 nm SnO_X is 3.2 × 10^{17} cm^{-3} and the value of the corresponding Φ is 4.44 eV. Third, we obtained Φ values of 10 and 5 nm SnO_X by adding the relative ΔV_{BI} to Φ of 15 nm, which were 4.45 and 4.46 eV, respectively. Finally, Φ was interpreted as N_D, 2.2 × 10^{17} cm^{-3} for 10 nm and 1.3 × 10^{17} cm^{-3} for 5 nm, and the calculated N_D values were input into the simulations to extract the *FF*s.

A dotted line plot of the variation in *FF* with d_{SnOx} was drawn to compare the average *FF* values obtained from the experiments with the predicted *FF* values obtained from the corrected simulation, as shown in Fig. 5.30(a). For the 5 nm scenario, the simulated *FF* value overlapped perfectly with the experimental value, whereas a small gap of 0.57% was observed for 10 nm, which could be attributed to the scattering of experimental statistics. Now, our simulation results are in good agreement with the experimental results, and the band diagrams are partially shown in Fig. 5.30(b) for deeper insight. The height of the potential barrier at the C_{60}/ SnO_X interface was 60 meV, irrespective of d_{SnOx}, as χ remained constant in the simulations across all scenarios. The energy gap between the CBM and E_{Fn}

decreased as d_{SnOx} increased, suggesting that a higher density of electrons was present in both C_{60} and SnO_X films. These findings reveal the working mechanism responsible for the enhanced conductivity observed in thicker SnO_X within in the complete device.

Based on the above analysis of V_{OC}, J_{SC} and *FF*, the SnO_X film thickness is likely to influence the recombination rate at a given carrier density at the perovskite/C_{60} interface through the shift of equilibrium Fermi level. Initially, the increase in SnO_X film thickness reduces the work function of bare SnO_X, indicating that the Fermi level in SnO_X shifts up towards the vacuum energy as thickness increases. Subsequently, SnO_X exhibits a significantly lower work function compared to that of bare C_{60}, which moves the Fermi level at the perovskite/C_{60} interface up towards the conduction band of C_{60}. We can assume that recombination at the perovskite/C_{60} interface is dominated by interfacial SRH recombination with a rate $R_{int,SRH}$. The SRH recombination rate is described by a rational function as given by [108]

$$R_{int,SRH}=\frac{np-n_i^2}{n/S_p+p/S_n} \tag{5.13}$$

which produces a maximum recombination rate for a given product *np* of electron (*n*) and hole (*p*) densities on either side of the interface if the capture of electrons from the C_{60} and holes from the perovskite by the interfacial trap is exactly equally likely. This condition can be expressed by the two terms in the denominator of Eq. 5.13 being equal ($n/S_p=p/S_n$) or by saying that the electron and hole capture rates must be equal ($S_n n=S_p p$). Here, S_n is the interfacial recombination velocity of electrons and S_p the interfacial recombination velocity of holes. This condition of avoiding similar capture rates is a fundamental and generic optimization criterion for solar cells [109-111] and is for instance the reason why silicon solar cells benefit from smaller space charge region widths as this minimizes regions with similar electron and hole densities [112]. In this specific situation, we conclude that the shift in Fermi level due to the increase in SnO_x thickness is likely leading to a higher asymmetry in electron and hole densities on either side of the interface and thereby reduces the recombination rate at a given *np*-product without the need to reduce e.g. the interfacial defect density which would directly enter the values of S_n and S_p.

In conclusion, this study elucidates the influence of SnO_X buffer layer thickness on the photovoltaic parameters of single-junction PSCs, providing a valuable reference for comprehending the operational mechanism of SnO_X in perovskite top cells. The variations in V_{OC}, J_{SC}, and *FF* of PSCs have been examined independently as a function of d_{SnOx} utilizing both experimental and simulation methods. The analysis of the PL and $Q_{e,PV}$ results revealed that thicker SnO_X layers, with fully developed physical properties such as conductivity, suppress nonradiative interface recombination in completed devices. Through calculation and comparison of the *FF*, p*FF* and FF_{id}, we found that the increased thickness of SnO_X enhances the *FF* primarily by reducing the R_S of PSCs. This enhancement is attributed to thicker SnO_X film providing both superior conductivity and a more favorable band diagram in the perovskite/C_{60}/SnO_X region. Therefore, thicker SnO_X layers provide an overall enhanced selectivity for the contact for charge carrier collection. To demonstrate the latter point, UPS and SCLC measurements were conducted to construct band diagrams and evaluate the thickness-dependent work function in practical applications. Both methodologies reveal a shift in the work function of SnO_X with variations in the film thickness. Subsequent numerical device simulations demonstrate that the enhanced conductivity of thicker SnO_X films can be attributed to the presence of a higher density of electrons in both C_{60} and SnO_X films, resulting from the reduced energy barrier between the CBM and electron Fermi level, thus elucidating the underlying mechanism responsible for the *FF* improvement. Furthermore, the analysis of V_{OC}, J_{SC} and *FF* demonstrates that the thicker SnO_X films reduce the recombination rate at the perovskite/C_{60} interface due to the shift in Fermi level.

6. Transparent Conductive Oxides Development and Setup Process for Semi-transparent Perovskite Solar Cells

Tandem solar cells are challenging to fabricate due to the stringent performance requirements of subcells and difficult to analyze owing to their complex structures. Consequently, semi-transparent perovskite solar cells are typically fabricated and investigated as a reference to address the corresponding issues associated with the insertion of window stack in perovskite top cells. This chapter primarily focuses on three sections: semi-transparent device fabrication, TCO materials development using magnetron sputtering (Sec. 3.4.2), and investigation of the origin of sputter-induced damage. The majority of the sections pertain to ITO, with only Sec. 6.2.2. relating to IZO, as the IZO target was installed after a year of optimizing semi-transparent perovskite solar cells and investigating the origin of sputtering damage.

6.1. Setup process

Prior to implementing the window stack in perovskite/silicon tandem solar cells, it is customary to apply it to semi-transparent perovskite solar cells to assess potential sputtering damage and evaluate the optoelectrical properties of the window stack. Consequently, semi-transparent devices serve as a crucial reference for the optimization of both TCO films and buffer layers in perovskite top cells.

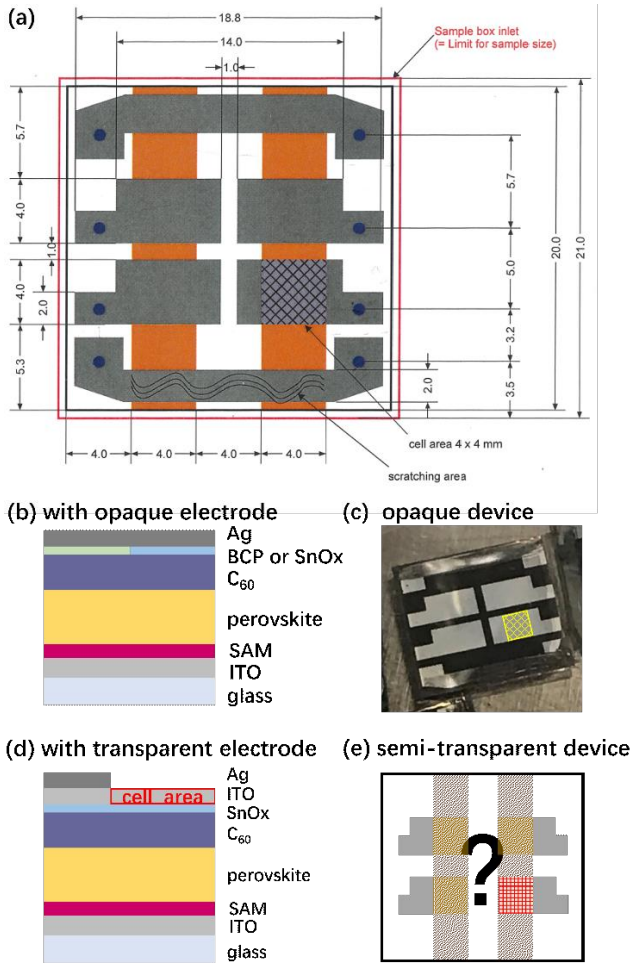

Figure 6.1.: *a) Draft of the perovskite solar cell. b) Cross-sectional configuration and c) top view of the opaque device. d) Cross-sectional configuration and e) top view of the semi-transparent device.*

6.1.1. Device configuration and mask design

In Fig. 6.1(a), the cell area of the opaque PSCs (0.16 cm^2) is determined by the overlap of the ITO films (orange stripes) on the glass substrate and the opaque Ag electrode (grey

patterns) deposited through a precisely patterned deposition mask, and four PSCs can be simultaneously fabricated on the same glass substrate. The cross-sectional schematic and top view of an opaque device ("Structure A or B") are presented in Fig. 6.1(b) and (c), respectively, in which the location of one cell is highlighted in yellow for reference. The distinctions between the configurations of opaque and semi-transparent PSCs include the application of the ITO layer subsequent to SnO_X deposition and the pattern of Ag electrode, as illustrated in Fig. 6.1(d). In Fig. 6.1(e), the active area of the semitransparent device, highlighted in red, is determined by the overlap of the ITO stripes on the glass substrate and the patterned ITO atop the SnO_X, providing insight into the potential appearance of the semitransparent PSCs.

In our lab, four opaque cells with an active area of 0.16 cm^2 were fabricated simultaneously on a 4 cm^2 ITO-coated glass substrate, where the SAM/perovskite/C_{60}/BCP layer stack was prepared from bottom to top to fully cover the substrate. Due to the non-conductivity of the underlying BCP layer, electrical isolation of four devices is achieved by the patterned Ag electrode (Fig. 6.1(a, c)). Regarding the fabrication of semi-transparent devices, the preparation of the SAM/perovskite/C_{60} layer stack should be on full area as well; however, whether the window stack should be prepared on a full area or through a well-patterned deposition mask is an important consideration that should be addressed. When the ITO film is deposited over the entire surface, the patterned Ag electrode can no longer ensure electrical isolation between the four semi-transparent solar cells due to the excellent lateral conductivity of the ITO film. Consequently, the four cells would be connected in parallel, resulting in an exceptionally high J_{SC}. Therefore, a precisely patterned deposition mask must be utilized during the sputtering process of the front-sided ITO. Due to the poor lateral conductivity, the SnO_X buffer layer can be fully or partially deposited on the substrate; consequently, whether to utilize a precisely patterned deposition mask during the ALD process can be decided flexibly, contingent upon the specific experimental operating conditions. To facilitate the comparison between the performance of opaque and semi-transparent devices, I followed the previous design that four cells are prepared on same substrate simultaneously.

The ALD and sputtering systems utilized for depositing the window stack are integrated into the JOSEPH system outside the glovebox under high vacuum, wherein the samples were transferred between different clusters in JOSEPH using a robot without compromising the vacuum. Consequently, mounting the deposition mask to the cells in the glovebox prior to ALD-SnO_X would be more advantageous than mounting it prior to ITO

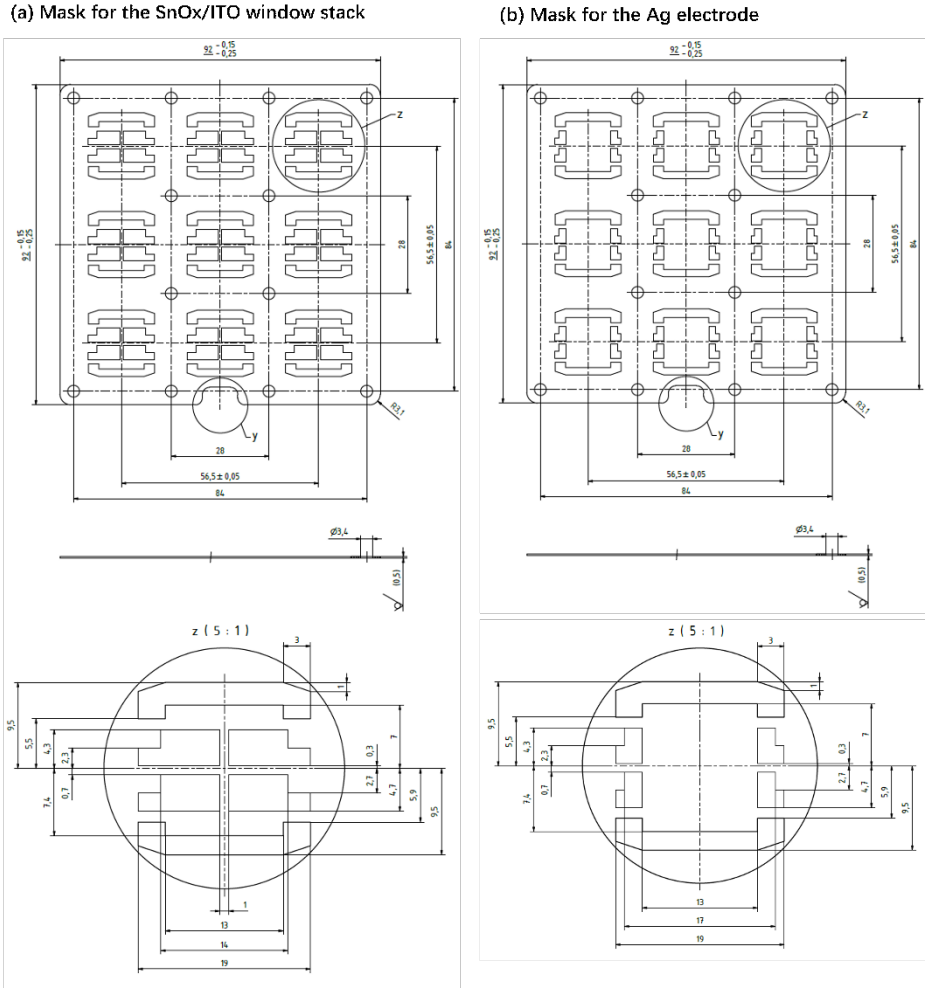

Figure 6.2.: *Drafts of deposition masks for a) SnOx/ITO window stack and b) Ag electrode in semi-transparent perovskite solar cells.*

sputtering. This approach eliminates the necessity to remove the samples from the JOSEPH system after SnO_X deposition, transfer them to the glovebox in ambient air, mount the deposition mask designed for ITO, and transfer them back to JOSEPH in air again for subsequent ITO sputtering. Such a process not only consumes time but also potentially

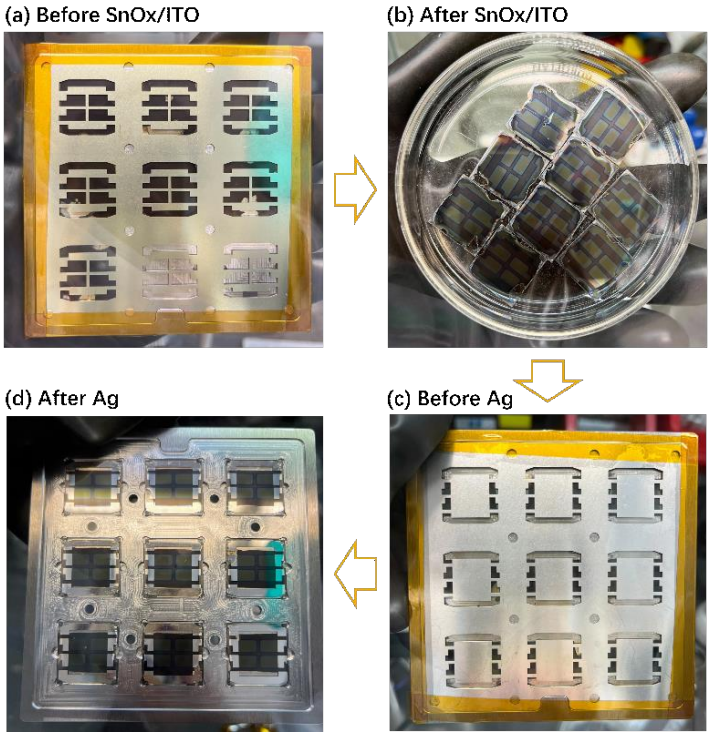

Figure 6.3.: *Images of the fabrication flow of the SnO_X/ITO/Ag stack a) before and b) after the deposition of the SnO_X/ITO stack, and c) before and d) after the evaporation of Ag.*

results in unnecessary contamination at the SnO_X/ITO interface and material degradation during transportation, leading to device performance deterioration. Therefore, the SnO_X and ITO layers were prepared through the same deposition mask, and the schematic was presented in Fig. 6.2(a), which was identical to that used to deposit the opaque Ag electrode. Additionally, a new deposition mask was designed for the Ag electrode in semi-transparent devices to allow for top illumination, which did not cover the cell area but only covered the irregular edge of the window stack, and the schematic was depicted in Fig. 6.2(b).

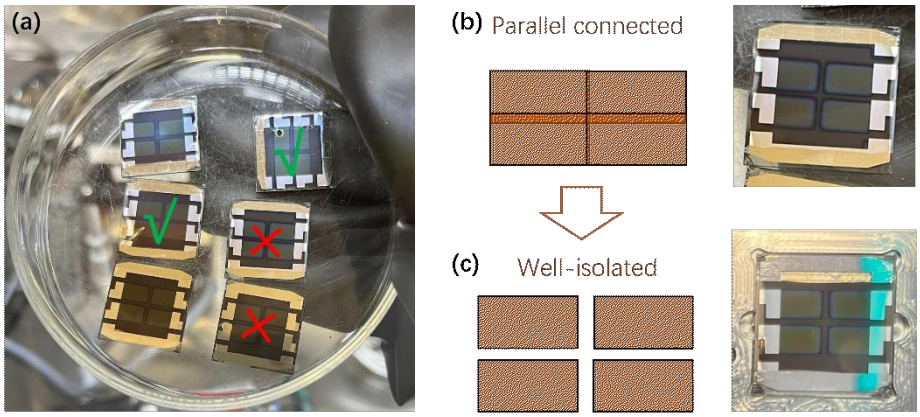

Figure 6.4.: *(a) Images of semi-transparent perovskite solar cells with and without ITO layers overlap. The cross and tick symbols denote parallel-connected and isolated devices, respectively. Schematics and realistic representations of (b) the parallel connection of four cells with indistinct boundaries due to the actual area of the patterned ITO layers exceeding the opening area on the deposition mask, and (c) four well-isolated cells with distinct boundaries.*

6.1.2. Device fabrication

In semi-transparent devices, SAM, perovskite, and C_{60} films are prepared to fully cover the ITO/glass substrate, following a procedure similar to that employed in the fabrication of opaque PSCs. However, two deposition masks are required to obtain the patterned window stack and metal electrode in subsequent steps. Figure 6.3 depicts the alignment of samples with the deposition masks prior to the deposition of the SnO_X/ITO/Ag stack and illustrates the resultant appearance of the patterned films. As shown in Fig. 6.3(d), a small piece of Ag was evaporated at the tail of the patterned ITO film to collect electrons.

During the initial phase of device fabrication, a challenge was encountered wherein the four patterned ITO layers on the same substrate exhibited indistinct boundaries and overlapped with one another, resulting in a parallel connection of four semi-transparent solar cells, as illustrated in Fig. 6.4(a, b). Consequently, an overestimated J_{SC} value of approximately 25–40 mA/cm^2 was obtained from *JV* measurements conducted without an illumination mask. However, J_{SC} was underestimated when an illumination mask was

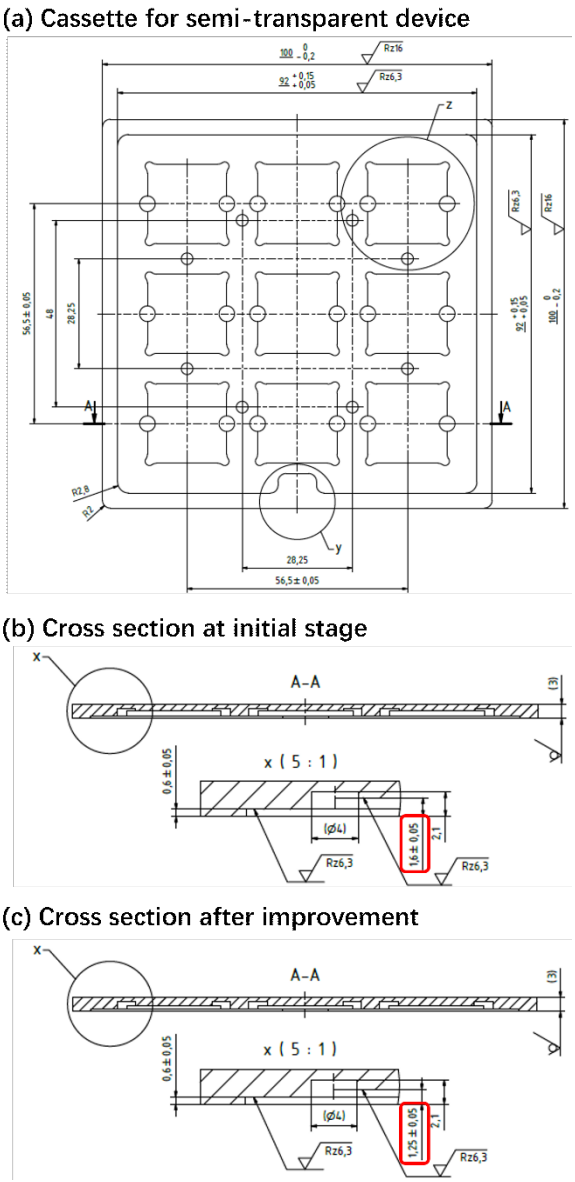

Figure 6.5.: *(a) Drafts of the cassette utilized in conjunction with deposition masks for the fabrication of semi-transparent perovskite solar cells. Cross-sectional schematics of the cassette (a) with an initial depth and (b) with a reduced depth as highlighted in red.*

applied, as the photon-generated electrons migrated from the illuminated cell to adjacent cells in darkness through the overlapped ITO films. To address this issue, it is necessary to physically isolate the four patterned ITO layers on the same substrate, which necessitates improvements in the mask design.

At the initial stage, the depth of the cassette utilized for semi-transparent device preparation was 1±0.05 mm, while the thickness of the glass/ITO substrate was 0.7 mm, indicating a vertical gap of 0.3±0.05 mm between the mask and sample surface. Consequently, the shadowing effect occurs due to the deposition mask not being tightly attached to the sample surface, resulting in the actual area of the patterned ITO layer exceeding that of the opening area defined by the mask. For the preparation of opaque devices, standard (0.7 mm-thick) and thick (1.1 mm-thick) ITO/glass substrates were both used, necessitating a depth of 1±0.05 mm for the cassette. However, the issue arising from continued use of this original cassette in the preparation of semi-transparent devices was not foreseen. Consequently, a minor modification is necessary for the design: the depth of the cassette should be reduced from 1±0.05 to 0.65±0.05 mm, which closely approximates the standard thickness of the substrate, while maintaining the other parameters in the draft, as illustrated in Fig. 6.5. With this improvement in mask design, four patterned ITO layers exhibit distinct boundaries without overlapping, as illustrated in Fig. 6.4(c), demonstrating successful electrical isolation. Consequently, the problem of parallel connection of semi-transparent PSCs was effectively resolved.

6.2. Development of transparent conductive oxides

6.2.1. Tin-doped Indium Oxide (ITO)

To achieve high-efficiency semi-transparent solar cells, we initially designed masks to ensure the fabrication of functional devices. Subsequently, it was necessary to develop the TCO film that meets all the requirements as a crucial component in the window stack, particularly low parasitic absorption and excellent lateral conductivity. In this study, RF magnetron sputtering is utilized to prepare TCO films, and several deposition parameters significantly influence the final optoelectrical properties. However, when multiple characteristics must be considered for material development, achieving a balance between

various factors (e.g., optical and electrical properties) presents a significant challenge, as different types of characteristics are often incompatible with one another. As a conductive oxide material, TCOs have a relatively high density of free carriers (electrons or holes), which is generally accompanied by free carrier absorption (FCA). This phenomenon refers to the interaction of the free carriers in a material with photons in the infrared (IR) and visible regions, in which the electrons absorb energy and become excited to higher energy states, resulting in the absorption of electromagnetic radiation in the corresponding spectrum.

ITO is a tin-doped indium oxide (In_2O_3:Sn), commonly referred to as Indium Tin Oxide, and typically comprises 10 wt.% SnO_2 and 90 wt.% In_2O_3. In_2O_3 is a semiconductor characterized by a wide bandgap and high transparency but exhibits poor conductivity. The incorporation of Sn increases the carrier concentration in In_2O_3 due to its donor effect [113] and oxygen vacancies [114], thereby effectively enhancing the conductivity [115]. However, excessive Sn not only augments the undesirable light absorption of free carriers in the infrared wavelength region, resulting in diminished transparency, but also induces distortions or inhomogeneous distribution of the crystalline structure, ultimately compromising the conductivity and mechanical properties. Extensive material research and experimental findings have demonstrated that 10 wt. % represents the optimal weight ratio to maintain favorable electrical conductivity without significantly impairing optical transparency. In our lab, we utilized In_2O_3/SnO_2 95/5 wt. % at the initial stage, as reduced Sn participation allows for enhanced transparency at the expense of conductivity deficit. For the semi-transparent device, we did not allocate significant resources to reducing the R_S caused by the ITO film through the utilization of the Ag frame and additional Ag grids to decrease the electron travel distance within the ITO films before collection by Ag, which was analogous to the Ag electrode design in tandem devices. This decision was based on the small active area of the semi-transparent device (0.16 cm^2) and the consideration that expending additional energy on this complex electrode design was not necessary for transitional architecture. The primary objective of optimizing ITO in semi-transparent perovskite solar cells should be to mitigate sputtering damage and ensure the proper function of the window stack in the perovskite top cell.

Effect of gas flow ratio

During the sputtering process, Ar, as the working gas, fills the reaction chamber and provides the targeted atoms with energy to be ejected from the solid target. Concurrently, a small amount of O_2 must be incorporated into this process to replenish the oxygen that may be lost during sputtering and to ensure the optimal stoichiometry of the TCO film. In the absence of O_2, ejected metal atoms or oxide molecules may form a suboxide or oxidation state deficit in the film, resulting in the formation of oxygen vacancies. Although oxygen vacancies enhance the electrical conductivity of TCO films due to the increase in carrier concentration, they can significantly impair transparency due to high absorption. Therefore, the addition of a small amount of O_2 can effectively prevent the formation of excessive oxygen vacancies and balance the transparency and conductivity of the film. In our laboratory, diluted O_2 was utilized as the oxygen source instead of pure O_2, which can be attributed to the improved control of the balance between transparency and conductivity. Thus, when referring to O_2 in the sputtering process, it specifically denotes diluted O_2 in Ar with a volume ratio of 1% (Ar/O_2 1%).

The impact of the gas flow ratio (r_{O_2}) on the optoelectrical properties of the ITO films was initially investigated by increasing the Ar/O_2 1% flow rate from 1 to 3 sccm while maintaining the total gas rate constant at 15 sccm, which resulted in a decrease in the Ar flow rate from 14 to 12 sccm. The corresponding r_{O_2} values were calculated to be 6.7% with a gas flow rate of Ar/O_2 1%: Ar = 1:14 sccm, 13% with a gas flow rate of Ar/O_2 1%: Ar = 2:13 sccm, and 20% with a gas flow rate of Ar/O_2 1%: Ar = 3:12 sccm. In Fig. 6.6(a, b), we compare the A and R_{SH} of bare ITO films as a function of r_{O_2} deposited on Corning glass with the same film thickness of 105±5 nm. Theoretically, the presence of a higher fraction of O_2 will lead to an improvement in the film transparency. This is due to two factors: firstly, the formation of metal oxide with an ideal stoichiometry as a result of stronger oxidation effect, which has a lower density of free electrons; secondly, the subsequent formation of insufficient oxygen vacancies also implies a lower density of free carriers because oxygen vacancies act as donors in ITO films and introduce free carriers. Consequently, the reduction in the free carrier density due to an increase in r_{O_2} decreases the parasitic absorption losses of the ITO film at wavelengths above 1000 nm, as shown in Fig. 6.6(a). However, the reduction in the concentration of free carriers due to the increasing r_{O_2} deteriorates the electrical conductivity of the ITO films as R_{SH} increases by approximately 100 Ω/sq, as shown in Fig. 6.6(b).

Effect of working pressure

Increasing the working pressure during the TCOs sputtering process can effectively mitigate the sputtering damage to the fragile underlying layers caused by the bombardment of energetic ions in the plasma. This is due to a higher molecular density of Ar present at elevated working pressures, which results in an increased frequency of collisions between the ejected target atoms or ions and Ar^+, free electrons, and molecules in the plasma. Consequently, the kinetic energy of these particles decreases upon reaching the surface of the substrate. This moderated film deposition mitigates sputtering damage. An additional advantage of reducing the working pressure is the formation of more homogeneous and compact films, as high-energy target atoms or ions result in various structural defects and increased surface roughness. However, a higher frequency of collisions also presents certain disadvantages; for instance, it affects the kinetic energy of Ar^+ as well, suggesting that a lower density of atoms was ejected from the target by less energetic Ar^+, resulting in a decrease in the deposition rate. Furthermore, the TCO films deposited at high pressure exhibit a lower density of free carriers generated by the oxygen vacancies compared to those at low pressure, which benefits transparency but reduces electrical conductivity. Thus, a delicate balance must be considered in this process.

The working pressure (p_{ITO}) during ITO sputtering process was varied from 0.2 to 0.7 Pa in increments of 0.2 Pa to investigate its impact on the optoelectrical properties, while other parameters, such as r_{O_2} and film thickness, remained constant. In Fig. 6.6 (c), the absorption curves of the three scenarios overlap at wavelengths between 300 and 900 nm, and a discrepancy is observed in the infrared spectrum, where parasitic absorption decreases as the pressure increases. Based on the aforementioned discussion, the reduction in A is attributed to the lower density of free carriers. Figure 6.6 (d) illustrates the R_{SH} values as a function of p_{ITO}, in which R_{SH} increases significantly from 1100±100 Ω/sq to 35±5 Ω/sq as the working pressure increases by 0.5 Pa. The y-axis was presented in a logarithmic scale due to variations spanning two orders of magnitude. Although the high-pressure sample exhibited the lowest parasitic absorption losses, the extremely large R_{SH} value exceeding 1000 Ω/sq and potentially sputtering damage indicate that 0.7 Pa would not be an optimal choice for the fabrication of semi-transparent solar cells. From a balanced perspective, the ITO film deposited under an intermediate pressure of 0.5 Pa would be the most suitable option.

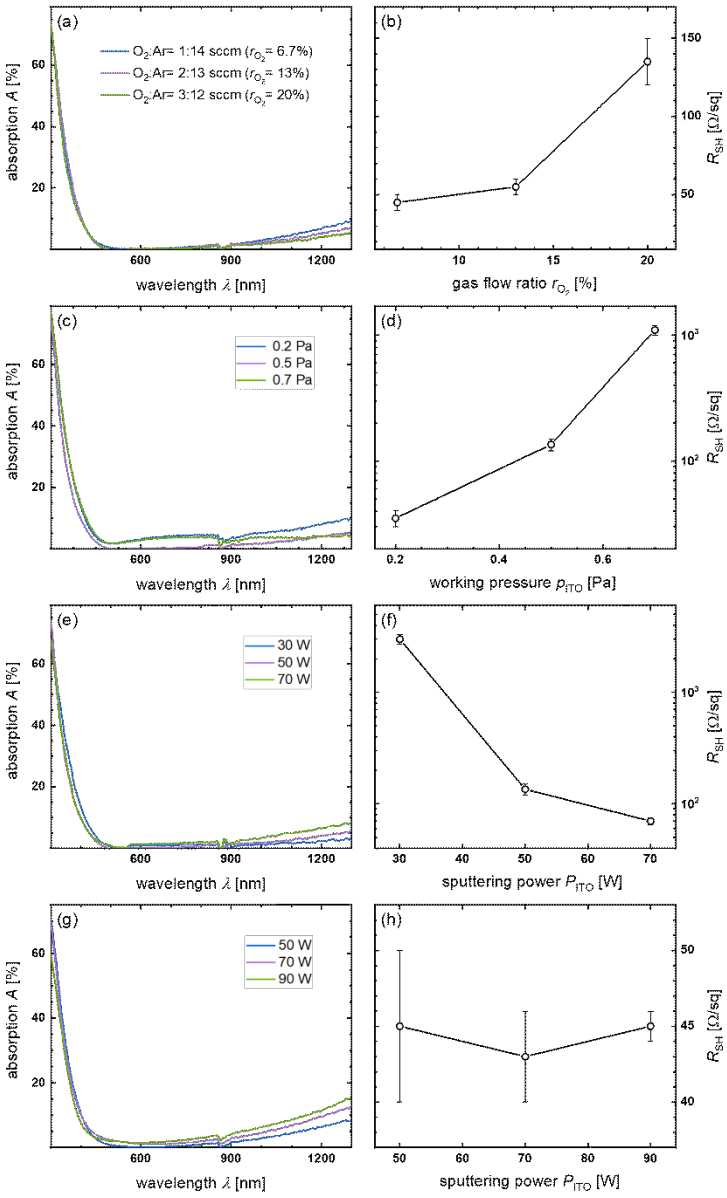

Figure 6.6.: *Absorption and sheet resistance of bare ITO films deposited on Corning glass as a function of (a, b) the gas flow ratio r_{O_2}, (c, d) working pressure p_{ITO}, and (e-h) sputter power P_{ITO}.*

Effect of sputter power

An increase in sputtering power directly correlates with an increase in the applied voltage between the solid target and the substrate. The advantages of elevated sputtering power include enhanced electrical conductivity, which is attributed to a higher carrier concentration, and an increased deposition rate due to a higher density of the ejected target atoms and ions. However, the target atoms and ions acquire greater kinetic energy under high voltage and consequently introduce more substantial sputtering damage to the substrate during film formation due to bombardment on the surface, resulting in increased surface roughness and performance deterioration.

Given that the variation in r_{O_2} between 6.7% and 20% does not significantly affect the optoelectrical properties of the ITO films (Fig. 6.6(a, b)), an investigation into the effect of sputtering power (P_{ITO}) on two cases of either low or high ratio r_{O_2} was conducted. In the first batch of optimization, the P_{ITO} was increased from 30 to 70 W in increments of 20 W with a low r_{O_2} of 6.7%, and the corresponding optoelectrical results are presented in Fig. 6.6 (e, f). It was observed that parasitic absorption, particularly at long wavelengths (900-1300 nm), increased as the P_{ITO} increased. However, the ITO film deposited at 30 W exhibited the lowest absorption but an extremely large R_{SH} of approximately 3000 Ω/sq, which was inadequate for an ideal transparent electrode. The conductivity of the ITO film deposited at a high P_{ITO} of 70 W was optimal with a small R_{SH} of 70±5 Ω/sq, but its optical characteristic was inferior to that of the ITO deposited at 50 W, whose R_{SH} value of 100 Ω/sq was also acceptable for an ideal transparent electrode. Consequently, 50 W was determined to be the optimal P_{ITO} rather than 70 W, considering the comparable optoelectrical properties and moderate potential sputtering damage. In the second batch of optimization, r_{O_2} was set to 20% and 50 W was used as the initial P_{ITO} because the R_{SH} of the ITO film increased by 30 times as the sputtering power decreased from 50 to 30 W in the previous case. The P_{ITO} was increased from 50 to 90 W in increments of 20 W, and the optoelectrical characteristics of the ITO films as a function of the P_{ITO} are illustrated in Fig. 6.6(g, h). A regular change in parasitic absorption was observed, while an increase in P_{ITO} did not further improve the lateral conductivity, suggesting an optimum P_{ITO} of 50 W due to its good conductivity, low absorption, and minimal sputtering damage.

Effect of pre-heating temperature

In the fabrication chain of SHJ solar cells, the pre-heating temperature (T_{ITO}) during the ITO sputtering process is typically set to 150 °C to form a crystallized film. Given that the perovskite film can scarcely withstand temperatures above 100 °C, the temperature must be carefully controlled within 100 °C during the fabrication process of the perovskite top cell, suggesting that the ITO film deposited at such a low temperature should be amorphous. Consequently, this study focused on comparing the optoelectrical properties of the bare ITO films deposited at 40±2 ℃ and room temperature (22±2 ℃) without extensive temperature optimization. The A, R_{SH}, n_{ref}, and κ were measured; however, the difference was not significant, with the exception of a slight increase in the R_{SH} of approximately 20 Ω/sq at room temperature. Furthermore, room-temperature sputtering offers advantages in terms of time and thermal energy conservation.

6.2.2. Zinc-doped Indium Oxide (IZO)

IZO is a zinc-doped indium oxide (In_2O_3:Zn), commonly referred to as Indium Zinc Oxide. The IZO target typically comprises 10 wt.% ZnO and 90 wt.% In_2O_3, which is precisely the weight ratio utilized in this study and was installed subsequent to the ITO target in our laboratory. IZO films demonstrate superior optoelectrical properties compared to ITO films for two primary reasons. Firstly, the electron mobility within IZO is higher due to the incorporation of Zn, which enhances the crystal structure and reduces electron scattering. This increased mobility enables IZO films to maintain excellent conductivity even at lower carrier concentrations. Secondly, the optical absorption losses in the infrared spectrum are diminished owing to the lower density of free carriers. Consequently, IZO films frequently exhibit improved electrical conductivity without compromising transparency.

IZO films were initially deposited utilizing the same sputtering parameters as the optimal ITO film. The A and n_{ref} of 110±5 nm-thick IZO films were measured and plotted alongside that of the ITO film, as illustrated in Fig. 6.7. A comparative analysis of electrical properties, including R_{SH} and additional electrical parameters (e.g. carrier concentration, electron mobility, and resistivity) obtained through Hall measurements, was conducted between the ITO and IZO films, as presented in Table 1. The results demonstrate that the IZO film exhibits lower parasitic absorption loss at wavelengths exceeding 400 nm,

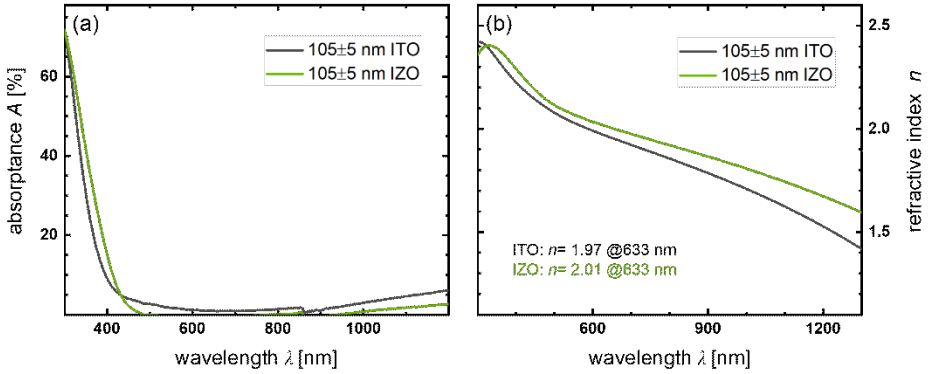

Figure 6.7.: *Comparison between a) absorptance and b) refractive index of bare ITO and IZO films deposited on Corning glass using the same sputter parameters.*

attributable to a reduced carrier concentration of 3.83×10^{20} cm^{-3} compared to that of ITO at 5.01×10^{20} cm^{-3}, which effectively diminished the FCA. Due to the increase in electron mobility from 29.8 cm^2/Vs (ITO) to 42.8 cm^2/Vs (IZO), the reduction in carrier concentration does not result in an increase in the R_{SH} of IZO, which remains low (38±5 Ω/sq) and comparable to that of ITO (40±5 Ω/sq) at the same film thickness. In conclusion, the substitution of ITO film with IZO film effectively reduces the absorption loss across nearly the entire wavelength range without compromising electrical conductivity, owing to higher mobility. The sole disadvantage observed was a decrease in the deposition rate from 3.1 to 2.2 nm/min.

Table 1. *Comparison of electrical properties between bare ITO and IZO films deposited on Corning glass using the same sputter parameters.*

Material properties	Bias voltage [V]	Deposition rate [nm/min]	Sheet resistance [Ω/sq]	Mobility [cm^2/Vs]	Carrier concentration [10^{20} cm^{-3}]	Resistivity [10^{-4} Ωcm]
ITO	84±1	3.1±0.14	40±5	29.8	5.01	4.2
IZO	80±1	2.2±0.11	38±5	42.8	3.83	3.8

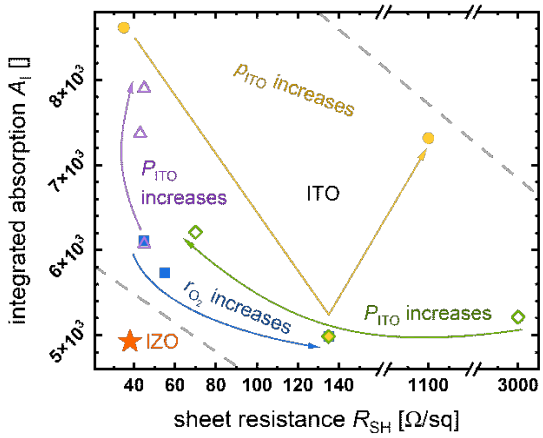

Figure 6.8.: *Optoelectrical properties of ITO and IZO films.*

Figure 6.8 illustrates the relationship between R_{SH} and integrated absorption (A_I) for the ITO and IZO films as a function of sputtering parameters. The arrows indicate the increases of r_{O_2}, p_{ITO} and P_{ITO}. For ITO films, the A_I decreases while R_{SH} increases as r_{O_2} increases (full square symbol); with increasing P_{ITO}, the A_I increases and R_{SH} either remains constant or decreases (open triangle/square symbol); upon higher p_{ITO}, the A_I initially decreases and subsequently increases, whereas the R_{SH} continuously increases (full circle symbol). It is noteworthy that the IZO film demonstrates both the lowest parasitic absorption loss and electrical transport loss in comparison to the optimum ITO film.

6.3. Mitigation of sputter-induced damage

When PSCs with an inverted structure (p-i-n) are applied as the top cells in perovskite/silicon tandem solar cells, the HTL, perovskite layer, ETL, and transparent electrode are fabricated sequentially on the silicon bottom cells. TCOs have been widely used as transparent electrodes in numerous optoelectronic devices including perovskite/silicon tandem solar cells. A significant concern regarding the application of TCOs is that the sputtering process tends to damage the underlying organic layers,

particularly the perovskite layer [52,116]. Regarding the concern of performance deterioration, various strategies have been developed to minimize or even completely mitigate the sputtering damage, such as inserting buffer layer [117,118], using a soft sputtering deposition by lowering sputter power density [119], or adopting pulsed laser deposition as an alternative technique [120]. Although a soft sputtering process holds promise for minimizing sputtering damage, our investigation on the optoelectrical properties of ITO revealed that decreasing the P_{ITO} from 50 W to 30 W led to a dramatic increase in the R_{SH} from 40 Ω/sq to 2000 Ω/sq, resulting in a significant series resistance loss and ultimately deteriorating device performance. Therefore, a holistic evaluation, balancing considerations of sputtering damage with the intricate balance of optical and electrical properties of TCOs, is necessary, especially for their application in perovskite/silicon tandem solar cells.

The use of a SnO_X buffer layer is a well-known approach to avoid sputtering damage [121,122]. Instead of optimizing the window stack in tandem solar cells, it was initially optimized in semi-transparent perovskite solar cells as a reference for addressing the corresponding issues in perovskite top cells caused by the insertion of TCOs. In Chapter 5, the window layers were decoupled using a transitional "Structure B" (Fig. 5.7), and the potential issues related to the insertion of the SnO_X film and the presence of the adjacent C_{60}/SnO_X interface were effectively addressed to provide a reliable optimization environment for the subsequent ITO layer (Fig. 5.11(f)). Consequently, only four issues caused by the ITO insertion need to be considered: (1) sputtering damage, (2) electrical losses caused by electron transport within ITO, (3) parasitic absorption, and (4) electrical losses due to the contact resistivity at the SnO_X/ITO interface. Among these, the absence of sputtering damage is the most critical prerequisite for the preparation of high-efficiency perovskite/silicon tandem solar cells. Therefore, we systematically investigated the sputter-damage-dependent S-shaped current-voltage characteristics, the effective methods for damage mitigation, and the origin of sputtering damage, which can guide the optimization of the sputtering process and selection of appropriate buffer layers for tandem devices.

Initially, a semi-transparent perovskite solar cell was fabricated without an SnO_X buffer layer, resulting in an efficiency below 7% with the presence of a pronounced S-shape, as illustrated in Fig. 6.9(b), indicating a large R_S and low R_{SH}. Subsequently, an SnO_X buffer layer was incorporated with a film thickness of 8 nm, equivalent to the typical thickness for BCP layer utilized in opaque PSCs. The insertion of SnO_X led to the complete

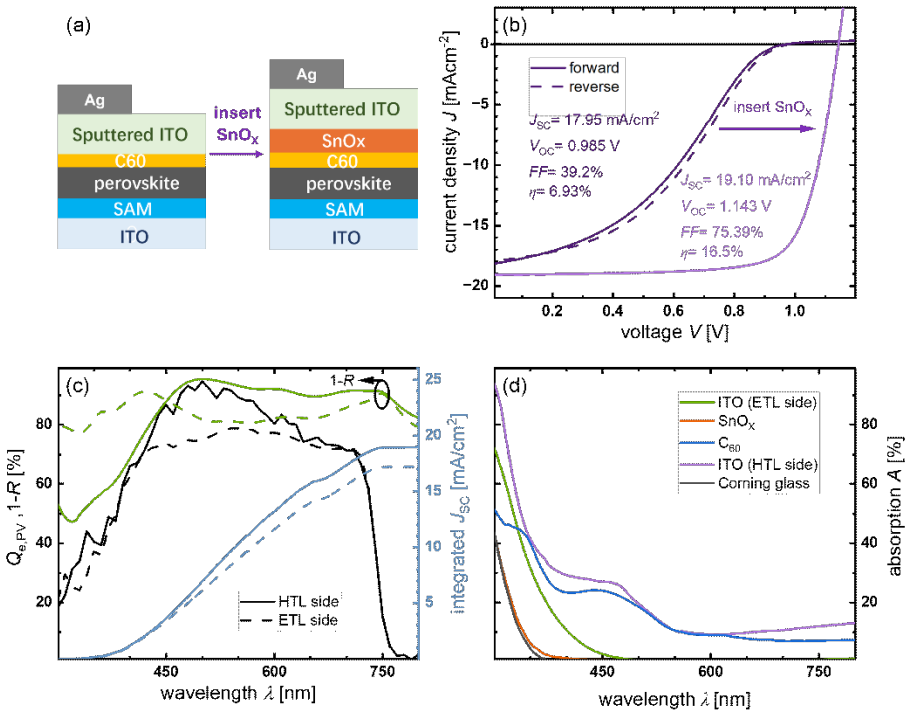

Figure 6.9.: *(a) Schematic of the semi-transparent perovskite solar cells before and after the insertion of* 8 *nm* SnO_X *buffer layer. (b) Comparison of the JV curves of representative semi-transparent perovskite solar cells without and with* 8 *nm* SnO_X *buffer layer. (c)* $Q_{e,PV}$ *spectra, 1 - reflectance, and integrated* J_{SC} *of the semi-transparent device with* 8 *nm* SnO_X *upon dual-side illumination. (d) Absorptance of the corning glass and the bare* C_{60}*,* SnO_X*, and ITO films deposited on corning glass.*

elimination of the S-shape and a significant increase in the *FF* from 39.20% to 75.39%, with additional improvements observed in J_{SC} and V_{OC}. These findings demonstrate that the SnO_X buffer layer is crucial for mitigating sputtering damage. Consequently, we examined the performance of semi-transparent perovskite solar cells as a function of d_{SnOx}.

Prior to thickness optimization, the influence of the C_{60}/SnO_X/ITO layer stack on J_{SC} was evaluated through $Q_{e,PV}$ and reflection measurements. The $Q_{e,PV}$ and 1-*R* of the

representative semi-transparent device with 8 nm SnO_X were measured upon dual side illumination, as shown in Fig. 6.9(c), wherein the integrated J_{SC} values corresponded well with the values extracted from the *JV* measurement. Although the reflection losses were lower upon illumination at the ETL side due to a smaller 1-*R* at wavelengths below 450 nm, the parasitic absorption losses that determined the vertical gap between the 1-*R* and $Q_{e,PV}$ spectra increased significantly compared to that of the measurement from the HTL side. This increase can be primarily attributed to an extremely high parasitic absorption of the thick C_{60} layer at short wavelengths, as shown in Fig. 6.9(d). When measured from the HTL side, the value of 1-*R* was lower than 60% at wavelengths below 400 nm, which could be primarily attributed to the reflection losses at the air/glass and ITO/SAM/perovskite interfaces, whereas the reflection loss was considerably lower when measured from the opposite side. Owing to a much lower parasitic absorption of the ITO and SAM on the HTL side at short wavelengths than that of the C_{60}/SnO_X/ITO layer stack close to the ETL side, no significant difference was present in the final $Q_{e,PV}$ spectra upon dual side illumination at wavelengths below 450 nm. However, the $Q_{e,PV}$ spectra measured from the ETL side at the wavelengths of 450-700 nm were much lower than that of its counterpart due to an increase in the reflection losses, which originated from a high reflectance of the ITO film on the ETL side at certain wavelengths. When measured from the ETL side, the parasitic absorption loss within the wavelength range of 450-550 nm decreased to almost zero owing to a reduced *A* of bare C_{60} film. Once the wavelength exceeded 550 nm, the parasitic absorption losses upon dual side illumination increased continuously. Consequently, the combined effect of the reflection and absorption losses resulted in a J_{SC} loss of approximately 1 mA/cm^2 with the illumination direction shifting from HTL to ETL side.

To determine the optimal thickness of buffer layer, the J_{SC}, V_{OC}, *FF*, and η statistics of the semi-transparent perovskite solar cells were investigated as a function of d_{SnOx}, as illustrated in Fig. 6.10(a-d). It should be noted that the *JV* measurement was conducted from the HTL side to exclude the additional impact of the layer stack on the opposite side. In Fig. 6.10(a), η increased as d_{SnOx} increased before reaching a maximum value at 15 nm; further increase demonstrated negligible influence on the cell performance. In conjunction with the working mechanism of SnO_X in PSCs (Chap. 5), the optimal thickness of 15 nm can be attributed to several factors: 1) suppression of nonradiative recombination at the ETL-sided interfaces, 2) a reduced series resistance due to a higher density of electrons within the thick SnO_X layer, and 3) a robust buffer effect against ion bombardment during the ITO sputtering

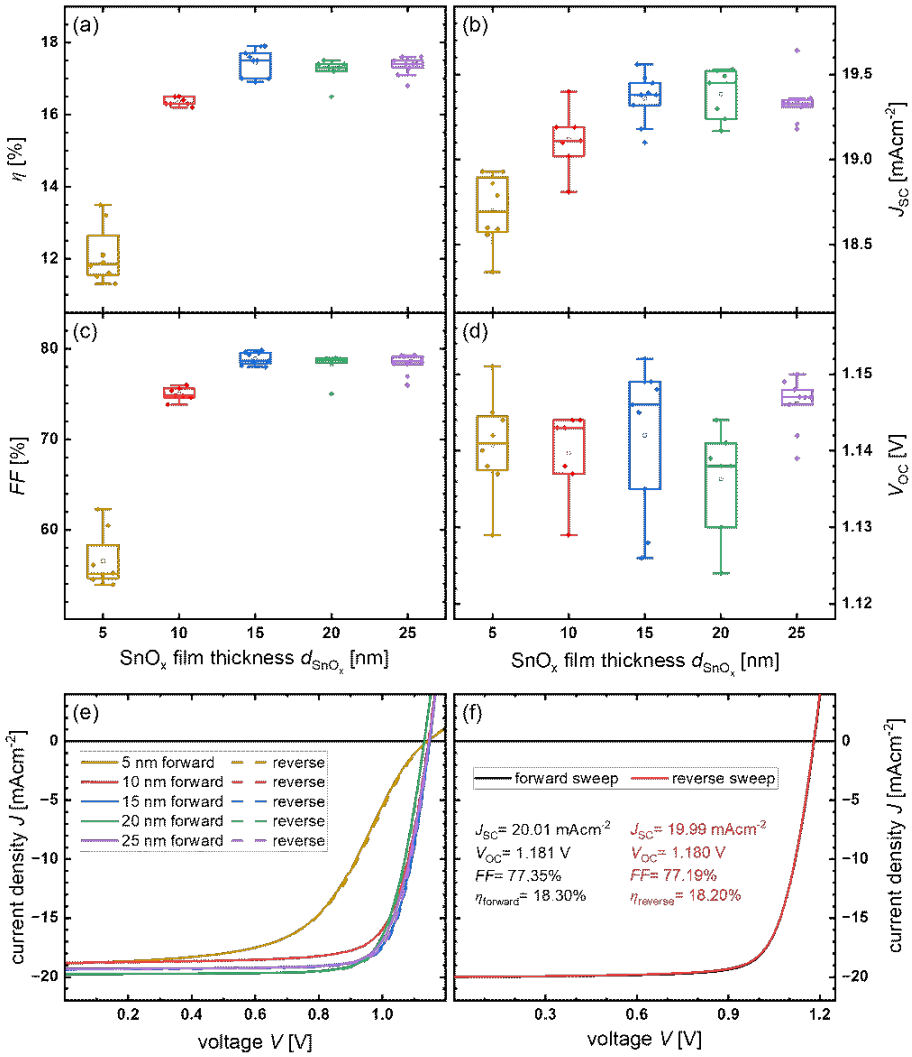

Figure 6.10.: *(a) η, (b) J_{SC}, (c) FF, and (d) V_{OC} statistics of semi-transparent perovskite solar cells as a function of SnO_X film thickness d_{SnOx}. JV curves of (e) the representative semi-transparent perovskite solar cells with increasing SnO_X film thickness d_{SnOx} and (f) with a champion efficiency.*

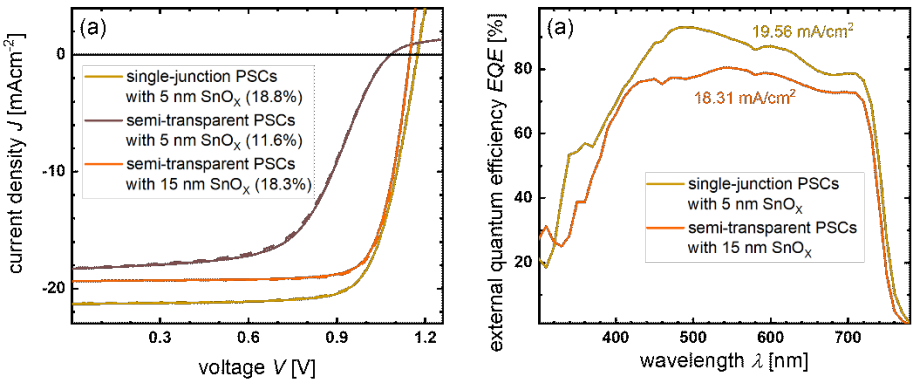

Figure 6.11.: *Current density-voltage (JV) curves and $Q_{e,PV}$ of single-junction and semi-transparent perovskite solar cells with SnO_X buffer layers. Solid and dashed lines represent the forward and reverse sweeps, respectively.*

process. Consequently, a maximum efficiency of 18.3% was achieved for the semi-transparent PSCs, as demonstrated in Fig. 6.10(f), indicating a successful development of the window stack that met the criteria for high-efficiency perovskite/silicon tandem solar cell fabrication.

Sputtering damage can be readily observed in the *JV* curve of a complete device, manifesting in an S-shaped manner. In comparison to the performance of the semi-transparent device without a buffer layer (Fig. 6.9(b)), the incorporation of a 5 nm SnO_X buffer layer resulted in a twofold increase in η; however, pronounced S-shaped *JV* curves were still evident, as illustrated in Fig. 6.10(e). As the thickness increased further, the S-shape completely disappeared. To investigate this phenomenon, opaque PSCs were fabricated with a distinct device architecture of glass/ITO/SAM/perovskite/C_{60}/SnO_X/Ag, incorporating a 5 nm thick SnO_X buffer layer. The performance of a representative opaque device was analyzed in conjunction with that of semi-transparent counterparts, which employed both 5 nm and 15 nm SnO_X buffer layers. Figure 6.11 presents the *JV* curves and corresponding $Q_{e,PV}$ spectra derived from the representative opaque and semi-transparent devices. With a 15 nm thick SnO_X buffer layer, the opaque PSC exhibited an η of 18.8% with an ideal diode shape, while a pronounced S-shape was observed in the semi-transparent counterpart, accompanied by a lower η of 11.6%. These findings strongly suggest that the

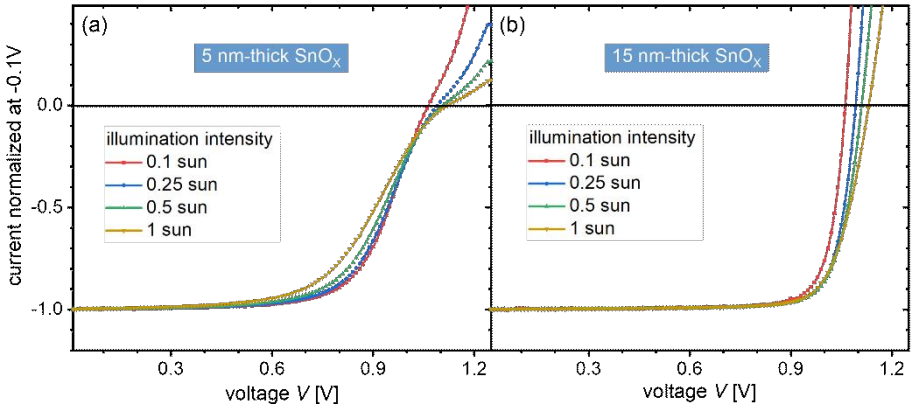

Figure 6.12.: *JV curves at several illumination intensities, from* 0.1 *to* 1 *sun, normalized at* -0.1 *V, for a) semi-transparent perovskite solar cells with a* 5 *nm-thick SnO_X film and b) with a* 15 *nm-thick SnO_X film. We adapted the method based on the analyses of current–voltage data as a function of illumination intensity to reveal the origin of the S-shape [123].*

S-shape is primarily attributable to sputtering damage rather than variations in band alignment resulting from the insertion of the SnO_X buffer layer.

The emergence of S-shapes in the *JV* characteristics is commonly attributed to energetic barriers at the contacts [47,52,123,124] for several reasons, such as insulating interfaces [123], imbalanced charge transport [125], unfavorable energetic alignment [126], and Fermi-level pinning by interface states [127]. We adapted the method described in Ref. 61 to reveal the origin of the S-shape. A semi-transparent device with a 5 nm-thick SnO_X film, exhibiting a pronounced S-shaped *JV* curve, was subjected to illumination across intensities ranging from 0.1 to 1 sun. In Fig. 6.12(a), the obtained *JV* curves were normalized at -0.1 V, where the current was saturated. V_{OC} increased as the illumination intensity increased, and the curves crossed near the X-axis, suggesting the presence of an extraction barrier for electrons. For comparison, the same method was applied to a semi-transparent device with a 15 nm-thick SnO_X film, revealing a markedly reduced crossing in the non-S-shaped *JV* curves at various light intensities, as shown in Fig. 6.12(b). Therefore, the presence of an extraction barrier at the SnO_X/ITO interface is the reason for the S-shape observed in the *JV* curve of the semi-transparent device with a 5 nm-thick SnO_X film, likely stemming from band alignment issues at the interface. By increasing the SnO_X thickness to

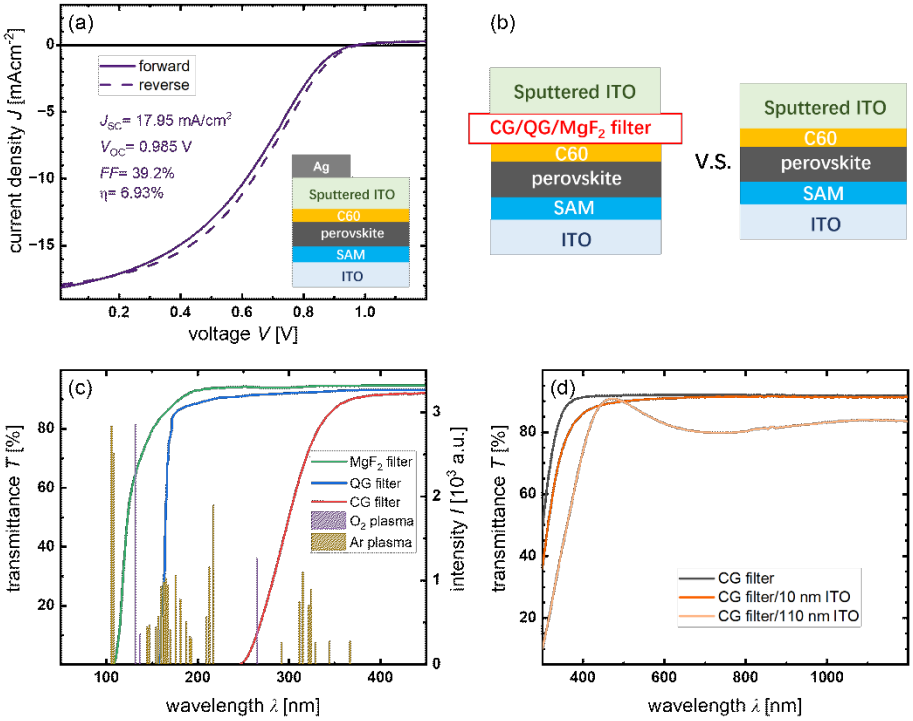

Figure 6.13.: *(a) JV curves of the semitransparent perovskite solar cells without SnO_X buffer layer. The sketch of device is inserted. (b) Sketches of samples with and without optical filters. (c) Transmittance spectra of three filters and the optical emission spectrum of oxygen/argon plasma [128]. (d) Transmittance of bare and ITO-covered CG filters.*

15 nm, the S-shape disappeared, resulting in a significant enhancement of the J_{SC}, V_{OC}, and *FF* of the semi-transparent PSC. The reasons for this remarkable improvement were addressed in the subsequent section.

6.4. Origin of sputtering damage during ITO deposition

Sputtering damage significantly impairs the performance of semi-transparent PSCs, as illustrated in Fig. 6.13(a), consequently reducing the efficiency of perovskite/silicon tandem

solar cells. The conventional understanding of the origin of sputtering damage is attributed to high-kinetic-energy ion bombardment and/or plasma radiation generated during sputtering [129-131]. Zanoni et al. reported that the accelerated particles, together with side effects such as plasma radiation and process-induced heat, can easily damage soft organic semiconductor layers, resulting in leakage currents, efficiency deterioration and lifetime degradation [129]. Mariotti et al. have revealed that the plasma UV radiation during sputtering has a negative impact on the path length of particles and the kinetic energy of hitting substrate [131]. However, two critical issues have been overlooked. First, previous investigations did not address the structural alterations in sputtering-prone layers, including defects, lattice strain, and chemical bonds within films or on their surfaces [132-134]. Second, although considerable attention has been directed towards the combined effects of ion bombardment and plasma radiation, the distinct influence of each factor on films, stacks, and devices remains largely unexplored. To address this gap, we utilized various optical filters to decouple ion bombardment and plasma radiation, allowing us to investigate their individual effects on bare films, layer stacks, and complete devices. Our methodology aims to shed light on the factors causing sputtering damage in perovskite-related devices and the resulting structural changes in susceptible layers. This research will not only help us understand the mechanisms underlying performance deterioration during TCO sputtering but also guide the optimization of the sputtering process and the selection of appropriate buffer layers prior to the fabrication of transparent electrodes.

6.4.1. Decouple plasma radiation and ion bombardment

First, we decoupled the possible sources of sputtering damage during ITO deposition through two experiments: 1) covering the samples using an optical filter with a specific cutoff wavelength in transmittance and 2) exposing the samples directly to the plasma. Sketches of the samples are shown in Fig. 6.13(b). An optical filter is the key tool for decoupling plasma radiation and ion bombardment, allowing us to investigate their individual impacts and shed light on the factors causing sputtering damage; however, it cannot be used as a buffer layer to mitigate the damage. During the ITO sputtering process, the shielded samples were only accessible to oxygen/argon plasma radiation, because the filters blocked the bombardment of ions and other particles. In contrast, samples that were not covered with a filter were exposed to the entire sputtering process, including plasma

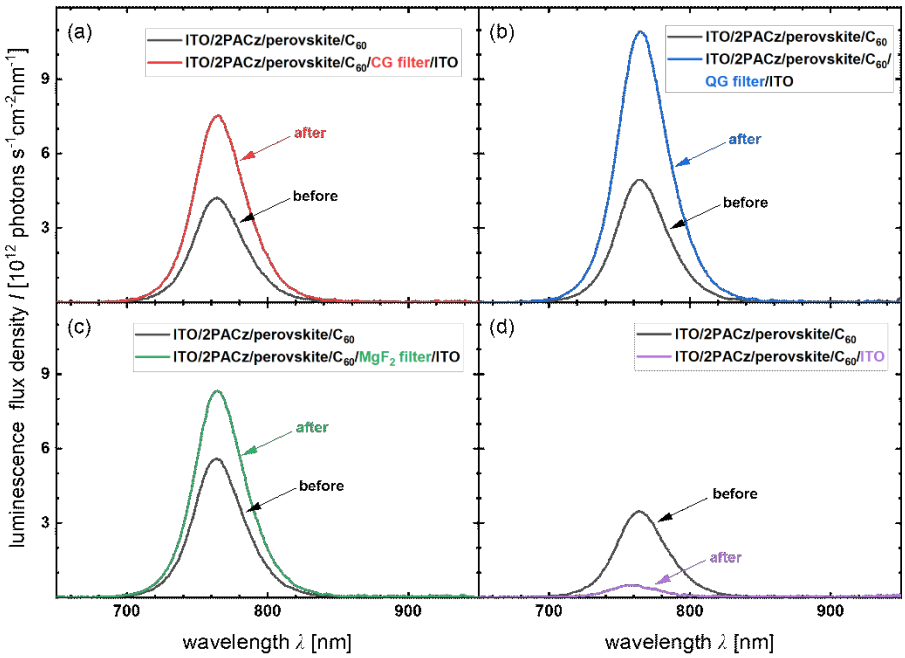

Figure 6.14.: *PL spectra of stacks shielded by (a) corning glass (CG), (b) quartz glass (QG), (c) magnesium fluoride-coated glass (MgF_2), and (d) without filter before and after ITO sputtering.*

radiation and high-kinetic-energy ion bombardment. Therefore, we distinguished between the effects of plasma radiation and ion bombardment on the glass/ITO/2PACz/perovskite/C_{60} stack during ITO sputtering, where 2PACz and C_{60} acted as the HTL and ETL, respectively, by comparing the results from samples with and without filter covering. Three optical filters were utilized: corning glass (CG), quartz glass (QG), and magnesium fluoride-coated glass (MgF_2). The transmittance curves of these filters and the optical emission spectra of oxygen and argon plasmas generated during sputtering are shown in Fig. 6.13(c). The CG filter allows photon transmission with wavelengths above 250 nm, which enables approximately 10% transmittance at the emission peak of 265.5 nm related to the oxygen plasma and up to 90% transmittance at emission peaks ranging from 290 to 370 nm associated with argon plasma. The QG filter has a cutoff wavelength of 160 nm, enabling up to 90% transmittance of the argon plasma at shorter emission

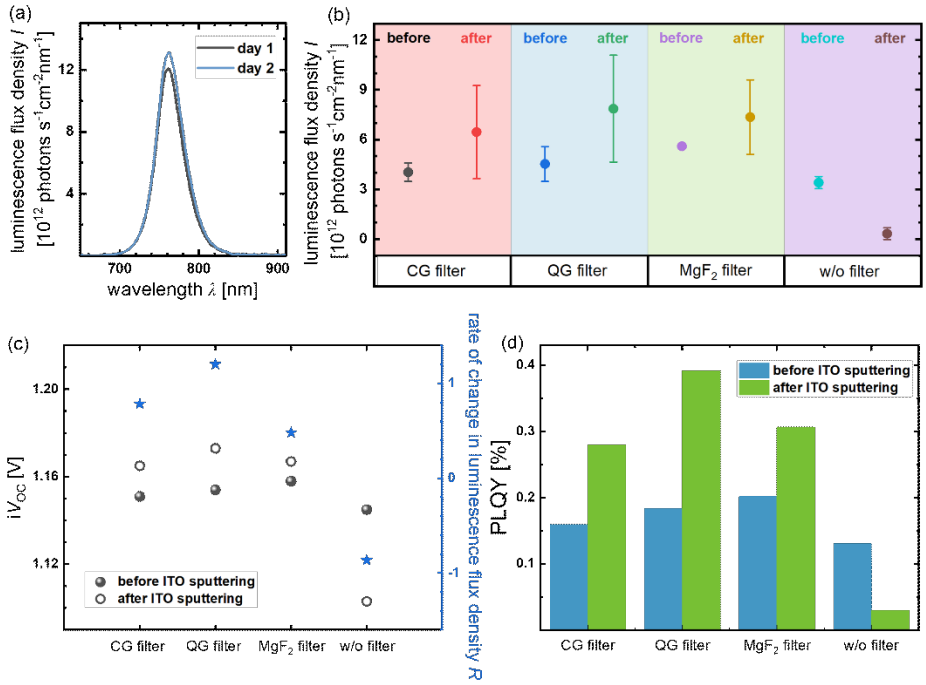

Figure 6.15.: *(a) Short-term stability of the samples for PL measurements. (b) Statistical data of PL intensity, (c) rate of change in PL intensity and its implied open-circuit voltage (iV_{OC}), and (d) PLQY of stacks shielded by CG filter, QG filter, MgF_2 filter, w/o filter before and after ITO sputtering.*

wavelengths. The MgF_2 filter extends the minimum transmission wavelength to 110 nm, which is transparent to strong oxygen plasma at approximately 131 nm. The exposure time to plasma radiation was 35 min, which was also the deposition time, implying that a 110 nm ITO film was deposited on top of either the filter or C_{60} at the end of the experiments. Notably, the transparency of the highly transparent ITO increased as the layer thickness decreased, indicating a potential shift towards the optical filter with increased thickness as the exposure time increased, although this outcome was inevitable. The transmittance curves of both the 10 nm and 110 nm ITO films deposited on the CG filter are given in Fig. 6.13(d) for reference. In the early stage of sputtering, the thin ITO film exhibited almost complete transparency to plasma radiation. However, it has become challenging to

accurately assess the impact of the exposure time to plasma radiation on the PL and determine the optimal exposure time because of the inherent filtering effect of thick ITO. Although pure plasma treatment without sputtering is an alternative method, it fails to replicate authentic experimental conditions effectively.

Second, we studied the absolute PL spectra and quantum yields of the covered and uncovered samples with a distinct architecture of ITO/2PACz/perovskite/C_{60} using a PL setup from QY.Berlin, because PL spectroscopy is a suitable tool for studying the effects of process variations on nonradiative recombination in semiconductors. The higher the PL intensity at a given excitation, the higher the fraction of radiative recombination and the lower the fraction of unwanted nonradiative recombination. As process variations typically primarily affect nonradiative recombination, comparing absolute or relative PL intensities as a function of sample geometry or processing is a simple but effective strategy for evaluating changes in recombination without requiring electrical contacts. Figure 6.14 shows the PL spectra of stacks shielded by different filters and without filters before and after ITO sputtering. It is evident that the PL intensities of the layer stacks shielded by the optical filters exhibit an enhancement under different plasma radiation conditions. However, the PL intensity decreased significantly when the ITO was directly sputtered onto the C_{60} film, as shown in Fig. 6.14(d). The FWHM values before and after ITO sputtering in the four scenarios are listed in Table 2, with negligible changes. Moreover, the statistics of the PL intensity in the four scenarios demonstrated the good reproducibility of the intensity variation as shown in Fig. 6.15(a, b). The results reveal that sputtering damage to the underlying stack primarily arises from ion bombardment, and the resulting degradation far outweighs any gain from plasma radiation.

Table 2. *The full width at half maximum (FWHM) values before and after ITO sputtering in the four scenarios*

	FWHM [nm]			
	CG filter	QG filter	MgF_2 filter	Without filter
Before ITO	41.8	41.8	41.7	41.3
After ITO	42.3	41.4	41.6	40.7

To examine the positive effect of plasma radiation, the rate of change in the luminescence flux density was plotted against the implied open-circuit voltage (iV_{OC}) of each sample before and after ITO sputtering, as depicted in Fig. 6.15(c). iV_{OC} increased as

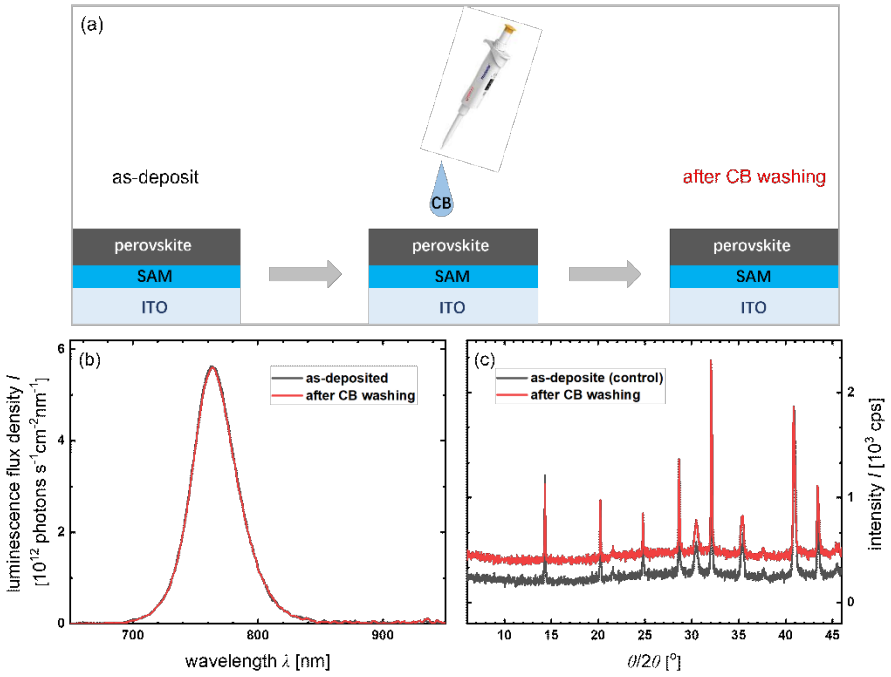

Figure 6.16.: *(a) Sketches of sample processing. (b) PL spectra and (c) XRD patterns of the perovskite before and after CB washing.*

the PL intensity increased when the ions were completely blocked by the filters. This observation indicates that the oxygen/argon plasma radiation effectively suppressed the nonradiative recombination in the glass/ITO/2PACz/perovskite/C_{60} stacks, a finding further corroborated by the photoluminescence quantum yield (PLQY) results presented in Fig. 6.15(d). Given that previous reports have found correlations between lattice strain and nonradiative recombination [135-137], further investigations of XRD were carried out to study the change in lattice strain within perovskite films. The findings are discussed in the next section.

6.4.2. Impact of plasma radiation

XRD was carried out to study the variation in the crystal structure and lattice strain in the perovskite films after ITO sputtering under the above two conditions. Three types of samples are prepared on the glass/ITO substrate for XRD characterization. “Perovskite control” represents the as-deposit perovskite film; “plasma radiation” represents the perovskite film treated with plasma radiation during ITO deposition process, while the CG filter was removed before XRD measurement; “plasma radiation & ion bombardment” represents the perovskite film with the C_{60} and top sputtered ITO layers being washed away by dynamically spin-coating chlorobenzene (CB) solution before XRD measurement. The CB washing process and the preparation process of three types of samples are presented in Figure 6.16(a) and Figure 6.17(a), respectively. The PL spectra and XRD patterns of the perovskite before and after CB washing prove that the CB solution dissolved C_{60} but did not affect the perovskite layer, as shown in Fig. 6.16(b, c).

The XRD patterns of the samples of “perovskite control”, “plasma radiation”, and “plasma radiation & ion bombardment” are shown in Fig. 6.17(b). Diffraction peaks corresponding to the various crystal planes of the perovskite are observed in the specially treated perovskite films (red and blue lines) and the “perovskite control” (purple line). The XRD patterns of three samples contain the same typical perovskite peak at ~14°, corresponding to the (100) crystallographic plane. This observation indicates that ITO sputtering did not change the crystal structure of the perovskite. Furthermore, there is no evidence of phase segregation, as no side peak was found at 11.6°, which is related to the photoinactive hexagonal δ-phase of $FAPbI_3$ [138]. The XRD patterns of the samples also included three specific peaks of ITO (labeled #), which originated from the ITO-coated glass. We observed that the diffraction peak of (200) broadened slightly and red-shifted to angles larger than 28.63° after the perovskite/C_{60} stack was treated with plasma radiation, as depicted in Fig. 6.17(c). In addition, the same broadening of other four diffraction peaks was observed after plasma radiation, including (100), (110), (111), and (210), suggesting the presence of lattice strain in perovskite films [139].

Williamson–Hall (W–H) method was utilized to estimate the lattice strain within the perovskite films by analyzing the diffraction peak broadening in-depth [140], which can be attributed to the crystallite-size-induced broadening β_L (Eq. 6.1) and strain-induced broadening β_e (Eq. 6.2).

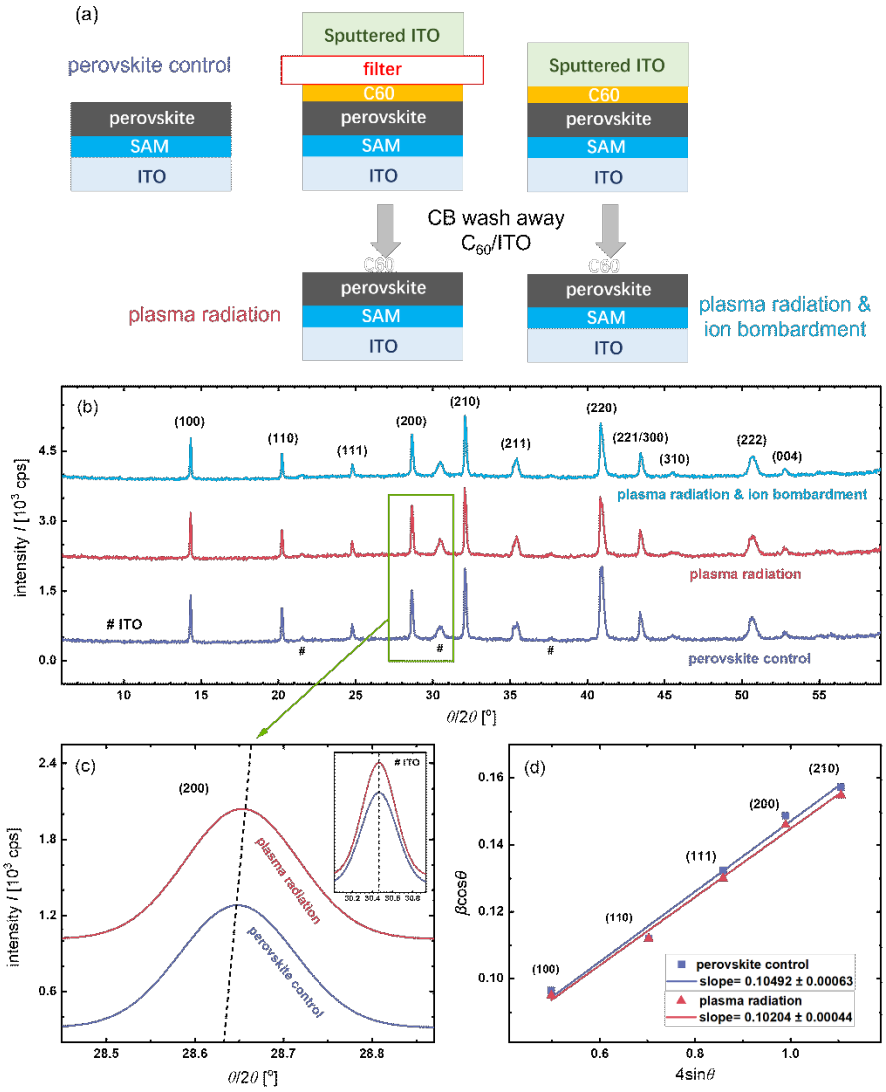

Figure 6.17.: *(a) Sketches of sample processing. (b) XRD patterns of the control perovskite film, perovskite film covered using an optical filter, and perovskite film exposed directly to plasma. (c) Magnified (*200*) plane diffraction peaks and ITO characteristic peaks. (d) Williamson–Hall plots for each sample. The zoomed-in operation of the XRD patterns and the different magnifications of the x- and y-axes make the shapes of the magnified peaks different from those of the original one.*

$$\beta_L = \frac{K\lambda}{L\cos\theta} \tag{6.1}$$

where β is the FWHM of the diffraction peak, L is the crystallite size, and λ is the X-ray wavelength. The strain-induced broadening β_e (Eq. 6.2) is calculated from

$$\beta_e = C\varepsilon\tan\theta \tag{6.2}$$

where ε is the strain and C is a constant value (typically ≈ 4). If both contributions are present, then the combined effects should be determined by convolution. A simple sum is assumed to be a convolution for simplification (Eq. 6.3).

$$\beta\cos\theta = C\varepsilon\sin\theta + \frac{K\lambda}{L} \tag{6.3}$$

The size and strain components can be obtained from the intercept ($K\lambda/L$) and slope (ε) by plotting $\beta\cos\theta$ versus $4\sin\theta$, respectively. In general, the fabrication process determines the crystallite size of the perovskites [141]. In this study, the contribution of the β_L component could be neglected because the perovskite films were prepared simultaneously using the same spin-coating and post-annealing processes, resulting in the same crystallite size. The W-H plots of the perovskite control and the perovskite film treated with plasma radiation are shown in Fig. 6.17(d), where the broadening diffraction peaks are considered as a function of the diffraction angle. The positive slopes of the fitting curves indicate the presence of lattice expansion in both samples. The slope of the W-H plots of the perovskite film treated with plasma radiation was 0.10204 ± 0.00044, which was smaller than the slope of 0.10492 ± 0.00063 for the perovskite control, suggesting relaxation of the lattice strain. In principle, the release of lattice strain contributes to the yield of higher iV_{OC} due to the reduction in defect concentration and the suppression of nonradiative recombination [135]. In the previous analysis of PL spectra, we observed an increase in the iV_{OC} of the glass/ITO/2PACz/perovskite/C_{60} stacks after plasma radiation and inferred that

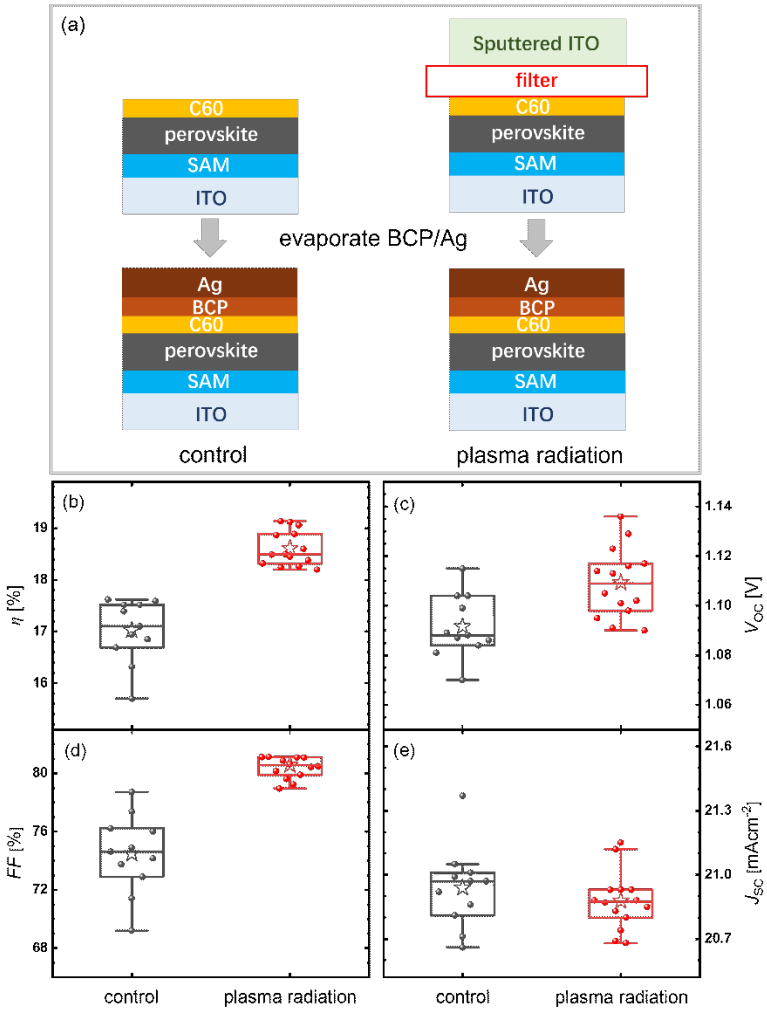

Figure 6.18.: *(a) Sketches of sample processing. (b) η, (c) V_{OC}, (d) FF, and (e) J_{SC} statistics of the control perovskite solar cells and cells treated with plasma radiation prior to the deposition of the BCP/Ag layers.*

plasma radiation reduced nonradiative recombination within the perovskite films by releasing the lattice strain [137,142]. It also illustrates that ion bombardment was the

dominant cause of sputtering damage in this study, instead of plasma radiation. However, in the absence of a reliable method for decoupling the oxygen and argon plasma, we cannot determine whether oxygen plasma or argon plasma is the primary source of sputtering damage. When examining the reasons behind the relaxation of lattice strains due to plasma radiation, we should recognize that the light-induced alterations in lattice strain depend on various parameters, including photon energy [143], wavelength [144], intensity, and duration of illumination [145,146]. Given the potential of each of these factors to impact lattice strain through distinct mechanisms and considering that plasma radiation was not identified as the primary contributor to sputtering damage, we refrained from conducting a separate and comprehensive study in the present work. Further research and analysis are necessary to compressively address this unresolved aspect.

To evaluate the impact of plasma radiation on the performance of single-junction PSCs, both the control and the "plasma radiation" PSCs with the same architecture given by glass/ITO/2PACz/perovskite/C_{60}/BCP/Ag were fabricated. The preparation process and device configurations are presented in Figure 6.18(a). The control devices adhere to a standard procedure, while the "plasma radiation" devices undergo a slightly different manufacturing process. In the case of the "plasma radiation" devices, after preparing the glass/ITO/2PACz/perovskite/C_{60} stacks, they were promptly covered with CG filters. Subsequently, they were transferred to a sputtering chamber for post-treatment with plasma radiation during ITO sputtering. Importantly, it should be noted that the CG filters effectively block ions during this process. Following the plasma radiation treatment, the samples were returned to a glovebox for deposition of the BCP/Ag layers. Compared with the control devices, the "plasma radiation" devices exhibit an average efficiency enhancement of more than 1%, as depicted in Fig. 6.18(b). The enhanced η of PSCs following exposure to plasma radiation can be attributed to the relaxation of lattice strain. This relaxation effectively suppresses nonradiative recombination within the perovskite films, thereby enabling a more efficient collection of carriers, which results in an increase in the V_{OC} and *FF*, as shown in Fig. 6.18(c-e).

6.4.3. Impact of ion bombardment

From XRD results, it has been revealed that the lattice strain in perovskite film was efficiently relaxed due to plasma radiation during ITO sputtering process. However,

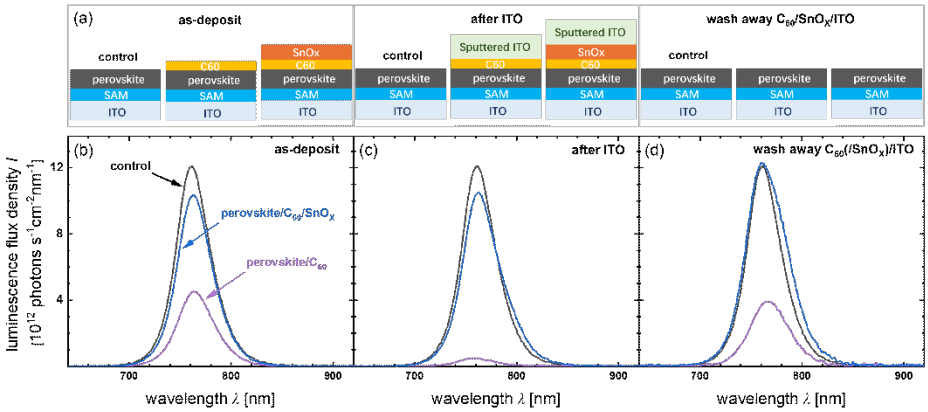

Figure 6.19.: *(a) Sketches of sample processing. PL spectra of (b) the as-deposit stacks, (b) the stacked after ITO sputtering, and (d) the stacks with C_{60}/(SnO_x/)ITO layers washing away.*

whether ion bombardment is damaging to the perovskite film is still difficult to determine. To investigate the impact of ion bombardment, three samples were fabricated for PL analysis: (i) the glass/ITO/2PACz/perovskite stack (control), (ii) the glass/ITO/2PACz/perovskite/C_{60} stack, and (iii) the glass/ITO/2PACz/perovskite/C_{60}/SnO_X stack, wherein a SnO_X buffer layer was incorporated to mitigate sputtering damage during subsequent treatments. The device configurations and corresponding PL spectra are presented in Fig. 6.19. Upon comparison of the PL spectra presented in Fig. 6.19(a) and (b), no degradation in the PL intensity was observed in the sample containing SnO_X (blue) subsequent to ITO sputtering. In contrast, the PL intensity of the sample without SnO_X is notably diminished (purple). However, the results only illustrate the damage to the entire stack without revealing the impact on the perovskite films individually. Therefore, an identical configuration of glass/ITO/2PACz/perovskite was obtained for three scenarios by washing away the C_{60}/(SnO_X)/ITO layer stack using CB, and was studied to exclude any interference from other films, particularly C_{60}. After washing away the C_{60}/(SnO_X/)ITO films, their PL spectra were re-measured and compared with that of the control sample, which was an as-prepared glass/ITO/2PACz/perovskite stack, as shown in Fig. 6.19(d). We observed that the PL signals of the sample containing SnO_X and the control sample almost coincided, whereas the PL intensity of the sample without SnO_X degraded significantly. This observation demonstrates that the absence of a buffer layer damages the underlying

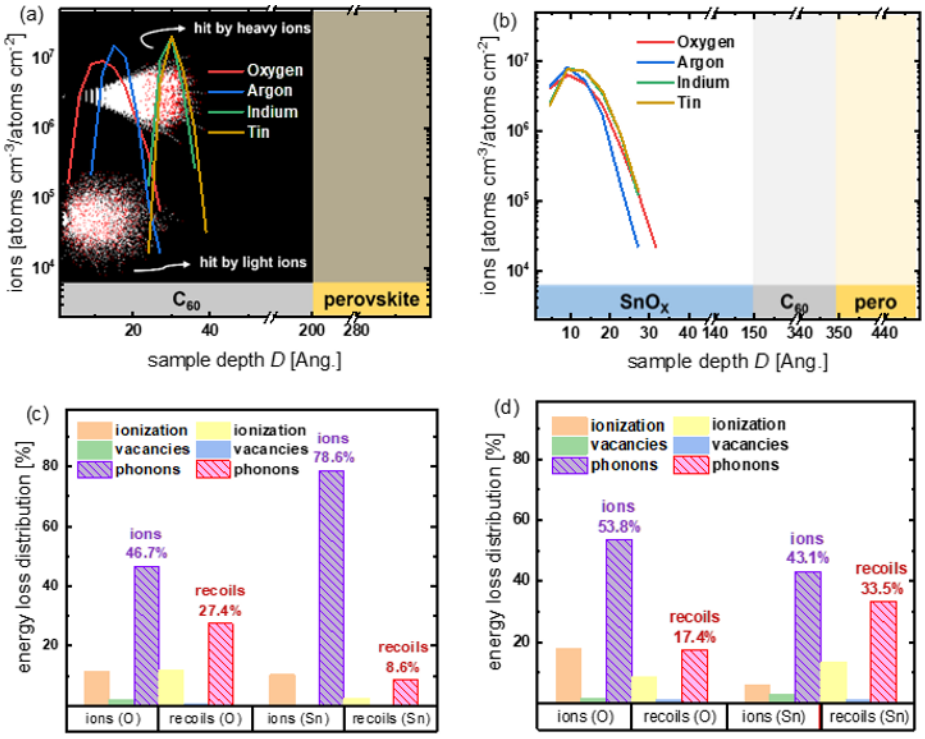

Figure 6.20.: *Penetration depth profile of ions involved in sputtering plasma in (a) the perovskite/C_{60} stack with the distribution of stopped and moving atoms displayed on a black background and (b) the perovskite/C_{60}/SnO_X stack. Energy loss distribution of ions and recoils after oxygen and tin ion bombardment in (c) perovskite/C_{60} stack and (d) perovskite/C_{60}/SnO_X stack.*

perovskite film after the ITO sputtering. We also observed that the PL intensity of the perovskite/C_{60}/SnO_X sample was higher than that of the perovskite/C_{60} sample, suggesting that the SnO_X treatment enhanced the PL intensity. SnO_X is likely to have a much lower work function than bare C_{60}, which will move the Fermi level at the perovskite/C_{60} interface up towards the conduction band of C_{60}. This will reduce the hole concentration in the perovskite at the interface, thereby reducing the recombination rate at a given Fermi level splitting. This leads to enhanced PL.

To determine whether sputtering damage to the perovskite film is associated with ion penetration, SRIM Monte Carlo simulations were carried out to simulate the penetration depth of the negative ions with an initial kinetic energy of 85 eV, which was calculated from the voltage between the target and substrate during ITO sputtering. The density setup of perovskite, C_{60} and SnO_X were 4.59 g/cm^3, 1.65 g/cm^3, 6.85 g/cm^3, respectively. The damage model was Ion Distribution and the basic plot was Quick Calculation of Damage and Ion Distribution with Recoils projected on Y-plane. Figure 6.20(a) shows the ion distributions of oxygen, argon, indium, and tin in the perovskite/C_{60} stack as a function of the penetration depth. Oxygen and argon ions have penetration depths of ~3 nm, whereas tin and indium ions have maximum penetration depths of ~4 nm. All impinging ions eventually stopped penetrating to a depth of less than 5 nm from the surface and remained in the C_{60} film. The white and red dots displayed in the black background represent the moving ions and stopped atoms ejected from their original site when collisions transfer more than the displacement energy (E_{disp}). The radial and spherical distributions of the atoms were attributed to the penetration of the heavy and light ions, respectively. For semiconductors, the typical values of E_{disp} are about 15 eV [147], which is significantly lower than the initial kinetic energy of ions. Subsequently, vacancies were created near the surface owing to the collisions between the ions and lattice atoms as well as the collisions between the recoiling atoms and other lattice atoms. Recoiling atoms, also known as recoils, are atoms that are knocked out of their lattice sites, thus creating vacancies and interstitials [147]. The SRIM software predicts the number of vacancies in the C_{60} layer left by the knocked-out lattice atoms, as presented in Fig. 6.21(a). Based on the PL and simulation results, we postulate that a large number of carriers may recombine with the assistance of vacancy defects left by the knocked-out lattice atoms near the C_{60} surface, leading to significant degradation of the PL intensity.

During the TCO sputtering process, the incident ions with high kinetic energies collide with the lattice atoms close to the sample surface, and part of the energy is transferred to the atoms, leading to bond breakage or other structural changes [52,116], while the remaining energy enables the ions to penetrate deeper into the sample, eventually stopping movement with the remaining energy released as phonons. Figure 6.20(c) shows the energy loss distribution generated from the SRIM simulations. Oxygen ions, the most abundant species in the plasma [148], generate phonons with 46.7% of their initial kinetic energy of 85 eV, and the recoils contribute an additional 27.4%. Tin ions, the heaviest atoms in the plasma, generated phonons with 78.6% of their initial kinetic energy, and recoils

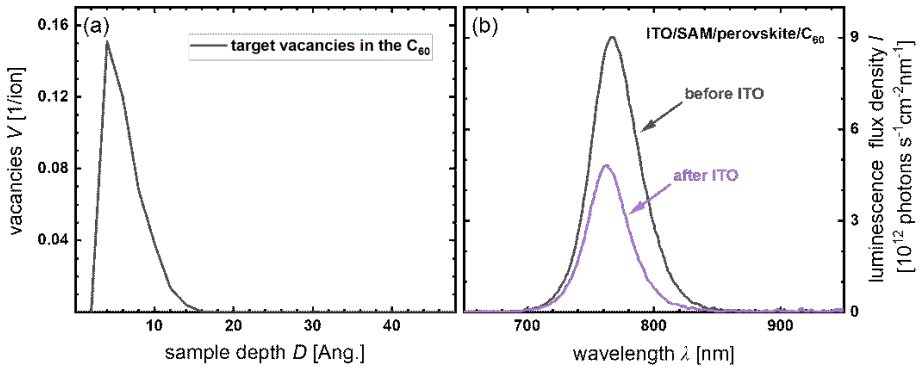

Figure 6.21.: *(a) Distribution of target vacancies in the C_{60} layer after the lattice atoms were knocked out of the original site by oxygen ions. (b) Spectra of the stacks with* 35 *nm-thick C_{60} before and after ITO sputtering.*

contributed an additional 8.6%. Therefore, the total energy of phonons was 63 eV per incident oxygen ion and 74 eV per incident tin ion within the range of the phonon dispersion relation of C_{60} [149]. It is well known that heat transport in dielectric solids is mainly through the elastic vibration of the lattice, also described as phonon propagation.[150] According to the simulation results, the impinging ions did not penetrate the C_{60} film to reach the perovskite surface; therefore, we speculate that the sputtering damage on the perovskite film is related to phonon propagation. Phonons are quantized lattice vibration modes and are responsible for heat conduction in most non-metallic solids [151]. In the ITO sputtering process, phonons propagate into the perovskite layer in the direction of the film thickness and heat the perovskite surface. However, the energy of phonons reaching the perovskite layer is less than the total energy obtained from ions and atoms due to phonon scattering, including scattering by imperfections [152], intrinsic-structure scattering combined with internal-boundary scattering [153], and scattering at solid-solid interfaces [154]. Considering the low energy required to break the chemical bonds in hybrid halide perovskites, such as C-C bonds (3.73 eV), the elevated temperature was perhaps already sufficient to dissociate the bonds at the perovskite surface [155]. Besides, previous reports have revealed that heat can easily degrade the formamidinium cation (FA^+) by breaking the C=N double bonds [156-158]. Investigation of the chemical bonds at the perovskite surface after ITO sputtering is discussed in detail later.

When SnO_X is introduced as a buffer layer, the extra 15 nm thick solid film naturally

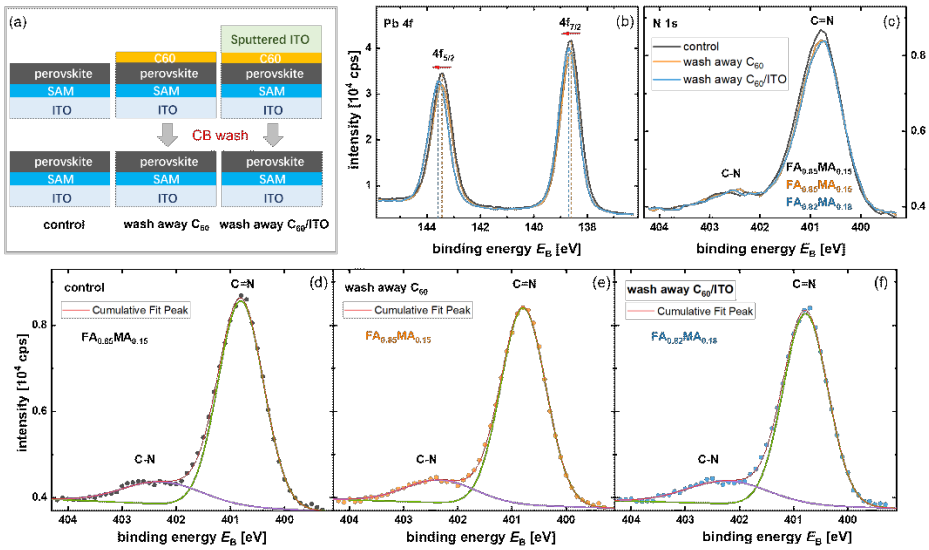

Figure 6.22.: *(a) Sketches of sample processing. XPS spectra of (b) Pb 4f and (c) N 1s of three samples. N 1s peak fitting of (d) the controlled perovskite film, (e) perovskite films with C_{60}, and (f) C_{60}/ITO washed away.*

has a higher potential to protect the underlying perovskite against ion bombardment. To compare the effect of the thickness variations of the stacks, PL spectra were obtained for the glass/ITO/2PACz/perovskite/C_{60} stacks using 35 nm thick C_{60} films, while the conventional thickness of C_{60} was 20 nm. In Fig. 6.21(b), the reduction in PL intensity after ITO sputtering demonstrated that the double layers of C_{60}/SnO_X outperformed the single layer of C_{60} for the same layer thickness. This is mainly because phonons lose a large amount of energy in the SnO_X layer and at the C_{60}/SnO_X interface because of scattering. The ion distribution in the perovskite/C_{60}/SnO_X stack as a function of target depth was also studied, as shown in Fig. 6.20(b). These results demonstrate that all ions had a similar maximum penetration depth of ~3 nm; however, the penetration depth of the heavy ions was less than that in the perovskite/C_{60} stack, which may be associated with the specific mass and atomic radius. The specific mass of SnO_X (6.85 g/cm^3) is three times higher than that of the C_{60} (1.65 g/cm^3) [159]. The fact reflects that the impinging ions collide with more atoms per unit volume and lose energy quicker in the SnO_X film, so the heavy ions have a shorter penetration distance. Because the radius of light ions is much smaller than

that of heavy ions, the penetration depth of light ions is less likely to be affected. From the energy loss distribution depicted in Fig. 6.20(d), we conclude that the oxygen ions generated phonons with 53.8% of their initial kinetic energy of 85 eV, and those produced by the recoils accounted for another 17.4%. Tin ions generated phonons with 43.1% of their initial kinetic energy, and recoils produced 33.5%. Therefore, the total energy of the phonons is 61 eV per incident oxygen ion and 72 eV per incident tin ion within the range of the phonon dispersion curve of SnO_X [160]. Both energies are smaller than the total energy of the phonons in the perovskite/C_{60} stack (63 and 74 eV). These results can be explained in terms of E_{disp}, which refers to the minimum kinetic energy required to permanently knock atoms away from the lattice sites. The struck atoms gain energy from a collision, and this energy and the energy of incident ions are released as phonons only if they are lower than the E_{disp} of the lattice [147]. The E_{disp} of Sn is 22 eV, lower than the E_{disp} of C of 25 eV [161], which means the incident ions and the struck atoms with kinetic energy between 22~25 eV could transfer energy to phonons in the C_{60}, but this is not the case in the SnO_X. Therefore, the total energy of phonons in the perovskite/C_{60} stack was slightly higher than that of phonons in the samples with SnO_X layers.

High-resolution XPS measurements were used to gain insights into the localized chemical bonding changes on the surface of the perovskite films after ITO sputtering (Sec. 3.1.3). The sample configurations are presented in Fig. 6.22(a): (i) perovskite control (as-prepared), (ii) perovskite with C_{60} washed away, and (iii) perovskite with C_{60}/ITO washed away. The binding energy (BE) of the Pb core level was affected by the elements bonded to it. Figure 6.22(b) compares the Pb 4f core level spectra of three samples, wherein the specific peaks of Pb $4f_{7/2}$ (~138.6 eV) and Pb $4f_{5/2}$ (~143.4 eV) were present in all samples. The BE of the two Pb 4f peaks of the perovskite with C_{60} washed away (orange curve) overlapped with the peaks of the perovskite control (black curve), indicating that the chemical states of Pb were not affected by washing away C_{60} with CB. A slight shift to a higher BE for both the Pb $4f_{7/2}$ and $4f_{5/2}$ peaks was observed after ITO sputtering (blue curve). This can be attributed to the thermal degradation of the perovskite because the Pb spectra shift toward the direction of mixed halide perovskite decomposition into PbI_2 and $PbBr_2$ [162], which is triggered by the temperature rise at the perovskite surface owing to phonon propagation.

Figure 6.22(c) depicts the core level of N 1s, in which two peaks located at the BE of ~400.8 eV and ~402.4 eV representing nitrogen in C=N and C-N bonds confirm the presence of the FA^+ and methylammonium cations (MA^+), respectively [163]. Figure 6.22(d-f) depicts N 1s peak fitting of three samples in detail. The nitrogen atomic ratio of

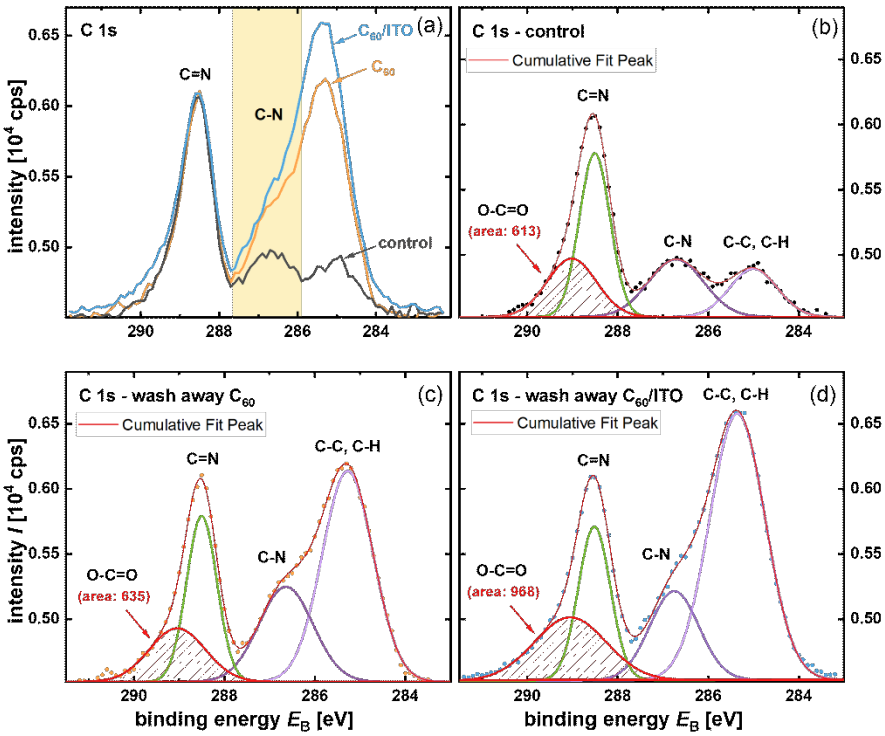

Figure 6.23.: *XPS spectra of (a) C 1s peaks of three samples. The relevant C 1s peak fitting of (b) the controlled perovskite film, (c) perovskite films with C_{60}, and (d) C_{60}/ITO washed away.*

FA^+:MA^+ in the perovskite control and the perovskite with C_{60} washed away was calculated to be 0.85:0.15. However, the FA^+: MA^+ ratio decreased to 0.82:0.18 after ITO sputtering, suggesting minor loss of FA^+. Meanwhile, the signals of carbon in C-N (~288.5 eV) and C=N (~286.7 eV) bonds found in the C 1s core level spectra also proved the coexistence of FA^+/MA^+ [163], as shown in Fig. 6.23, where a shoulder peak to the left of the C=N bonds became apparent with ITO sputtering. The deconvoluted C 1s peak of each sample and integrated area under the deconvoluted peaks were fitted using Gaussian functions. The C 1s peak at a BE of ~289.1 eV present in all the samples should be associated with the double-bonded oxidized carbon species O-C=O [164]. The integrated area under the O–C=O bond peaks increased slightly from 613 cps eV to 635 cps eV when the C_{60} layer was washed

away. However, after the ITO sputtering, there was a pronounced increase in the integrated area to 967 cps eV. From the SRIM simulation results, we know that oxygen ions cannot penetrate through the C_{60} film and reach the perovskite surface; thus, the dramatic increase in the integrated area under the peak of O-C=O bonds is estimated to be associated with the formation of carbon dangling bonds due to phonon propagation dissociating chemical bonds, which immediately re-bond to the oxygen atoms in the water from ambient air during the transfer of the samples from the glovebox to the XPS spectrometer. The XPS data for the deconvoluted peaks of the C=N bonds in the C 1s core level spectra of the three samples are listed in Table 3. The ratio of the integrated area under the O=C-O/C=N bond peaks did not change as C_{60} was washed away, suggesting that this approach had a negligible effect. After the ITO sputtering, the ratio increases from 0.37 to 0.48. Analysis of the C=N bonds in the C 1s core level spectra shows that there is an increase in the O=C-O bonds and perhaps a minor loss of FA^+ at the perovskite surface under the effect of ITO sputtering. The peaks observed at a lower BE of ~285.2 eV was attributed to C-C and C-H bonds, which were detected in the contamination of the perovskite surface. The intensities of these peaks increased significantly owing to the removal of C_{60} and C_{60}/ITO with residual impurities. The integrated area under the deconvoluted peaks of the C-N bonds has not been discussed in detail because it is strongly affected by residual impurities, which are difficult to control during transportation.

Table 3. *XPS data for the deconvoluted peaks of C=N bonds in the C 1s core level spectra of the three samples.*

Samples	Ration of O=C-O/C=N	FWHM [eV]	Max height [cps]	E_B [eV]
Control	0.36	0.80 (±0.07)	1257	288.5 (±0.01)
Wash away C_{60}	0.37	0.79 (±0.04)	1271	288.5 (±0.01)
Wash away C_{60}/ITO	0.48	0.83 (±0.04)	1180	288.5 (±0.01)

In Fig 6.24(a-c), the spectral levels of Cs 3d and I 3d for the three samples almost overlap, while the core spectral level of Br 3d shifted slightly as C_{60} was washed away, but no further shift was observed after the ITO sputtering. A shoulder peak at a BE of 530.2 eV in the O1s core level spectra is associated with the ITO residues with C_{60}/ITO washed away [165], and the strong peaks at ~533.0 eV distinguished in all samples were responsible for the surface absorbed water species, as shown in Fig 6.24(d-f). The results demonstrate that

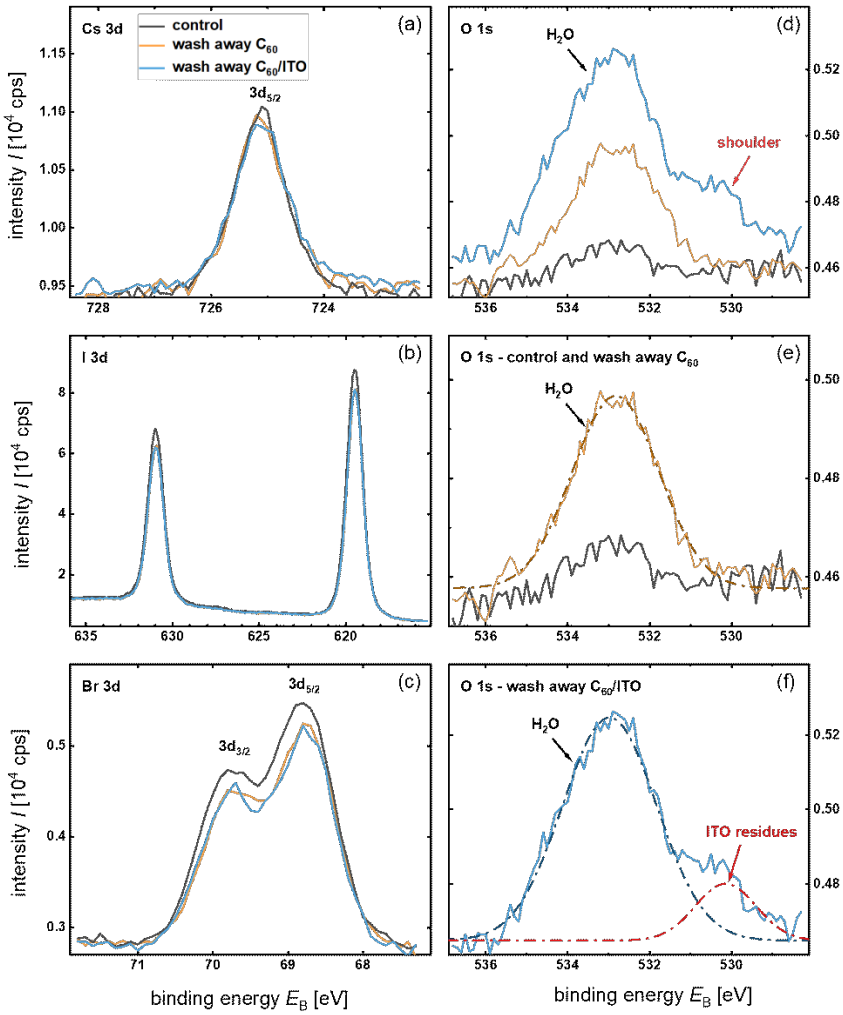

Figure 6.24.: *XPS spectra of (a) Cs 3d, (b) I 3d, (c) Br 3d and (d-f) O1s peaks of three samples.*

a minor loss of FA^+ owing to the dissociation of C=N bonds is the major cause of ion-bombardment-induced sputtering damage to the perovskite film.

In conclusion, our investigation revealed that the sputtering damage of ITO to

perovskite/C_{60} stacks primarily originates from ion bombardment rather than plasma radiation. In contrast, plasma radiation exhibits great potential for suppressing nonradiative recombination within perovskite films. Direct exposure of the perovskite/C_{60} stack to plasma results in the generation of vacancy defects within a few nanometers of the C_{60} surface because of collisions between the impinging ions and lattice atoms. These vacancies likely serve as centers for nonradiative recombination, leading to the deterioration of iV_{OC} and, consequently, a reduction in device efficiency. XPS measurements showed that C=N bonds at the perovskite surface dissociated under plasma irradiation owing to phonon propagation, resulting in a minor loss of FA^+, potentially undermining the device performance. The introduction of an SnO_X buffer layer with a critical thickness of 15 nm guarantees the presence of adequate phonon scattering events within the SnO_X layer. Moreover, the C_{60} surface becomes the first solid-solid interface reached by phonons during propagation instead of the perovskite surface, where phonon scattering increases and thermal conduction deteriorates. Consequently, the energy carried by phonons that ultimately reach the perovskite surface is too low to initiate chemical bond dissociation.

We have summarized the reasons for SnO_X buffer layer mitigating the sputtering damage into two aspects: 1) Less kinetic energy was transferred to phonons owing to better film properties. 2) It is difficult for phonons to propagate to the perovskite surface owing to scattering within the SnO_X layer and C_{60}/SnO_X interface. Moreover, we have summarized the following suggestions on how to choose a buffer layer for perovskite/silicon tandem solar cells: 1) high transparency can reduce parasitic absorption losses, 2) high specific mass can reduce the penetration depth of impinging ions, 3) low displacement energy can reduce the kinetic energy transferred to phonons, and 4) more internal boundaries can increase the probability of phonon scattering. In cases 3) and 4), a thicker buffer layer can better support the prevention of phonon propagation. Based on these revealed mechanisms, the remarkable improvement in the performance of semi-transparent PSCs (Fig 6.11(a)) can be attributed to the effective protection of the perovskite/C_{60} stack from sputtering damage achieved by employing a 15 nm thick SnO_X buffer layer, in contrast to the 5 nm thickness because the energy required a certain thickness to be released after the ion penetration motion stopped.

7. Efficiency Improvement of Perovskite/Silicon Tandem Solar Cells

Establishing a stable fabrication chain for high-efficiency perovskite/silicon tandem solar cells is the primary objective of this research, which typically necessitates a prolonged process of development and optimization. In this chapter, this extended process was summarized and divided into three sections according to the different stages of efficiency improvement. Initially, the workflow of tandem fabrication was tested with all the requisite deposition equipment, masks, and sources prepared, with the objective of producing tandem solar cells with an efficiency exceeding zero, which serves as the foundation for further efficiency enhancement. Due to the suboptimal efficiency of both tandem and single-junction solar cells, we identified deficiencies in numerous aspects, such as the utilization of inappropriate tools and the suboptimal status of key films, which resulted in damage to the functional layers, poor optoelectrical properties, interfacial band misalignment, inadequate passivation quality, and other issues. Therefore, a systematic troubleshooting process was implemented to address these problems sequentially in the most efficacious manner. Subsequently, a series of methods were employed to enhance the optical response, facilitate electron collection, and suppress carrier recombination in tandem solar cells. Additionally, several colleagues contributed to the efficiency improvement through their work on wafer texturing, transporting layers, perovskite composition and interfacial passivation, thereby making it a collaborative effort. During the efficiency optimization process, the surface treatment typically applied to the silicon bottom cells prior to the preparation of perovskite top cells was found to effectively improve the *FF* of tandem solar cells. Therefore, a systematic investigation of the impact of surface treatment on both tandem and subcells was ultimately conducted to elucidate the surface-treatment-dependent *FF*, which can guide further efficiency improvements.

7.1. From 9% to 19%: Workflow and troubleshooting

7.1.1. Workflow testing

We have established a stable baseline that enables the reliable fabrication of high-efficiency SHJ solar cells, which has demonstrated potential for manufacturing high-efficiency perovskite/silicon tandem solar cells. To prepare high-quality silicon bottom cells, several modifications were implemented in the fabrication process for baseline. Firstly, the rear-sided ITO/Ag stack and front-sided ITO layer were sputtered onto the center of the silicon bottom cell through a precisely defined deposition mask rather than full-area coverage in SHJ solar cells. The area of the patterned ITO and Ag layers was set to 1.1 cm × 1.1 cm, slightly larger than the active area (1 cm^2) of tandem solar cells to account for potential misalignment between patterned layers. Secondly, the layer thickness of the front-sided ITO as ICL was reduced from 70 nm to 30 nm to block shunt pathways due to an increasing R_{SH}. Thirdly, instead of terminating the fabrication of SHJ solar cells with a screen-printed Ag electrode and an evaporated MgF_2 ARC, the fabrication of silicon bottom cells was terminated with cutting, which separated the bottom cells from large silicon wafers. However, due to the absence of laser cutting in the initial stage, the wafers were manually cut using a scribing pen, resulting in irregular shapes with non-uniform sizes and potential damage to the bottom cells. The comparison between the workflows of single-junction SHJ solar cell and silicon bottom cell are presented in Fig. 7.2(a) step-by-step, along with the comparison between the workflows of single-junction PSC and perovskite top cell. The configuration of perovskite top cells was analogous to that of the semi-transparent devices (Fig. 6.1(d)). In comparison to the workflow of single-junction PSCs, two primary modifications were implemented in the fabrication process for top cells. Firstly, the 8 nm full-area BCP layer was substituted with a patterned window stack (1.1 cm × 1.1 cm), comprising a 10 nm SnO_X buffer layer and a 110 nm ITO transparent electrode. Secondly, the 80 nm Ag electrode that entirely covered the active area of single-junction PSC was replaced with a 100 nm U-shaped Ag frame. This frame surrounded and partially contacted the edge of the patterned ITO layer for electron collection, as illustrated in the inset image of Fig. 7.1(b), which subsequently defined the active area of the tandem solar cell.

For the initial batch for workflow testing, all materials, fabrication processes, and parameters that differed from single-junction devices were unoptimized, as the primary

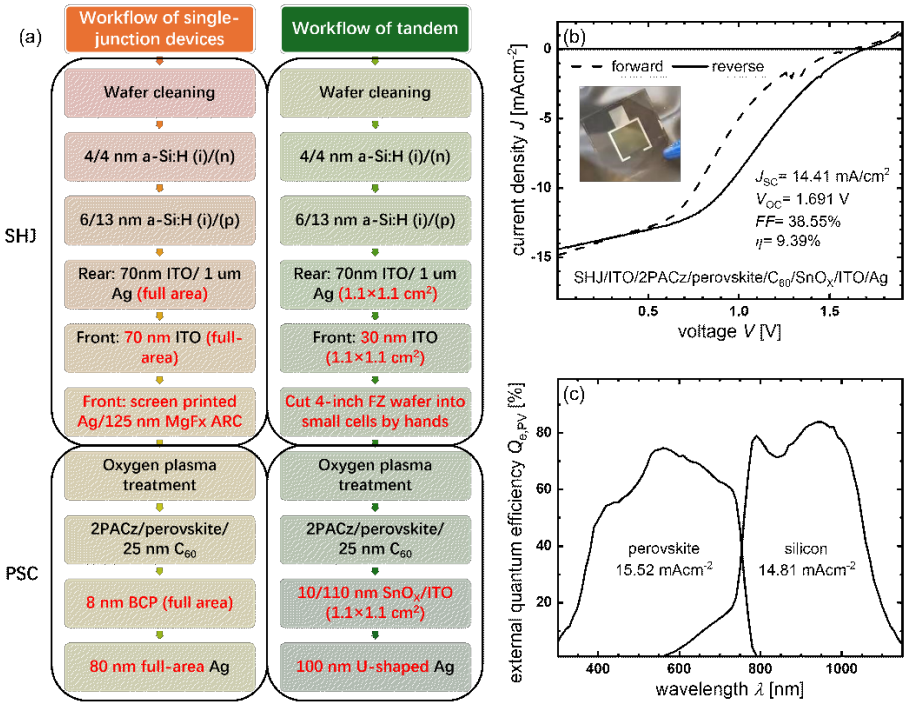

Figure 7.1.: *(a) Comparisons between the workflows of single-junction silicon heterojunction solar cell and silicon bottom cell, along with the comparison between the workflows of single-junction perovskite solar cell and perovskite top cell. The differences are highlighted in red. (b) JV curves of the perovskite/silicon tandem solar cells exhibiting the highest efficiency in the initial batch for workflow testing. The inset image depicts a tandem device. (c) Corresponding $Q_{e,PV}$ spectra of the perovskite top cell and silicon bottom cell.*

objective was to assess whether the entire workflow enabled the production of devices with efficiency above zero. The results were promising, as the output efficiency of only one of the five cells was 0%, while the other four functioned with efficiencies ranging between approximately 4% and 10%. The *JV* curves of the tandem solar cell with the highest efficiency of 9.39% were depicted in Fig. 7.1(b), although the presence of a pronounced S-shape indicated shunt and large R_S losses. The corresponding $Q_{e,PV}$ spectra revealed that the

current was limited by the silicon bottom cell, as shown in Fig. 7.1(c). Due to the complex configuration of the tandem device, it is challenging to intuitively diagnose the problematic layers and interfaces that result in poor efficiency and to effectively optimize those layer stacks. Consequently, a systematic troubleshooting process was necessary to identify and subsequently address a series of underlying issues.

7.1.2. Troubleshooting

As all layers in single-junction PSCs underwent varying degrees of change when the glass/ITO substrate was substituted with silicon bottom cells, particularly the organic layers prepared using solution-based methods, the troubleshooting process primarily focuses on addressing issues related to the perovskite top cell. On one hand, the established materials, for instance the HTL, perovskite, and ETL, may not perform optimally; on the other hand, the emerging buffer layer, transparent electrode, adjacent interfaces, and U-shaped Ag electrode are most likely to result in performance deterioration prior to targeted optimization. The composition of the perovskite utilized for workflow testing was $Cs_{0.05}(FA_{0.83}MA_{0.17})_{0.95}Pb(I_{0.83}Br_{0.17})_3$ with a E_g of 1.63 eV, and the HTL and ETL were 2PACz and C_{60}, respectively. No passivation layers were employed at the interfaces between the perovskite and the transporting layers. However, the champion efficiency of single-junction PSC ("Structure A") that was also prepared using 2PACz/$Cs_{0.05}(FA_{0.83}MA_{0.17})_{0.95}Pb(I_{0.83}Br_{0.17})_3$/$C_{60}$ was 19.1%, which is lower than the published state-of-the-art efficiencies (>20%) with a similar configuration and identical E_g of perovskite, indicating potential for further optimization.

To enhance the average efficiency of "structure A", several modifications were implemented. Firstly, Me-4PAC was substituted for 2PACz as the HTL, facilitating a higher iV_{OC} due to improved band alignment. The concentration and spin-coating program for Me-4PACz remained consistent with those of 2PACz. Secondly, based on published simulation results indicating that 1.68 eV was the optimal E_g for perovskite in perovskite/silicon tandem solar cells, the E_g was increased to 1.68 eV by elevating the bromide ratio from 17% to 22%. The resulting composition was $Cs_{0.05}(FA_{0.73}MA_{0.22})_{0.95}Pb(I_{0.78}Br_{0.22})_3$. Thirdly, an organic halide salt, PEAI, was introduced at the perovskite/C_{60} interface as a passivation layer to mitigate defects and suppress non-radiative recombination [166]. The perovskite precursor was deposited onto the Me-4PACz layer using a two-consecutive step spinning

program, replacing the previously employed one-step spin-coating method (5500 rpm/4 s acceleration/35 s). The initial step of the two-consecutive step spinning program (2000 rpm/4 s acceleration/15 s) was designed to rapidly form a conformal coating of the perovskite film on the substrate. Additionally, 0.2 mg/mL PMMA was incorporated into the perovskite precursor to enhance wettability, further promoting conformal coating. A comparative analysis of device performance was conducted between perovskite layers spin-coated for short (35 s) and long (60 s) durations in the second step (6000 rpm/5 s acceleration), while maintaining other parameters constant. As illustrated in Fig. 7.2(a-d), "structure A" with an extended spin-coating duration in the second step demonstrated superior efficiencies, attributable to the enhanced removal of solvents and antisolvents, which is conducive to perovskite crystallization. Consequently, the second step parameters were established as 6000 rpm/5 s acceleration/60 s.

During the spin-coating process, perovskite precursor solutions—typically containing lead salts and organic halides—encounter difficulties in rapidly forming solid films due to the low volatility of solvents (e.g., DMF). The application of an anti-solvent (e.g., chlorobenzene, toluene, anisole, or ethyl acetate) onto the spinning substrate coated with perovskite precursor rapidly displaces or precipitates the solvents in the precursor, thereby accelerating nucleation and promoting crystallization of perovskite grains. Through the selection of an appropriate anti-solvent and optimization of its dropping time, the grain size, morphology, and distribution within the perovskite film can be precisely controlled. This optimization ultimately enhances both the efficiency and long-term stability of the solar cells due to improved light absorption and carrier transport. 300 μL of anisole continued to be utilized as the anti-solvent for the new perovskite composition, and the time to drop anisole ($t_{anisole}$) was optimized. The results presented in Fig. 7.2(e-h) demonstrated that dropping anisole onto the spinning substrate at thirty seconds before the end of the spin-coating program was the optimal condition, as earlier dropping ensures sufficient time for anti-solvent evaporation. In addition to improving the film quality of perovskite, a passivation layer of PEAI was employed to passivate the iodide vacancies on the perovskite surface, thereby significantly enhancing efficiency and reducing statistical dispersion, as shown in Fig 7.3(a). V_{OC} and *FF* were enhanced due to the suppression of the charge recombination and charge accumulation, while J_{SC} remained approximately constant, as illustrated in Fig 7.3(b-d).

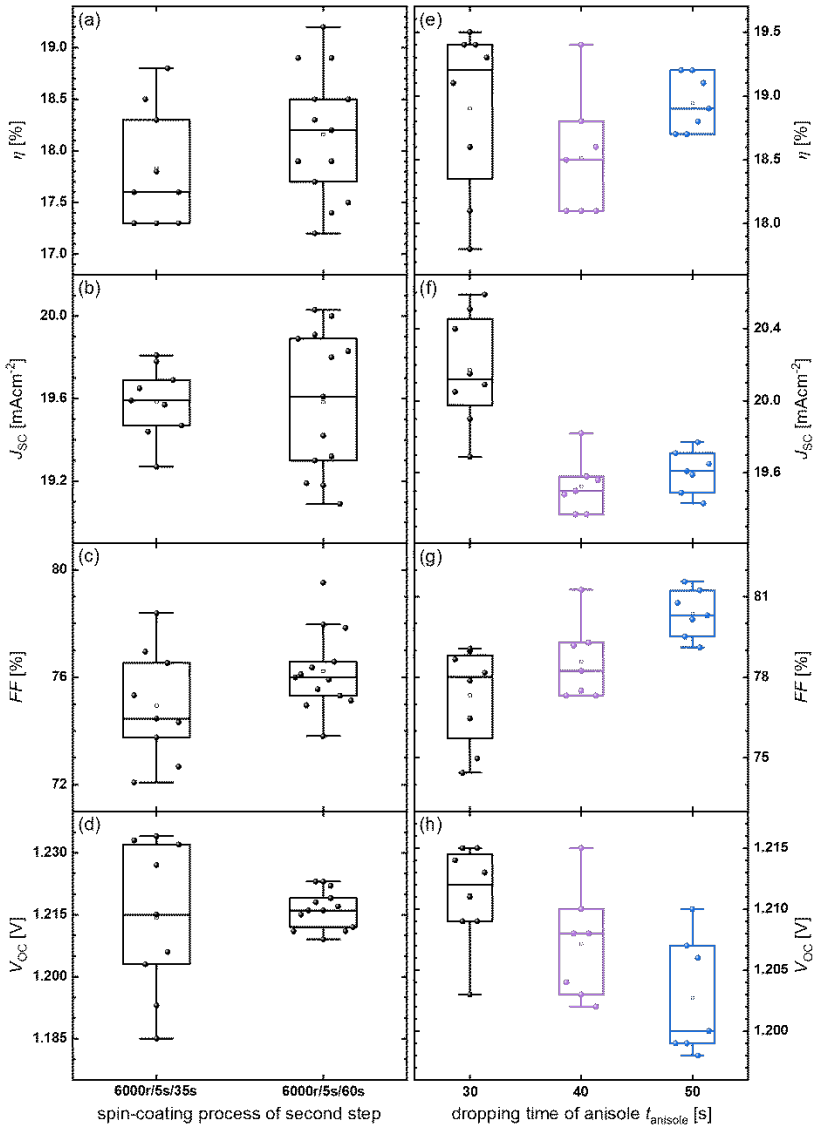

Figure 7.2.: *(a) η, (b) J_{SC}, (c) FF, and (d) V_{OC} statistics of the perovskite solar cells ("structure A") using either a short or a long spin-coating process of second step for perovskite. (e) η, (f) J_{SC}, (g) FF, and (h) V_{OC} statistics of the perovskite solar cells ("structure A") as a function of the dropping time of antisolvent $t_{anisole}$ at second step of spin-coating process for perovskite.*

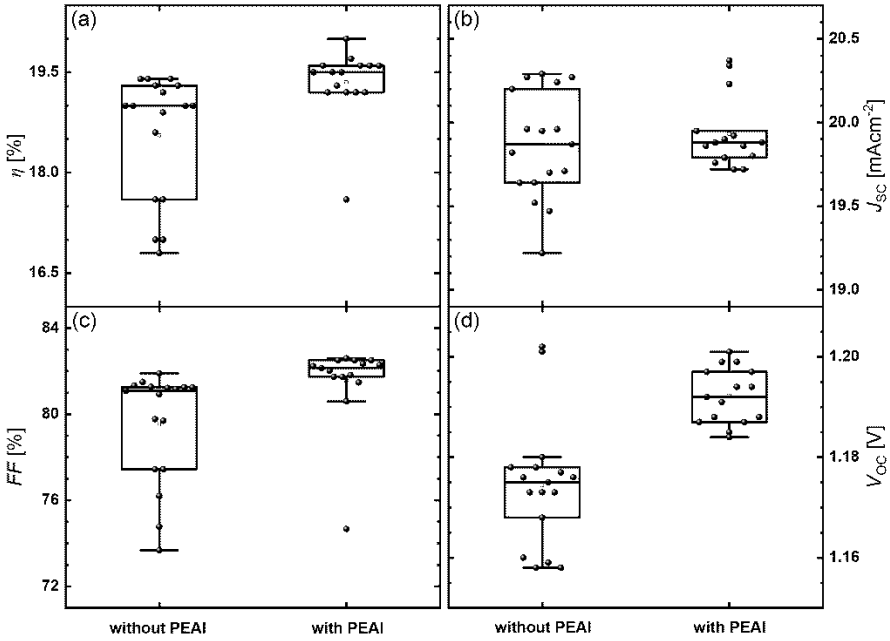

Figure 7.3.: *(a) η, (b) J_{SC}, (c) FF, and (d) V_{OC} statistics of the perovskite solar cells ("structure A") without and with PEAI passivation layer atop perovskite.*

In summary, the statistics of the "structure A" before and after all the optimizations, including the replacement of HTL, optimization in the E_g and film quality of perovskite, and interfacial passivation, were plotted in Fig. 7.4(a-d) for an intuitive comparison. After the 2PACz/$Cs_{0.05}(FA_{0.87}MA_{0.13})_{0.95}Pb(I_{0.87}Br_{0.13})_3$/$C_{60}$ stack was replaced by the Me-4PACz/$Cs_{0.05}(FA_{0.73}MA_{0.22})_{0.95}Pb(I_{0.78}Br_{0.22})_3$/PEAI/$C_{60}$ stack, the device efficiencies improved significantly by at least 1% , wherein the *FF* increasing by roughly 3% and V_{OC} by 60 mV, which compensated for the slight reduction in the J_{SC} by approximately 0.5 mAcm^{-2} owing to a broadened E_g. The cross-sectional schematic and top view of "Structure A" were presented in Fig. 7.4(e), and the *JV* curves of the solar cells with champion efficiencies were depicted in Fig. 7.4(f). The champion η of 20.6% after optimization was close to the best reported efficiency record of the PSCs with an inverted structure and an equivalent large E_g of 1.68 eV, indicating that the established materials performed optimally for further implementation in tandem device. However, when the

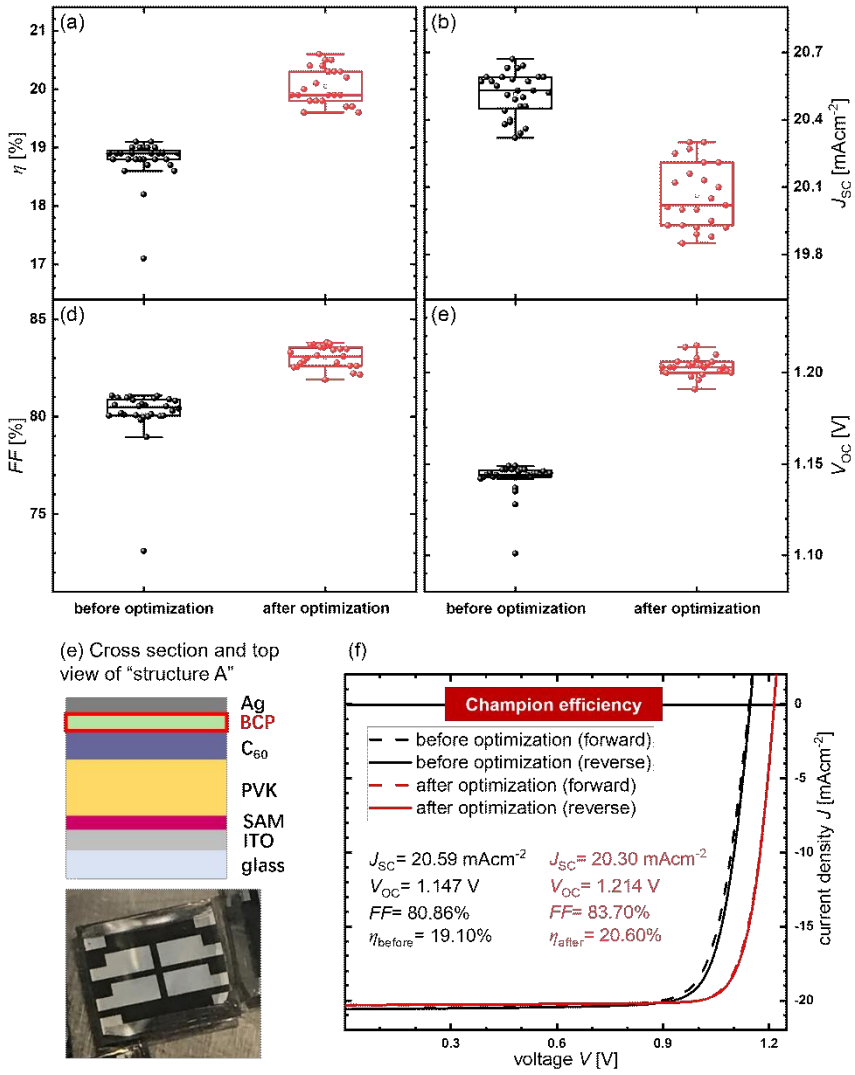

Figure 7.4.: *(a) η, (b) J_{SC}, (c) FF, and (d) V_{OC} statistics of the perovskite solar cells ("structure A") before and after the perovskite stack optimization. (e) Schematic of the cross section and realistic top view of "structure A". (f) Comparison of the JV curves of champion efficiencies before and after optimization.*

optimized established materials were prepared on the mirror-polished silicon bottom cells, the perovskite precursor exhibited extremely poor wettability, as the glass substrate with a relatively rough surface possesses a superior capacity for retaining precursor compared to the highly planar silicon wafer [167]. Through the substitution of Me-4PACz with MeO-2PACz, the perovskite precursor exhibited the capacity to fully cover the surface of mirror-polished silicon bottom cell, thereby facilitating the formation of a pinhole-free perovskite film in tandem solar cells.

Table 1. *Summary of the methodologies utilized for targeted optimization from bottom to top and the resultant enhancements.*

Targeted optimization	Resultant enhancements
Bottom cell: manual cutting →laser cutting	(i) Precisely control the size and shape of silicon bottom cell; (ii) avoid hidden cracks in silicon wafer; (iii) improve alignment between patterned layers. @Tandem device
HTLs: 2PACz → Me-4PACz	Enhance the band alignment at the HTL/perovskite interface to increase V_{OC}. @Structure A
HTLs: Me-4PACz→ MeO-2PACz	Improve the wettability of perovskite precursor on silicon bottom cell. @Tandem device
Perovskite: $Cs_{0.05}(FA_{0.83}MA_{0.17})_{0.95}Pb(I_{0.83}Br_{0.17})_3$ @E_g of 1.63 eV → $Cs_{0.05}(FA_{0.73}MA_{0.22})_{0.95}Pb(I_{0.78}Br_{0.22})_3$ + PMMA additive @E_g of 1.68 eV	(i) increase E_g to increase V_{OC}; (ii) incorporate PMMA additive to improve the wettability of perovskite precursor for a conformal coating; (iii) optimize the spin-coating program to improve perovskite crystallization; (iv) optimize the $t_{anisole}$ to improve the film quality of perovskite. @Structure A
Interfacial passivation: perovskite/C_{60} → perovskite/PEAI/C_{60}	Passivate the perovskite/C_{60} interface to reduce defects, suppress charge recombination and accumulation, increasing V_{OC} and *FF*. @Structure A
Cassette for perovskite top cell: initial → mid-term → advanced version (Chap. 4)	(i) mount the sample with it facing upwards instead of downwards to protect sample surface from scratches; (ii) decrease the side length of the slot to improve alignment between patterned layers; (iii) decrease the slot depth to avoid any vertical vibration of samples and press the sample surface tightly to the mask; (iv) fix the mask by screws instead of tapes to avoid sample moving out of the slot. @Tandem device

ALD-SnO_X: average η of 16% @inhomogeneous film → 18% @homogeneous film (Chap. 5)	Increase the flow rate of carrier gas, the pulse length of two precursors, and the pre-heating temperature of Sn precursor to address the inhomogeneity issue and statistical dispersion. @Structure B
ALD-SnO_X: average η of 18% → 20% (Chap. 5)	Optimize the T_{ALD}, R_{ALD}, and d_{SnOx} to reduce defects, facilitate carrier transport, suppress non-radiative recombination, and reduce R_S. @Structure B
Cassette for semi-transparent device: parallel connected cells → well-isolated cells (Chap. 6)	Decrease the slot depth to press the sample surface tightly to the mask to avoid shadowing effect. @Semi-transparent device
Sputtered-ITO & IZO: Optoelectrical characteristics (Chap. 6)	Optimize the r_{O2}, p_{ITO} and P_{ITO} to reduce parasitic absorption loss and electrical transport loss.
Sputtered-ITO: sputter damage → sputter-damage-free (Chap. 6)	Optimize the d_{SnOx} to mitigate sputter damage and S-shape in *JV* curves. @Semi-transparent device
Cassette for perovskite top cell: non-centered → centered U-shaped Ag electrode (Chap. 4)	(i) Decrease the side length of the slot to improve alignment between patterned layers; (ii) decrease the slot depth and fix the mask by screws instead of tapes to avoid sample moving out of the slot. @Tandem device

Regarding the emerging buffer layer, transparent electrode, adjacent interfaces, and U-shaped Ag electrode that are most likely to result in performance deterioration prior to targeted optimization, the diagnosis and problem-solving are challenging due to the complex configuration of the tandem device and require considerable duration. Consequently, the troubleshooting procedure was divided into a series of independent tasks based on the order of preparation in the tandem fabrication chain, which was effectively addressed using different transitional structures (chap. 5 and 6). The performance of the PSCs with "structure A", "structure B", and of the semi-transparent perovskite solar cells before and after troubleshooting/optimization are summarized and presented in Fig. 7.5(a-d). The two instances of performance decline caused by the insertion of SnO_X (structure B) and ITO (semi-transparent), respectively, were both significantly reduced after optimization, suggesting that this window stack is now suitable for utilization in tandem solar cells. Meanwhile, the deposition masks of perovskite top cells that were utilized for the workflow testing were improved to the mid-term version for better protection, alignment and determination of film area (Chap. 4). The methodologies utilized for targeted optimization

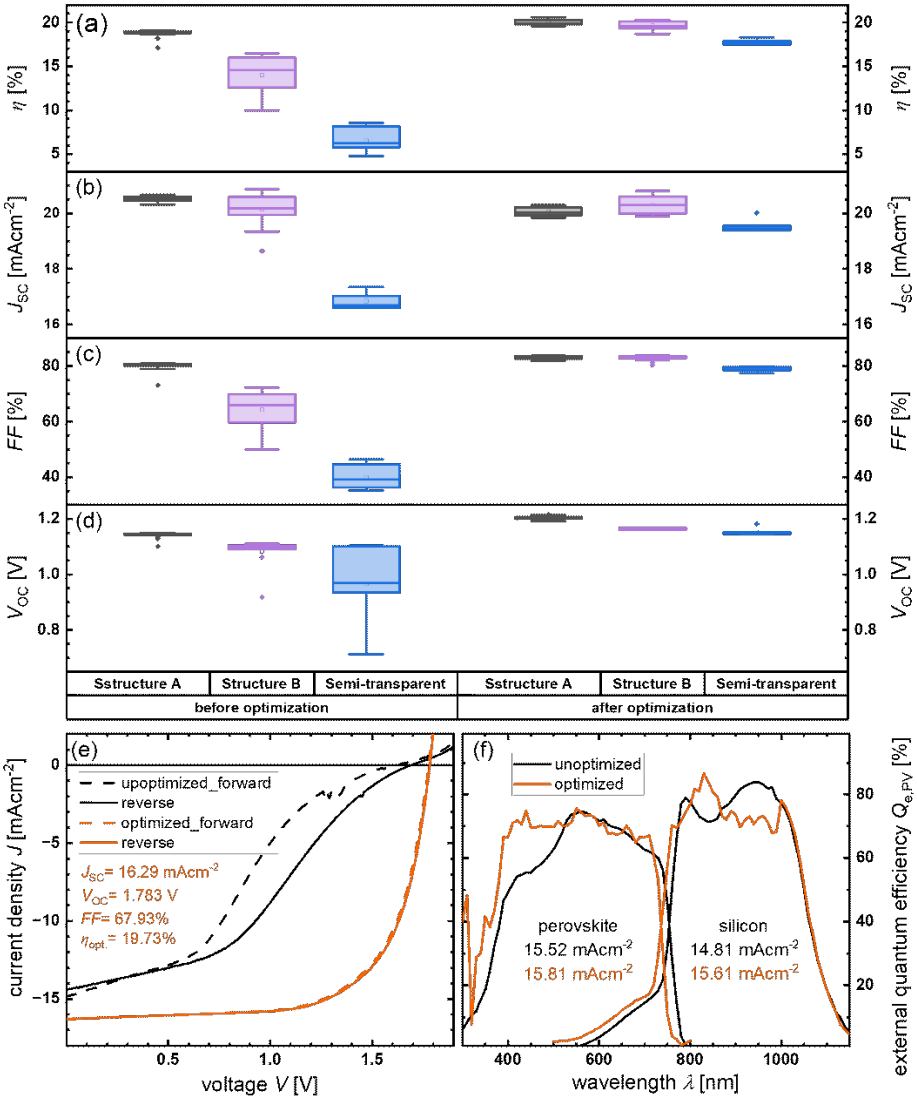

Figure 7.5.: *(a) η, (b) J_{SC}, (c) FF, and (d) V_{OC} statistics of the perovskite solar cells with "structure A", "structure B", and of the semi-transparent perovskite solar cells. Comparison of (e) the JV curves and (f) corresponding $Q_{e,PV}$ spectra of the unoptimized and optimized tandem solar cells.*

and the resultant enhancements are systematically organized and summarized in Table 1. In comparison to the optimal η of 9.39% achieved by the tandem solar cell for workflow testing, the champion η increased to 19.73% following the aforementioned comprehensive optimization, and the corresponding *JV* curves are presented in Fig. 7.5(e). This improvement was attributed to enhancements in all photovoltaic parameters, particularly the *FF* with an eliminated S-shape. The associated $Q_{e,PV}$ spectra exhibited an increase in photogenerated current for both subcells, as illustrated in Fig. 7.5(d).

7.2. From 19% to 31%: optoelectrical optimization

When the tandem solar cells with the highest η of 19.73% were fabricated in our laboratory, the world record for monolithic perovskite/silicon heterojunction tandem solar cells was 29.83% with an identical active area of 1 cm^2, achieved by the research group from HZB [167]. The corresponding photovoltaic parameters of our highest-performing device comprise a J_{SC} of 16.29 $mAcm^{-2}$, a V_{OC} of 1.783 V, and a *FF* of 67.93%, while for the HZB's highest-performing device, these parameters were 19.45 $mAcm^{-2}$, 1.90 V, and 80.90%, respectively. To reduce this performance disparity, various methodologies were implemented to enhance the η of our tandem solar cells, which are discussed in the subsequent sections.

7.2.1. From planar to nanotexture

First, the silicon substrates were changed from the DSP wafers with a planar surface to the DST wafers with a nanotextured surface for the improvement in J_{SC} due to better light trapping (Sec. 4.1.1). A planar surface is typically achieved through various polishing methods, including mechanical polishing, chemical polishing and chemical-mechanical planarization (CMP). Figure 7.6(a) presents images of the silicon bottom cells prepared on the wafers with diverse surface morphologies, wherein the appearance of the bottom cells with a planar surface prepared by CMP (mirror-polished) and by chemical polishing (alkaline-polished) exhibit distinct differences due to varying surface roughness. The surface morphology of the alkaline-polished silicon wafer was characterized using an optical microscope under increasing magnification, as shown in Fig. 7.6(b), while the

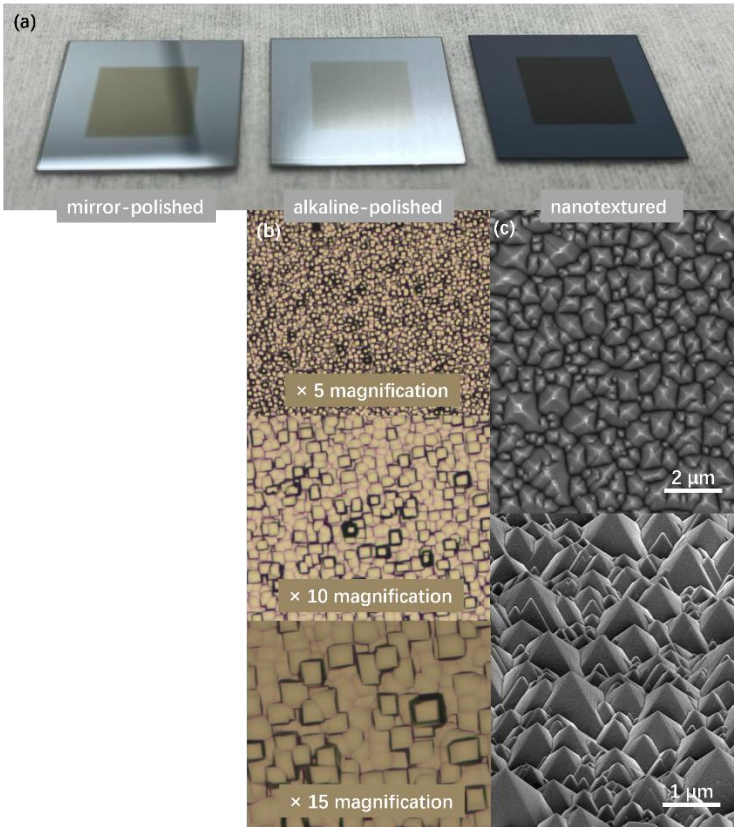

Figure 7.6.: *(a) Images of the silicon bottom cells using mirror-polished, alkaline-polished and nanotextured silicon wafers. (b) Optical microscope images of the top view of an alkaline-polished silicon wafer under increasing magnifications. (c) Top and cross-sectional images of a nano-textured silicon wafer.*

mirror-polished surface cannot be observed under any microscope due to high reflectivity. Figure 7.6(c) presents the top and cross-sectional SEM images of the nanotextured silicon wafer with lots of pyramids standing upright on the surface, which is achieved through the application of anisotropic etching solutions (e.g., KOH) to selectively etch (100) planes, forming pyramid-like structures. The application of mirror-polished wafers in 2T perovskite/silicon tandem solar cells presents two significant challenges. Firstly, the

extremely low surface roughness impedes the retention of the perovskite precursor due to a large contact angle, which increases the likelihood of pinhole formation. This phenomenon adversely affects device performance and yield [167], particularly with respect to V_{OC} and *FF*. Secondly, unlike nanotextured wafers that provide reflected incident light with a secondary opportunity to enter the silicon bottom cell, the high reflectivity of mirror-polished wafers results in substantial reflection losses. Furthermore, the silicon bottom cells fabricated on nanotextured wafers with pyramid dimensions below 1 μm facilitate the conformal coating of the perovskite layer through solution-based methodologies typically employed in the fabrication of high-efficiency perovskite/silicon tandem solar cells. As a result, double-sided nanotextured silicon wafers, rather than double-sided alkaline-polished silicon wafers, were utilized to prepare silicon bottom cells for subsequent optimization.

To evaluate the current gain resulting from a change in surface morphology of the silicon substrate from planar to textured, tandem solar cells were fabricated on two types of wafers: DSP FZ and DST CZ. To conformally cover the pyramids, the film thickness of perovskite in tandem devices was doubled to approximately 1 μm compared to the single-junction PSCs and was maintained constant, which prevented direct contact between HTL and ETL in the active area and consequently avoided the presence of non-diode *JV* curves. Furthermore, the HTL was modified from a single layer of MeO-2PACz to double layers of mix SAMs/PTAA, wherein the mix SAMs consisted of the Me-4PACz and MeO-2PACz in a volume ratio of 1:1, and the composition of perovskite was adjusted from $Cs_{0.05}(FA_{0.73}MA_{0.22})_{0.95}Pb(I_{0.78}Br_{0.22})_3$ to $Cs_{0.05}(FA_{0.8}MA_{0.15})_{0.95}Pb(I_{0.75}Br_{0.25})_3$ with an identical E_g of 1.68 eV. These adjustments was implemented to guarantee a conformal coating of the perovskite film on the nanotextured substrate. The comparison of the *JV* curves and corresponding $Q_{e,PV}$ spectra of planar and nanotextured tandem solar cells is given in Fig. 7.7(a, b). In addition to the optical enhancement in two subcells with the substrate shifted from planar to nanotextured, resulting in photogenerated current gains of 0.1~0.2 $mAcm^{-2}$, a significant increase in *FF* was observed, which could be attributed to a larger current gain in the silicon bottom cell as compared to that of the perovskite top cell. As FZ wafers are typically about a few tens to a hundred micrometers thicker than CZ wafers, the current gain due to improved light trapping of the dual-sided nanotextured surface was offset by the current loss owing to a thinner CZ wafer, thereby rendering the total current gain of tandem solar cells insignificant. Indeed, it was observed that the current gain resulting from the utilization of a thicker DST CZ wafer was imperceptible at the current stage because the J_{SC} of the tandem device was limited by the photogenerated

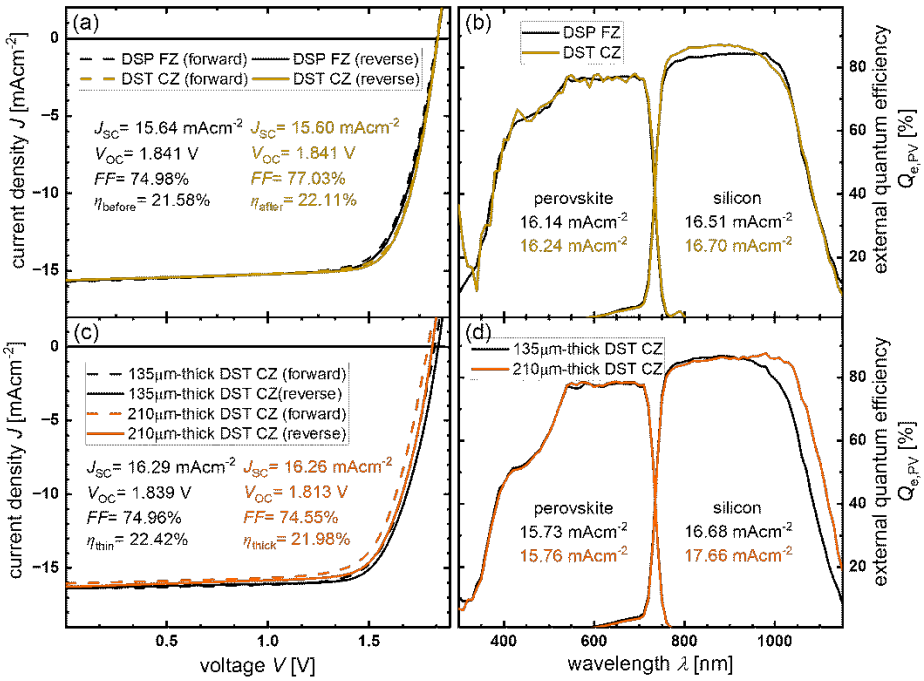

Figure 7.7.: *Comparison of the (a) JV curves and (b) corresponding $Q_{e,PV}$ spectra between the tandem solar cells fabricated using the DSP FZ and DST CZ silicon wafers. Comparison of the (c) JV curves and (d) corresponding $Q_{e,PV}$ spectra between the tandem solar cells fabricated using the* 135 *µm-thick and* 210 *µm-thick DST CZ silicon wafers.*

current of the perovskite top cell. In Fig. 7.7(c), by increasing the thickness of DST CZ wafers from 135 to 210 µm, the V_{OC} decreased due to a higher density of intrinsic defects in the thick wafer while the J_{SC} of tandem device was unaffected. A pronounced enhancement in the optical response at infrared wavelengths above 900 nm boosted the integrated current of the silicon bottom cell from 16.68 to 17.66 mAcm^{-2}, as shown in Fig. 7.7(d). Since the absorption coefficient is inversely proportional to the wavelength of incident light, increasing the thickness of silicon wafer is only effective in enhancing the optical response at long wavelengths. As the J_{SC} of 2T tandem solar cell was limited by the perovskite top cell with a lower integrated current of 15.76 mAcm^{-2}, the current gain in bottom cell failed to improve the overall J_{SC}.

7.2.2. Utilization of antireflective coating

The ARC is typically used to increase the J_{SC} of solar cells by reducing the light reflection from the film surface, thus allowing more incident light to enter the material, which utilizes the principle of interference by adjusting the refractive index and film thickness to fulfill the destructive interference condition following $d = \lambda/4n_{ref}$. For high-efficiency perovskite/silicon tandem solar cells, the predominant choice for ARC is MgF_2 [26,27]. Additionally, the texture cover can be utilized to enhance current due to a comparable light trapping effect [168]. The texture cover employed in our laboratory, designated as foil, was composed of an anti-fouling fluoropolymer topcoat and a durable non-yellowing high-end acrylic with a regular geometric texture sheet. The SEM image of the foil surface and the image of a tandem solar cell utilizing a foil ARC were presented in Fig. 7.8(a, b). Both types of ARCs were investigated in this study to enhance the current density of tandem devices, including a single foil ARC, a single MgF_2 ARC deposited via thermal evaporation, and double MgF_2/foil ARCs. The partial configurations of the tandem solar cells employing diverse ARCs were illustrated in Fig. 7.8(a).

Figure 7.8(b-g) presents the *JV* curves and corresponding $Q_{e,PV}$ spectra of the tandem solar cells without and with ARC, among which only the *JV* curves in Fig. 7.8(b) were measured without a protective glass inserted between the sun simulator and the tandem device, thus the J_{SC} was approximately 1 $mAcm^{-2}$ higher than that in other two scenarios. The impact of the protective glass utilized for measurements in ambient air will be discussed separately later. The implementation of a single foil ARC in tandem device increased the η from 22.01% to 24.39% primarily due to a significant increase in the J_{SC} of approximately 1 $mAcm^{-2}$ as extracted from *JV* characteristics, while the photogenerated current integrated using the $Q_{e,PV}$ spectra demonstrates that the current gain was nearly 0.5 $mAcm^{-2}$ due to the optical enhancement of the perovskite top cell in the wavelengths of 400~800 nm. The reason for this discrepancy could be attributed to the removal of the protective glass during *JV* measurement in the glovebox. For the scenario of MgF_2 ARC, the optical enhancement of the perovskite top cell enabled a significant current gain of around 1.5 $mAcm^{-2}$, as presented in Fig. 7.8(e), and a noteworthy phenomenon was observed that the current-limited subcell changed from the perovskite top cell to the silicon bottom cell. Although the shift of current-limited subcell resulted in a J_{SC} gain of less than 1.5 $mAcm^{-2}$, the η still increased by 2% because the *FF* also increased due to current mismatch, as shown in Fig. 7.8(d). Furthermore, double MgF_2/foil ARCs that were obtained by placing foil on top of

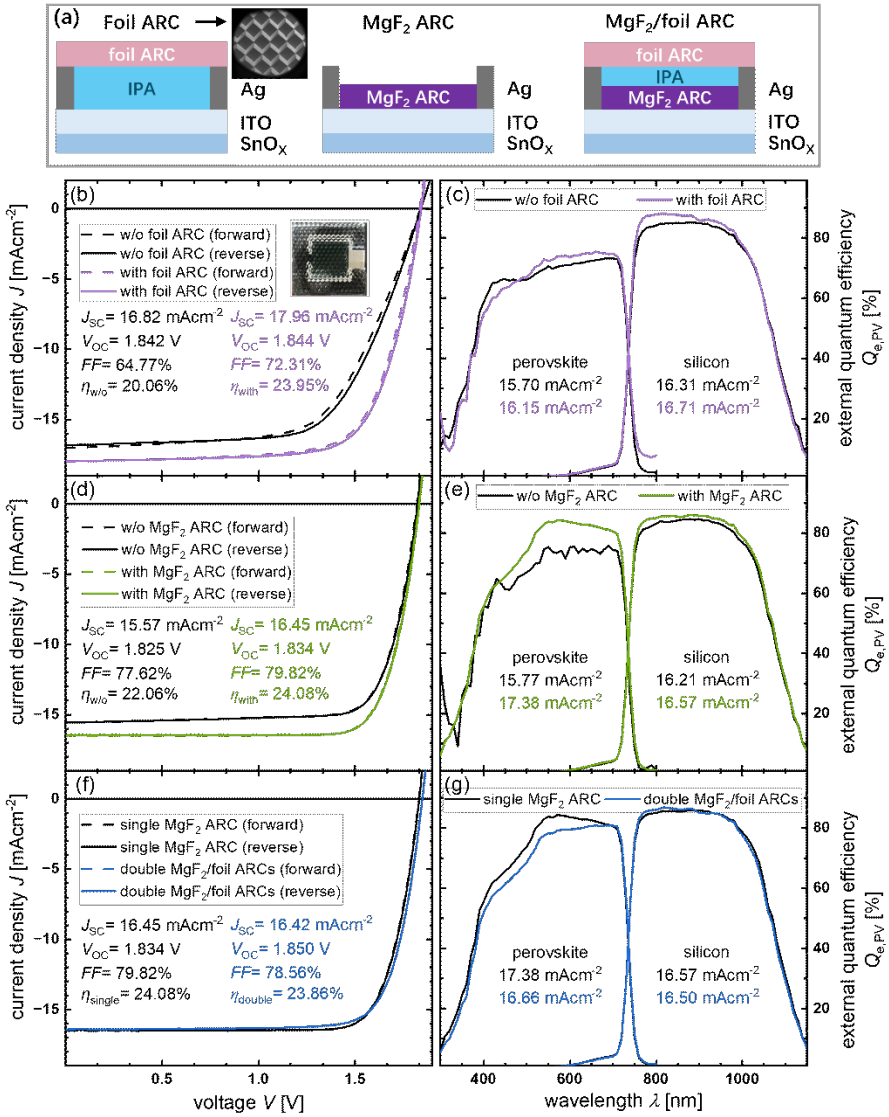

Figure 7.8.: *(a) Partial configurations of the tandem solar cells enploying diverse antireflective coating ARC. The SEM image of the foil surface was inserted. Comparison of the JV curves and corresponding $Q_{e,PV}$ spectra of the tandem solar cells without and with (b, c) foil ARC, (d, e) MgF_2 ARC, and f, g) double MgF_2/foil ARCs. The image of a tandem solar cell employed a foil ARC was inserted.*

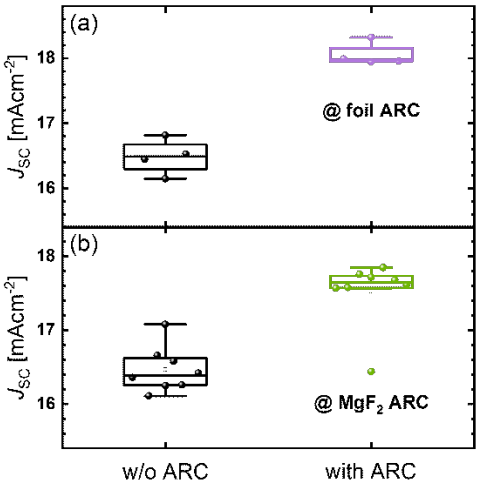

Figure 7.9.: *Statistics of the J_{SC} of tandem solar cells without and with a single a) foil and b) MgF_2 ARC.*

MgF_2 were implemented for evaluating whether the optical enhancement from both single ARC can be simultaneously. The *JV* curves and corresponding $Q_{e,PV}$ spectra of the tandem solar cells that were terminated with either a single MgF_2 ARC or double MgF_2/foil ARCs were compared in Fig. 7.8(f, g). The results demonstrate that the current gain from the implementation of double MgF_2/foil ARCs was equivalent to that from the utilization of a single ARC without further improvement.

Statistics of the J_{SC} of tandem solar cells without and with a single foil or MgF_2 ARC were compared in Fig. 7.9. The results demonstrate that both effectively improved the J_{SC} of tandem solar cells to an identical level. From a practical perspective, several issues arose with the use of foil: 1) Foil was attached to the surface of the tandem device through a liquid film of isopropanol, rendering it susceptible to movement on the surface due to the underlying liquid film and difficult to fix at the correct position; 2) The ITO film was prone to partial detachment when the foil was removed from the sample; 3) Ag electrodes were susceptible to deformation and detachment from the sample surface due to prolonged immersion in isopropanol solution; 4) Extended storage led to partial or complete volatilization of the isopropanol solution, resulting in gaps between the foil and the sample surface, leading to the detachment of foil and ultimately deteriorating the anti-reflection

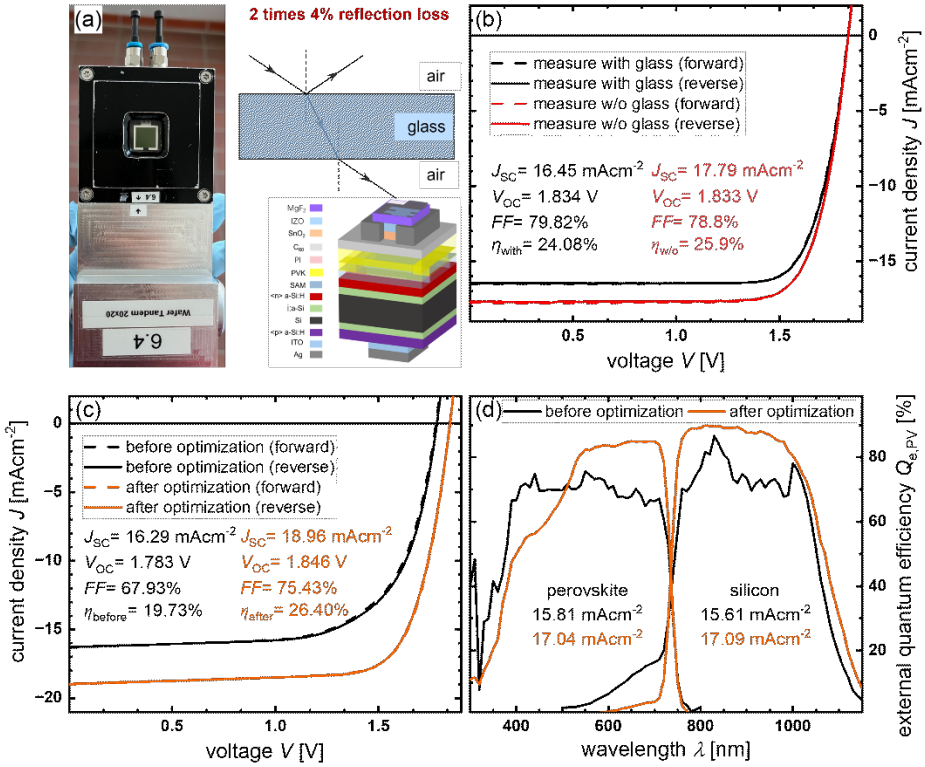

Figure 7.10.: *(a) Image of the measurement box with a tandem solar cell inside and schematic of reflection losses due to the glass lid. (b) JV curves of tandem solar cells without and with the glass of lid during measurement. Comparison of (c) the JV curves and (d) corresponding $Q_{e,PV}$ spectra of the tandem solar cells with champion efficiencies before and after the optimization of substrate morphology and ARC.*

effect. Therefore, MgF_2 was a more suitable choice than foil based on improved device performance and operational feasibility of the ARC, while double ARCs were not necessarily advantageous due to similar performance.

In our lab, the *JV* measurement was conducted in an N_2-filled glovebox using a measurement box, as depicted in Fig. 7.10(a), while the $Q_{e,PV}$ measurement was performed in ambient air using the same measurement box. Due to the inherent instability of perovskite

when exposed to ambient air, the tandem solar cell was positioned behind a protective quartz glass window in a sealed nitrogen-filled measurement box during $Q_{e,PV}$ measurement to prevent performance degradation. Consequently, the light source from the $Q_{e,PV}$ setup underwent two reflections at the air/glass interface prior to illuminating the devices, as depicted in Fig. 7.10(a), ultimately resulting in an underestimated current due to the reflection loss, which was calculated to be approximately 8%. During *JV* measurement, the tandem solar cell was similarly positioned behind a protective quartz glass window to avoid the artificial discrepancy of the current extracted from *JV* characteristics and $Q_{e,PV}$ spectra, but failed to reflect the true current value. Therefore, the performance of a representative tandem solar cell was measured with and without a protective glass to exclude the negative impact of artificial reflection loss, and the *JV* curves were presented in Fig. 7.10(b). The J_{SC} significantly increased from 16.45 to 17.79 mA/cm^{-2} with an increment ratio of 8.15%, which corresponded well with the calculated reflection loss, and the resultant η increased by almost 2%. Figure 7.10(c) demonstrates the champion η of 26.40% that was achieved by incorporating the aforementioned optical optimization in tandem fabrication, substantially higher than the champion η of 19.73% obtained before optimization (Fig. 7.5(e)). Compared with the photocurrent density of 17.04 mAcm^{-2} integrated using the $Q_{e,PV}$ spectra, the *JV* characteristics exhibited a higher J_{SC} value of 18.96 mAcm^{-2} due to the removal of the protective glass during *JV* measurements in the glovebox.

7.2.3. Optimization of Ag electrode

The electrical losses negatively impacted the device performance due to the lateral transportation of electrons within the ITO layer of the window stack before collection by the Ag electrode, particularly affecting the *FF*. For the semi-transparent PSCs, the active area of 0.16 cm^2 results in a maximum lateral transportation distance of electrons within the ITO layer of 4 mm. The application of a U-shaped Ag frame surrounding the patterned ITO film could potentially reduce this maximum distance by half to 2 mm, suggesting the possibility of achieving a higher *FF* in the semi-transparent PSCs. For similar purposes, a U-shaped Ag frame was incorporated atop the window stack to complete the fabrication of tandem solar cells, reducing the maximum distance of lateral electron transportation within the ITO layer from 10 to 5 mm. However, this reduced maximum transport distance of 5 mm still resulted in significant electrical losses, because the active area of the tandem device

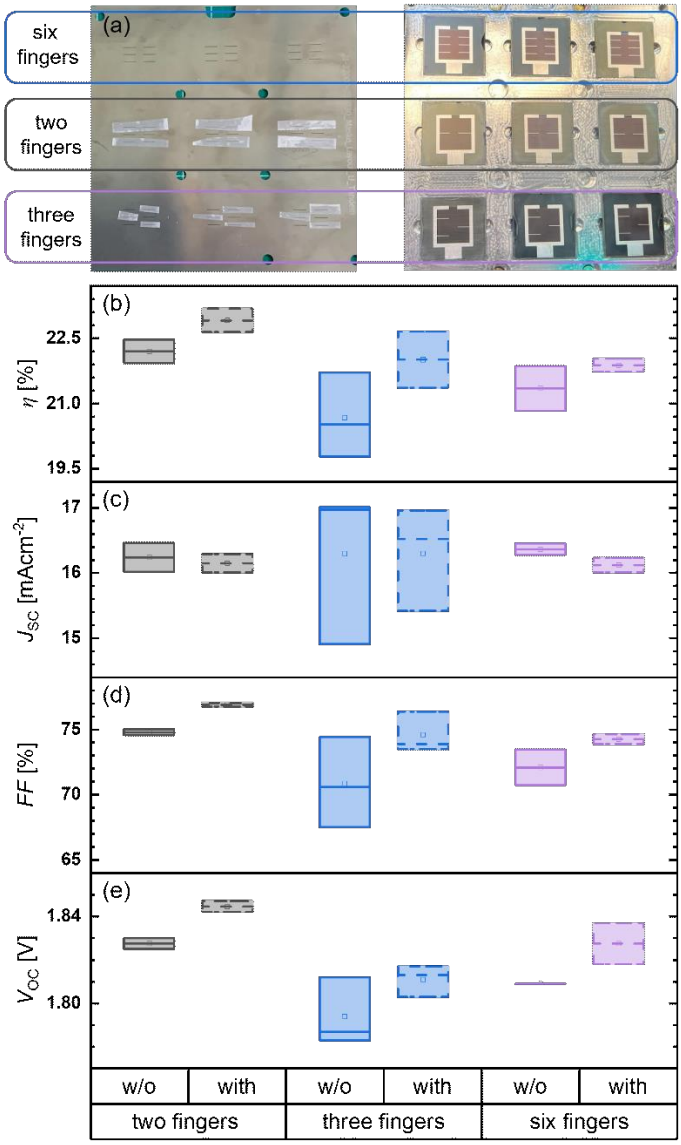

Figure 7.11.: *(a) Images of deposition masks and tandem solar cells after the deposition of Ag fingers. Comparison of (b) η, (c) J_{SC}, (d) FF, and (e) V_{OC} statistics of the tandem solar cells without and with two, three, and six Ag fingers.*

(1 cm^2) was more than six times larger than that of its semi-transparent counterpart, and this increase in area not only extended the maximum transport distance of electrons but also increased the difficulty in forming a pinhole-free perovskite light-absorbing layer, both of which impede high *FF*. The implementation of Ag fingers, also known as Ag grids, in the active area of SHJ solar cells has been demonstrated to effectively reduce electrical losses due to the decrease in the lateral transportation distance of electrons within the ITO layer, and subsequently, it was applied to monolithic tandem solar cells for the same purpose. In 2021 and 2023, the commonly reported width for Ag fingers was 100 μm [25,169], while the number of fingers (two, three, six) and their corresponding patterns varied among research groups without explicit justification.

A small tricky was employed to evaluate three existing finger patterns using a single deposition mask with nine identical patterns, as illustrated in Fig. 7.11(a). The three untaped patterns in the first row comprise six fingers, while the three taped patterns in the second and third rows consist of two and three fingers, respectively. This preliminary testing approach using a single deposition mask offers multiple advantages: a) a single batch of Ag deposition enables comparison between the performance of tandem solar cells employing Ag fingers with varying numbers and patterns; 2) once the optimal number and pattern of Ag fingers have been determined, the nine patterns on the deposition mask can be made consistent by applying tape, reducing the time and cost associated with re-manufacturing the deposition mask; and 3) the number and pattern of Ag fingers can be flexibly adjusted through the application of tape, depending on the requirements at different stages of efficiency improvement. The corresponding top view images of the nine tandem solar cells after the deposition of Ag fingers were depicted in Fig. 7.11(a), wherein the three devices in the first, second, and third rows employed six, two, and three Ag fingers, respectively. The statistics of the tandem solar cell without and with two/three/six Ag fingers were summarized in Fig. 7.11(b-e). Irrespective of the number and pattern of deposited Ag fingers, all tandem devices exhibited improved performance, primarily due to a significant *FF* gain exceeding 2% and an increase in V_{OC} of approximately 20 mV. This improvement was attributed to the decrease in the maximum transport distance of electrons, which effectively reduced the electrical losses caused by R_S, and to the likelihood of trap-assisted recombination prior to collection by the Ag electrode. A slight reduction in J_{SC} was attributed to the light shading induced by the opaque Ag fingers, and the shading ratio, defined as the total area of fingers to the active area of device, was calculated to be 0.8%, 1.2%, and 2.4% with increasing Ag fingers. The maximum transport distance of the tandem devices employing two Ag fingers was the longest among the three scenarios, and the

optical losses from light shading were minimal, while the opposite was observed for the scenario utilizing six Ag fingers. However, the contradictions in electrical and optical response by using Ag fingers did not indicate that three fingers were the optimal choice, which should be considered in conjunction with the thickness and R_{SH} of the ITO layer of the window stack. As reported in the literature, the utilization of six Ag fingers [25,26,169] was the mainstream choice for high-efficiency perovskite/silicon tandem solar cells.

7.2.4. Some critical layers

Nanotextured tandem solar cells outperformed than the planar counterpart due to significant current gain, and thus the perovskite layer thickness was intentionally increased to approximately 1 μm to ensure complete coverage of the pyramids on the nanotextured wafers. However, the low yield of the tandem solar cells prepared on the nanotextured silicon wafers obtained from industrial photovoltaic manufacturers demonstrated that not all pyramid sizes can be effectively controlled below 1 μm. The presence of even a single large pyramid exceeding 1 μm in the active area results in poor efficiency of the tandem device due to direct contact between the HTL and ETL, leading to shunting and potentially misrepresenting the true outcome of optimization. The occurrence of a small number of significantly larger pyramids presented a substantial challenge to the reproducibility and efficiency enhancement of nanotextured tandem solar cells. Consequently, planar tandem solar cells were simultaneously utilized for performance optimization prior to the preparation of uniformly nanotextured (< 1 μm) silicon wafers by our research group.

Regarding the nanotextured tandem devices, the perovskite top cell with a structure mix SAMs/4 nm PTAA/1 μm $Cs_{0.05}(FA_{0.8}MA_{0.15})_{0.95}Pb(I_{0.75}Br_{0.25})_3$/20 nm C_{60}/15 nm SnO_X/110 nm ITO/120 nm U-shape Ag frame was prepared on the nanotextured silicon bottom cells, wherein the perovskite layer was sufficiently thick to fully cover the pyramids and the mix SAMs/PTAA hole transporting bilayers were utilized to reduce charge-collection losses [170]. While the 1 μm-thick perovskite layer was no longer necessary for the planar tandem device, as it absorbed the majority of the incident light, only a small portion of the light reached and was absorbed by the silicon bottom cells, resulting in a low J_{SC}. In addition to the unfavorable current, the V_{OC} and FF of tandem solar cells were also affected by the thick perovskite due to a higher density of intrinsic defects and a scaling loss related to the finite conductivity of the transport layers. To further enhance the

efficiency of tandem solar cells, the HTL/perovskite layer stack was initially optimized using the opaque PSCs with "structure A", which allows the exclusion of other factors. The hole transporting bilayers of mix SAMs/PTAA were substituted with MeO-2PACz and the composition of the perovskite layer was modified from $Cs_{0.05}(FA_{0.8}MA_{0.15})_{0.95}Pb(I_{0.75}Br_{0.25})_3$ to $Cs_{0.05}(FA_{0.77}MA_{0.23})_{0.95}Pb(I_{0.77}Br_{0.23})_3$ with a reduced thickness while maintaining the same E_g of 1.68 eV. Second, the layer thickness of C_{60} decreased from 20 to 10 nm to reduce parasitic absorption losses; however, the corresponding current gain was observed exclusively in tandem devices rather than opaque PSCs, attributable to the direction of illumination during *JV* measurement. Figure 7.12(a-d) presented the comparison of the statistics between the opaque PSCs with "structure A" before and after the optimization of the HTL/perovskite/C_{60} layer stack. The optimum η increased from 19.28% to 21.15% with the average values of *FF* and V_{OC} increased by approximately 1.8% and 40 mV, respectively, which could be attributed to the enhanced valence band alignment at the HTL/perovskite interface and the suppression of nonradiative recombination. Although the implementation of a thinner perovskite light-absorbing layer decreased the mean J_{SC} value of opaque PSCs, a greater proportion of incident light would be absorbed by the silicon bottom cells when this thinner perovskite layer was utilized in the perovskite top cell, ultimately increasing the J_{SC} of the tandem device when the silicon bottom cell was the current-limited subcell.

Third, the 110 nm ITO transparent electrode was substituted with a 50 nm IZO transparent electrode to decrease the parasitic absorption of the window stack and enhance the current of tandem devices. Figure 7.12(e) illustrates the optical characteristics of 110 nm ITO and 50 nm IZO bare films deposited on quartz glass, demonstrating a significant reduction in the absorption spectrum at both the short wavelengths below 400 nm and the long wavelengths exceeding 900 nm due to a lower carrier concentration and suppressed FCA (Sec. 6.2.2), suggesting that the optical response of the perovskite top cell and the silicon bottom cell at the corresponding wavelength range would be enhanced simultaneously. It should be noted the thickness reduction inevitably increases the R_{SH} of TCO films according to the following equation

$$R_{SH} = \frac{\rho}{t} \qquad [7.1]$$

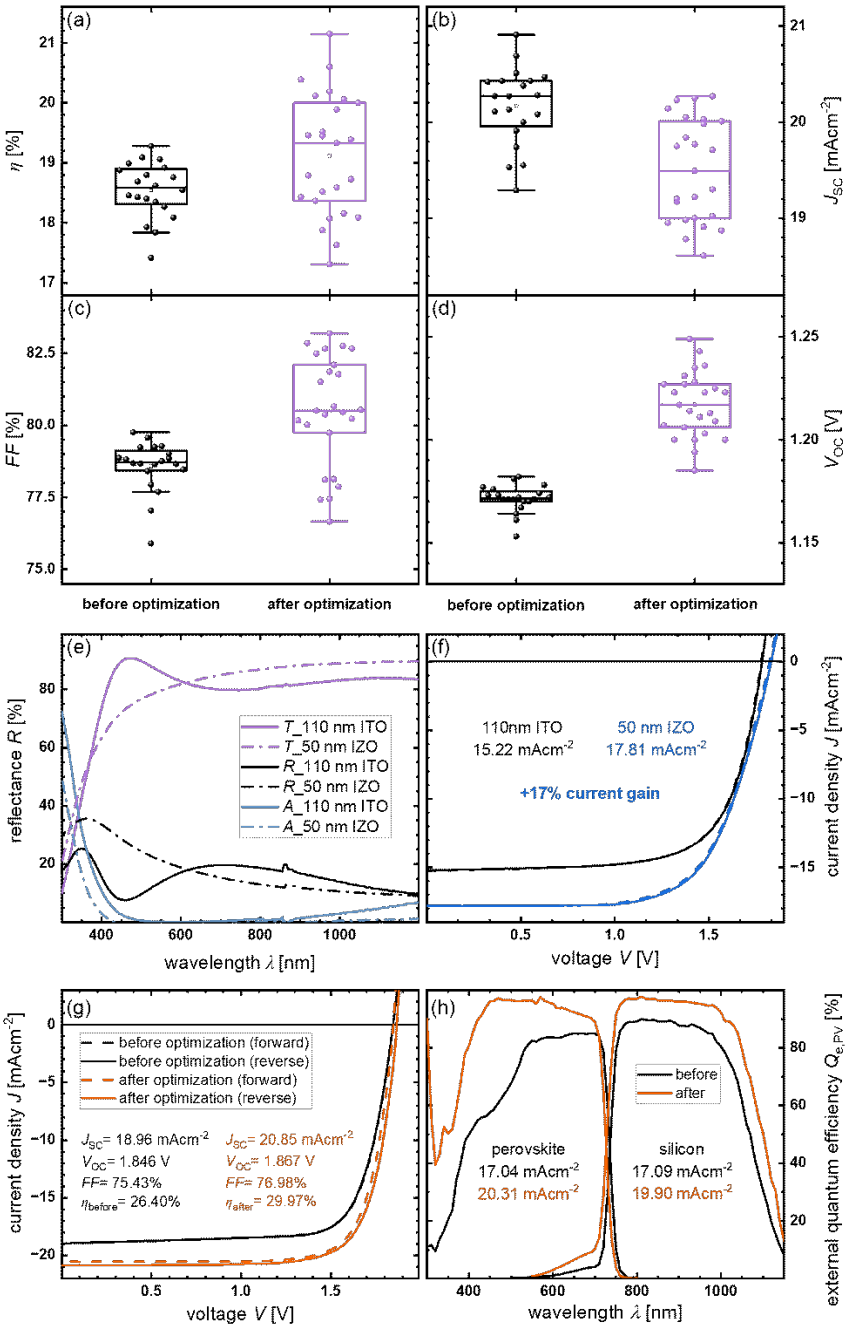
(a)
(b)
(c)
(d)
η [%]
J_SC [mAcm^-2]
FF [%]
V_OC [V]
before optimization
after optimization
(e)
(f)
reflectance R [%]
T_110 nm ITO
T_50 nm IZO
R_110 nm ITO
R_50 nm IZO
A_110 nm ITO
A_50 nm IZO
wavelength λ [nm]
110nm ITO
15.22 mAcm^-2
50 nm IZO
17.81 mAcm^-2
+17% current gain
current density J [mAcm^-2]
voltage V [V]
(g)
(h)
before optimization (forward)
before optimization (reverse)
after optimization (forward)
after optimization (reverse)
J_SC= 18.96 mAcm^-2
V_OC= 1.846 V
FF= 75.43%
η_before= 26.40%
J_SC= 20.85 mAcm^-2
V_OC= 1.867 V
FF= 76.98%
η_after= 29.97%
perovskite
17.04 mAcm^-2
20.31 mAcm^-2
silicon
17.09 mAcm^-2
19.90 mAcm^-2
before
after
external quantum efficiency Q_e,PV [%]

Figure 7.12.: *Comparison of (a) η, (b) J_{SC}, (c) FF, and (d) V_{OC} statistics of single-junction perovskite solar cells with "structure A" before after the optimization of the HTL/perovskite/C_{60} layer stack. (e) Comparison of transmittance, reflectance and absorption between* 110 *nm ITO and* 50 *nm IZO bare films deposited on quartz glass. (f) Comparison of the JV curves of the representative tandem solar cells employing a* 110 *nm ITO and* 50 *nm IZO transparent electrode. Comparison of (g) the JV curves and (h) corresponding $Q_{e,PV}$ spectra of the tandem solar cells exhibiting champion efficiencies before and after the optimization of the HTL/perovskite/C_{60} layer stack, transparent and Ag electrodes.*

where ρ and t are the resistivity and the thickness of the conductive materials, respectively. The R_{SH} of 50 nm IZO film was 80±5 Ω/sq, which was larger than the R_{SH} of 80±5 Ω/sq of 110 nm ITO film. The implementation of Ag fingers effectively reduces the R_S losses caused by the lateral transport of the electrons within the TCO layer with a larger R_{SH} through decreasing the maximum transport distance of electrons, which is dependent on the following equation

$$R_S = R_{SH}\frac{L}{W} \qquad [7.2]$$

where L is the length in direction of current flow and W is the width of the electrode. From the practical perspective, L represents the maximum transport distance of 1.2 mm as six fingers were utilized in tandem solar cells, and W was constant. By employing a thinner IZO transparent electrode in tandem solar cells, a promising current gain of approximately of 17% was obtained from the *JV* characteristics in Fig. 7.12(f).

All the aforementioned optimizations were employed in the fabrication of tandem solar cells to evaluate performance enhancement, including the HTL/perovskite layer stack, the layer thickness of C_{60}, the materials and layer thickness of the transparent electrode, and the Ag fingers. Prior to optimization, the tandem structure was nanotextured SHJ/1 nm mix SAMs/4 nm PTAA/1 µm $Cs_{0.05}(FA_{0.8}MA_{0.15})_{0.95}Pb(I_{0.75}Br_{0.25})_3$/20 nm C_{60}/15 nm SnO_X/ 110 nm ITO/120 nm U-shape Ag frame, while the nanotextured SHJ/1 nm MeO-2PACz/ 1 µm $Cs_{0.05}(FA_{0.77}MA_{0.23})_{0.95}Pb(I_{0.77}Br_{0.23})_3$/10 nm C_{60}/15 nm SnO_X/50 nm IZO/120 nm U-

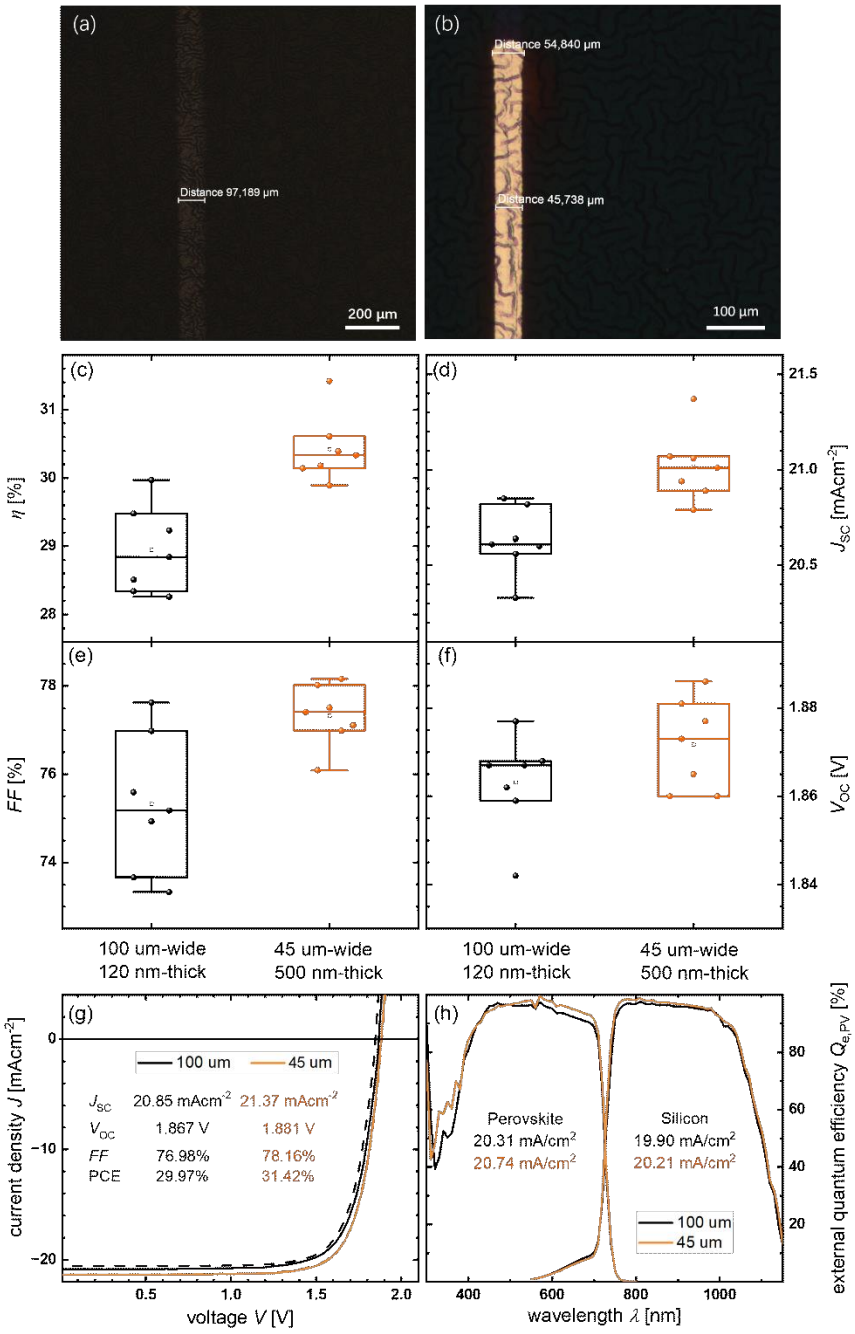
(a)
Distance 97,189 µm
200 µm
(b)
Distance 54,840 µm
Distance 45,738 µm
100 µm
(c)
η [%]
(d)
J_{SC} [mAcm^{-2}]
(e)
FF [%]
(f)
V_{OC} [V]
100 um-wide
120 nm-thick
45 um-wide
500 nm-thick
100 um-wide
120 nm-thick
45 um-wide
500 nm-thick
(g)
100 um
45 um
J_{SC} 20.85 mAcm^{-2} 21.37 mAcm^{-2}
V_{OC} 1.867 V 1.881 V
FF 76.98% 78.16%
PCE 29.97% 31.42%
current density J [mAcm^{-2}]
voltage V [V]
(h)
Perovskite
20.31 mA/cm^2
20.74 mA/cm^2
Silicon
19.90 mA/cm^2
20.21 mA/cm^2
100 um
45 um
wavelength λ [nm]
external quantum efficiency $Q_{e,PV}$ [%]

Figure 7.13.: *Optical microscope images of the Ag fingers deposited on tandem solar cells with a width of (a)* 100 *µm and (b)* 45 *µm. Schematic of the experimental flow. Comparison of (c) η, (d) J_{SC}, (e) FF, and (f) V_{OC} statistics of the tandem solar cells using either* 100 *µm-wide,* 120 *nm-thick Ag fingers or* 45 *µm-wide,* 500 *nm-thick Ag fingers. Comparison of (e) the JV curves and (f) corresponding $Q_{e,PV}$ spectra of the tandem solar cells with champion efficiencies before and after Ag electrode optimization.*

shape Ag frame/120 nm Ag fingers (six) represented the new structure after optimization. Figure 7.12(g) presents a comparative analysis of the *JV* curves for the champion devices, wherein all photovoltaic parameters exhibited improvement, particularly J_{SC} . The corresponding $Q_{e,PV}$ spectra demonstrate a significant optical enhancement for both perovskite top and silicon bottom cells across the entire wavelength range, as presented in Fig 7.12(h). A current gain of 1.89 mAcm^{-2} was achieved through the utilization of a thinner C_{60} film and a thinner IZO film with superior optoelectrical properties compared to the ITO film (Sec. 6.2.2). A voltage gain of 21 mV can be primarily attributed to the enhanced valence band alignment at the HTL/perovskite interface and the suppression of nonradiative recombination, while a *FF* gain of 1.55% resulted from both the optimized HTL/perovskite layer stack and the implementation of six Ag fingers, which significantly reduced the R_S losses.

Finally, the shadow ratio of six Ag fingers to the active area was reduced from 2.22% to 1.08% through decreasing the finger width from nearly 100 µm to approximately 45 µm, which further enhances J_{SC}. Figure 7.13(a, b) presented the optical microscope images of both fat and narrow Ag fingers deposited on tandem solar cells. The η, J_{SC}, *FF*, and V_{OC} statistics of the tandem solar cells employing either 100 µm-wide, 120 nm-thick or 45 µm-wide, 500 nm-thick Ag fingers were compared in Fig. 7.13(c-f), wherein an approximate gain of 0.4 mAcm^{-2} and 2% were observed for both average J_{SC} and *FF* due to the reduced shading ratio and increased height-to-width ratio of Ag electrode. With the average η increased by exceeding 1%, a maximum efficiency of 31.42% was obtained. The comparison of *JV* curves and corresponding $Q_{e,PV}$ spectra of tandem solar cells with champion efficiencies were provided in Fig. 7.13(g, h), wherein the perovskite top and silicon bottom cells exhibited similar current gain. In summary, with a series of optoelectrical optimizations, encompassing surface morphology, selection of materials,

layer thickness and device structure, the highest efficiency of tandem solar cells effectively increased from 19% to 31% with all photovoltaic parameters being improved.

7.3. From 31% to 33%: surface treatment

Although semi-transparent PSCs have a similar configuration to that of the perovskite top cell, different substrates significantly affected the coverage of HTL and the crystalline growth of the perovskite layer due to alterations in morphology and wettability of the substrate surface. Surface treatment on the ITO-coated substrate is critical for achieving high-efficiency perovskite-related solar cells, which removes chemical residuals on the surface, improves surface wettability and modifies the work function of ITO. The question arises whether it is appropriate to directly transfer the surface treatment from single-junction to tandem devices. In this section, the impact of O_2 plasma treatments, which are used for cleaning the surface of the commercial ITO-coated glass substrate prior to the spin-coating of organic layer stack in our laboratory, on the performance of tandem solar cells was studies through a systematic characterization of the electrical and structural properties of relevant bare films and layer stacks, providing insight into the significance of surface treatment for the ICL, HTL and perovskite layers.

7.3.1. Impact of surface treatment on tandem solar cell

Prior to the spin-coating of HTL, the silicon bottom cell underwent O_2 plasma treatment for 12 min at a power of 50 W, a procedure directly adapted from the fabrication process of single-junction PSCs. In this process, the duration and power of O_2 plasma treatment were specifically optimized to remove chemical residuals, enhance surface wettability, and achieve an optimum Φ for the commercial ITO film on the glass substrate to fabricate high-efficiency PSCs. Although the highest η of our tandem solar cells fabricated using DST CZ silicon substrate has surpassed 30%, further efficiency enhancement necessitates addressing the issue of a low *FF* below 80% (Fig. 7.13(g)), which significantly constrains the device performance relative to J_{SC} and V_{OC}. Considering (1) the modifying effect of O_2 plasma treatment on the Φ of ITO film, and (2) the distinct role of the ITO film as the transparent electrode in single-junction PSCs and as the ICL in perovskite/silicon tandem solar cells,

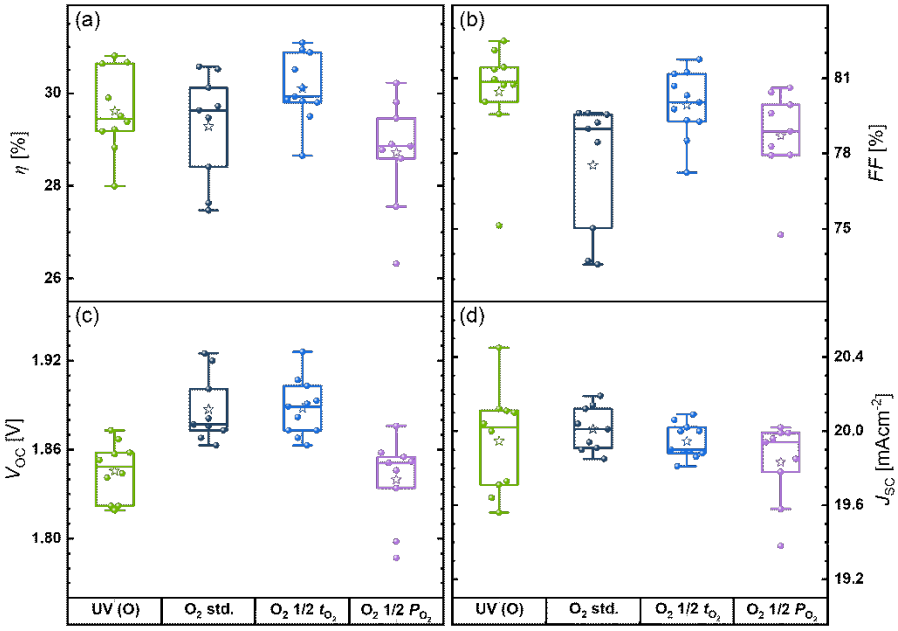

Figure 7.14.: *Comparison of (a) η, (b) J_{SC}, (c) FF, and (d) V_{OC} statistics of the tandem solar cells with the silicon bottom cells treated by O_2 plasma and UV(O) treatments.*

the optimization of surface treatment on the silicon bottom cells was necessary and essential for achieving high *FF*.

Initial experiments were conducted to examine the effects of various surface treatments on tandem solar cell performance. Four distinct surface treatment protocols were applied to the silicon bottom cells before HTL spin-coating: (i) standard O_2 plasma treatment (O_2 std.) for 12 min at 50 W, (ii) half-duration O_2 plasma treatment (O_2 1/2 t_{O_2}) for 6 min at 50 W, (iii) half-power O_2 plasma treatment (O_2 1/2 P_{O_2}) for 12 min at 25 W, and (iv) UV(O) treatment for 50 min with default parameters. Statistical analysis of the treated tandem devices, presented in Figure 7.14, revealed that UV(O) and O_2 1/2 t_{O_2} treatments enhanced the average *FF* value to over 80% compared to the O_2 std. treatment, while O_2 1/2 P_{O_2} showed no *FF* improvement. Nevertheless, the extended UV(O) treatment led to a significant reduction in V_{OC} for the tandem devices relative to the O_2 1/2 t_{O_2} treatment, as illustrated in Fig. 7.14(c). This decline was attributed to the dehydrogenation

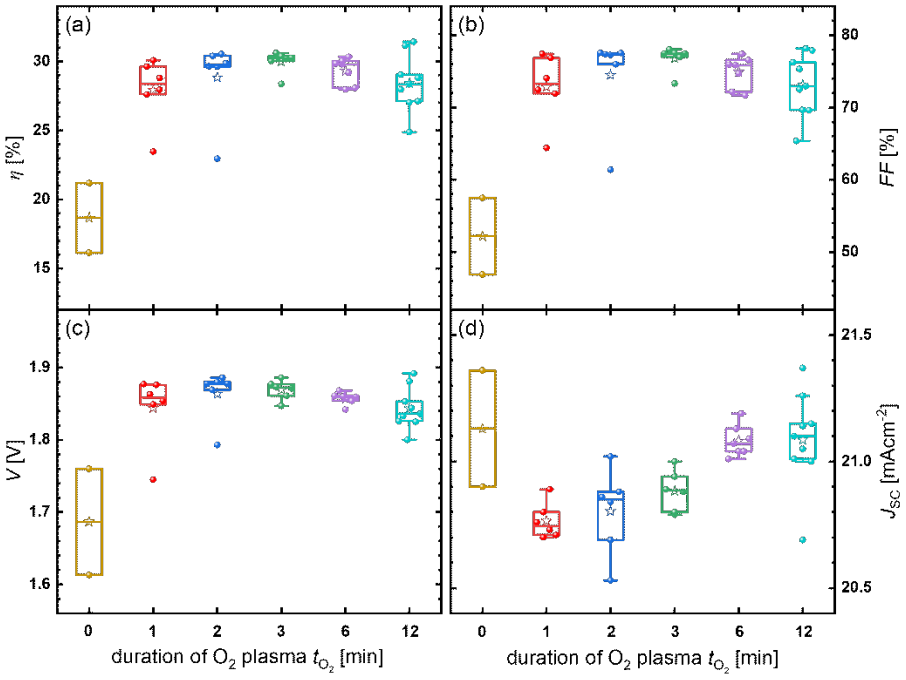

Figure 7.15.: *Comparison of (a) η, (b) J_{SC}, (c) FF, and (d) V_{OC} statistics of the tandem solar cells with the silicon bottom cells treated by O_2 plasma treatment as a function of treatment duration t_{O_2}.*

of the interfacial passivation in the silicon bottom cells and was substantiated by additional experiments that demonstrated a marked decrease in V_{OC} for single-junction SHJ solar cells following 50 min UV(O) treatment. Given that J_{SC} remained relatively constant across all four scenarios, the tandem devices processed with O_2 1/2 t_{O_2} treatment prior to HTL spin-coating achieved the highest η. These findings suggest that shortening the O_2 plasma treatment duration is an effective strategy for enhancing the *FF* of tandem solar cells.

A comprehensive optimization of the O_2 plasma treatment duration (t_{O_2}) was conducted to examine the variations in device performance as a function of treatment duration ranging from 0 to 12 min, while maintaining a constant power of 50 W. As illustrated in Fig. 7.15, when silicon bottom cells were not subjected to O_2 plasma treatment (t_{O_2} = 0 min), the average η was below 20% and the J_{SC} exhibited artificially high values

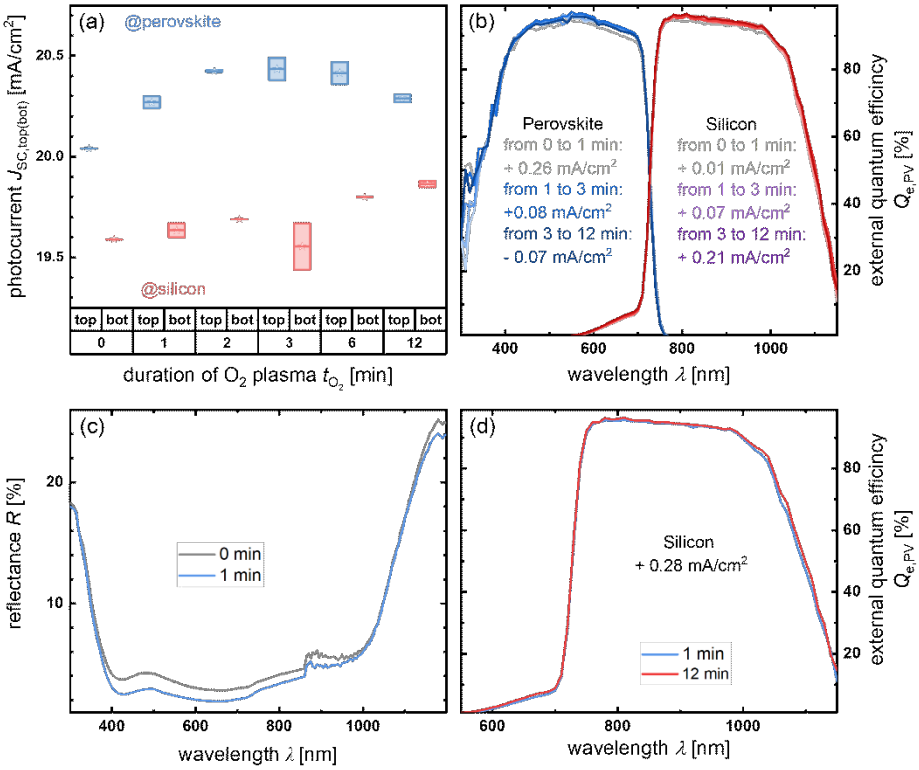

Figure 7.16.: *(a) Integrated short-circuit current density statistics of the perovskite top cells and silicon bottom cells in the tandem solar cells as a function of the duration of O_2 plasma treatment t_{O_2}. (b) $Q_{e,PV}$ spectra of representative tandem solar cells with increasing treatment duration.*

due to significant shunting. In contrast, the average η markedly improved to approximately 30% upon application of O_2 plasma prior to the spin-coating of HTL, even with a minimal t_{O_2} of 1 min. As t_{O_2} increased to 3 min, the average η reached its maximum value with minimal variance, subsequently declining with further increases in t_{O_2} due to deterioration of both *FF* and V_{OC}. The trends observed in *FF* and V_{OC} closely mirrored those of η, while J_{SC} continued to increase with prolonged treatment duration. To elucidate the changes in J_{SC}, V_{OC}, and *FF* as a function of t_{O_2}, systematic measurements and characterizations were

conducted to thoroughly examine the corresponding films and layer stacks susceptible to the O_2 plasma treatment.

The photocurrent statistics of the perovskite top and silicon bottom cells with increasing t_{O_2}, as determined by $Q_{e,PV}$ measurement, are depicted in Figure 7.16(a). These findings reveal that the J_{SC} of the tandem device was constrained by the photocurrent of the silicon bottom cell, which exhibited an increase proportional to t_{O_2}. Conversely, the perovskite top cell's photocurrent peaked at 3 min. Notably, the current mismatch between subcells also reached its maximum at 3 min, coinciding with the highest *FF* observed for this time frame (Fig. 7.15(b)). Figure 7.16(b) presents the $Q_{e,PV}$ spectra of representative tandem solar cells, indicating that for t_{O_2} values below 3 min, optical enhancement was predominantly observed at short wavelengths, yielding a photocurrent gain of approximately 0.26 $mAcm^{-2}$ in the perovskite top cell. When t_{O_2} surpassed 3 min, the primary optical enhancement transitioned to longer wavelengths, resulting in a photocurrent gain of about 0.21 $mAcm^{-2}$ in the silicon bottom cell. As illustrated in Figure 7.16(c), a comparison of reflectance spectra for representative tandem solar cells with and without 1 min O_2 plasma treatment demonstrates that the 0.26 $mAcm^{-2}$ photocurrent gain in the perovskite top cell was attributable to significantly reduced reflection losses across its entire wavelength range. In contrast, Figure 7.16(d) shows that 12 min of O_2 plasma treatment, compared to the 1 min scenario, equivalently enhanced the infrared response of silicon bottom cells at wavelengths exceeding 1000 nm, consequently increasing the photocurrent by 0.28 $mAcm^{-2}$.

7.3.2. Impact of surface treatment on silicon bottom cell

Figure 7.15(c) demonstrates that the V_{OC} of tandem solar cells decreased as the t_{O_2} exceeded 3 min. To investigate the underlying cause, we initially examined the effect of the O_2 plasma treatment on the performance of the silicon bottom cells and the alterations in the corresponding films that are susceptible to the surface treatment. Considering the characteristics of O_2 plasma treatment, two factors are most likely to contribute to the degradation of silicon bottom cells: (1) the etching effect of partially ionized O_2, comprising equal numbers of positive ions, electrons, and neutrals [171], on the ITO surface; (2) the degradation effect of UV light [172,173], generated by plasma radiation, on the hydrogen passivation for silicon layers. An experiment was designed to assess the impact

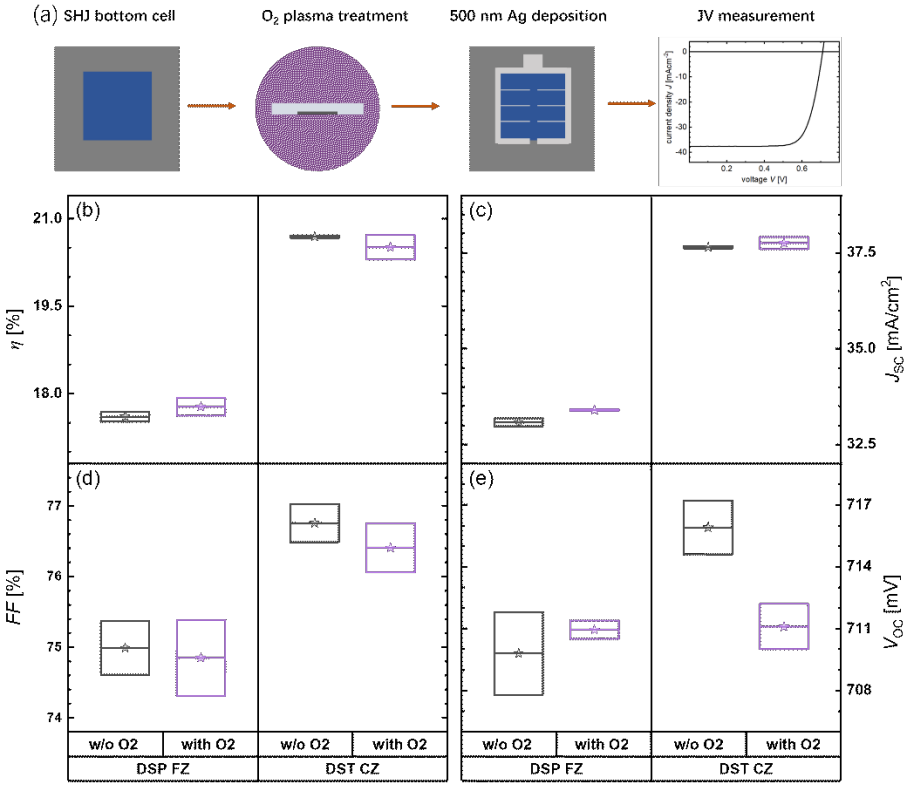

Figure 7.17.: *(a) Schematic of the experimental flow. Comparison of (b) η, (c) J_{SC}, (d) FF, and (e) V_{OC} statistics of the silicon bottom cells fabricated using two types of wafers without and with O_2 plasma treatment before top Ag electrode deposition.*

of O_2 plasma treatment on the performance of complete silicon bottom cells fabricated using either DSP FZ or DST CZ silicon wafers, with identical fabrication procedures. Figure 7.17(a) presents the schematic of the experimental procedure: first, half of the silicon bottom cells were subjected to O_2 plasma treatment for 12 min, while the remaining half were not treated; second, 500 nm Ag frame and fingers were thermally evaporated on the top surface of both untreated and treated silicon bottom cells simultaneously; finally, all the complete cells underwent *JV* measurement, and the corresponding statistical results were plotted in Fig. 7.17(b-e). In the case of DST CZ, the O_2 plasma treatment marginally

decreased the average η value compared to the untreated counterpart due to reductions of approximately 3% and 5 mV in *FF* and V_{OC}, respectively, which is consistent with the typical behavior of unencapsulated silicon solar cells under UV exposure. Conversely, the performance of silicon bottom cells fabricated on DSP FZ wafers slightly improved due to a small current gain, while the *FF* and V_{OC} remained unaffected. These results suggest that the reduction in the V_{OC} of the tandem solar cells was partially attributable to the UV degradation of the silicon bottom cells during the extended O_2 plasma treatment. Furthermore, compared to the CZ silicon wafers with a higher density of intrinsic defects and shorter carrier lifetime, the FZ wafers appear to be a more suitable choice for the preparation of high-efficiency perovskite/silicon tandem solar cells due to their UV-degradation-resistant nature.

KPFM mapping was conducted to characterize the etching effect on the ITO layer by comparing the surface roughness of DST silicon bottom cells without (t_{O_2} = 0 min) and with (t_{O_2} = 3 min) O_2 plasma treatment. It was observed that the mean roughness (Ra) of the ITO surface in the DST silicon bottom cells decreased significantly from 109 nm for the scenario of t_{O_2} = 0 min to 66.3 nm for t_{O_2} = 3 min, as illustrated in Fig. 7.18(a, f). The corresponding topography histogram in Fig. 7.18(b, g) also exhibited a less dispersed distribution after O_2 plasma treatment. These findings suggest that the surface roughness of the ITO layer in the silicon bottom cells decreased due to the etching effect of the O_2 plasma. Figure 7.18(c, h) presents the results of surface potential mapping of the ITO layer without and with O_2 plasma treatment, wherein a reduction was observed in the potential mean roughness from 124 to 91 mV, indicating a more homogeneous potential distribution on the ITO surface following O_2 plasma treatment. The corresponding potential histogram in Fig. 7.18(d, i) also exhibited a less dispersed distribution after O_2 plasma treatment. From both theoretical and practical perspectives, the reductions in surface and potential roughness of the ITO layer in the silicon bottom cells are advantageous for the conformal coverage of the subsequent SAM molecules and the vertical growth of perovskite crystalline. Additionally, UPS measurements were performed to monitor the ϕ of the ITO layer in the silicon bottom cells, and the results demonstrate that the O_2 plasma treatment for 3 min significantly increased the ϕ of the ITO layer, as depicted in Fig. 7.18 (e, j). The increment in the ϕ of the ICL is expected to affect both V_{OC} and *FF* of tandem solar cells; however, further investigations are required to gain deeper insight into this phenomenon.

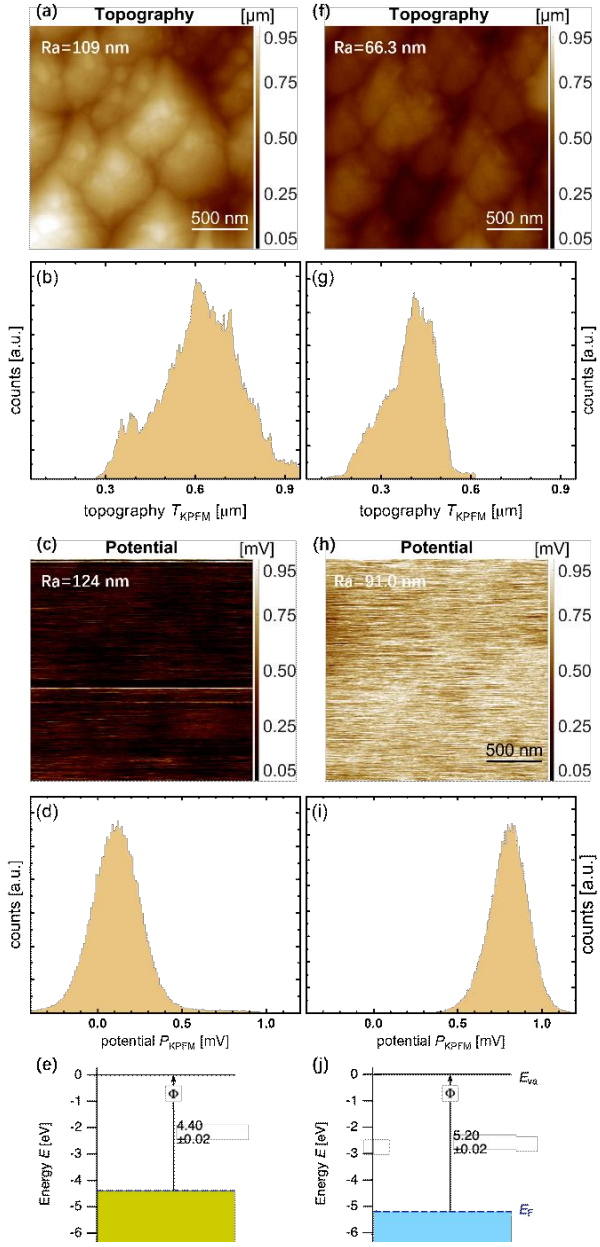

Figure 7.18.: *(a) KPFM surface roughness mapping, (b) corresponding topography histogram, (c) KPFM surface potential mapping, (d) corresponding potential histogram,*

and (e) schematic of the energy levels of the ITO layer in the DST silicon bottom cells without O_2 plasma treatment. (f) KPFM surface roughness mapping, (g) corresponding topography histogram, (h) KPFM surface potential mapping, (i) corresponding potential histogram, and (j) schematic of the energy levels of the ITO layer in the DST silicon bottom cells with O_2 plasma treatment.

7.3.3. Impact of surface treatment on perovskite top cell

For the perovskite top cell, the implementation of O_2 plasma treatment for substrate cleaning significantly influences the properties of subsequent organic layers prepared using a solution-based spin-coating method. Initially, high-resolution XPS measurement and KPFM potential mapping were conducted to elucidate the coverage of MeO-2PACz molecules atop the ITO layer. Figure 7.19(a, e) and (b, f) compare the indium and phosphorus core spectra of two samples: MeO-2PACz spin-coated onto the DST silicon bottom cells without and with O_2 plasma treatment. The coverage factors of MeO-2PACz on the ITO layer were calculated by the phosphorus-to-indium (P:In) atomic ratio, where the phosphorus atom originates from the -$PO(OH)_2$ group of the MeO-2PACz molecule and indium was one of the main components of ITO, which determines the molecular concentration of spin-coated MeO-2PACz and reflects the extent of film coverage [23]. The coverage factors were calculated to be 0.21 and 0.26 for the samples without and with O_2 plasma treatment, respectively. The increase in the coverage factor indicates that the O_2 plasma treatment implemented on the silicon bottom cells effectively enabled more conformal coverage of MeO-2PACz molecules on the ITO surface. Figure 7.19(c, g) and (d, h) compare the KPFM potential mapping and corresponding potential histogram of both samples, wherein the half-reduced Ra of surface potential from 137 to 67 mV and a less dispersed potential distribution also demonstrated a more conformal distribution of MeO-2PACz molecules on the ITO surface with the silicon bottom cell treated by O_2 plasma. Consequently, these results demonstrate that the O_2 plasma treatment effectively improves the conformal coverage of MeO-2PACz due to a less rough ITO surface with homogeneous potential distribution.

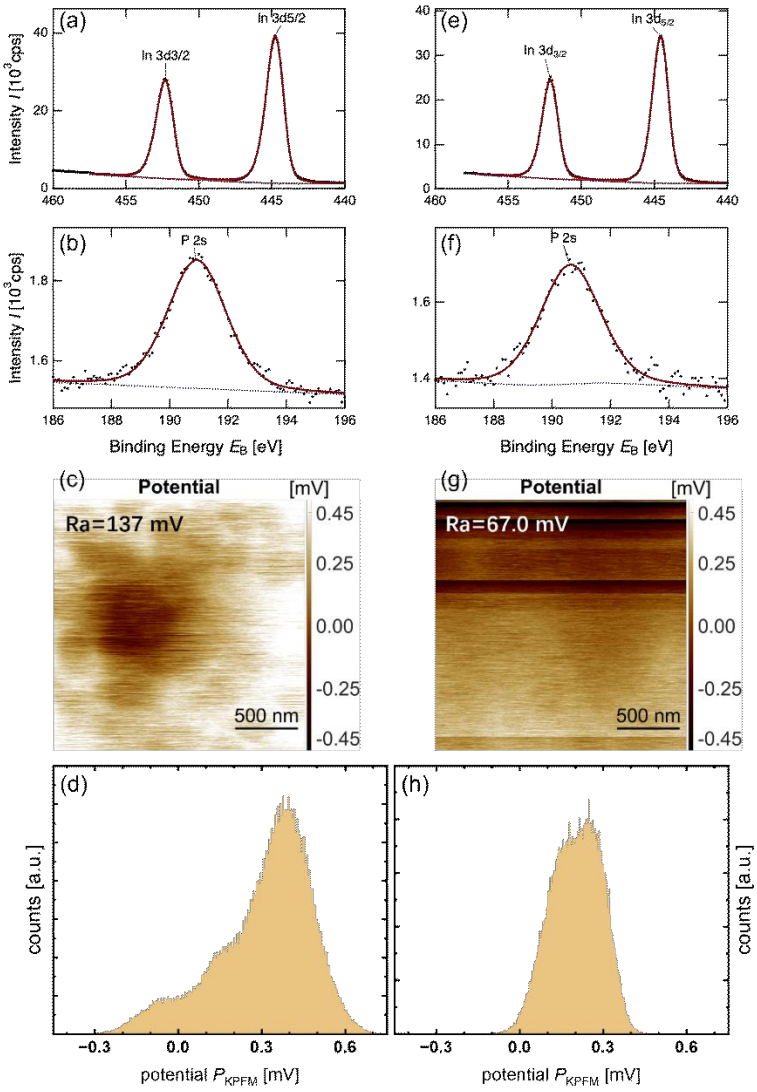

Figure 7.19.: *(a) Indium core spectra, (b) phosphorus core spectra, (c) KPFM surface potential mapping, and (d) corresponding potential histogram of the MeO-2PACz layer spin-coated onto the DST silicon bottom cells without O_2 plasma treatment. (e) Indium core spectra, (f) phosphorus core spectra, (g) KPFM surface potential mapping, and (h) corresponding potential histogram of the MeO-2PACz layer spin-coated onto the DST silicon bottom cells with O_2 plasma treatment.*

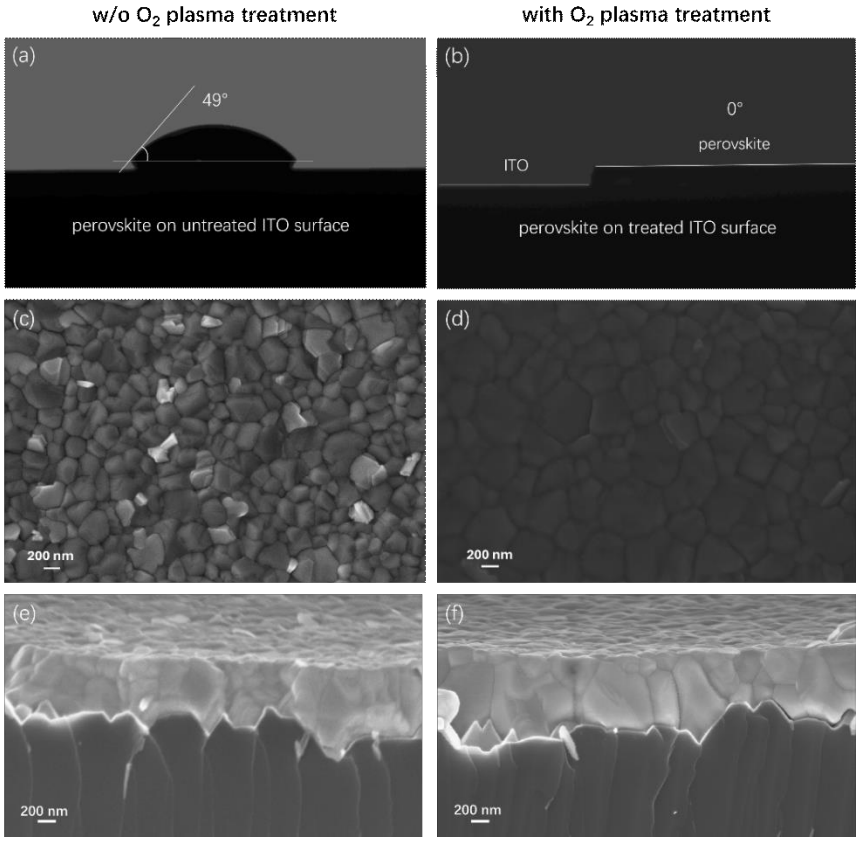

Figure 7.20.: *Contact angle of the perovskite precursor on the different ITO surfaces (a) without and (b) with O_2 plasma treatment. Top-view SEM images of the SHJ/MeO-2PACz/perovskite layer stack (c) without and (d) with O_2 plasma treatment. Cross-section SEM images of the SHJ/MeO-2PACz/perovskite layer stack (e) without and (f) with O_2 plasma treatment.*

The wettability of perovskite precursors on the substrate surface is equally critical as the substrate morphology for the vertical growth of perovskite crystalline. Contact angle measurements were conducted to investigate the impact of O_2 plasma treatment on the wettability of the perovskite precursor on the surface of the semi-device with a structure of nano-textured SHJ/MeO-2PACz. From a macroscopic perspective, the perovskite precursor

rapidly spread on the surface of the semi-device cleaned by O_2 plasma treatment prior to the spin-coating of MeO-2PACz. In Fig 7.20(a, b), the contact angle of 49° measured from the untreated sample was completely eliminated once O_2 plasma treatment was implemented, demonstrating that the wettability of the perovskite precursor was significantly improved. Subsequently, SEM measurements were conducted on the nanotextured SHJ/MeO-2PACz/perovskite layer stack to compare the crystallization of the perovskite layer. The top view SEM images of the layer stack without and with the implementation of O_2 plasma treatment are presented in Fig. 7.20(c, d), wherein an increase in grain size and decrease in film roughness were observed from the perovskite layer spin-coated on the treated silicon bottom cell compared to the untreated counterpart. The corresponding cross-section SEM images measured on the same samples illustrate that for the treated sample, the size of a portion of the perovskite grains was equivalent to the layer thickness, and the adjacent grain boundaries are perpendicular to the substrate surface, as shown in Fig. 7.20(f). However, for the untreated sample, the grain size of the perovskite was significantly smaller than the layer thickness, resulting in a higher density of grain boundaries with random orientations and rough surface, as shown in Fig. 7.20(e). The larger the grain size, the fewer the grain boundaries. The horizontal grain boundary generally acts as a recombination center for charge carriers, and its negative impact on final device performance is difficult to mitigate. In contrast, the vertical boundary typically acts as a shunting pathway, but it can be effectively blocked by surface passivation of the crystallized perovskite film. The ideal case for carrier transport within the crystallized perovskite film would be transport through a single grain with a size as large as the layer thickness instead of transport through grain boundaries. These results demonstrate that O_2 plasma treatment effectively improved the wettability of the perovskite precursor on the silicon bottom cells, consequently improving the crystallization of the perovskite layer, enhancing optical response, and suppressing carrier recombination.

Prior to the optimization of the surface treatment, the highest η of tandem solar cells was 31.24% with a suboptimal *FF* of 78.16%. It was observed that reducing the t_{O_2} of the O_2 plasma treatment that was implemented onto the silicon bottom cells significantly improved the *FF* to 81.78%, resulting in an optimal η of 32.84%, as illustrated in Fig 7.21(a). A corresponding voltage gain of 53 mV could be attributed to the changes in the ϕ of the ITO layer and the density of grain boundaries within the perovskite layer. Comparison of the $Q_{e,PV}$ spectra in Fig 7.21(b) revealed that the silicon bottom cell was the current-limiting subcell, and the photocurrent decreased from 20.21 to 20.01 $mAcm^{-2}$ due to a reduction in

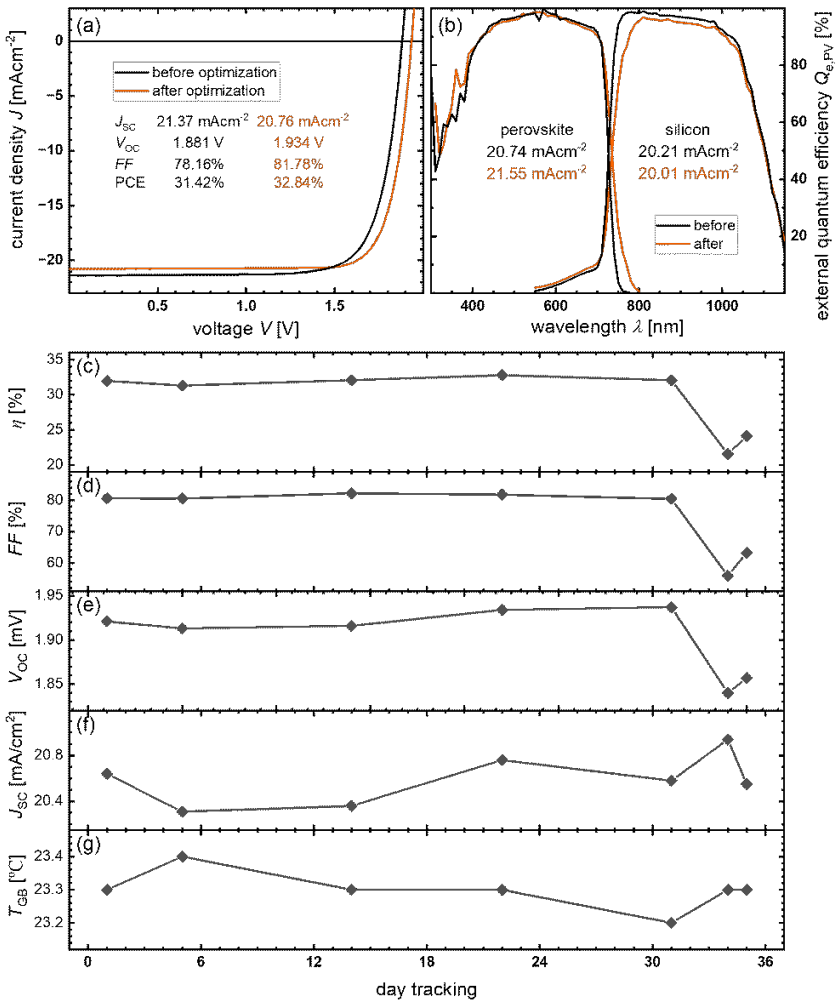

Figure 7.21.: *Comparison of (a) the JV curves and (b) corresponding $Q_{e,PV}$ spectra of the tandem solar cells with champion efficiencies before and after the optimization of surface treatment. (c-g) Performance tracking of champion device.*

the optical response at the long wavelength range of 700-1100 nm. However, the corresponding enhanced optical response at wavelengths of 700-800 nm improved the photocurrent of the perovskite top cell from 20.74 to 21.55 mAcm^{-2}, which was perhaps

related to the increased layer thickness of perovskite due to the increased grain size. The current mismatch between the two subcells increased significantly from 0.53 to 1.54 $mAcm^{-2}$, which partially contributed to the *FF* gain. Stability tracking was conducted for the champion device by measuring the *JV* curves and the temperature inside the N_2-filled glovebox (T_{GB}) during measurements on different days. Figure 7.21(c-f) presents the changes in η, *FF*, V_{OC}, J_{SC}, and T_{GB} as a function of the day of *JV* measurements, wherein η, *FF*, and V_{OC} remained nearly constant from day 1 to day 31, while a significant performance decay was observed on day 34 due to shunting. The J_{SC} and T_{GB} fluctuated within ranges of 20.3-21.0 $mAcm^{-2}$ and 23.2-23.4 ℃, respectively. These results demonstrate that the perovskite/silicon tandem solar cells exhibited good stability for over a month when stored in the N_2-filled glovebox at room temperature, and the η slightly increased during the period of stability tracking.

Prior to the surface treatment, a wet-chemical cleaning methodology was generally implemented to obtain clean substrates for the fabrication of high-efficiency PSCs. In our laboratory, the commercial ITO-coated glass substrates were typically ultrasonically cleaned with organic solvents (acetone and isopropanol) and subsequently stored in containers filled with clean isopropanol, which has been established as a standard cleaning process. Prior to the spin-coating of the transporting layer, the glass substrates were removed from the isopropanol-filled containers, dried with clean N_2, treated with O_2 plasma, and immediately transferred to the glovebox. As demonstrated by preliminary experiments in our laboratory, the ultrasonic cleaning with acetone and isopropanol did not affect the performance of complete SHJ solar cells; however, a potential peel-off of the back Ag electrode might cause issues. Therefore, the ultrasonic cleaning was substituted with dynamic spin-coating and was utilized on the silicon bottom cells prior to the O_2 plasma treatment to investigate whether it could further improve the η of tandem devices. An advantage of the wet-chemical cleaning is the removal of dirt particles on the surface of the silicon bottom cells that were introduced during the laser cutting process and the initialization of the surface status to a similar level. In tandem-related literature, only a subset of research groups adopts similar wet-chemical methods using ethanol [167] to clean the silicon bottom cells before surface treatments without indicating the resultant enhancement. In this study, the silicon bottom cells fabricated with DST FZ silicon wafers were divided into two groups: (i) as-prepared and (ii) wet-chemical cleaned by dynamic spin-coating ethanol and isopropanol (3000r/3s/30s). Subsequently, both groups were treated by O_2 plasma for 3 min and fabricated into complete tandem solar cells

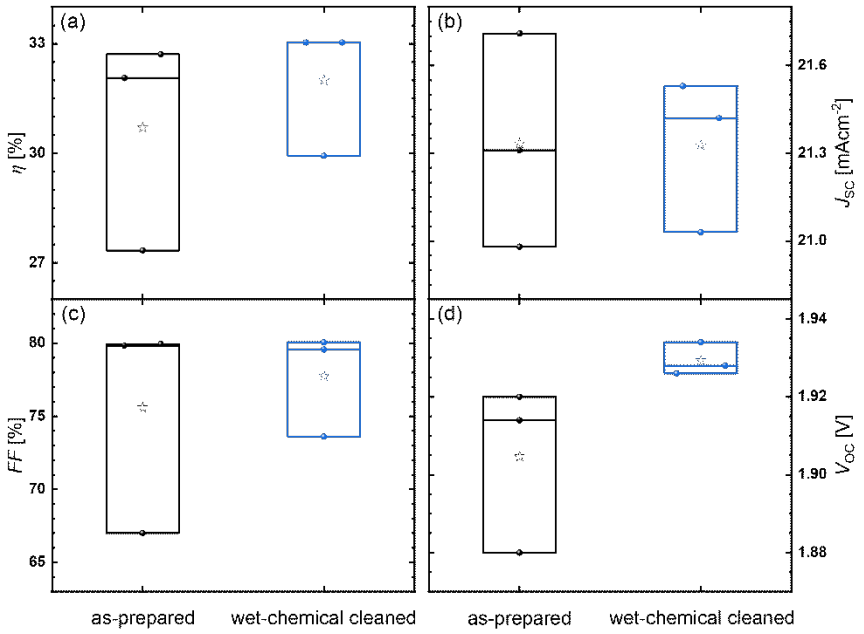

Figure 7.22.: *Comparison of (a) η, (b) J_{SC}, (c) FF, and (d) V_{OC} statistics of tandem solar cells without and with wet cleaning of silicon bottom cells prior to O_2 plasma treatment for 3 min.*

simultaneously under the same preparation conditions. Consequently, the question of whether the wet-chemical cleaning of the silicon bottom cells improves or degrades the performance of the perovskite/silicon tandem solar cells was addressed through comparing the device performance of these two groups. In Fig. 7.22, the wet-chemical cleaned tandem solar cells exhibited the highest η of 33% and a reduced statistical dispersion compared to that of the as-prepared counterpart, which was primarily due to a significant voltage gain with minimum dispersion, while the J_{SC} and *FF* were minimally affected. The results demonstrate that the wet-chemical cleaning of the silicon bottom cells prior to the O_2 plasma treatment further improved the η of tandem devices and reduced the statistical dispersion.

In conclusion, the implementation of surface treatment is essential for achieving high-efficiency perovskite-related solar cells, and meticulous optimization of the treatment process is necessary for solar cells fabricated on diverse substrates, as it affects the

properties of the treated layer in multiple aspects, thereby influencing the growth and function of subsequent layers. Consequently, the concurrent modifications in multiple critical layers due to surface treatment will have a complex and significant impact on device performance.

8. Summary and Outlook

The objective of this thesis was to develop monolithic perovskite/silicon tandem solar cells and systematically enhance their efficiency to approach the world record. In particular, it focuses on the C_{60}/SnO_X/ITO contact as the final and decisive step in the development of high-efficiency tandem devices, wherein (i) the development and optimization of the fabrication process for perovskite/silicon tandem solar cells, (ii) the development and optimization of tin oxide as the buffer layer and study of working mechanisms, (iii) the development and optimization of transparent conductive oxides as transparent electrode in the perovskite top cells and semi-transparent perovskite solar cells, and (iv) the improvement of workflow and efficiency for tandem solar cells have been investigated. From an experimental standpoint, all approaches are directed towards the development of high-efficiency monolithic perovskite/silicon tandem solar cells. Concurrently, from a scientific research perspective, a comprehensive understanding of the working mechanism of tin oxide buffer layer and the origin of sputtering damage induced by transparent conductive oxides is thoroughly explored through both experiments and numerical simulations to offer valuable insights. This chapter summarizes the principal findings of this thesis and provides recommendations for further research endeavors.

8.1. Fabrication process of solar cells

8.1.1. Summary

For the development and optimization of the fabrication process for monolithic perovskite/silicon tandem solar cells, we first determined the device configurations according to both the configurations that were reported by tandem-related literature and the

configurations of the single-junction silicon heterojunction and perovskite solar cells fabricated in our institute. After figuring out the composition and function of each film, the preparation tools, reactive sources, the film thickness, area, pattern and alignment in the tandem devices were determined subsequently. With the sample structure finalized, the initial version of the deposition mask was designed and put into use. Due to the lack of experience in preparing monolithic perovskite/silicon tandem solar cells at the initial phase, we encountered a lot of unexpected problems when using the initial masks, including film misalignment, superficial scratching, dual-sided depositing, excessive area, random movement of sample, and mask bending. In fact, depending on the chamber's construction and features of various deposition tools that are required for the preparation of specific films either in full area or in targeted patterns, the way of placing sample is diverse: (i) flat or vertical, (ii) facing upwards or down; and (iii) rotating or stationery. By taking these factors into consideration, the second (mid-term) version was designed, and the practical use proved that most of the problems encountered previously had been resolved. However, the problem of film misalignment still existed as the thin silicon wafers moved around in the slot during rotation and transportation and even moved out of the slot when the cassette was flipped over, consequently seriously affected cell performance. Therefore, after careful consideration, the wafers were designed to be tightly pressed by the deposition mask and holder in the last (advanced) version of cassette without leaving any space and possibility for any movement. With the continues optimization of deposition masks, both efficiency and yield of tandem solar cells were effectively enhanced, and most importantly, a stable fabrication chain was established that allows for repeatable preparation of tandem solar cells, laying a good foundation for subsequent efficiency evolution and related fundamental research.

8.1.2. Outlook

Upscaling

Due to (i) the limited working space in the deposition chambers, such as thermal evaporator (C_{60}, Ag, MgF_2), ALD (SnO_X) and magnetron sputtering (ITO, IZO), and (ii) strict requirements on the area of the patterned films, up to 9 cells were prepared simultaneously in one batch of experiments. By the end of 2024, the maximum number of the tandem devices that could be prepared in a single batch in our lab has been upscaled from 9 to the

upper limit of 16 through the adjustment of our previous cassette and deposition masks, but the resultant statistics are still limited and cannot support the simultaneous comparison between a large number of cell performance under a wide range of conditions. Therefore, it is still necessary to further upscale the output of tandem solar cells that can be prepared in one batch through upgrading the deposition tools.

Sample transport

The entire fabrication chain of tandem solar cells takes place in the wetbench, PECVD, sputtering tools, laser cutting, spin-coater in the glovebox, thermal evaporator and ALD, which are distributed in different laboratories. The sample transport from one tool to another involves transport between different laboratories and working atmosphere (N_2, ambient air, and vacuum). During the entire process, the impact of unwanted contamination and even material degradation on cell performance are difficult to evaluate, thereby we should strictly control the introduction of these potential disadvantages, such as transporting samples using a N_2-filled transport box to avoid direct contact with air.

8.2. Tin oxide buffer layer

8.2.1. Summary

Materials and devices

At the initial phase of developing tandem solar cells, we found that the unoptimized SnO_X film exhibited extremely poor homogeneity, which affects both the efficiency and yield due to imperfect mitigation of sputter damage, poor electrical properties and passivation quality. After the adjustment of deposition parameters, a homogeneous SnO_X film with saturated growth was prepared and utilized to fabricate opaque perovskite solar cells. With the optimization of reaction temperature in, precursor ratio, and SnO_X film thickness, the performance of the opaque perovskite solar cells incorporating a SnO_X between C_{60} and Ag

electrode was close to that of the reference devices employing BCP, suggesting that the robust materials properties and ohmic electrical contacts at adjacent interfaces lay a good foundation for further fabrication of semi-transparent and tandem solar cells.

Working mechanism

Similar to the BCP film, the SnO_X is an insulating film as well, and they are in the same place in the perovskite-related solar cells. Theoretically, the risk of obtaining a low efficiency increases with a thicker insulating film employed in a solar cell. During the optimization process of perovskite solar cells incorporating a SnO_X, we observed that the increase in the SnO_X film thickness from 5 to 15 nm enhanced the device efficiency to a maximum value and further thickness increment did not deteriorate cell performance. However, the phenomenon is contrast to what we observed in the reference devices employing BCP, wherein further increase in the BCP film thickness significantly reduced the device efficiency. From existing publications, independent research has rarely been conducted on the working mechanisms of SnO_X as a buffer layer in the perovskite/silicon tandem solar cells. Therefore, we conducted a series of experiments, characterizations, and simulations to understand the working mechanism of SnO_X at the C_{60}/Ag interface in inverted PSCs, which can serve as an ideal reference for understanding the working mechanism of SnO_X in perovskite top cells. Both the photoluminescence and quantum efficiency measurements revealed that thicker SnO_X layer suppresses nonradiative interface recombination in completed devices. The comprehensive analysis of the *FF*, p*FF* and FF_{id} demonstrated that the thicker SnO_X layer enhances the *FF* primarily by reducing the series resistance. The characterization of energy levels and corresponding device simulations were conducted to draw the band diagram. The results illustrated a shift in the work function of SnO_X with variations in the film thickness that was attributed to the presence of a higher density of electrons in both C_{60} and SnO_X films, providing both superior conductivity and a more favorable band diagram in the perovskite/C_{60}/SnO_X region.

8.2.2. Outlook

Internal series resistance

To investigate the working mechanism of SnO_X as a buffer layer in tandem solar cells, device simulations were employed to generate the band diagram of perovskite solar cells

incorporating SnO_X with increasing film thickness. Through the optimization of characterization methods and iterative adjustment of input parameters, such as work function, carrier mobility and series resistance, the simulated *FF* value aligned perfectly with the experimental value. In the SCAPS software, the total series resistance of a complete solar cell comprises external and internal components. The internal component is embedded within the band diagram, which is affected by a combination of the parameters of all layers, and thus cannot be manually input, while the external one can be input by users on the main panel. The total series resistance can be experimentally determined by measuring the J_{SC} and V_{OC} of a complete solar cell at varying illumination intensities, and the external component can be extracted from the SCAPS simulations. Consequently, the internal component embedded within the band diagram, which cannot be obtained directly through experiments, can be calculated by subtracting the external component from the total series resistance using a combination of intensity-dependent J_{SC}/V_{OC} measurements and SCAPS simulations.

8.3. Semi-transparent solar cells

8.3.1. Summary

Materials and devices

Semi-transparent perovskite solar cells are typically investigated as a reference for addressing the corresponding issues associated with the insertion of window stack in perovskite top cells due to the complex structures of tandem devices. Consequently, we designed masks for the patterned SnO_X/ITO/Ag stack and established the fabrication process for semi-transparent perovskite solar cells according to the existing configuration of opaque devices. However, we encountered a challenge at the initial phase wherein the four patterned ITO layers on the same substrate overlapped with one another due to the shadowing effect, resulting in a parallel connection of four semi-transparent solar cells and overestimated J_{SC}. By reducing the depth of the cassette, four patterned ITO layers were physically isolated. Subsequently, the ITO and IZO films were both developed through the optimization of gas flow ratio, working pressure, sputtering power, and pre-heating

temperature, which resulted in substantial variation in absorptance and sheet resistance, primarily by influencing the free carrier density of the bare films. A comparative analysis of the optical and electrical characteristics between ITO and IZO demonstrates that IZO exhibits both the lowest parasitic absorption loss and electrical transport loss, indicating its superior performance for application in tandem solar cells. The implementation of ITO film in the semi-transparent perovskite solar cells revealed another challenge, sputtering damage, and our initial experiments illustrate the effectiveness of SnO_X buffer layer on damage mitigation. After the optimization of buffer layer thickness, the sputtering damage was mitigated by incorporating a 15 nm SnO_X with diode JV curves, whereas a pronounced S-shaped presented when no buffer layer or a 5 nm SnO_X was implemented. The intensity-dependent JV measurements were conducted to investigate the sputtering-damage-induced S-shape and the corresponding results demonstrate that the presence of an extraction barrier at the SnO_X/ITO interface is the reason for the emergence of S-shapes in the *JV* characteristics of semi-transparent perovskite solar cells.

Working mechanism

The conventional understanding of the origin of sputtering damage is attributed to the high-kinetic-energy ion bombardment and/or plasma radiation generated during sputtering; however, the distinct influence of each factor on underlying films, stacks, and devices remains largely unexplored. To investigate the origin of sputtering damage, we decoupled the ion bombardment and plasma radiation during ITO deposition through optical filters, which allowed for the radiation from plasma while blocking the bombardment of ions and other particles. The photoluminescence and X-ray diffraction measurements reveal that the plasma radiation might reduce nonradiative recombination within the perovskite films by releasing the lattice strain, while ion bombardment was the dominant cause of sputtering damage. The photoluminescence measurement conducted on the perovskite, following the removal of C_{60}/(SnO_X)/ITO films, demonstrates that the absence of a buffer layer adversely affects the underlying perovskite film subsequent to ITO sputtering. SRIM Monte Carlo simulations indicate that all high-kinetic ions cease penetration at a depth of less than 5 nm from the surface, remaining within the C_{60} film, thereby creating vacancies and facilitating trap-assisted carrier recombination. During the ion penetration process, the majority of the initial kinetic energy is dissipated as phonons, as evidenced by the energy loss distribution. Subsequent X-ray photoelectron spectroscopy measurements performed on the perovskite

film surface reveal a minor loss of FA^+ due to the dissociation of C=N bonds. This investigation elucidates that the sputtering-induced damage of ITO to perovskite/C_{60} stacks primarily originates from ion bombardment rather than plasma radiation. Conversely, plasma radiation exhibits significant potential for suppressing nonradiative recombination within perovskite films.

8.3.2. Outlook

Lattice strains and light treatment

The quantitative analysis of the X-ray diffraction patterns among the perovskite films without and with plasma radiation using the Williamson–Hall method indicates the presence of lattice expansion in both samples. The relaxation of the lattice strain was observed after plasma radiation, which reduced defect concentration and suppressed nonradiative recombination, consequently yielding higher iV_{OC}. We recognize that the light-induced alterations in lattice strain depend on photon energy, wavelength, intensity, and duration of illumination. Given the potential of each of these factors to influence lattice strain through distinct mechanisms, a separate and comprehensive investigation should be conducted on the light-induced alterations in lattice strain within the perovskite film. The identification of factors that facilitate the relaxation of lattice strain can serve as a reference for the targeted selection of light treatment on perovskite, which exhibits significant potential for further enhancing the performance of perovskite-based solar cells.

Alternative buffer layer

The selection of a robust buffer layer with minimal parasitic absorption and appropriate band alignment to adjacent films is crucial for achieving high-efficiency perovskite/silicon tandem solar cells and presents potential for further efficiency enhancements. Although SnO_X buffer layers deposited using atomic layer deposition have been demonstrated to effectively shield the perovskite from sputtering damage, this deposition technique has inherent limitations, such as low deposition rate and limited reaction chamber capacity, which could impede the upscaling and industrialization of tandem devices. Consequently,

we have provided recommendations for selecting a buffer layer for perovskite/silicon tandem solar cells based on our findings during the investigation of the origin of sputtering damage. These recommendations facilitate the evaluation of properties among various materials prepared using diverse deposition techniques as potential buffer layers.

8.4. Perovskite/silicon tandem solar cells

8.4.1. Summary

Materials and devices

The initial step in fabricating high-efficiency tandem solar cells is producing a tandem solar cell with an efficiency exceeding zero, which serves as the foundation for further efficiency enhancement. We tested the entire workflow of perovskite/silicon tandem solar cells from wafer cleaning to final metallization by fabricating an initial batch of devices with unoptimized materials and processes using preliminary deposition masks, resulting in a maximum efficiency of approximately 9%. These initial results demonstrate the feasibility of preparing functional tandem devices; however, numerous issues within the preparation workflow require identification and resolution. Single-junction perovskite solar cells with diverse transitional structures were designed and utilized to address challenges related to specific layers and adjacent interfaces, including transporting layers, perovskite, interfacial passivation layer, buffer layer, and transparent electrode. All of these materials were systematically optimized to achieve optimal device performance. Additionally, the cutting methodologies for silicon bottom cells and the deposition masks for perovskite top cells were continuously improved, consequently resulting in an efficiency increase of approximately 10% and significant enhancement in the yield of perovskite/silicon tandem solar cells. For the second 10% efficiency improvement, the optimization primarily focused on optical response: (1) the silicon bottom cells with planar surface were substituted by those with nanotextured surface, which effectively reduced the reflection loss; (2) antireflective coating was utilized after the final metallization for the same reason; (3) Ag fingers were deposited atop ITO and connected to the U-shaped Ag frame, which effectively reduced the electrical loss; (4) the HTL/perovskite layer stack was optimized to enhance

valence band alignment at the interface and suppress nonradiative recombination; (5) the C_{60} layer thickness was decreased and the thick ITO layer was substituted with a thin IZO layer, both of which reduced the parasitic absorption loss. Consequently, the champion efficiency of the perovskite/silicon tandem solar cell was significantly improved from 19% to 31%.

Working mechanism

In the process of enhancing the efficiency of perovskite/silicon tandem solar cells, it has been founded that the surface treatment of the silicon bottom cells is crucial for achieving a high *FF*. To elucidate the underlying mechanism, the impact of O_2 plasma treatment on tandem devices and individual subcells was investigated. The results of external quantum efficiency measurements demonstrate that the duration of O_2 plasma treatment on silicon bottom cells exerts a distinct influence on the photocurrent of perovskite top and silicon bottom cells. Kelvin probe force microscope measurements conducted on the surface of ITO interconnection layer without and with O_2 plasma treatment revealed alterations in topography and potential distribution, wherein the surface and potential mean roughness both decreased with reduced dispersion, potentially due to plasma etching. This phenomenon is advantageous for the conformal coverage of the subsequent SAM molecules and the vertical growth of perovskite crystalline. Furthermore, O_2 plasma treatment increased the work function of ITO, as evidenced by ultraviolet photoelectron spectroscopy measurements, which is likely to affect the *FF* of tandem devices. Regarding the perovskite top cells, X-ray photoelectron spectroscopy and potential mapping were conducted to elucidate the coverage of MeO-2PACz molecules on the ITO layer. The increase in the coverage factor and decrease in mean roughness indicates that the O_2 plasma treatment applied to the silicon bottom cells effectively facilitated more uniform coverage of MeO-2PACz molecules on the ITO surface. Subsequent analyses of contact angle and scanning electron microscopy demonstrate that the improved wettability of the perovskite precursor on the silicon bottom cells, resulting from O_2 plasma treatment, effectively promoted the crystallization of the perovskite layer, consequently enhancing optical response and suppressing carrier recombination. Overall, the surface treatment not only exerts significant influence on the physical and electrical properties of the interconnection layer, thereby affecting the performance of silicon bottom cells, but also impacts the coverage and

crystallization of the subsequent SAM and perovskite light-absorbing layer, respectively, and consequently, the performance of perovskite top cells.

8.4.2. Outlook

UV(O) treatment

The surface treatments commonly employed in the fabrication of perovskite/silicon tandem solar cells include O_2 plasma and UV(O) treatments. Our initial investigation into the impact of UV(O) treatments demonstrated a significant *FF* gain while exhibiting V_{OC} decay compared to the O_2 plasma counterpart. The *FF* gain may be attributed to the increases in the work function of the ITO interconnection layer; however, further device simulations are necessary to elucidate the band diagram of tandem solar cells, analyze the band alignment, carrier transport, and consequently, examine the working mechanism of the interconnection layer in monolithic tandem solar cells. The V_{OC} decay following UV(O) treatments has been demonstrated to be associated with UV degradation, and a post-annealing process applied to the silicon bottom cell can effectively mitigate this decay, which was evidenced by our initial investigation as well. Consequently, further research is warranted to investigate the effects of UV(O) treatments on the performance of perovskite/silicon tandem solar cells, as this approach demonstrates significant potential for improving the *FF* without compromising the V_{OC} of monolithic perovskite/silicon tandem solar cells. A comparative analysis of the mechanisms by which UV(O) treatment and O_2 plasma treatment enhance the performance of tandem devices will provide valuable insights into the characteristics of optimal surface treatments.

Silicon bottom cells

External quantum efficiency analysis indicates that the J_{SC} of our champion tandem solar cell was limited by the photocurrent of the silicon bottom cell, necessitating further optimizations to enhance the optical response of bottom cells. Firstly, the symmetric nanotextured silicon substrate with small pyramids (< 1 μm) on both sides should be replaced with an asymmetric textured silicon substrate featuring small pyramids (< 1 μm)

on the front side and industrialized size pyramids (3~5 μm) on the back side, which can effectively improve the infrared response of silicon bottom cells, resulting in higher photocurrent. Secondly, a rear reflector comprising screen-printed Ag grids and a MgF_2 antireflective coating should be implemented between the ITO and Ag electrode at the back side of the silicon bottom cell, which can reduce reflection loss and plasmonic absorption loss at the ITO/Ag interface. Lastly, the phosphorus-doped hydrogenated amorphous silicon with a refractive index of 3.8 that was incorporated at the front side of the silicon bottom cell should be substituted with phosphorus-doped hydrogenated nanocrystalline silicon oxide with a lower refractive index of 2.6. This substitution can reduce reflection loss at the interface between the interconnection layer and crystalline silicon substrate, as the loss progressively decreases with increasing refractive index due to positive interference effects.

A. Abbreviations and symbols

$a(E)$	Absorptance
$\Phi_{\mathbf{inc}}(E)$	Photon flux of incident light
$\phi(E)$	Emitted photon flux
$\phi_{\mathbf{bb}}(E)$	Photons flux of the black body from environment
$\Phi_{\mathbf{sun}}$	Photons flux of sun spectrum
η	Solar cell efficiency
α	Absorption coefficient
μ	Charge carrier mobility
λ	Wavelength
ρ	Resistivity
ρ_{c}	Contact resistivity
σ	Electrical conductivity
$\rho_{\mathbf{c,SnOx/ITO}}$	Contact resistivity at the SnOx/ITO interface
$\rho_{\mathbf{SnOx}}$	Resistivity of SnO_X
ε	Permittivity
θ	Scan degree
$\phi_{\mathbf{AM}1.5}(\lambda)$	Photo flux of the standard AM1.5 spectrum
ϕ	Work function
χ	Electron affinity
$\mu_{\mathbf{n}}$	Electron mobility
$\mu_{\mathbf{p}}$	Hole mobility
$\varepsilon_{\mathbf{r}}$	Relative dielectric permittivity
$\beta_{\mathbf{L}}$	Crystallite-size-induced broadening
$\beta_{\mathbf{e}}$	Strain-induced broadening
β	FWHM of the XRD diffraction peak

A	Absorptance
$A_{\mathbf{I}}$	Integrated absorption
d	Thickness
$d_{\mathbf{SnOx}}$	Film thickness of SnOx
$e(E)$	Emission of black body at a certain temperature
$E_{\mathbf{g}}$	Bandgap
E	Photon energy
$E_{\mathbf{g,Si}}$	Bandgap of silicon
ΔE_F	Average quasi-Fermi level splitting
$\Delta E_{\mathbf{F,rad}}$	Maximum achievable Fermi level splitting in the absence of nonradiative (defect) recombination
$E_{\mathbf{VAC}}$	Vacuum energy
$E_{\mathbf{V}}$	Valence band
$E_{\mathbf{C}}$	Conduction band
$E_{\mathbf{F_n}}$	Electron Fermi energy
$E_{\mathbf{disp}}$	Displacement energy
$E_{\mathbf{B}}$	Binding energy
FF	Fill factor
$FF_{\mathbf{id}}$	Ideal fill factor
$\Delta FF_{\mathbf{R_s}}$	FF loss caused by series resistance
$\Delta FF_{\mathbf{nid}}$	FF losses due to $n_{\mathrm{id}} > 1$
pFF	Pseudo fill factor
G_{ALD}	ALD deposition rate
hv	Photon energy
I	Current
i$V_{\mathbf{OC}}$	Implied open-circuit voltage
$J_{\mathbf{SC,SQ}}$	Maximum short-circuit current density
$J_{\mathbf{rec,SQ}}$	Recombination current density
$J_{0,\mathbf{SQ}}$	Saturated current density
$J_{\mathbf{SC,2T}}$	Total current density at short circuit of two-terminal tandem solar cell
$J_{\mathbf{SC,top}}$	Short-circuit current density of top cell
$J_{\mathbf{SC,bot}}$	Short-circuit current density of bottom cell

$J_{\mathbf{G,top}}$	Photogenerated current of top cell
$J_{\mathbf{G,bot}}$	Photogenerated current of bottom cell
$J_{\mathbf{RZ}}$	Current flows through the RZ circuit
$J_{\mathbf{SC}}$	Short-circuit current density
$J_{\mathbf{mpp}}$	Current density extracted at the MPP
$J_{\mathbf{f}}$	Forward bias current
$J_{\mathbf{r}}$	Reverse bias current
$J_{\mathbf{SC,Q_{e,PV}}}$	Photocurrent integrated using the $Q_{\mathrm{e,PV}}$ spectrum
$k_{\mathbf{B}}$	Boltzmann constant
κ	Extinction coefficient
$k_{\mathbf{rad}}$	Radiative-recombination coefficient
l	Contact length
L	Distance between two adjacent pads
n	Concentration of electrons
$n_{\mathbf{i}}$	Intrinsic carrier concentration
$n_{\mathbf{ref}}$	Refractive index
$N_{\mathbf{C}}$	Effective density of states of the conduction band
$N_{\mathbf{V}}$	Effective density of states of the valence band
$n_{\mathbf{id}}$	Ideality factor
$N_{\mathbf{D}}$	Doping concentration
p	Concentration of holes
P	Power density
$P_{\mathbf{max}}$	Maximum power density
$P_{\mathbf{max,out}}$	Maximum output power density
$P_{\mathbf{max,in}}$	Maximum input power density
$P_{\mathbf{top}}$	Power of top cell
$P_{\mathbf{bot}}$	Power of bottom cell
$P_{\mathbf{RZ}}$	Power of RZ circuit
$P_{\mathbf{RT}}$	Power of RZ circuit
$\Delta P_{\mathbf{RT}}$	Excessive power of RT circuit
$P_{\mathbf{mpp}}$	Power extracted at the MPP
$p_{\mathbf{ITO}}$	Working pressure during ITO sputtering
$P_{\mathbf{ITO}}$	ITO sputtering power

P_{O_2}	Power of O_2 plasma treatment
q	Elementary charge
$Q_{e,PV}$	External quantum efficiency
$Q_{e,lum}$	External quantum efficiency of the PL emission
r_{O_2}	Gas flow ratio of Ar/O_2
R_S	Series resistance
R_{SH}	Sheet resistance
R	Reflectance
$R_{S,SnOx/ITO}$	Contact resistance at the SnO_X/ITO interface
$R_{S,SnOx}$	Intrinsic resistance of SnO_X layer
$R_{S,ITO}$	Resistance generated within the full ITO layer owing to the lateral flow of current
$R_{SH,ITO}$	Sheet resistance of the full ITO film
R_{ALD}	Pulse length ratio of H_2O/TDMASn
$R_{int,SRH}$	SRH recombination rate
R_a	Mean roughness
S_{front}	Surface recombination velocity at front interface
S_{rear}	Surface recombination velocity at the rear interface
S_n	Recombination velocity of the electrons
S_p	Recombination velocity of the holes
$T(\lambda)$	Transmittance
T	Temperature
T_{ALD}	ALD reaction temperature
T_{ITO}	Pre-heating temperature during the ITO sputtering process
$t_{anisole}$	Time to drop anisole
t_{O_2}	O_2 plasma treatment duration
T_{GB}	Temperature in the N_2-filled glovebox
V	Bias voltage
V_{OC}	Open-circuit voltage
$V_{bot(top)}$	Partial bias voltage of bottom (top) cell
$V_{OC,2T}$	Open-circuit voltage of two-terminal tandem solar cell
$V_{OC,top}$	Open-circuit voltage of top cell
$V_{OC,bot}$	Open-circuit voltage of bottom cell

V_{mpp}	Voltage extracted at the MPP
V_{BI}	Built-in voltage
ΔV_{BI}	Relative shifts of built-in voltage
v_{OC}	Normalized open-circuit voltage
v_{th}	Thermal velocity
W	Width of the Ag pad
w	Vertical distance between the Ag contacts
x	Stoichiometry number
Y_{em}	Emitted photon flux
Y_{rec}	Recombination flux
2PACz	[2-(9H-Carbazol-9-yl)ethyl]phosphonic Acid
4F-PEAI	4-Fluoro-Phenethylammonium iodide
As	Arsenic
Ag	Silver
Ar	argon
Ar^+	Argon ion
a-Si:H (i)	intrinsic hydrogenated amorphous silicon
a-Si:H (p)	boron-doped hydrogenated amorphous silicon
a-Si:H (n)	phosphorus-doped hydrogenated amorphous silicon
AZO	Al-doped zinc oxide
a-SiO_X:H (i)	intrinsic hydrogenated amorphous silicon oxide
a-SiOx:H	hydrogenated amorphous silicon oxide
BCP	Bathocuproine
Br	Bromide
Cu	Copper
Cu(In,Ga)Se_2	Copper Indium Gallium Diselenide
C_{60}	fullerene
CdTe	Cadmium telluride
c-Si (n)	n-type crystalline silicon
c-Si	crystalline silicon
CO_2	Carbon dioxide
CH_4	Methane
C	Carbon
Cs	Cesium

CsI	Cesium iodide
CB	chlorobenzene
DMF	Dimethylformamid
DMSO	Dimethyl sulfoxide
MDA	dimethylamino ligand
EDAI	ethylenediammonium diiodide
EA	ethyl acetate
FA	formamidine
FA^+	formamidinium cation
FAI	Formamidinium Iodide
HeI	Helium iodide
HCl	hydrochloric acid
HF	hydrofluoric acid
H_2	Hydrogen
HDMA	dimethylamine
H_2O	Water
ITO	indium tin oxide
IZO	indium zinc oxide
IWO	tungsten-doped indium oxide
In_2O_3	Indium oxide
In_2O_3:Sn	tin-doped indium oxide
In_2O_3:Zn	zinc-doped indium oxide
I	Iodine
Ga	Gallium
GaAs	Gallium arsenide
InP	Indium phosphide
InGaAs	indium gallium arsenide
LiF	lithium fluoride
MgF_2	Magnesium fluoride
$MDACl_2$	methylenediammonium dichloride
MA	methylammonium
MA^+	methylammonium cations
MABr	Methylammonium Bromide
Me-4PACz	[4-(3,6-dimethyl-9H-carbazol-9-yl)butyl]phosphonic acid
MAI	Methylammonium iodide

MeO-2PACz	[2-(3,6-Dimethoxy-9H-carbazol-9-yl)ethyl]phosphonic Acid
nc-SiO_X	nanocrystalline silicon oxide
N_2	Nitrogen
O_3	ozone
O_2	Molecular oxygen
O	Oxygen
PI	piperazinium iodide
PH_3	Phosphine
Pb	Lead
PbI_2	Lead iodide
$PbBr_2$	Lead bromide
PMMA	poly(methylmethacrylate)
PTFE	Polytetrafluoroethylene
PTAA	Poly[bis(4-phenyl)(2,4,6-trimethylphenyl)amine]
PEAI	phenethylammonium iodide
Si	silicon
SiNP	silicon nanoparticle
spiro-OMeTAD	2,2',7,7'-Tetrakis[N,N-di(4-methoxyphenyl)amino]-9,9'-spirobifluorene
SnO_X	Tin oxide
SiO_2	silicon oxide
SiH_4	Silane
Sn	Tin
TCO	transparent conductive oxide
TiO_2	Titanium oxide
TDMASn	Tetrakis (dimethylamino)tin(IV)
ZTO	zinc tin oxide
ZnO	Zinc oxide
AR	Anti-Reflection
ARC	Antireflective Coating
ALD	Atomic Layer Deposition
BE	Binding Energy
CAE	Constant Analyzer-Energy
CVD	Chemical Vapor Deposition
CZ	Czochralski

CBM	Conduction Band Minimum
CG	Corning Glass
CMP	Chemical-Mechanical Planarization
DC	Direct Current
DSP	Double-sided polished
DI	Deionized
DST	Double-Sided Textured
DOS	Effective density of states
ETL	Electron Transport Layer
EPFL	Swiss Federal Technology Institute of Lausanne
FWHM	Full-Width at Half-Maximum
FZ	Foat-Zone
FCA	Free Carrier Absorption
HTL	Hole Transporting Layer
HZB	Helmholtz-Zentrum Berlin
HOMO	Highest Occupied Molecular Orbital
ICL	Interconnection Layer
JV	Current Density-Voltage
JOSEPH	Jülich Online Semiconductor Growth Experiment for Photovoltaics
$\boldsymbol{JV_{dark}}$	Dark JV
$\boldsymbol{JV_{id}}$	Ideal JV Curve
KAUST	King Abdullah University of Science and Technology
LM	Loading Module
LISSY	Large Inline Sputter System
LOMO	Lowest Unoccupied Molecular Orbital
MPP	Maximum Power Point
MSE	Mean Square Error
MS	Metal-Semiconductor
NREL	Nation Renewable Energy Laboratory
PV	Photovoltaic
PL	Photoluminescence
PE	Path Energy
PVD	Physical Vapor Deposition
PSCs	Perovskite Solar Cells

PECVD	Plasma-Enhanced Chemical Vapor Deposition
PM	Process Module
p*JV*	Pseudo-JV
PLQY	Photoluminescence Quantum Yield
QDR	Quick Dump Rinse
QSE	Quantum Size Effects
QG	Quartz Glass
RF	Radio Frequency
RCA	Radio Corporation of America
S-Q	Shockley-Queisser
ssPL	Steady-State Photoluminescence
SHJ	Silicon Heterojunction Solar Cells
SEM	Scanning Electron Microscopy
SCLC	Space-Charge-Limited Current
SRIM	Stopping and Range of Ions in the Matter
SCPAS	Solar Cell Capacitance Simulator
SAM	Self-Assembled Monolayer
SSP	Single-Sided Polished
SRH	Shockley-Read-Hall
T	Terminal
TOPCon	Tunnel Oxide Passivating Contacts
TEM	Transmission Electron Microscopy
TLM	Transfer Length Method
TPC	Transparent Passivating Contact
UV	Ultraviolet
UNSW	University of New South Wales
UV-Vis-NIR	Ultraviolet-Visible-Near Infrared Spectroscopy
UPS	Ultraviolet Photoelectron Spectroscopy
UHV	Ultra-High Vacuum
UV(O)	Ultraviolet/Ozone
VUV	Vacuum Ultraviolet
VBM	Valence Band Maximum
W-H	Williamson–Hall
XPS	X-ray Photoelectron Spectroscopy
XRD	X-Ray Diffraction

B. List of Publications

Publications related to this work

Original

1. **Q. Yang**, W. Duan, A. Eberst, B. Klingebiel, Y. Wang, A. Kulkarni, A. Lambertz, K. Bittkau, Y. Zhang, S. Vitusevich, U. Rau, T. Kirchartz, K. Ding, *Origin of sputter damage during transparent conductive oxide deposition for semitransparent perovskite solar cells*, **Journal of Materials Chemistry A** 12, 14816 – 14827 (2024)
2. **Q. Yang**, K. Bittkau, A. Eberst, U. Rau, K. Ding, *The Impact of Interface Recombination on the External Quantum Efficiency of Silicon Solar Cells*, **Solar Energy Materials and Solar Cells** 273, 112953 (2024)
3. **Q. Yang**, K. Bittkau, B. Klingebiel, T. Kirchartz, U. Rau, K. Ding, *Toward the Working Mechanisms of Tin Oxide as Buffer Layer in Perovskite/Silicon Tandem Solar Cells*, **Applied Physics Reviews** 12, 021403 (2025)

Conference

1. **Q. Yang**, K. Bittkau, B. Klingebiel, U. Rau, T. Kirchartz, K. Ding, *Towards the Working Mechanisms of Tin Oxide as Buffer Layer in Perovskite/Silicon Tandem Solar Cells*, 2024 IEEE 52nd Photovoltaic Specialist Conference (PVSC), 0620-0620 (2024)

Other publications

1. **Q. Yang**, Z. Liu, Y. Lin, W. Liu, M. Liao, M. Feng, Y. Zhi, J. Zheng, L. Lu, D. Ma, Q. Han, H. Cheng, Z. Yang, K. Ding, W. Duan, H. Chen, Y. Wang, Y. Zeng, B. Yan, J. Ye,

Passivating Contact with Phosphorus-Doped Polycrystalline Silicon-Nitride with an Excellent Implied Open-Circuit Voltage of 745 mV and Its Application in 23.88% Efficiency TOPCon Solar Cells. **Solar RRL** 5, 2100644 (2021)

2. W. Duan, G. Mains, H. Gebrewold, K. Bittkau, A. Lambertz, B. Xu, V. Lauterbach, A. Eberst, N. Nicholson, L. Korte, M. Yaqin, K. Zhang, **Q. Yang**, U. Rau, K. Ding, *Enhancing the Selectivity and Transparency of the Electron Contact in Silicon Heterojunction Solar Cells by Phosphorus Catalytic Doping*. **Advanced Functional Materials** 34, 2310552 (2024)
3. Q. Tang, W. Duan, A. Lambertz, K. Bittkau, M. A. Yaqin, Y. Zhao, K. Zhang, **Q. Yang**, D. Qiu, F. Gunkel, M. Weber, U. Rau, K. Ding, *85% indium reduction for high-efficiency silicon heterojunction solar cells with aluminum-doped zinc oxide contacts*. **Solar Energy Materials and Solar Cells** 251, 112120 (2023)
4. J. Sun, Y. Zhang, J., **Q. Yang**, G. Yu, X. Yang, Z. Ying, J. Sheng, H. He, C. Shou, G. Qin, J. Ye, *An Efficient Modification at the Hole Transporting Layer/Electrode Interface for High-Performance Ag-Electrode-Based Perovskite Solar Cells*, **Physica status solidi (a)** 219, 2200272 (2022)
5. Y. Zhang, W. Liu, J. Sun, C. Shou, G. Yu, **Q. Yang**, W. Yang, B. Yan, J. Sheng, J. Ye, *ITO/SnO_2 Interface Defect Passivation via Atomic Layer Deposited Al_2O_3 for High-Efficiency Perovskite Solar Cells*. **Physica status solidi (a)** 218, 2100406 (2021)

C. Curriculum Vitae

Personal details

Name	Qing Yang
Data of birth	September 25th, 1995
Place of birth	Hubei, China
Citizenship	Chinese

Education

2001-2007	Xishui Second Primary School
2007-2010	Xishui Experimental Middle School
2010-2013	Xishui Number One Middle School
2013-2017	Wuhan Institute of Technology, Wuhan, China Bachelor in chemical engineering and technology Bachelor in English
2017-2020	University of Chinese Academy of Science, Beijing, China & Ningbo Institute Materials technology and Engineering, Ningbo, China Master in Materials Engineering
04/2021-now	PhD student at the Forschungszentrum Jülich GmbH, IMD-3, Photovoltaics

References

[1] M. A. Green, E. D. Dunlop, G. Siefer, M. Yoshita, N. Kopidakis, K. Bothe, and X. Hao, Prog. Photovolt.: Res. Appl. **31**, 3 (2023).

[2] W. Shockley and H. J. Queisser, J. Appl. Phys. **32**, 510 (1961).

[3] Z. Zhu, K. Mao, and J. Xu, J. Energy Chem. **58**, 219 (2021).

[4] A. De Vos, J. Phys. D: Appl. Phys. **13**, 839 (1980).

[5] J. Y. Kim, J.-W. Lee, H. S. Jung, H. Shin, and N.-G. Park, Chem. Rev. **120**, 7867 (2020).

[6] M. A. Green, E. D. Dunlop, M. Yoshita, N. Kopidakis, K. Bothe, G. Siefer, D. Hinken, M. Rauer, J. Hohl-Ebinger, and X. Hao, Prog. Photovolt.: Res. Appl. **32**, 425 (2024).

[7] J. P. Mailoa, C. D. Bailie, E. C. Johlin, E. T. Hoke, A. J. Akey, W. H. Nguyen, M. D. McGehee, and T. Buonassisi, Appl. Phys. Lett. **106** (2015).

[8] B. G. Lewis and D. C. Paine, MRS Bull. **25**, 22 (2000).

[9] Q. Yang, W. Duan, A. Eberst, B. Klingebiel, Y. Wang, A. Kulkarni, A. Lambertz, K. Bittkau, Y. Zhang, and S. Vitusevich, J. Mater. Chem. A (2024).

[10] G. Kirchhoff, Annalen der Physik **185**, 275 (1860).

[11] D. Abou-Ras, T. Kirchartz, and U. Rau, *Advanced characterization techniques for thin film solar cells*. (Wiley Online Library, 2011).

[12] T. Tiedje, E. Yablonovitch, G. D. Cody, and B. G. Brooks, IEEE Trans. Electron Devices **31**, 711 (1984).

[13] B. Jackson, Phylon (1940-1956) **16**, 5 (1955).

[14] Y. Du, B. Xu, G. Wang, Y. Miao, B. Li, Z. Kong, Y. Dong, W. Wang, and H. H. Radamson, Nanomater. **12**, 741 (2022).

[15] S. Essig, C. Allebé, T. Remo, J. F. Geisz, M. A. Steiner, K. Horowitz, L. Barraud, J. S. Ward, M. Schnabel, and A. Descoeudres, Nat. Energy **2**, 1 (2017).

[16] C. Yang, W. Hu, J. Liu, C. Han, Q. Gao, A. Mei, Y. Zhou, F. Guo, and H. Han, Light Sci. Appl. **13**, 227 (2024).

[17] J. Werner, A. Walter, E. Rucavado, S.-J. Moon, D. Sacchetto, M. Rienaecker, R. Peibst, R. Brendel, X. Niquille, and S. De Wolf, Appl. Phys. Lett. **109** (2016).

[18] J. Werner, C.-H. Weng, A. Walter, L. Fesquet, J. P. Seif, S. De Wolf, B. Niesen,

and C. Ballif, J. Phys. Chem. Lett. **7**, 161 (2016).
[19] J. Zheng, H. Mehrvarz, C. Liao, J. Bing, X. Cui, Y. Li, V. R. Gonçales, C. F. J. Lau, D. S. Lee, and Y. Li, ACS Energy Lett. **4**, 2623 (2019).
[20] K. A. Bush, A. F. Palmstrom, Z. J. Yu, M. Boccard, R. Cheacharoen, J. P. Mailoa, D. P. McMeekin, R. L. Hoye, C. D. Bailie, and T. Leijtens, Nat. Energy **2**, 1 (2017).
[21] L. Mazzarella, Y. H. Lin, S. Kirner, A. B. Morales-Vilches, L. Korte, S. Albrecht, E. Crossland, B. Stannowski, C. Case, and H. J. Snaith, Adv. Energy Mater. **9**, 1803241 (2019).
[22] F. Sahli, J. Werner, B. A. Kamino, M. Bräuninger, R. Monnard, B. Paviet-Salomon, L. Barraud, L. Ding, J. J. Diaz Leon, and D. Sacchetto, Nat. Mater. **17**, 820 (2018).
[23] E. Aydin, E. Ugur, B. K. Yildirim, T. G. Allen, P. Dally, A. Razzaq, F. Cao, L. Xu, B. Vishal, A. Yazmaciyan, A. A. Said, S. Zhumagali, R. Azmi, M. Babics, A. Fell, C. Xiao, and S. De Wolf, Nat. **623**, 732 (2023).
[24] P. Tockhorn, J. Sutter, A. Cruz, P. Wagner, K. Jager, D. Yoo, F. Lang, M. Grischek, B. Li, J. Li, O. Shargaieva, E. Unger, A. Al-Ashouri, E. Kohnen, M. Stolterfoht, D. Neher, R. Schlatmann, B. Rech, B. Stannowski, S. Albrecht, and C. Becker, Nat. Nanotechnol. **17**, 1214 (2022).
[25] S. Mariotti, E. Köhnen, F. Scheler, K. Sveinbjörnsson, L. Zimmermann, M. Piot, F. Yang, B. Li, J. Warby, and A. Musiienko, Sci. **381**, 63 (2023).
[26] E. Ugur, A. A. Said, P. Dally, S. Zhang, C. E. Petoukhoff, D. Rosas-Villalva, S. Zhumagali, B. K. Yildirim, A. Razzaq, and S. Sarwade, Sci. **385**, 533 (2024).
[27] J. Liu, Y. He, L. Ding, H. Zhang, Q. Li, L. Jia, J. Yu, T. W. Lau, M. Li, and Y. Qin, Nat. **635**, 596 (2024).
[28] Y. Hishikawa, N. Nakamura, S. Tsuda, S. Nakano, Y. K. Y. Kishi, and Y. K. Y. Kuwano, Jpn. J. Appl. Phys. **30**, 1008 (1991).
[29] N. F. Mott and R. W. Gurney, *Electronic processes in ionic crystals*. (Clarendon Press, Oxford, 1940).
[30] M. A. Lampert and R. B. Schilling, in *Semiconductors and semimetals* (Elsevier, 1970), Vol. 6, pp. 1.
[31] D. A. Shirley, Phys. Rev. B **5**, 4709 (1972).
[32] C. Powell, J. Electron Spectros. Relat. Phenomena **47**, 197 (1988).
[33] B. D. Ratner and D. G. Castner, Surface analysis–the principal techniques **51** (2009).
[34] T. Mueller, *Heterojunction solar cells (a-Si/c-Si): investigations on PECV deposited hydrogenated silicon alloys for use as high-quality surface passivation and emitter/BSF*. (Logos Verlag Berlin GmbH, 2009).
[35] S. Klein, *Microcrystalline Silicon Prepared by Hot Wire CVD: Preparation and Characterisation of Material and Solar Cells*. (TU München, 2004).
[36] J. F. Ziegler, M. D. Ziegler, and J. P. Biersack, Nuclear Instruments and Methods in Physics Research Section B: Beam Interactions with Materials

and Atoms **268**, 1818 (2010).
[37] M. Burgelman, P. Nollet, and S. Degrave, Thin solid films **361**, 527 (2000).
[38] A. Fell, IEEE transactions on electron devices **60**, 733 (2012).
[39] A. Fell, K. C. Fong, K. R. McIntosh, E. Franklin, and A. W. Blakers, IEEE Journal of Photovoltaics **4**, 1040 (2014).
[40] A. Fell, K. R. McIntosh, M. Abbott, and D. Walter, *in Proceedings of the Proceedings of the 23rd International Photovoltaic Science and Engineering Conference*, 2013.
[41] A. Richter, J. Benick, F. Feldmann, A. Fell, M. Hermle, and S. W. Glunz, Sol. Energ. Mat. Sol. Cells **173**, 96 (2017).
[42] A. Richter, J. Benick, A. Fell, M. Hermle, and S. W. Glunz, Prog. Photovolt.: Res. Appl. **26**, 342 (2018).
[43] A. Richter, J. Benick, R. Müller, F. Feldmann, C. Reichel, M. Hermle, and S. W. Glunz, Prog. Photovolt.: Res. Appl. **26**, 579 (2018).
[44] S. M. George, Chem. Rev. **110**, 111 (2010).
[45] P. J. Kelly and R. D. Arnell, Vacuum **56**, 159 (2000).
[46] A. Al-Ashouri, E. Köhnen, B. Li, A. Magomedov, H. Hempel, P. Caprioglio, J. A. Márquez, A. B. Morales Vilches, E. Kasparavicius, and J. A. Smith, Sci. **370**, 1300 (2020).
[47] J. Werner, G. Dubuis, A. Walter, P. Löper, S.-J. Moon, S. Nicolay, M. Morales-Masis, S. De Wolf, B. Niesen, and C. Ballif, Sol. Energy Mater. Sol. Cells **141**, 407 (2015).
[48] E. Aydin, M. De Bastiani, X. Yang, M. Sajjad, F. Aljamaan, Y. Smirnov, M. N. Hedhili, W. Liu, T. G. Allen, L. Xu, E. Van Kerschaver, M. Morales-Masis, U. Schwingenschlögl, and S. De Wolf, Adv. Funct. Mater. **29**, 1901741 (2019).
[49] K. Ellmer and T. Welzel, J. Mater. Res. **27**, 765 (2012).
[50] P. Carcia, R. McLean, M. Reilly, Z. Li, L. Pillione, and R. Messier, J. Vac. Sci. Technol. A: Vac. Surf. Films **21**, 745 (2003).
[51] Q. H. Fan, M. Deng, X. Liao, and X. Deng, J. Appl. Phys. **105** (2009).
[52] H. Kanda, A. Uzum, A. K. Baranwal, T. A. N. Peiris, T. Umeyama, H. Imahori, H. Segawa, T. Miyasaka, and S. Ito, J. Phys. Chem. C **120**, 28441 (2016).
[53] M. Köhler, M. Pomaska, P. Procel, R. Santbergen, A. Zamchiy, B. Macco, A. Lambertz, W. Duan, P. Cao, B. Klingebiel, S. Li, A. Eberst, M. Luysberg, K. Qiu, O. Isabella, F. Finger, T. Kirchartz, U. Rau, and K. Ding, Nat. Energy **6**, 529 (2021).
[54] M. Jošt, E. Köhnen, A. B. Morales-Vilches, B. Lipovšek, K. Jäger, B. Macco, A. Al-Ashouri, J. Krč, L. Korte, B. Rech, R. Schlatmann, M. Topič, B. Stannowski, and S. Albrecht, Energy & Environmental Science **11**, 3511 (2018).
[55] A. J. Mackus, C. MacIsaac, W. H. Kim, and S. F. Bent, J. Chem. Phys. **146**, 052802 (2017).
[56] H. J. Jeong and J. S. Park, in *Amorphous Oxide Semiconductors: IGZO and Related Materials for Display and Memory* (2022), pp. 213.

[57] G. Chistiakova, M. Mews, R. G. Wilks, M. Bär, and L. Korte, J. Vac. Sci. Technol. A: Vac. Surf. Films **36** (2018).
[58] E. Köhnen, M. Jošt, A. B. Morales-Vilches, P. Tockhorn, A. Al-Ashouri, B. Macco, L. Kegelmann, L. Korte, B. Rech, R. Schlatmann, B. Stannowski, and S. Albrecht, Sustain. Energy Fuels **3**, 1995 (2019).
[59] Z. Xiong, L. Wu, X. Zhou, S. Yang, Z. Liu, W. Liu, J. Zhao, W. Li, C. Yu, and K. Yao, Small **20**, 2308024 (2024).
[60] A. Richter, J. Benick, F. Feldmann, A. Fell, M. Hermle, and S. W. Glunz, Sol. Energy Mater. Sol. Cells **173**, 96 (2017).
[61] A. Magomedov, A. Al-Ashouri, E. Kasparavičius, S. Strazdaite, G. Niaura, M. Jošt, T. Malinauskas, S. Albrecht, and V. Getautis, Adv. Energy Mater. **8**, 1801892 (2018).
[62] N. Shibayama, H. Kanda, T. W. Kim, H. Segawa, and S. Ito, APL Mater. **7** (2019).
[63] J. Wang, J. Li, Y. Zhou, C. Yu, Y. Hua, Y. Yu, R. Li, X. Lin, R. Chen, H. Wu, H. Xia, and H. L. Wang, J. Am. Chem. Soc. **143**, 7759 (2021).
[64] J. C. Wang, X. C. Ren, S. Q. Shi, C. W. Leung, and P. K. L. Chan, Org. Electron. **12**, 880 (2011).
[65] C. Chen, S. Zhang, S. Wu, W. Zhang, H. Zhu, Z. Xiong, Y. Zhang, and W. Chen, RSC Adv. **7**, 35819 (2017).
[66] S. Asgary, H. M. Moghaddam, A. Bahari, and R. Mohammadpour, Sol. Energy **213**, 383 (2021).
[67] I. Miccoli, F. Edler, H. Pfnur, and C. Tegenkamp, J. Phys. Condens Matter **27**, 223201 (2015).
[68] T. Kirchartz, J. A. Márquez, M. Stolterfoht, and T. Unold, Adv. Energy Mater. **10** (2020).
[69] U. Rau, Phys. Rev. B - Condens. Matter Mater. Phys. **76**, 085303 (2007).
[70] R. T. Ross, J. Chem. Phys. **46**, 4590 (1967).
[71] W. Shockley and H. J. Queisser, J. Appl. Phys. **32**, 510 (1961).
[72] Q. Yang, K. Bittkau, A. Eberst, U. Rau, and K. Ding, Sol. Energy Mater. Sol. Cells **273** (2024).
[73] P. M. Salomé, B. Vermang, R. Ribeiro-Andrade, J. P. Teixeira, J. M. Cunha, M. J. Mendes, S. Haque, J. Borme, H. Aguas, and E. Fortunato, Adv. Mater. Interfaces **5**, 1701101 (2018).
[74] E. McVay, A. Zubair, Y. Lin, A. Nourbakhsh, and T. Palacios, ACS Appl. Mater. Interfaces **12**, 57987 (2020).
[75] M. Hatamvand, S. Gholipour, M. Chen, Y. Zhou, T. Jiang, Z. Hu, Y. Chen, and W. Huang, J. Chem. Eng. **460**, 141788 (2023).
[76] K. Ding, U. Aeberhard, F. Finger, and U. Rau, Phys. Status Solidi Rapid Res. Lett. **6**, 193 (2012).
[77] D. F. Swinehart, J. Chem. Educ. **39**, 333 (1962).
[78] N. Shibayama, H. Kanda, T. W. Kim, H. Segawa, and S. Ito, APL Mater. **7**, 031117 (2019).

[79] M. A. Green, Sol. cells **7**, 337 (1982).
[80] T. Kirchartz, F. Deledalle, P. S. Tuladhar, J. R. Durrant, and J. Nelson, J. Phys. Chem. Lett **4**, 2371 (2013).
[81] K. Tvingstedt and C. Deibel, Adv. Energy Mater. **6**, 1502230 (2016).
[82] Y. Yuan, G. Yan, C. Dreessen, T. Rudolph, M. Hulsbeck, B. Klingebiel, J. Ye, U. Rau, and T. Kirchartz, Nat Mater (2024).
[83] M. Stolterfoht, C. M. Wolff, J. A. Márquez, S. Zhang, C. J. Hages, D. Rothhardt, S. Albrecht, P. L. Burn, P. Meredith, T. Unold, and D. Neher, Nat. Energy **3**, 847 (2018).
[84] P. Wurfel, *Physics of solar cells*. (Wiley-Vch, 2005).
[85] F. Peña-Camargo, J. Thiesbrummel, H. Hempel, A. Musiienko, V. M. Le Corre, J. Diekmann, J. Warby, T. Unold, F. Lang, D. Neher, and M. Stolterfoht, Appl. Phys. Rev. **9**, 021409 (2022).
[86] D. Grabowski, Z. Liu, G. Schöpe, U. Rau, and T. Kirchartz, Solar RRL **6**, 2200507 (2022).
[87] M. N. Mullings, C. Hägglund, and S. F. Bent, J. Vac. Sci. Technol. A: Vac. Surf. Films **31**, 061503 (2013).
[88] D. Menzel, A. Al-Ashouri, A. Tejada, I. Levine, J. A. Guerra, B. Rech, S. Albrecht, and L. Korte, Adv. Energy Mater. **12**, 2201109 (2022).
[89] K. Akaike, K. Kanai, H. Yoshida, J. y. Tsutsumi, T. Nishi, N. Sato, Y. Ouchi, and K. Seki, J. Appl. Phys. **104**, 023710 (2008).
[90] P. Schulz, L. L. Whittaker-Brooks, B. A. MacLeod, D. C. Olson, Y. L. Loo, and A. Kahn, Adv. Mater. Interfaces **2**, 1400532 (2015).
[91] Z.-L. Guan, J. B. Kim, H. Wang, C. Jaye, D. A. Fischer, Y.-L. Loo, and A. Kahn, Org. Electron. **11**, 1779 (2010).
[92] K. Akaike, K. Kanai, H. Yoshida, J. y. Tsutsumi, T. Nishi, N. Sato, Y. Ouchi, and K. Seki, J. Appl. Phys. **104**, 023710 (2008).
[93] F. Staub, H. Hempel, J.-C. Hebig, J. Mock, U. W. Paetzold, U. Rau, T. Unold, and T. Kirchartz, Phys. Rev. Appl. **6**, 044017 (2016).
[94] Z. Xing, S.-H. Li, P.-Y. Xu, H.-R. Tian, L.-L. Deng, Y.-R. Yao, B.-W. Chen, F.-F. Xie, M.-W. An, and D.-Q. Yun, Chem. Res. Chin. Univ. **38**, 75 (2022).
[95] L. Kavan, L. Steier, and M. Grätzel, J. Phys. Chem. C. **121**, 342 (2017).
[96] M. Sendner, P. K. Nayak, D. A. Egger, S. Beck, C. Müller, B. Epding, W. Kowalsky, L. Kronik, H. J. Snaith, A. Pucci, and R. Lovrinčić, Mater. Horiz. **3**, 613 (2016).
[97] K. Rajshekar and D. Kannadassan, J. Comput. Electron. **20**, 2331 (2021).
[98] J. A. Röhr, Phys. Rev. Appl. **11**, 054079 (2019).
[99] J. Siekmann, A. Kulkarni, S. Akel, B. Klingebiel, M. Saliba, U. Rau, and T. Kirchartz, Adv. Energy Mater. **13**, 2300448 (2023).
[100] N. F. Mott and R. W. Gurney, *Electronic processes in ionic crystals*. (1940).
[101] O. Çiçek, S. Kurnaz, A. Bekar, and Ö. Öztürk, Compos. B Eng. **174**, 106987 (2019).
[102] F. Schulte, Surf. Sci. **55**, 427 (1976).

[103] K. Choi, H.-C. Wen, H. Alshareef, R. Harris, P. Lysaght, H. Luan, P. Majhi, and B. Lee, *in Proceedings of the Proceedings of 35th European Solid-State Device Research Conference.*, 2005.
[104] V. Nádaždy, K. Gmucová, P. Nádaždy, P. Siffalovic, K. Vegso, M. Jergel, F. e. Schauer, and E. Majkova, J. Phys. Chem. C. **122**, 5881 (2018).
[105] J. Chrzanowski and B. Bieg, Appl. Surf. Sci. **540**, 148363 (2021).
[106] Z. Xing, S.-H. Li, P.-Y. Xu, H.-R. Tian, L.-L. Deng, Y.-R. Yao, B.-W. Chen, F.-F. Xie, M.-W. An, and D.-Q. Yun, Chem. Res. Chin. Univ., 1 (2022).
[107] L. Kavan, L. Steier, and M. Grätzel, J. Phys. Chem. C **121**, 342 (2017).
[108] J. Haddad, B. Krogmeier, B. Klingebiel, L. Krückemeier, S. Melhem, Z. Liu, J. Hüpkes, S. Mathur, and T. Kirchartz, Adv. Mater. Interfaces **7**, 2000366 (2020).
[109] T. Kirchartz, J. Bisquert, I. Mora-Sero, and G. Garcia-Belmonte, Phys. Chem. Chem. Phys. **17**, 4007 (2015).
[110] J. Hüpkes, U. Rau, and T. Kirchartz, Sol. RRL **6**, 2100720 (2022).
[111] B. Das, Z. Liu, I. Aguilera, U. Rau, and T. Kirchartz, Mater. Adv. **2**, 3655 (2021).
[112] M. Stocks, A. Cuevas, and A. Blakers, Prog. Photovoltaics Res. Appl. **4**, 35 (1996).
[113] Y. Shigesato and D. C. Paine, Appl. Phys. Lett. **62**, 1268 (1993).
[114] M. Mizuno, T. Miyamoto, T. O. T. Ohnishi, and H. H. H. Hayashi, Jpn. J. Appl. Phys. **36**, 3408 (1997).
[115] H. Kim, a. C. Gilmore, A. Pique, J. Horwitz, H. Mattoussi, H. Murata, Z. Kafafi, and D. Chrisey, J. appl. phys. **86**, 6451 (1999).
[116] Q. H. Fan, M. Deng, X. Liao, and X. Deng, J. Appl. Phys. **105**, 033304 (2009).
[117] E. Aydin, C. Altinkaya, Y. Smirnov, M. A. Yaqin, K. P. S. Zanoni, A. Paliwal, Y. Firdaus, T. G. Allen, T. D. Anthopoulos, H. J. Bolink, M. Morales-Masis, and S. De Wolf, Matter **4**, 3549 (2021).
[118] Z. Ma, Y. Dong, R. Wang, Z. Xu, M. Li, and Z. Tan, Adv Mater **35**, e2307502 (2023).
[119] M. Härtel, B. Li, S. Mariotti, P. Wagner, F. Ruske, S. Albrecht, and B. Szyszka, Sol. Energy Mater. Sol. Cells **252**, 112180 (2023).
[120] D. Hamaguchi, S.-i. Kobayashi, T. Uchida, Y. Sawada, H. Lei, and Y. Hoshi, Jpn. J. Appl. Phys. **55**, 106501 (2016).
[121] M. Jošt, L. Kegelmann, L. Korte, and S. Albrecht, Adv. Energy Mater. **10**, 1904102 (2020).
[122] Y. Smirnov, L. Schmengler, R. Kuik, P. A. Repecaud, M. Najafi, D. Zhang, M. Theelen, E. Aydin, S. Veenstra, and S. De Wolf, Adv. Mater. Technol. **6**, 2000856 (2021).
[123] W. Tress and O. Inganäs, Sol. Energy Mater. Sol. Cells **117**, 599 (2013).
[124] O. J. Sandberg, J. Kurpiers, M. Stolterfoht, D. Neher, P. Meredith, S. Shoaee, and A. Armin, Adv. Mater. Interfaces **7**, 2000041 (2020).
[125] W. Tress, A. Petrich, M. Hummert, M. Hein, K. Leo, and M. Riede, Appl.

Phys. Lett. **98** (2011).
[126] J. Wagner, M. Gruber, A. Wilke, Y. Tanaka, K. Topczak, A. Steindamm, U. Hörmann, A. Opitz, Y. Nakayama, H. Ishii, J. Pflaum, N. Koch, and W. Brütting, J. Appl. Phys. **111**, 054509 (2012).
[127] A. M. Cowley and S. M. Sze, J. Appl. Phys. **36**, 3212 (1965).
[128] Y. Kuang, B. Macco, B. Karasulu, C. K. Ande, P. C. Bronsveld, M. A. Verheijen, Y. Wu, W. M. Kessels, and R. E. Schropp, Sol. Energ. Mat. Sol. Cells **163**, 43 (2017).
[129] K. P. Zanoni, A. Paliwal, M. A. Hernández-Fenollosa, P. A. Repecaud, M. Morales-Masis, and H. J. Bolink, Adv. Mater. Technol. **7**, 2101747 (2022).
[130] E. Aydin, C. Altinkaya, Y. Smirnov, M. A. Yaqin, K. P. Zanoni, A. Paliwal, Y. Firdaus, T. G. Allen, T. D. Anthopoulos, and H. J. Bolink, Matter **4**, 3549 (2021).
[131] S. Mariotti, K. Jäger, M. Diederich, M. S. Härtel, B. Li, K. Sveinbjörnsson, S. Kajari-Schröder, R. Peibst, S. Albrecht, and L. Korte, Sol. RRL **6**, 2101066 (2022).
[132] H. Kanda, A. Uzum, A. K. Baranwal, T. N. Peiris, T. Umeyama, H. Imahori, H. Segawa, T. Miyasaka, and S. Ito, J. Phys. Chem. C **120**, 28441 (2016).
[133] S. Zhu, X. Yao, Q. Ren, C. Zheng, S. Li, Y. Tong, B. Shi, S. Guo, L. Fan, and H. Ren, Nano Energy **45**, 280 (2018).
[134] M. Härtel, B. Li, S. Mariotti, P. Wagner, F. Ruske, S. Albrecht, and B. Szyszka, Sol. Energ. Mat. Sol. Cells **252**, 112180 (2023).
[135] T. W. Jones, A. Osherov, M. Alsari, M. Sponseller, B. C. Duck, Y.-K. Jung, C. Settens, F. Niroui, R. Brenes, C. V. Stan, Y. Li, M. Abdi-Jalebi, N. Tamura, J. E. Macdonald, M. Burghammer, R. H. Friend, V. Bulović, A. Walsh, G. J. Wilson, S. Lilliu, and S. D. Stranks, Energy Environ. Sci. **12**, 596 (2019).
[136] J. T.-W. Wang, Z. Wang, S. Pathak, W. Zhang, D. W. deQuilettes, F. Wisnivesky-Rocca-Rivarola, J. Huang, P. K. Nayak, J. B. Patel, and H. A. M. Yusof, Energy Environ. Sci. **9**, 2892 (2016).
[137] G. Kim, H. Min, K. S. Lee, D. Y. Lee, S. M. Yoon, and S. I. Seok, Sci. **370**, 108 (2020).
[138] M. Saliba, T. Matsui, J. Y. Seo, K. Domanski, J. P. Correa-Baena, M. K. Nazeeruddin, S. M. Zakeeruddin, W. Tress, A. Abate, A. Hagfeldt, and M. Gratzel, Energy Environ. Sci. **9**, 1989 (2016).
[139] J. Zhao, Y. Deng, H. Wei, X. Zheng, Z. Yu, Y. Shao, and J. H. Jeffrey E. Shield, Sci. Adv. **3**, eaao5616 (2017).
[140] G. Williamson and W. Hall, Acta Metall **1**, 22 (1953).
[141] G. Su, R. Yu, Y. Dong, Z. He, Y. Zhang, R. Wang, Q. Dang, S. Sha, Q. Lv, Z. Xu, Z. Liu, M. Li, and Z. a. Tan, Adv. Energy Mater. **14**, 2303344 (2023).
[142] H. Tsai, R. Asadpour, J.-C. Blancon, C. C. Stoumpos, O. Durand, J. W. Strzalka, B. Chen, R. Verduzco, P. M. Ajayan, and S. Tretiak, Sci. **360**, 67 (2018).
[143] O. Carp, Prog. Solid State Chem. **32**, 33 (2004).

[144] M. A. Boda, C. Chen, X. He, L. Wang, and Z. Yi, J. Am. Ceram. Soc. **106**, 3584 (2023).
[145] H. Tsai, R. Asadpour, J.-C. Blancon, C. C. Stoumpos, O. Durand, J. W. Strzalka, B. Chen, R. Verduzco, P. M. Ajayan, S. Tretiak, J. Even, M. A. Alam, M. G. Kanatzidis, W. Nie, and A. D. Mohite, Science **360**, 67 (2018).
[146] T. C. Wei, H. P. Wang, T. Y. Li, C. H. Lin, Y. H. Hsieh, Y. H. Chu, and J. H. He, Adv. Mater. **29**, 1701789 (2017).
[147] J. F. Ziegler, M. D. Ziegler, and J. P. Biersack, *SRIM–The stopping and range of ions in matter (2010)*. (2010).
[148] T. Welzel and K. Ellmer, Vak. Forsch. Prax. **25**, 52 (2013).
[149] J. Yu, R. K. Kalia, and P. Vashishta, Appl. Phys. Lett. **63**, 3152 (1993).
[150] P. G. Klemens, Proc. R. Soc. Lond. A. Math. Phys. Sci. **208**, 108 (1951).
[151] Y. K. Koh, in *Encyclopedia of Nanotechnology* (Springer, Dordrecht, 2012), pp. 2704.
[152] J. M. Ziman, *Electrons and phonons: the theory of transport phenomena in solids*. (Oxford university press, 2001).
[153] G. K. Chang and R. E. Jones, Phys. Rev. **126**, 2055 (1962).
[154] D. G. Cahill, Microscale Thermophys. Eng. **1**, 85 (1997).
[155] H.-K. Kim, D.-G. Kim, K.-S. Lee, M.-S. Huh, S. H. Jeong, and K. I. Kim, Appl. Phys. Lett. **86**, 183503 (2005).
[156] E. J. Juarez-Perez, L. K. Ono, and Y. Qi, J. Mater. Chem. A **7**, 16912 (2019).
[157] F. C. Schaefer, I. Hechenbleikner, G. A. Peters, and V. Wystrach, Chem. Soc. **81**, 1466 (1959).
[158] W. T. M. Van Gompel, R. Herckens, G. Reekmans, B. Ruttens, J. D'Haen, P. Adriaensens, L. Lutsen, and D. Vanderzande, J. Phys. Chem. C **122**, 4117 (2018).
[159] F. Lang, M. Jost, K. Frohna, E. Kohnen, A. Al-Ashouri, A. R. Bowman, T. Bertram, A. B. Morales-Vilches, D. Koushik, E. M. Tennyson, K. Galkowski, G. Landi, M. Creatore, B. Stannowski, C. A. Kaufmann, J. Bundesmann, J. Rappich, B. Rech, A. Denker, S. Albrecht, H. C. Neitzert, N. H. Nickel, and S. D. Stranks, Joule **4**, 1054 (2020).
[160] K. Parlinski and Y. Kawazoe, Eur. Phys. J. B. **13**, 679 (2000).
[161] M. Nastasi, J. Mayer, and J. K. Hirvonen, *Ion-Solid Interactions - Fundamentals and Applications*. (Cambridge University Press, 1996).
[162] I. S. Zhidkov, D. W. Boukhvalov, A. F. Akbulatov, L. A. Frolova, L. D. Finkelstein, A. I. Kukharenko, S. O. Cholakh, C.-C. Chueh, P. A. Troshin, and E. Z. Kurmaev, Nano Energy **79**, 105421 (2021).
[163] T. J. Jacobsson, J. P. Correa-Baena, E. Halvani Anaraki, B. Philippe, S. D. Stranks, M. E. Bouduban, W. Tress, K. Schenk, J. Teuscher, J. E. Moser, H. Rensmo, and A. Hagfeldt, J. Am. Chem. Soc. **138**, 10331 (2016).
[164] J. C. Vickerman and I. S. Gilmore, *Surface Analysis – The Principal Techniques*. (John Wiley & Sons, 2009).
[165] J. S. Kim, P. K. H. Ho, D. S. Thomas, R. H. Friend, F. Cacialli, G.-W. Bao,

and S. F. Y. Li, Chem. Phys. Lett. **315**, 307 (1999).
[166] Q. Jiang, Y. Zhao, X. Zhang, X. Yang, Y. Chen, Z. Chu, Q. Ye, X. Li, Z. Yin, and J. You, Nat. Photonics **13**, 460 (2019).
[167] P. Tockhorn, J. Sutter, A. Cruz, P. Wagner, K. Jäger, D. Yoo, F. Lang, M. Grischek, B. Li, and J. Li, Nat. Nanotechnol. **17**, 1214 (2022).
[168] C. Ulbrich, A. Gerber, K. Hermans, A. Lambertz, and U. Rau, Prog. Photovolt.: Res. Appl. **21**, 1672 (2013).
[169] X. Y. Chin, D. Turkay, J. A. Steele, S. Tabean, S. Eswara, M. Mensi, P. Fiala, C. M. Wolff, A. Paracchino, and K. Artuk, Sci. **381**, 59 (2023).
[170] Y. Wang, S. Akel, B. Klingebiel, and T. Kirchartz, Adv. Energy Mater. **14**, 2302614 (2024).
[171] M. Sugawara, *Plasma etching: fundamentals and applications*. (OUP Oxford, 1998).
[172] A. Sinha, J. Qian, S. L. Moffitt, K. Hurst, K. Terwilliger, D. C. Miller, L. T. Schelhas, and P. Hacke, Prog. Photovolt.: Res. Appl. **31**, 36 (2023).
[173] H. Ye, S. Huang, C. Qian, Z. Sun, Y. Chen, X. Song, Y. Zhang, N. Wang, Y. Hu, and Y. Yang, Sol. RRL **7**, 2300334 (2023).

Acknowledgements

I would like to thank all those who made this work possible. Specific thanks are due to the following people for their contributions:

- Prof. Dr. Uwe Rau for the supervision and examination of this thesis, for providing the opportunity to conduct my doctoral research at IMD3 and ensuring excellent working conditions, for teaching the photovoltaics course and guidance in tandem-based research.
- Dr. Kaining Ding for being an excellent supervisor who keeps me on the right track, for continuous support during my whole studies, for his ingenious ideas and his criticism, for his excellent advice on this thesis, daily research, internal collaboration and communication.
- Dr. Weiyuan Duan for her assistance with my start in institute and advice about everything concerning tandem solar cells.
- Dr. Benjamin Klingebiel for being experienced engineers who provided professional knowledge, continuous assistance with everything, and for being a good friend.
- Prof. Dr. Thomas Kirchartz for his excellent ideas and discussion about experiments and simulations, and his advice about paper writing, submission and revision.
- Dr. Karsten Bittkau for fruitful discussions that gave direction for the work on interface-recombination-dependent quantum efficiency, for daily discussion and assistance with optical characterizations.
- Dr. Zhifa Liu for his knowledge and assistance in perovskite-related experiments and issues.
- Johannes Pfennings for his expertise concerning mask design and long discussion on mask improvements.
- Dr. Jürgen Huepkes for his assistance with the sputtering tools and legal challenges.
- Alexander Eberst for his assistance in writing this thesis, for inspiring discussion about the work of sputtering damage.
- Dr. Andreas Lambertz, Volker Lauterbach, Alain Doumit, Hildegard Siekmann for their groundwork in silicon bottom cells, for being reliable in everting they do.

- Prof. Dr. Svetlana Vitusevich, Yongqiang Zhang, Denys Pustovyi for their continuous assistance in characterizations which are unavailable in our institute.
- Quntao Tang, Depeng Qiu, Huimin Li, Genghua Yan, Ye Yuan, Haijin Li, Bingbing Chen for valuable suggestions and assistance in both scientific research and career development.
- Binbin Xu, Kai Zhang, Yanxin Liu, Yaqin Muhammad Ainul, Gaosheng Huang, Nan Sun for taking classes, doing experiments, attending conferences, partying together.
- The many who assisted with experiments and characterization: Wilfried Reetz, Silke Lynen, Brigitte Zwaygardt, Christian Bock, Markus Hülsbeck, Dorothea Lennartz, Irina Kühn, Niklas Scheer.
- All colleagues in Jülich.
- Finally, I would like to express my deepest thanks to my family for continuous support and encouragement.

Band / Volume 699
Ab Initio-based large-scale Atomistic Simulations of Cathode Materials for Secondary Batteries: From Computational Methodologies to Applications towards improved Structural and Chemical Stability
K. Köster (2026), x, 204, x pp
ISBN: 978-3-95806-898-8

Band / Volume 700
Materials Design, Processing and Application of Proton-Conducting Oxides for Electrochemical Energy Conversion
Y. Zeng (2026), vii, 117 pp
ISBN: 978-3-95806-899-5

Band / Volume 701
Accelerating the discovery of alkaline-stable anion exchange membrane materials via computational exploration
F. P. Tipp (2026), xii, 135 pp
ISBN: 978-3-95806-900-8

Band / Volume 702
Methods for Investigating the Structure-Performance Correlation in Membrane Electrode Assemblies
N. Utsch (2026), XIII, 138, LXVII pp
ISBN: 978-3-95806-901-5

Band / Volume 703
Hot-Spot Formation in Cu(In,Ga)Se_2 Thin Film Solar Cells
S. Nofal (2026), xvii, 131 pp
ISBN: 978-3-95806-903-9

Band / Volume 704
Machine Learning Guidance of Manufacturing Process of Solid Oxide Cells
T. Le Dinh (2026), xxi, 122 pp
ISBN: 978-3-95806-904-6

Band / Volume 705
Drivers of spatiotemporal variability of European terrestrial ecosystem processes
C. Poppe Téran (2026), 254 pp
ISBN: 978-3-95806-905-3

Schriften des Forschungszentrums Jülich
Reihe Energie & Umwelt / Energy & Environment

Band / Volume 706
Characterization of Nitrogen Reduction Reaction Catalysts for the electrochemical Ammonia Synthesis
D. Sachse (2026), xi, 235, 6 pp
ISBN: 978-3-95806-907-7

Band / Volume 707
Autonomous Image Analysis to Accelerate the Discovery and Integration of Energy Materials
A. Colliard Granero (2026), xiv, 156 pp
ISBN: 978-3-95806-910-7 (Print)
ISBN: 978-3-95806-911-4 (E-Book)

Band / Volume 708
Effect of Soil Mechanical Properties, Root Tip Geometry, and Mucilage on Penetration Restistance to Root Growth
R. K. Janakiram (2026), xxviii, 98 pp
ISBN: 978-3-95806-914-5 (Print)
ISBN: 978-3-95806-915-2 (E-Book)

Band / Volume 709
European Energy Transition – Germany in the Heart of Europe
T. Klütz, P. Dunkel, T. Busch, J. Linssen, D. Stolten (2026), V, 54 pp
ISBN: 978-3-95806-916-9 (Print)
ISBN: 978-3-95806-917-6 (E-Book)

Band / Volume 710
Development of High-Efficiency Perovskite/Silicon Tandem Solar Cells
Q. Yang (2026), 264 pp
ISBN: 978-3-95806-920-6 (Print)
ISBN: 978-3-95806-921-3 (E-Book)

Weitere ***Schriften des Verlags im Forschungszentrum Jülich*** unter
http://wwwzb1.fz-juelich.de/verlagextern1/index.asp

Energie & Umwelt / Energy & Environment
Band / Volume 710
ISBN 978-3-95806-921-3

Mitglied der Helmholtz-Gemeinschaft

JÜLICH
Forschungszentrum